

**MODELING OF FOREST ABOVE-GROUND
BIOMASS AND EVAPOTRANSPIRATION
DYNAMICS**

Xin Tian

Examining committee:

Prof.dr.ir. A. Veldkamp
Prof.dr. A.K. Skidmore
Prof.dr. H-J Hendricks Franssen
Prof. E. Chen

University of Twente
University of Twente
Forschungszentrum Juelich
Chinese Academy of Forestry

ITC dissertation number 270
ITC, P.O. Box 217, 7500 AE Enschede, The Netherlands

ISBN 978-90-365-3882-4
DOI 10.3990/1.9789036538824

Cover designed by Benno Masselink
Printed by ITC Printing Department
Copyright © 2015 by Xin Tian



UNIVERSITY OF TWENTE.

ITC

FACULTY OF GEO-INFORMATION SCIENCE AND EARTH OBSERVATION

MODELING OF FOREST ABOVE-GROUND BIOMASS AND EVAPOTRANSPIRATION DYNAMICS

DISSERTATION

to obtain
the degree of doctor at the University of Twente,
on the authority of the rector magnificus,
prof.dr. H. Brinksma
on account of the decision of the graduation committee,
to be publicly defended
on Thursday 23 April 2015 at 13.45 hrs

by

Xin Tian

born on 26/02/1979

in Tianzhu, Guizhou, P.R.China

This thesis is approved by
Prof.dr. Zhongbo Su, promotor
Prof.dr. Zengyuan Li, promotor
Dr.ir. Christiaan van der Tol, co-promotor

Dedicated to my late parents.

Acknowledgements

Sitting in my chair and viewing some homing birds in the sky at dusk, I was reminded of the following verse: “I leave no trace of wings in the air, but I am glad I have had my flight”, from *Fireflies* by Rabindranath Tagore (1928). I recently realized that I must soon say “goodbye” to some of the people I know after finalizing this thesis for my PHD work at ITC. To acknowledge the help I have received from people who have faithfully supported me during my PHD study, here, on this Thanksgiving Day, I express sincere thanks.

Ten years ago, I met Prof. Bob Su on the beautiful island of Gulangyu in Xiamen City, China, during the kickoff symposium of the “Dragon Programme”, the largest international cooperation platform for Earth observation between the Ministry of Science and Technology (MOST) of the P.R.China and the European Space Agency (ESA). I was impressed by his enthusiasm, his persistence in scientific interests, his humor, and his humility during conversation. One year later, I met Prof. Su again, on another island, Santorini in Greece, when I was still a symposium tea boy. After discussions with Prof. Zengyuan Li, the supervisor of my Master’s work, Prof. Su decided to provide a chance to me to study for my PHD at ITC.

First and foremost I offer my sincerest gratitude to my promoter Prof. Bob Su and co-promoter Prof. Zengyuan Li, for their extraordinary support throughout my PHD study and for their patience and knowledge whilst allowing me the room required to work in my own way. They gave me the opportunity to undertake this study and also extended my view of scientific research. Every time I was inundated by “hydrology” or suspended in the “atmosphere”, Prof.Su knew how to draw me back the right way. His deep insights into the scientific issues and his broad knowledge of science directed me to undertake a study with scientific significance. As a result of his invaluable guidance and advice, I am now finally finishing my PHD study. Prof. Li has been tolerant to my mistakes and, since I joined his research team, has inspired me to do my work (and my job) with scientific exactitude. He provided much support during my work. The manner and attitude of both of my mentors motivated me to be ingenuous and humble in life, as well as penetrating, enthusiastic and serious in science. I attribute the skill of my doctoral degree to their encouragement and efforts.

I feel indebted to my two co-promoters, Dr. Christiaan van der Tol and Prof. Xin Li. Christiaan taught me much regarding eco-hydrological processes and helped clarify my manuscripts and my thesis. From him, I was able to learn how to find scientific gaps and then how to write scientific manuscripts. His elaborate and everlasting

help and guidance made this study valuable. He is also a close friend of mine and many fruitful discussions between the two of us improved my study. His office door was always open without an advanced appointment. To him I am ever grateful. Great appreciation is also given to Prof. Xin Li for his excellent organization of the Watershed Allied Telemetry Experimental Research (WATER) experiment, which provided the required data for running the models. Prof. Li eventually taught me how to fish rather than just giving me a fish. He directed me in the types of studies that had previously been undertaken and suggested studies for my work on the Heihe River Basin (HRB). My study also benefited from his countless instruction and support. He examined each manuscript I wrote and provided invaluable suggestions for them. Our first email exchange often recurs to me; in the email I asked for help with the study area and asked some scientific questions. Although he did not know me at the time, he replied to me immediately with much kindness and modesty.

I am deeply grateful to Prof. Erxue Chen at my institute (Research Institute of Forest Resource Information Techniques (IFRIT), Chinese Academy of Forestry) for patient and constructive suggestions and guidance during my study, as well as during my job. His willingness to motivate me contributed tremendously to my study and work. On several occasions, he even helped me with some of my daily work at IFRIT so I would have time for this study.

Without their kind and scientific direction and instruction, this thesis would not have been completed!

My study would also have been impossible without the support of the ITC and I owe a great deal to various administrative departments including the education and research affairs department, the financial and economic affairs department, the library and archive service center, the ICT service center, and the reception and international hotel of ITC for their timely and intense help. I also thank Ms. Loes Colenbrander, Ms. Anke Koning and Ms. Tina Butt-Castro, who provided administrative support for my study. Special thanks are given to Prof. Tom Veldkamp (the Dean of ITC), Prof. Martien Molenaar, and other managers at ITC who provided excellent research organization and management.

I also owe thanks to colleagues in water resource department (WRS) at ITC and at IFRIT who shared interesting and meaningful talks and seminars. Special thanks are given to the director, Prof. Hongbo Ju, and the deputy directors, Prof. Hong Wang and Prof. Huiru Zhang of IFRIT, for allowing me to leave my job temporarily for studying abroad. Many thanks are given to colleagues, including Zhihai Gao, Lina

Bai, Yong Pang, Shiming Li, Qingwang Liu, Fengyu Wang, Bingxiang Tan, Honggan Wu, Ying Lu, Yingzhi Bao, Haisheng Xu, Dan Liu, Yaxin Wang, who helped during my absence from IFRIT.

Colleagues in the Cold and Arid Regions Environmental and Engineering Research Institute at the Chinese Academy of Sciences, particularly Prof. Mingguo Ma, Dr. Xufeng Wang, Dr. Xiaoduo Pan, Dr. Shuguo Wang and Dr. Tangtang Zhang are thanked for their hospitality and help during experiments, as well as for data and models.

I owe gratitude to Mr. Guocheng Zhang, Dr. Xiaohan Liao, Dr. Jiahong Li, from the National Remote Sensing Center of China (NRSCC), and Dr. Yves-Louis Desnos, Dr. Andrew Zmuda, from European Space Research Institute (ESRIN), for their efforts to the “Dragon Programme”, during which I was able to get to know Prof. Su and next to study at ITC.

I am grateful to my football buddies at ITC, Donghai Zheng, Alain P. Frances, Mustafa Gokmen and Cesar Cisneros Vaca, who let me enjoy an interesting life with them in the Netherlands. In my daily life in the Netherlands, I have been blessed with a friendly and cheerful Chinese community that is like a big family and I never felt homesick. Special thanks go to Longhui Li, Guangyi Wang, Yijian Zeng, Qiuju Zhang, Wei Ouyang, Xuelei Wang, Changbo Qin, Lei Zhong, Zhenshan Yang, Xia Li, Teng Fei, Meng Bian, Shi Pu, and Xiaojing Wu for hospitable receptions and their friendly compotation of beers, wines, and whiskies. Special thanks are given to Xuelong Chen for timely help and conversations regarding my thesis. I also owe appreciation to Tina Tian, Yanqiu Xing, Lichun Wang, Guofeng Wu and Tiejun Wang who shared useful experiences regarding study and life in the Netherlands. I thank my housemate Peng Wang for sharing meals and his fantastic piano playing; and new alumni, Xiaoling Wang, Cunbo Han, Xiaolong Yu, Xu Yuan, and Peiqi Yang for their accompaniment and help.

I am thankful to the Masters and PHD students at IFRIT, among them Min Yan, Mei Li, Chunmei Li, Wenwu Fan, Qi Feng, and Lei Zhao, who assisted me in conducting experiments, in data preparation, and in running models.

Finally, I feel deeply indebted to my late parents who passed away during the period of my study. As the old Chinese saying goes, “Tree prefer calm while wind not subside; Son choose filial while parents died”. I am deeply appreciative to my senior brothers for taking care of my family during my stay in the Netherlands. I also owe much to my wife, Dongying Fu, for accompanying me during the toughest

period of my life. She has often had to bear the first brunt of my frustration against the world with equanimity and love; but she has never hesitated to fully support my study and my work with encouragement and trust.

Abbreviation

3D	Three-Dimension
AET	Actual ET
AGB	Above-Ground Biomass
ALOS	Advanced Land Observation Satellite
ALS	Airborne Laser Scanning
ANPP	Above-Ground NPP
APAR	Absorbed Photosynthetically Active Radiation
ARVI	Atmospherically Resistant Vegetation Index
ASL	Atmospheric Surface Layer
ASTER	Advanced Spaceborne Thermal Emission and Reflection Radiometer
AWS	Automatic Weather Station
BAS	Bulk Atmospheric Similarity
Biome-BGC	Biome-BioGeochemical Cycles
BPLUT	Biome Parameter Look Up Table
CART	Classification and Regression Trees
CAS	Chinese Academy of Science
CCD	Charge Coupled Device
CCFG	Conversion of Cropland to Forest and Grassland
COMPLICATE	Complicate Observations and Multi-Parameter Land Information Constructions on Allied Telemetry Experiment
CW	Crown Width
DAO	Data Assimilation Office
DBH	Diameter at Breast Height
DEM	Digital Elevation Model
DSM	Digital Surface Model
DSW	Downwelling Short Wave
EB	Energy Balance
EC	Eddy Covariance
ED	Euclidean Distance
ESA	European Space Agency
ESRIN	European Space Research Institute
ET	Evapotranspiration
ETF	Evaporative Fraction
FAI	Frontal Area Index
FD	Fuzzy Distance
fPAR	Fraction of Absorbed Photosynthetically Active Radiation
GDEM	Global Digital Elevation Model

GEC	Geocoded-Ellipsoid Correction
GLAS	Geoscience Laser Altimeter System (GLAS)
GLASS	Global Land surface Satellite
GORT	Geometric–Optical and Radiative Transfer
GPP	Gross Primary Productivity
GRNNs	General Regression Neural Networks
GTC	Geo-coded Terrain Correction
HEIFE	Heihe Basin Field Experiment
HiWATER	Heihe Watershed Allied Telemetry Experimental Research
HRB	Heihe River Basin
HRG	HighResolution Geometrical
ICESat	Ice, Cloud, Land Elevation Satellite
InSAR	Interferometric SAR
IRI	Infrared Index
JAXA	Japan Aerospace Exploration Agency
<i>k</i> -NN	<i>k</i> -Nearest Neighbour
LAD	Leaf Area Density
LA	Leaf Area Index
LiDAR	Light Detection and Ranging
LOO	Leave-One-Out
LST	Land Surface Temperature
LUCC	Land Use Cover Change
LUE	Light Use Efficiency
MD	Mahalanobis Distance
MOD_17	MODIS MOD17 GPP Model
MOD16_ET	MODIS MOD16 ET
MOS	Monin–Obukhov Similarity
MOST	Ministry of Science and Technology, P.R. China
MPEs	Mean Percentage Errors
NASA	National Aeronautics and Space Administration
NDVI	Normalized Difference Vegetation Index
NEE	Net Ecosystem Exchange
NEP	Net Ecosystem Productivity
NPP	Net Primary Productivity
NRSCC	National Remote Sensing Center of China
NTSG	Numerical Terradynamic Simulation Group
PAIe	Effective Plant Area Index
PALSAR	Phased Array L-band Synthetic Aperture Radar
PAR	Photosynthetically Active Radiation

PC	Principle Components
POLInSAR	Polarimetric Interferometric SAR
QMs	Qilian Mountains
RF	Random Forest
RHS	Right Hand Side
RMSE	Root Mean Square Error
RVI	Ratio Vegetation Index
SAR	Synthetic Aperture Radar
SCS+C	Sun-Canopy-Sensor plus C
SD	Stand Density
SD00	Schaudt and Dickinson (2000)
SEBS	Surface Energy Balance System
SLC	Single Look Complex
SMLR	Stepwise Multiple Linear Regression
SPOT-5	Satellite Probatoire d'Observation de la Terre-5
SVM	Support Vector Machine
SVR	Support Vector Regression
SVs	Support Vectors
TCR	Topographically Corrected Radiance
TM	Landsat Thematic Mapper-5
TRC	Terrain Radiometric Correction
USGS	United States Geological Survey
VPD	Vapor Pressure Deficit
WATER	Watershed Allied Telemetry Experimental Research
WPL	Webb-Pearman-Leuning
WRF	Weather Research and Forecasting
WUE	Water Use Efficiency

Table of Contents

Chapter 1 Introduction	1
1.1 Background	2
1.1.1 The Role of Forests in The Global Carbon and Water Cycle	2
1.1.2 The Eco-hydrology of The Heihe River Basin	5
1.2 Research Problem	8
1.3 Objectives	9
1.4 Thesis Outline	11
Chapter 2 Evaluation of Parametric and Non-parametric Methods to Estimate Forest Above-Ground Biomass in The Qilian Mountains Using Multi-Parameter Remote Sensing Data.....	13
Abstract.....	14
2.1 Introduction.....	15
2.2 The Study Area and Data	18
2.3 Methodology	20
2.3.1 The k-NN Algorithm	20
2.3.2 Multidimensional Distance Measures.....	20
2.3.3 The Regression Methods	21
2.3.4 Forest AGB Calculation Based on Growth Equations.....	22
2.3.5 LiDAR Data Processing	22
2.3.6 SPOT-5 Data Processing	23
2.3.7 ALOS PALSAR Data Processing.....	23
2.3.8 Ancillary Data Preparation	24
2.3.9 Optimization of k-NN.....	24
2.4 Results and Discussion.....	25
2.4.1 Evaluation of k-NN Configurations.....	25
2.4.2 Estimations of Regression Models	26
2.4.3 Comparison of Results from The Best k-NN Configuration and LiDAR	27
2.5 Discussion.....	29
2.6 Conclusion	30
Chapter 3 Improvement of Estimating Forest Above-Ground Biomass over The Qilian Mountains Using Multi-Parameter Remote Sensing Data.....	33
Abstract.....	34
3.1 Introduction.....	35
3.2 Ground and Remote Sensing Data	36
3.3 Methodology	37
3.3.1 The SCS+C Radiometric Terrain Correction.....	37

3.3.2	Forest Discrimination	38
3.3.3	Regression Method	40
3.3.4	The k-NN Method	41
3.3.5	Construction of An Optimal k-NN	41
3.4	Results.....	42
3.4.1	The Regression Estimation	42
3.4.2	The k-NN Estimation.....	43
3.4.3	A Comparison of The Performance of The Two Methods	48
3.5	Discussion.....	48
3.6	Conclusion	51

Chapter 4 Modeling of Forest Above-Ground Biomass Dynamics Using Multi-source Remote Sensing Data and Incorporated Models53

	Abstract.....	54
4.1	Introduction.....	55
4.2	The Observations and Study Data.....	58
4.3	Description of Models.....	60
4.3.1	Random Forest.....	60
4.3.2	k-Nearest Neighbour.....	61
4.3.3	Support Vector Regression.....	61
4.3.4	The MOD_17 Model	63
4.3.5	The Biome-BGC Model	64
4.4	Methodology.....	65
4.4.1	Incorporating Random Forest with The k-Nearest Neighbour and The Support Vector Regression.....	65
4.4.2	Incorporating MOD_17 with Biome-BGC.....	66
4.4.3	Simulations of Carbon Fluxes and Conversion of NPP Estimates to Forest AGB Increments	68
4.5	Results.....	68
4.5.1	Determination of The Optimal Configurations for The k-Nearest Neighbour and Support Vector Regression	68
4.5.2	The Forest Above-Ground Biomass Estimation.....	69
4.5.3	Incorporation of The MOD_17 GPP Model with The Biome-BGC Model.....	71
4.5.4	Simulations of Annual Forest Carbon Flux and Dynamic Analyses of Forest AGB	75
4.6	Discussion.....	81
4.7	Conclusion	85

Chapter 5 Estimating Zero-Plane Displacement Height and Aerodynamic Roughness Length Using Synthesis of LiDAR and SPOT-5 Data.....	87
Abstract.....	88
5.1 Introduction.....	89
5.2 Site Observation.....	90
5.3 Methodology.....	91
5.3.1 Remote Sensing Models for Estimating d and z_{0m}	91
5.3.2 Model Sensitivity.....	93
5.3.3 Forest Structural Parameters Estimated by Remote Sensing Data.....	95
5.4 Results.....	98
5.4.1 Forest Structural Parameters Estimated from Airborne LiDAR and SPOT-5 Data.....	98
5.4.2 The d and z_{0m} Maps from Remote Sensing Models.....	100
5.4.3 Validation and Comparison of d and z_{0m} Results.....	101
5.5 Discussion.....	105
5.6 Conclusion.....	107
Chapter 6 Simulation of Evapotranspiration Using Time-Series Parameterization of The Surface Energy Balance System (SEBS) Over Forests Within The Qilian Mountains.....	109
Abstract.....	110
6.1 Introduction.....	111
6.2 The Observations and Study Data.....	113
6.3 Methodology.....	114
6.3.1 The Surface Energy Balance System.....	114
6.3.2 Roughness Length Models.....	116
6.3.3 Long-Term Parameterization for SEBS.....	117
6.4 Results.....	117
6.4.1 The Parameterization of SEBS.....	117
6.4.2 A Comparison of ET Estimates between EC Measurements, SEBS Simulations and MODIS MOD16 Products.....	118
6.4.3 Interannual ET Simulations Using SEBS.....	119
6.5 Discussion.....	124
6.6 Conclusion.....	126
Chapter 7 Synthesis.....	127
7.1 Introduction.....	128
7.2 Results.....	130
7.2.1 Estimations of Forest Above-Ground Biomass.....	130
7.2.2 Modeling of Forest Above-Ground Biomass Dynamics.....	131

7.2.3	The Long-Term Parameterization and Evapotranspiration	
	Simulation of The Surface Energy Balance System	132
7.3	Discussion and Conclusions.....	135
7.4	Limitations and Future Work.....	139
	Bibliography.....	143
	Summary	177
	Samenvatting.....	181
	Author's Biography	185
	ITC Dissertation List.....	186

List of Figures

Fig. 1-1 A sub-basin partition and land cover map of the HRB.	6
Fig. 1-2 Framework of this thesis.	12
Fig. 2-1 The location and terrain conditions of the QMs within the upper reach of the HRB.	19
Fig. 2-2 Correlation R (left) and RMSE (right) of LOO tests on the k -NN configurations.	25
Fig. 2-3 Correlation R (left) and RMSE (right) of the best performance for each distance measure.	26
Fig. 2-4 Relative difference map between the best k -NN and LiDAR estimations of forest AGB (in tonnes ha^{-1}).	28
Fig. 2-5 Histogram and accumulative probability distribution of the relative difference map.	28
Fig. 3-1 The decision tree for the forest and non-forest classification.	39
Fig. 3-2 The forest/non-forest map of the study area.	40
Fig. 3-3 The fitted results of the measured and predicted value based on a stepwise multiple linear regression.	43
Fig. 3-4 The R^2 and RMSE of the different k -NN configurations.	44
Fig. 3-5 The R^2 ((a) and (b)) and RMSE ((c) and (d)) of the three distance estimations based on uncorrected and corrected Feature (8) in Table 3-1.	45
Fig. 3-6 The grade distribution of forest AGB over QMs.	46
Fig. 3-7 The cross-validation of the optimum k -NN estimation using the SCS+C process.	47
Fig. 3-8 The cross-validation of the optimum k -NN estimation without a SCS+C process.	47
Fig. 3-9 The cross-validation results of the stepwise multiple linear regression.	48
Fig. 4-1 The overall flowchart of this study.	57
Fig. 4-2 Cross-validation for optimum SVR and k -NN estimations.	70
Fig. 4-3 The upscaled grade distribution of forest AGB over the study area (1 km resolution).	71
Fig. 4-4 Comparisons and validations of the GPPs from the original MODIS products and from the optimized MOD_17 GPP model.	72
Fig. 4-5 The best fit relationship between the GPPs from the Biome-BGC and MOD_17 models eight day outputs ($P < 0.001$).	73
Fig. 4-6 Comparisons and validations of the GPPs from the default and calibrated Biome-BGC.	74
Fig. 4-7 Comparisons and validations of the NEEs from the default and calibrated Biome-BGC.	75

Fig. 4-8 Validation of thirteen-years of annual forest AGB increments converted from the ANPPs of the calibrated Biome-BGC using calculations from tree ring data.	76
Fig. 4-9 The upscaled forest AGB reference map (1 km) in 2009 and the annual forest AGB increments from 2000 to 2012.	81
Fig. 5-1 Validation of HL (a), FBH (b), CW (c), SD (d) and PAIe (e) estimates from LiDAR and SPOT-5 data. HL for Lorey's mean height, FBH for first branch height, CW for crown width, SD for stand density and PAIe for effective plant area index.	99
Fig. 5-2 Area-wide d (left) and z_{0m} (right) maps based on CM88 (a, b), RA94 (c, d), SD00 (e, f) and NA08 (g, h) model (unit: meter). CM88, RA94, SD00 and NA08 are the models of Choudhury and Monteith (1988), Raupach (1994), Schaudt and Dickinson (2000) and Nakai et al. (2008), respectively.	101
Fig. 5-3 Histograms (black column) and accumulative probability (blue line) of relative difference of d (left) and z_{0m} (right) from CM88 (a, b), RA94 (c, d) and NA08 (e, f) on basis of SD00 estimates.	104
Fig. 6-1 The fitting regression of forest Lorey height (a) and FAI (b) against forest AGB based on measurements.	118
Fig. 6-2 Validation of the eight-day average SEBS simulated ET using EC measurements.	119
Fig. 6-3 Interannual dynamics of forest ET simulated by SEBS over the QMs from 2000 to 2012.	124
Fig. 7-1 Interannual ANPP, ET, WUE and the meteorological statistics for the growing seasons in forested areas over the QMs (the dash lines are the trendlines).	135

List of Tables

Table 2-1 k -NN configurations used in this chapter.	24
Table 2-2 Results of optimal k -NN estimations assessed by LOO procedure.	26
Table 3-1 Confusion matrix for the forest/non-forest map.	39
Table 3-2 The k -NN configurations used in this chapter.	41
Table 3-3 The results of optimal k -NN estimations assessed using the LOO cross-validation procedure for each feature vector (feature type).	44
Table 4-1 The calibrated parameter settings for the optimal configuration of the Biome-BGC model.	73
Table 4-2 Statistics of interannual average NPP, ANPP fluxes, and total amounts AGB of forests over the QMs from 2000 to 2012.	81
Table 5-1 Required inputs for the four tested roughness models.	91
Table 5-2 Sensitivities of the four models with different input parameter variations, as fractions of their reference values.	94
Table 5-3 Stepwise multiple linear regressions for the forest structural parameters used in this chapter.	96
Table 5-4 Input parameters based on tree measurements.	102
Table 5-5 Comparison of d and z_{0m} from remote sensing models using the site measurements as inputs with the EC measurements (unit: meter).	102
Table 5-6 Comparison of d and z_{0m} from remote sensing models using LiDAR and SPOT-5 estimates as inputs with the EC measurements (unit: meter).	103
Table 6-1 The statistics for interannual forest ET averages (ET) (unit: mm) simulated by SEBS over the QMs from 2000 to 2012.	120
Table 7-1 The statistics for interannual averages of forest ANPP (unit: gC m^{-2}), ET (unit: mm), and WUE (unit: kgC m^{-3}) over the QMs from 2000 to 2012.	134

Chapter 1

Introduction

1.1 Background

1.1.1 The Role of Forests in The Global Carbon and Water Cycle

Having the largest area, the widest geographic distribution, and some of the richest biodiversity on Earth, forests are extremely important to terrestrial ecosystems. Forests regulate surface water, biologically stored carbon, nutrients, and latent heat through transpiration and the evaporation of intercepted water. The exchange of matter and energy between forests and the atmosphere through the processes of photosynthesis and evapotranspiration (ET) improves the ecological environment (Singh et al., 2014).

Forests are particularly important for determining the storage and sequestration of carbon dioxide (CO₂) in the atmosphere. Carbon (C) stocks and fluxes are dynamic in forests and are affected by natural disturbances, weather and climate variability, anthropogenic activities, and growth and succession (Schimel et al., 2001; Nemani et al., 2003; Richardson et al., 2007). The current global C stock in forests was estimated by Pan et al. (2011) to be 861±66 Pg C, with 383±30 Pg C (44%) contained in soil (to 1 m depth), 73±6 Pg C (8%) contained in deadwood, 43±3 Pg C (5%) contained in litter, and 363±28 Pg C (43%) contained in live biomass (above- and below- ground biomass). Global forest above-ground biomass (AGB) is currently thought to account for approximately 90% (Schimel et al., 2001) of total terrestrial AGB. The removal of forests by felling or burning may release great amounts of this chemically stored carbon to the atmosphere.

Forests offset sources of CO₂, such as volcanic emissions and the combustion of fossil fuels, to the atmosphere (Schimel et al., 2001; Nemani et al., 2003; Richardson et al., 2007). They have been described as the “green lung” of our Earth, absorbing CO₂ during photosynthesis and, in return, releasing oxygen into the atmosphere. Net primary productivity (NPP) quantitatively describes the amount of atmospheric carbon sequestered by vegetation and accumulated as biomass.

From the 1980s to 1990s, in spite of a warming climate, global NPP increased due to eased climatic constraints on vegetation (Nemani, et al., 2003). However, over the past decade (2000-2009), the warmest decade since the 1880s when instrumental measurements of temperature began (Zhao and Running, 2010), global NPP has been found to slightly decrease. Between 1990-2007, the net absorption offset was estimated as 8.8 billion tonnes of CO₂ annually (approximate to the uptake of 2.5±0.4 Pg C year⁻¹ from 1990 to 1999 and 2.3±0.5Pg C year⁻¹ from 2000 to 2007), with approximately one-third of the CO₂ released from the burning of

fossil fuels (average 28 billion tonnes of CO₂ annually) (Pan et al., 2011). On one hand, interannual variations of NPP have been found to be negatively correlated with atmospheric CO₂ growth rates, indicating that global terrestrial NPP is a major driving force for the CO₂ growth rate. On the other hand, persistent warming and changes in climate have been found to lead to unprecedented changes in terrestrial vegetation growth and productivity (Piao et al., 2007, 2011; Ouyang et al., 2014).

Large-scale climate anomalies have also been found to impact regional annual NPP. Droughts in 2000 reduced NPP in North America and China. Droughts in 2002 reduced NPP in North America and Australia, and drought in 2003 reduced NPP in Europe (Ciais et al., 2005; Zhao and Running, 2010). The effects of climate constraint variations (i.e., temperature and precipitation) on ecological processes within forest ecosystems have already been stated (Gao et al., 2000; Berthelot et al., 2005; Zhang et al., 2011).

Pan et al. (2011) found, as compared to tropical intact forests from 1990–1999, that an approximate 23% decrease in the decadal C sink occurred from 2000 to 2007. The change can be attributed to deforestation in intact forests (8%) and the serious drought that occurred in the Amazon during 2005 (Phillips et al., 2009; Friedlingstein et al., 2010). Thanks to intensive national afforestation/reforestation programs over the past few decades that have led to ever increasing areas of planted forests, China's forest C sink increased by 34% between 1990 to 1999 and 2000 to 2007, and the biomass sink almost doubled (Pan et al., 2011).

In addition to the factors mentioned above, and as indicated by Michaletz et al. (2014), the biophysical composition of vegetation (including age, AGB, structure, etc.), growing season length, and local adaptation may also impact NPP variation. Local adaptation is subject to debate, with two views presented in the scientific literature. The first, implemented in many models, indicates that within the ecological relevant temperature range, the rate of vegetation growth responds in a fixed manner to weather variations (e.g. growth increases exponentially with temperature to a critical value, beyond which it gradually reaches a maximum and then decreases) (Berry and Bjorkman 1980; Huxman et al., 2004; Campo et al., 2013). In the second view, the adaption of the ecosystem to local conditions (i.e., thermal and edaphic tolerances) may alleviate the negative physiological response brought about by climate influences (Bonan 1993; Chapin 2003; Kerkhoff et al., 2005; Enquist et al., 2007).

By measuring the density of wood, and the height and width of different tree species over time and space, scientists have determined how much carbon is

absorbed. However, due to the diverse responses of forests to climate fluctuations across stand type and geographical location (Lindner et al., 2010), estimations for forest C sinks and fluxes under changing climate are variable. For example, while it has been estimated that 1–2 Pg C year⁻¹ are stored in the forests of the Northern Hemisphere, uncertainties in the estimations of C stocks and fluxes within various forest types are not well understood (Pan et al., 2011; Gray and Whittier, 2014). Many studies have debated the potential variation of terrestrial ecosystems due to climate change (Mohamed et al., 2004; Boisvenue et al., 2006; Huang et al., 2014; Sun and Mu, 2014), natural and human disturbances (Dury et al., 2011; Yu et al., 2011; Peters et al., 2013; Dai et al., 2014;), and organic growth (Pregitzer and Euskirchen, 2004; Russell et al., 2010; Vedrova 2011; Wang et al., 2011). Forest management may greatly benefit from a reduction in these uncertainties. For example, accurate data for carbon fluxes and stocks in forests are indispensable for international negotiations aimed at limiting the atmospheric concentrations of greenhouse gases.

Forests are not only a carbon sink; they also provide ecosystem services such as improving soil and water quality and capacity. The acquisition of CO₂ by vegetation is accompanied by transpiration - the loss of water vapour through the stomata that regulate gas diffusion between the leaf and the atmosphere. Transpiration, together with other evaporation losses termed ET, is a central process in the climate system and a nexus for energy, water, carbon cycles and tree growth (Berry et al., 2010; Govind et al., 2011). Jasechko et al. (2013) indicated that transpiration uses half of the solar energy absorbed by land surfaces and is by far the largest water flux from land, representing 80 to 90% of terrestrial ET. The result suggests that aspects of water cycling and improvements for biological fluxes (transpiration) (rather than physical (evaporation) fluxes) should be prioritized in climate models. The energy requirement of ET constrains CO₂ uptake and tree growth (Law et al., 2002; Jung et al., 2010) and, as statistically shown, even forest biodiversity (Hawkins et al., 2003; Krefl and Jetz, 2007). Forests, in general, have a lower surface albedo and, therefore, absorb more solar radiation than other terrestrial ecosystems (Betts, 2000). Changes in forest ecosystems result from the regulation of land and atmospheric energy budgets in response to weather and climate variations or climate change. Global land ET returns approximately 60% of annual land precipitation to the atmosphere and the ET from forests is approximately 45% of total terrestrial ET (Oki and Kanae, 2006). But large uncertainties exist in the ET estimations. Apart from ET, forests also affect the water cycle through rainfall interception, root water uptake, and soil development. Forest ET affects runoff, further influencing water storage on land and vapour in the atmosphere.

Forest ET and the carbon cycles are intrinsically coupled and drive feedbacks between the land and atmosphere. On one hand, forest ET impacts meteorological conditions through the turbulent exchange of momentum, heat, and moisture within the atmospheric surface layer (Koster et al., 2004). The partitioning of solar energy to forest ecosystem latent (λE) and sensible (H) heat fluxes exerts critical effects for atmospheric boundary layer (ABL) dynamics, thus directly impacting local, regional, or even global climate. For example, over the past 30 years, the loss of forest cover has been consistent with drying in the southern Amazon (Lee et al. 2011). Spracklen et al. (2012) found that the air above extensive vegetation produced at least twice as much rain as that above little vegetation. On the other hand, climate variations affect the various physical and physiological processes in forests that alter mass and energy exchange between the land and atmosphere. Thus, the interactions between forest processes and climate operate in both directions.

A substantial increase in water use efficiency (WUE), the ratio between net carbon uptake and ET, in temperate and boreal forests of the Northern Hemisphere over the past two decades was discovered by Keenan et al. (2013). The increase was caused by both increasing photosynthesis and net carbon uptake due to increasing atmospheric CO₂ levels and decreasing ET. A higher WUE for drier, warmer conditions during the early twenty-first century (2000–2009), as compared to that in the late twentieth century (1975–1998) for the Northern and Southern Hemispheres, was also found by Campos et al. (2013).

However, since forest ET has been found to be highly variable amongst various sites mainly due to climate conditions and variations (i.e., precipitation, meteorology, and solar energy) and forest characteristics (i.e., tree species, structure, and phenology), these global studies are not necessarily relevant for local forest management. Better modeling of local forest carbon and water exchange could lead to significant improvements in forest eco-hydrological knowledge, in particular for examining complex interactions between the terrestrial biosphere and atmosphere, and water circulation and climate change.

1.1.2 The Eco-hydrology of The Heihe River Basin

Climate change has been particularly evident in China (Piao et al., 2005; Ren et al., 2008, 2012), especially for the cold and arid regions of northwestern China. In these regions, mountains, hills and basins are straggled within the inland river basins. The mountainous areas, with sufficient precipitation, snowmelt and glacier melt runoff, generally, are headwaters of the entire basins. The middle and downstreams of inland river basins, with scarce precipitation, are water consumption areas (Cheng et al., 2014). These regions are characterized by scarce precipitation and

intensive ET which leads to sparse growth and a simple structure, but highly heterogeneous landscapes. Ecosystems in these regions are unique, but they are also sensitive to climate variation and change, and anthropogenic and natural disturbance. The sustainable development of forests and water are urgent issues. Current eco-hydrological problems include water-soil conservation, biodiversity protection, landscape perception (frangibility, adaptability, and sensitivity), as well as conflicts between economic development and ecosystem protection.

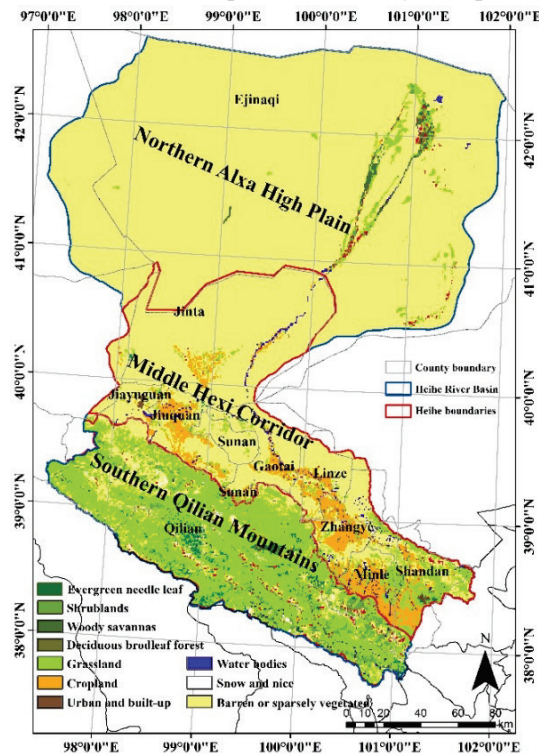


Fig. 1-1 A sub-basin partition and land cover map of the HRB.

Due to the intensive and extensive utilization of natural resources, partly resulting from rapid expansion of the population, terrestrial ecosystems have, to a large extent, deteriorated, while at the same time atmospheric gas concentrations, especially in areas with a strong coupling between the land and the atmosphere, have changed globally. The question is whether or not a critical point exists at which an ecosystem is permanently changed.

The question is particularly relevant for the Heihe River Basin (HRB). The HRB is the second largest inland river basin within the arid region of northwestern China (Fig. 1-1) and consists of three major geomorphic units, as follows: the southern Qilian Mountains (QMs), the middle Hexi Corridor, and the northern Alxa

Highland. Since they function as the water source that supports agricultural irrigation within the Hexi Corridor and maintain ecological viability within the northern Alxa Highland, the QMs are a hydrologically and ecologically important unit. As a result of headwater that has brought richness to regional people for thousands of years, the QMs have been called as “Mountain Momma of the Hexi Corridor”. The system is, however, currently vulnerable. The degradation of water resources within upper catchments can catalyse related environmental problems for middle and downstream reaches. Due to wood denudation, extensive grazing, and the excessive development of water resources, the QMs can hardly bear further degradation.

Deforestation within the QMs over the past half century has not only resulted in a deteriorating ecological environment, but, it has also, as indicated by a large decrease in the biological and hydrologic productivity of the land, weakened the function of vegetation for conserving water in well-developed soils. The forested area of the QMs decreased from 22.4% during the early 1950s to 12.4% during the 1990s (Wang and Cheng, 1999), when only approximately 820 km² of forested area remained. In addition, sparse wood and shrubbery areas decreased by 30%, amounting to 2000 km². Due to recent warming trends, over the past ~50 years, the glacier area decreased by 29.60% in the QMs (Wang et al., 2011). In some areas of the QMs, the rising rate of the snow line is ~2 - 6.5 meters year⁻¹, or even ~12.5 - 22.5 meters year⁻¹ in some areas (Liu et al., 2003). Although, in the past ~50 years, discharge of river water at the Yingluoxia Gorge, from the QMs, has not significantly changed, as a result of increased agricultural, and the industrial and household water demands of the population living within the Hexi Corridor, the water available for natural ecosystems located within the downstream basin has been decreasing until this century (Qin et al., 2012). It has led to serious ecological and environmental degradation such as the drying of lakes (both the East and West Juyan Lake), the die-off of forests (*Populus euphratica*), the acceleration of land desertification, and an increase in the frequency and intensity of sand storms.

The government of China responded to these problems in the 1980s by putting conservation legislation into effect that protects the QMs as a water-conservation forest area and that stimulates natural regeneration and tree planting. The aim of these measures was to improve ecosystem vigour - the capacity to recycle energy and matter as indicated by carbon stocks, carbon uptake, and ET. The initial protection of the forest (rather than afforestation), did not result in increasing ecosystem vigour as expected. The phenomena such as unhealthy growth, high mortality, pool abilities of water capacity and hazard resistance etc, imply the effect

of the static protection for vegetation (Gou et al., 2005; Liang et al., 2006; Xu et al., 2012; Zhao et al., 2012).

Clearly, there is a lack of understanding regarding how the hydrological and ecological system of the entire basin functions and regarding the role of headwater forests. A better understanding of both systems and roles could help improve the success of restoration efforts. With this idea in mind, two comprehensive and fruitful campaigns, Watershed Allied Telemetry Experimental Research (WATER) (Li et al., 2009a) and Heihe Watershed Allied Telemetry Experimental Research (HiWATER) (Li et al., 2013b), were conducted, beginning in 2007 and 2012, respectively, over the HRB. The campaigns consisted of simultaneous airborne, satellite-borne, and ground-based remote sensing experiments that focused on improvements for the observability, understanding, and predictability of hydrological and related ecological processes at the catchment scale. WATER and HiWATER opened the possibility for conducting synthesized modeling and analyses topic of this study. In short, using multi-disciplinary techniques (based on multi-parameter remote sensing, eco-hydrological, and meteorological knowledge), as well as comprehensive measurements (forest surveys, Eddy Covariance (EC) and dendrochronological measurements), long-term modeling of forest AGB dynamics (which is inherently linked with NPP or above-ground NPP (ANPP), long-term simulations of forest ET, and the impacts of climate variations on these estimates, and thus WUE), were conducted over the QMs.

1.2 Research Problem

The problem of sustainable forest and water resource management for the QMs results from a lack of knowledge in the following areas: (1) the carbon stock or AGB contained in forests, (2) the actual flux exchanges of carbon and water between the land and atmosphere, and (3) changes in the carbon fluxes and ET of the forests in response to climate variations. Using data collected during the WATER campaign, this knowledge gap can be reduced. Spatial data collected during the campaign made it possible to model land-atmosphere interactions. Considering the limitations of existing models, Santini et al. (2014) indicated that particular attention should be paid to the incorporation of such novel measurements to constrain the models. In this way, modelling errors propagated to further analyses, resulting in misleading conclusions with serious implications for society, as discussed by Valle et al. (2009), can be avoided. The systematic combination of measurements and technologies, and eco-hydrological models can reduce uncertainties in estimates for carbon and water fluxes on ecosystem scales (Zobitz et al., 2011, 2014).

1.3 Objectives

The following scientific questions were explored during this study: 1) To what extent can key eco-hydrological parameters (in this case: carbon stock, carbon uptake, and ET) be retrieved from the synthesis of multi-parameter remote sensing using various models in order to improve the sustainable development of forest ecosystems over cold and arid regions? 2) What are the functions of forests in carbon/ET fluxes and what are the likely impacts of climate variability on carbon/ET changes.

To estimate forest parameters, multi-parameter remote sensing data were combined. These parameters were further utilized to combine with the time-series of remote sensing products in order to perform simulations of the incorporated ecological models (process-based and remote-sensing-based) and the ET model. Finally, the interannual dynamics of forest carbon, ET and water use efficiency (WUE) were analyzed.

The specific objectives of this study were, as follows:

- (1) To determine an optimal method for estimating forest AGB using multi-parameter remote sensing data.

The predictive power of multi-sensor satellite data (including Satellite Probatoire d'Observation de la Terre-5 (SPOT-5) high resolution geometrical (HRG), multi-temporal dual-polarization Advanced Land Observing Satellite (ALOS) Phased Array type L-band Synthetic Aperture Radar (PALSAR), and airborne light detection and ranging (LiDAR)) data for the retrieval of AGB was evaluated. This evaluation was performed in an airborne campaign area using two methods, parametric (stepwise multiple linear regression) and non-parametric (k -Nearest Neighbour (k -NN)). To determine the appropriate method for estimating forest AGB, the performance of the parametric and non-parametric methods was compared.

- (2) To investigate an effective strategy for routine estimations of forest AGB over the Qilian Mountains.

To alleviate the impacts of terrain relief for estimating forest AGB, a notable terrain radiometric correction method was employed for preprocessing spectral features. Based on a refinement of performance for the foregoing methodology and for the sake of improving efficiency for feature configuration constructions in order to estimate forest AGB, the random forest (RF) was combined with k -NN and Support Vector Regression (SVR).

- (3) To improve the dynamic modeling of forest AGB by integrating forest AGB estimates and the corresponding annual forest carbon fluxes for the Qilian Mountains.

One strategy for integrating the ecological process model's (the Biome-BioGeochemical Cycles (Biome-BGC)) functions with those of the optimized remote sensing model (the MODIS-MOD17 (MOD_17)) was proposed in order to take advantage of their attributes. Driven by an accurate meteorological dataset downscaled from Weather Research and Forecasting (WRF) model simulations and a series of refined MODIS products (the leaf area index (LAI)) from Global Land Surface Satellite (GLASS) products, a time series (from 2000 to 2012) of forest carbon fluxes was simulated in order to explore the variability in forest productivity (gross primary productivity (GPP), NPP, and net ecosystem exchange (NEE)). Specific forest AGB estimates for one year (in this case 2009) were integrated with interannual forest AGB increments (after 2009) or decrements (before 2009) in order to obtain the forest AGB dynamics.

- (4) To use forest structure information to improve ET estimates.

In the airborne campaign area, accurate forest structure parameters retrieved from multi-source remote sensing data (SPOT-5 HRG and airborne LiDAR) were applied within four models in order to test their feasibilities and performances for estimating zero plane displacement height (d (m)) and aerodynamic roughness length (z_{0m} (m)). Based on the kB^{-1} model, the heat roughness length (z_{0h} (m)) was derived from z_{0m} using the outperforming model to optimize the turbulent flux parameterization scheme for the Surface Energy Balance System (SEBS). Dynamic information for forest structural parameters (tree height, frontal area index (FAI) and LAI) was also applied during this parameterization process.

In addition to a few original MODIS products (Normalized Difference Vegetation Index (NDVI), and land surface temperature (LST)), additional refined MODIS products (including Albedo, LAI) and meteorological datasets which were the same as those used in the Biome-BGC and MOD_17 models were applied within SEBS in order to reduce offsets resulting from the driving inputs. Thirteen year (from 2000-2012) simulations of SEBS were performed in order to determine forest ET dynamics.

- (5) To explore the impacts of climatic variations on forest carbon and ET dynamics within the Qilian Mountains.

The impacts of climate variations (the precipitation, temperature, vapor pressure deficit (VPD) and radiation) in growing seasons on forest carbon and ET dynamics were analyzed. Dividing annual forest ET into annual forest AGB dynamics could

provide implications for WUE corresponding to climate variations over the past 13 years.

1.4 Thesis Outline

Subsequent to this introduction, the following seven chapters are organized according to the objectives defined in **Section 1.3**.

The specific structure of this thesis is as follows:

Chapter 1 introduces the scientific background and provides a statement of the problem, a description of the study area and the related scientific questions; and defines the research objectives then presents the thesis outline.

Chapter 2 evaluates the performance of the parametric and non-parametric methods employed for estimating forest AGB based on multi-parameter remote sensing data, including airborne LiDAR, and spaceborne ALOS PALSAR and SPOT-5 HRG data, within a small watershed where an intensive airborne campaign was conducted.

Chapter 3 explores an alternative way to accurately estimate regional forest AGB over montane areas using the non-parametric method. The Landsat Thematic Mapper 5 (TM) and the Advanced Spaceborne Thermal Emission and Reflection Radiometer (ASTER) Global Digital Elevation Model (GDEM) products presented are expected to provide implications for the routine monitoring of forest AGB using free remote sensing data.

Chapter 4 proposes a strategy for incorporating the non-parametric models (incorporating the random forest (RF) with k -NN, and with SVR) to improve the efficiency of estimating the forest AGB map in 2009 over the QMs using high-dimensional remote sensing information, and proposes another strategy for incorporating the remote-sensing-based ecological model with the process-based model to improve spatiotemporal estimates of forest carbon fluxes (including GPP, NPP, and NEE). The results are then combined to improve the forest AGB dynamics by linking the forest AGB in 2009 with the interannual forest AGB increments (from 2000 to 2012) which were originally converted from interannual NPP estimates.

Chapter 5 parameterizes four notable remote-sensing-based models for aerodynamic roughness factors using multi-parameter remote sensing data including airborne LiDAR and spaceborne SPOT HRG, and evaluates the

performances of these four models using Eddy Covariance (EC) measurements. The outperforming model is shown to be ready for application over the QMs.

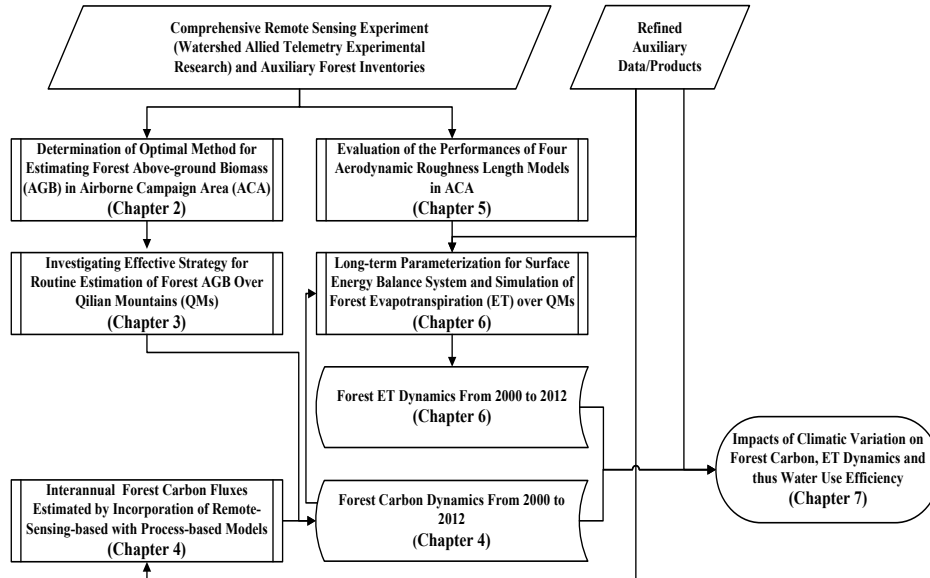


Fig. 1-2 Framework of this thesis.

Chapter 6 parameterizes the Surface Energy Balance System (SEBS) for the calculation of ET for forests over the QMs using remote sensing data. Specifically, the dynamics of two forest physical parameters (tree height and FAI) are linked to interannual forest AGB estimated from **Chapter 4** and applied in order to parameterize decadal roughness lengths for SEBS. Estimates of forest ET over the QMs result from the parameterized SEBS: a refined dataset that includes regional meteorological inputs and MODIS products applied to perform ET simulations over QMs forests for 13 years (from 2000 to 2012).

Chapter 7 analyzes the impacts of climate variations on the above mentioned forest's ANPP, ET and, thus, WUE and presents the major results, a discussion, and conclusions. Specific limitations and an outlook for relevant future work are also provided.

The framework of this study is shown in Fig. 1-2.

Chapter 2

Evaluation of Parametric and Non-parametric Methods to Estimate Forest Above-Ground Biomass in The Qilian Mountains Using Multi-Parameter Remote Sensing Data*

* This chapter is based on:

Tian, X., Su, Z. B., Chen, E. X., Li, Z. Y., van der Tol, C., Guo, J. P., & He, Q. S. (2012). Estimation of forest above-ground biomass using multi-parameter remote sensing data over a cold and arid area. *International Journal of Applied Earth Observation and Geoinformation*, 14, 160-168. DOI: 10.1016/j.jag.2011.09.01.

Abstract

Remote sensing is a valuable tool for estimating forest biomass in remote areas. This chapter explores retrieval of forest above-ground biomass (AGB) in an airborne campaign area located at the Qilian Mountains (QMs), using two different methods (non-parametric and parametric), field data, and three different remote sensing data: a Satellite Probatoire d'Observation de la Terre-5 (SPOT-5) high resolution geometrical (HRG) image, multi-temporal dual-polarization Advanced Land Observing Satellite (ALOS) Phased Array type L-band Synthetic Aperture Radar (PALSAR) and airborne light detection and ranging (LiDAR) data. The non-parametric method was applied in 300 different configurations, varying both the mathematical formulations and the data inputs (SPOT-5 and ALOS PALSAR), and the quality of the performance of each configuration was evaluated by leave-one-out (LOO) cross-validation against ground measurements. For the parametric method (the multiple linear regression), the same remote sensing data were used, but in one additional configuration the airborne LiDAR data were used for stepwise multiple linear regression (SMLR). The result of the best performing non-parametric configuration was satisfactory ($R = 0.69$ and root mean square error (RMSE) = 20.70 tonnes ha⁻¹). The results for the parametric methods were notoriously inaccurate, except for the case where airborne LiDAR data were included. The regression method with airborne low-density LiDAR point cloud data was the best of all tested methods ($R = 0.84$ and RMSE = 15.2 tonnes ha⁻¹). A cross comparison of the two best results showed that the non-parametric method performs nearly as well as the parametric method with LiDAR data, except for some areas where forests have a very heterogeneous structure. It is concluded that the non-parametric method with SPOT data is able to map forest AGB operatively over the cold and arid region as an alternative to the more expensive airborne LiDAR data.

2.1 Introduction

Describing and quantifying forest above-ground biomass (AGB) has become of importance to many scientific and societal tasks such as sustainable forest management, timber management, forest ecosystem productivity estimation, carbon sink evaluation, and studies of the role of forest in the global carbon cycle, and links between hydrology and ecology, etc. (Houghton et al., 1999, 2001; Foody, 2003; Zheng et al., 2004; Houghton, 2005; Palacios-Orueta et al., 2005; Lu, 2006). In conventional techniques on basis of statistical assessment (i.e., tree species, vertical structure, stand height, and stand density), the forest AGB information comes from expensive and time consuming field surveys by the high sampling intensity (Schroeder et al., 1997; Nelson et al., 1999; Parresol, 1999; Brown, 2002; Fournier et al., 2003; Woodbury et al., 2007). As an alternative, multi-parameter remote sensing techniques have been applied, in which remotely sensed data are used as proxy for quantitative forest AGB at various scales (Nelson et al., 1988; Le Toan et al., 1992; Ranson and Sun, 1994; Roy and Ravan, 1996; Ranson et al., 1997; Santos et al., 2002, 2003; De Jong et al., 2003; Coops et al., 2004; Luther et al., 2005; Thenkabail et al., 2004; Labrecque et al., 2006; Lu et al., 2005; Patenaude et al., 2005; Leboeuf et al., 2007; Tan et al., 2007; Lucas et al., 2008; Gonzalez et al., 2010).

However, the application of remote sensing data for the forest AGB estimation is complicated in heterogeneous forests, where the tree species, stand density, canopy closure and crown over-lap are variable. All these variables affect AGB, but it is difficult to differentiate them with remote sensing. In addition, topographic irregularities and various environmental conditions also affect the remote sensing signatures of the observed surfaces (Danson and Curran, 1993; Nelson et al., 2000a; Steininger, 2000; Foody et al., 2001; Saatchi et al., 2007). Both passive and active remote sensing measurements have been used for the estimation of forest AGB, each having different advantages and disadvantages.

Some passive remote sensing techniques make use of the sensitivity of the reflectance of forests to parameters like canopy cover, crown closure, leaf area index, which are in turn correlated with AGB. Many studies have investigated the relationship between forest AGB and satellite spectral values expressed as digital numbers, radiance, reflectance, or vegetation indices. Sensors with intermediate spatial resolution like Satellite Probatoire d'Observation de la Terre (SPOT), Landsat Thematic Mapper and Enhanced Thematic Mapper Plus data are commonly used for this purpose. Various correlations between forest AGB and the reflectance or vegetation indices were found and reported (Sader et al., 1989; Roy and Ravan,

1996; Nelson et al., 2000b; Steininger, 2000; Mutanga and Skidmore, 2004; Zheng et al., 2004; Hall et al., 2006; Labrecque et al., 2006; Rahman et al., 2008; Powell et al., 2008; Soenen et al., 2010).

Some active remote sensing techniques make use of the relation between Synthetic Aperture Radar (SAR) backscatter and forest AGB (Dobson et al., 1992; Le Toan et al., 1992; Ranson and Sun, 1994; Ranson et al., 1997; Luckman et al., 1997; Kasischke et al., 1997; Kurvonen et al., 1999; Kuplich et al., 2000; Yrjo, 2005). The advantage of SAR is that the signal is less prone to saturation with AGB than optical reflectance. Not all SAR bands are equally suitable: SAR backscatter in the P and L bands has a much stronger correlation with forest AGB than the C and X bands. The L-band has proven particularly valuable for AGB estimation (Lu, 2006). Some studies (Moghaddam et al., 2002; Amini and Sumantyo, 2009; Chen et al., 2009) found that the accuracy of forest AGB estimation improved when optical reflectance data were added to the SAR data as an additional source of information. The single most promising technique in active remote sensing is airborne laser scanning (ALS). ALS has recently led to a revolution in remote sensing of forest structure (Lefsky et al., 2002b; Popescu and Wynne, 2004; Maltamo et al., 2004; Reutebuch et al., 2005; Koukoulas and Blackburn, 2005; Salas et al., 2010), due to its unique ability to measure three-dimensional information (Nelson et al., 1988; Lefsky et al., 2002a; Lim and Treitz, 2004; Patenaude et al., 2004; Næsset, 2007; Lucas et al., 2008; Næsset and Gobakken, 2008; García et al., 2010).

In summary, there are several options for estimating forest AGB among the multi-parameter remote sensing data, differing in cost, spatial resolution, applicability and continuity. Optical remote sensing data is sensitive to the forest AGB, but the spectral signature saturates at a lower biomass level than the SAR data. SAR data are free of weather disturbance, but largely affected by topography and the quality depends on the waveform length (Sun et al., 2002). Airborne LiDAR is the most efficient technique to estimate forest AGB. It is also the most expensive technique, which makes it unsuited for routine applications.

Two methods exist for establishing (calibrating) the relation between remote sensing data and forest AGB with ancillary data: parametric and non-parametric. The parametric method employs multiple regressions, assuming that each forest attribute affects remote sensing signals at each wavelength in a unique and uncorrelated way (Lawrence and Ripple, 1998; Maselli and Chiesi, 2006; Rahman et al., 2008). The method is conceptually simple, but the success largely depends on the statistical robustness of the relationships. In reality a change in AGB rarely directly results in a change of remote sensing signatures. Consequently, the

conventional parametric method applied to remote sensing data usually fails to map forest AGB satisfactorily (Maselli and Chiesi, 2006), independent on the univariate or multivariate type of regression that is used.

The non-parametric k -Nearest Neighbour (k -NN) method is based on more flexible assumptions than the parametric method, and does not suffer from the same limitations. In the non-parametric method the AGB of a pixel is associated with that of the k 'nearest' pixels in terms of remote sensing observations for which field data of AGB are available. A training set of pixels for which both field measured AGB and remote sensing data are available is established first. This training set is further used to estimate the AGB of all other pixels by linking them to pixels with similar remote sensing data in the training set. A distance measure is defined for the differences between the remote sensing data of a pixel and the data in the training set. The k elements in the training set with the smallest values of d are used to compute AGB of that pixel as a weighted average. The method requires a representative set of ground data, covering the complete range of values for AGB, and remote sensing signals in the study area. The advantage of this method is that no assumptions are made about the nature of the relationship between AGB and remote sensing. This makes the method more robust in complex environments, and reasonable results can be achieved (Maselli et al., 2005). The k -NN method is an attractive tool for multi-source forest inventory (Franco-Lopez et al., 2001; Katila and Tomppo, 2001; Holmström and Fransson, 2003; Tomppo and Halme, 2004; Tomppo et al., 2009), and it has been operationally applied for various scale forest inventories in many countries (Fazakas et al., 1999; Holmström et al., 2001).

However, most applications of k -NN used medium resolution remote sensing data such as Landsat images (Franco-Lopez et al., 2001; Katila and Tomppo, 2001; Finley et al., 2006). Only few studies have used fine resolution imagery such as Quickbird, aerial photographs (Muinonen et al., 2001; Tuominen and Pekkarinen, 2005; Fuchs et al., 2009) and airborne SAR data (Holmström and Fransson, 2003). Since SPOT-5 data, with intermediate spatial resolution, is widely available, it is interesting to investigate the applicability of SPOT-5 with combination of current operative L-band ALOS PALSAR data for mapping forest AGB by k -NN algorithm.

This chapter investigates the performances of parametric and non-parametric methods for forest AGB by use of multi-parameter remote sensing data over a complex forest area in the Qilian Mountains (QMs), the upper reaches of Heihe River Basin (HRB), a cold and arid region, where only limited forest inventory data are available. The objectives of this chapter are (1) to evaluate the predictive power

of reflectance (SPOT-5) and SAR backscatter intensity (ALOS PALSAR) for the retrieval of forest AGB, (2) to evaluate different configurations of the non-parametric algorithm at pixel level, (3) to compare the parametric versus the non-parametric method, and (4) to identify the best k -NN algorithm for routine application of forest AGB mapping in a heterogeneous forest over a cold and arid region. For these objectives supporting ground data and data of an airborne LiDAR system have been used.

This chapter is organized as follows. After describing the test area, the data and models were presented. This is followed by a description of the optimization procedure for various k -NN configurations by leave-one-out (LOO) cross-validation and the assessments of pixel level estimation accuracy for both k -NN and regression models. The best results from k -NN and regression model were compared, and the results were presented and discussed.

2.2 The Study Area and Data

This chapter uses data collected in the framework of the Watershed Allied Telemetry Experimental Research (WATER) carried out at the HRB in Northwest China, in 2008 (Li et al., 2009a, 2011b). HRB, the second largest inland river basin in China, is located between 97°24'-102°10' E and 37°41'-42°42' N, with an area of about 130,000 km². It consists of three major geomorphic units: the southern QMs, the middle Hexi Corridor, and the northern Alxa Highland and accordingly, the landscapes are various, including glacier, frozen soil, alpine meadows, forests, irrigated crops, riparian ecosystem and desert (Gobi) (Fig. 1-1). Aiming to improve the understanding of physical processes of the land surface-atmosphere interaction at arid regions, the WATER project was composed of simultaneous airborne, satellite-borne remote sensing observations and ground based measurements.

The study area, the QMs, spans an area of 10,400 km² and consists of 72% alp, 27% fluvial area, and 1% oasis. The elevation varies from 1500 m to 6000 m above sea level (see Fig. 2-1). The QMs have a temperate continental mountainous climate. During winter, atmospheric circulation is controlled by the Mongolian anticyclone and conditions are cold and dry with little precipitation. When the atmospheric circulation is controlled by a continental cyclone during summer, the diurnal difference in temperature is dramatic. The difference in precipitation between summer and winter is large, and most of the year's precipitation falls during the summer with the annual rainfall being between 350 mm and 495 mm. Influenced by the climate and the terrain, prevalent vegetation types in the area are mountainous pastures, shrubs, and forests. The forest, consisting of *Picea crassifolia* mixed with a fairly small fraction of *Sabina przewalskii* trees, only survives on shady

slopes (between 2500 m and 3300 m in altitude), while sparse grass inhabits sunlit slopes. Vegetation density varies with terrain, soil, water, and climate factors. Due to a variety of environmental factors, the site is often used as a field laboratory for the development of remote-sensing biophysical parameter models.

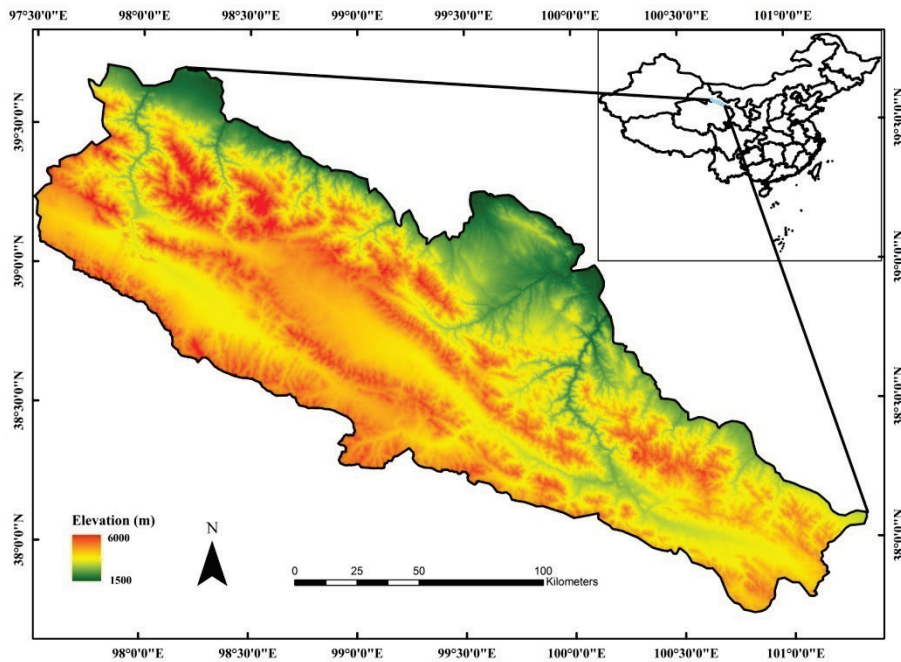


Fig. 2-1 The location and terrain conditions of the QMs within the upper reach of the HRB.

In June 2008, a campaign of airborne LiDAR (LiteMapper 5600 system, Riegl LMS-Q560 scanner) with the CCD (DigiCAM-H/22 camera) load together was carried out over the forest hydrology experimental area of WATER project, the Pailugou and Dayekou watersheds in QMs. The flight height was about 800 m above the local topography, and imaging coverage was about 10 km × 6 km. With the wavelength of 1550 nm, a pulse of 3.5 ns at 50 kHz, an overall cloud point density of about 1.88 hits m⁻² was acquired with this LiDAR system. After the campaign, a scene of SPOT-5 HRG image was acquired on 10 August 2008. Three dual-polarization (HH/HV) ALOS PALSAR images (level 1.1) (10 August 2007, 12 May and 27 June 2008) were acquired from Japan Aerospace Exploration Agency (JAXA).

Since the beginning of the campaign, an inventory survey on the forests has been carried out at 85 forest plots with two sizes (20 m × 20 m and 25 m × 25 m). The measurements include tree height (H, m), diameter breast height (DBH) (cm),

crown width at two orthotropic directions, first branch height and stand density. Trees with their DBH below 3 cm were not included in the survey. A set of total 75 forest plots was selected from the measurement database by following criteria: prevalence of forest plots dominated by *Picea crassifolia*; forest plots with independency with one another to avoid the spatial autocorrelation.

2.3 Methodology

2.3.1 The *k*-NN Algorithm

The *k*-NN method is one of the most widely known and routinely utilized non-parametric estimation methods for updating different scale forest inventories, even in complex landscapes (Maselli et al., 2005; Maselli and Chiesi, 2006). The attractiveness of the method is that it does not depend on the assumptions on the nature of the relationships linking ground reference forest plot measurement to the spectral data. Using the forest inventory data, parameters such as total wood volume, biomass, and age can be calculated for every pixel within the forest area. The estimated forest parameter value for a specified pixel (V_p) is calculated as a weighted mean value of the parameter's measurements of the i^{th} reference pixel (p_i) ($V_{p_i,p}$) at the k nearest samples in spectral space $\{i_1(p), \dots, i_k(p)\}$:

$$V_p = \sum_{i=1}^k W_{p_i,p} V_{p_i,p} \quad (2-1)$$

where $W_{p_i,p}$ are the weights assigned to each of the k samples proportional to the inverse squared distance ($d_{p_i,p}$) between the pixel to be estimated and the reference:

$$W_{p_i,p} = \frac{1/d_{p_i,p}^2}{\sum_{j=1}^k (1/d_{p_j,p}^2)} \quad (2-2)$$

and $d_{p_i,p}$ is multidimensional distance between target and reference pixel.

2.3.2 Multidimensional Distance Measures

The multidimensional distance can be derived in different ways. In this chapter, three forms of distance measures were used. The first one was Euclidean Distance (ED), the most used and simplest distance, defined as

$$d_{p_i,p}(ED) = \sum_{t=1}^T (x_{pit} - x_{pt})^2 \quad (2-3)$$

where x_{pit} and x_{pt} are the value of the t^{th} feature space variable for pixel p and for reference plot respectively.

The second distance was Mahalanobis Distance (MD). Contrary to ED, MD takes correlations between variables and variances of the variables into account, and is scale-invariant. The variance-covariance matrix of the feature space variables, C , is used to correct the factor of the multicollinearity of the feature space variables:

$$d_{pi,p}(MD) = (x_{pi} - x_p)' C^{-1} (x_{pi} - x_p) \quad (2-4)$$

where x_{pi} and x_p are the feature space vector for target and reference pixels respectively.

The third distance, Fuzzy Distance (FD), enhances the importance of the most informative bands for the specific parameters to be estimated, which is the modification of MD where the variance-covariance matrix is computed in a fuzzy way (Maselli, 2001; Chirici et al., 2008).

$$d_{pi,p}(FD) = (x_{pi} - x_p)' C^{*-1} (x_{pi} - x_p) \quad (2-5)$$

where C^* is the fuzzy variance-covariance matrix,

$$C^* = \frac{\sum_{j=1}^N Fz_j (X_j - M^*)(X_j - M^*)'}{\sum_{j=1}^N Fz_j} \quad (2-6)$$

where N is number of training pixels, X_j is spectral vector of training pixel j and M^* is fuzzy mean spectral vector of all training pixels,

$$M^* = \frac{\sum_{j=1}^N Fz_j X_j}{\sum_{j=1}^N Fz_j} \quad (2-7)$$

and Fz_j is membership grade of each reference pixel j ,

$$Fz_j = (2\pi)^{-1/2} D_z^{-1} e^{-1/2(Z_i - M_z)^2 / D_z} \quad (2-8)$$

where Z_i is value of the parameter at training pixel j , M_z is mean value of the parameter and D_z is the standard deviation of the parameter.

2.3.3 The Regression Methods

Parametric estimation by multiple linear regression method was also conducted to some feature types based on SPOT-5, ALOS PAL-SAR data and ancillary inputs. Considering that there were 21 possible independent variables for the regression based against LiDAR data (see Section 2.3.5), stepwise multiple linear regression (SMLR) method was used alternatively to select most significant variables (probability of F-to-enter = 0.05; probability of F-to-remove = 0.1).

The conventional multivariate regression model can be expressed as follows:

$$\hat{Y} = X_0 + a_1X_1 + \dots + a_iX_i \quad (2-9)$$

where \hat{Y} is the dependent parameter to be predicted, X_0 is the intercept, i is the number of independent variables, $a_{1\dots i}$ and $X_{1\dots i}$ are the regression coefficients and values of independent variables.

In this chapter, \hat{Y} referred to the forest AGB, $X_{1\dots i}$ were the remote sensing feature space variables such as spectral signatures or indices from SPOT-5 HRG, backscattering coefficients of multi-temporal HH/HV polarization ALOS PALSAR data and forest structure estimates (i.e., mean tree height, tree height quantiles and fractional canopy coverage (f_c)) from airborne low-density LiDAR data.

2.3.4 Forest AGB Calculation Based on Growth Equations

As the overwhelming tree species is *Picea crassifolia* in the study area, the following *Picea crassifolia* growth equations from Wang et al. (1998b), calibrated for the study area, were applied to calculate the individual tree AGB.

$$\gamma_{stock} = 0.0478 \times (DBH^2 \times H)^{0.8665} \quad (2-10)$$

$$\gamma_{branch} = 0.0061 \times (DBH^2 \times H)^{0.8905} \quad (2-11)$$

$$\gamma_{leaf} = 0.2650 \times (DBH^2 \times H)^{0.4701} \quad (2-12)$$

$$\gamma_{fruit} = 0.0342 \times (DBH^2 \times H)^{0.5779} \quad (2-13)$$

Where γ_{stock} , γ_{branch} , γ_{leaf} , γ_{fruit} , are biomass of stock, branch, leaf and fruit (kg), respectively.

Therefore, the forest plot AGB dataset for training or testing models was obtained by summing up the total tree AGB in the plot.

2.3.5 LiDAR Data Processing

The low-density LiDAR used in this chapter was processed to generate the digital elevation model (DEM) and to retrieve the forest structure parameters which were thereafter submitted to calibrate the SMLR with the forest plot AGB calculated from the inventories and Eqs. (2-10) ~ (2-13). Firstly, the outliers of LiDAR pulses (below the nominal ground surface or above the expected canopy height) were eliminated. After that, the remaining pulses were classified into ground points and vegetation points. The ground points were removed on basis of iterative slope analyses by Terrascan and MicroStation software and the vegetation points were normalized by considering different local terrain conditions. In order to reduce the influence of the low shrubs, a threshold of 1.3 m was defined to remove normalized points below it. At the mean time, DEM from ground points and the digital surface model (DSM) from vegetation points were acquired with 0.5 m resolution, which

were then used to compute the vegetation height as the difference between the DSM and DEM. In addition, the 0.5 m DEM was resampled to 20 m for geo-coding SPOT-5 HRG, ALOS PALSAR data, in order to make it consistent with the other remote sensing pixel sizes and forest plot sizes.

As AGB estimation is most sensitive to the tree height, the major independent variables for SMLR in this chapter were the mean height and height quantiles from LiDAR points (Magnussen and Boudewyn, 1998; Næsset, 2004; Lim and Treitz, 2004). The quantile describes the distribution and location of the sample, expressed as

$$P(X \leq \theta_p) = p \quad (2-14)$$

where $P(X \leq \theta_p)$ is the cumulative distribution function, X is the population, θ_p is the quantile of population X at p ($0 < p < 1$).

A total of 19 vegetation height quantiles was calculated by sorting the vegetation points in ascending order at each plot and classifying into classes from $p = 5\%$ to $p = 95\%$ (5% interval).

Another independent variable for establishing SMLR was the fractional vegetation cover f_c . All ground and vegetation points (higher than 1.3 m) were interpolated to generate the raster image. The fractional cover f_c was calculated as the ratio of the number of forest canopy grid cells G_{veg} (number of vegetation points) over the total number of grid cells in the raster image G_{tot} (overall points):

$$f_c = G_{veg} / G_{tot} \quad (2-15)$$

2.3.6 SPOT-5 Data Processing

The resampled DEM was used to carry out the geo-coded terrain correction (GTC) process for SPOT-5 HRG image with assistance of the airborne digital camera CCD image. The geographical error in terms of root mean square error (RMSE) was less than one pixel size. After GTC process, the original 10 m resolution SPOT-5 HRG data was resampled to 20 m. Next, topographic normalization was carried out by the sun-canopy-sensor plus C (SCS+C) method (Soenen et al., 2005) and finally atmospheric correction was carried out by the FLAASH module in ENVI software.

2.3.7 ALOS PALSAR Data Processing

As the level 1.1 ALOS PALSAR data is single look complex (SLC) product, the general pre-processing methods such as Radiometric Calibration, Multi-looking, GTC and terrain radiometric correction (TRC) were performed on these three temporal datasets. Similar to the procedure described in Section 2.3.6, the

resampled DEM was applied in the GTC and TRC processes for these SAR datasets with 20m × 20m resolution. In this chapter, only the HV polarization was used in the forest AGB estimation, because the HV polarization of 27 June image showed to have the highest correlation with AGB.

It should be mentioned that only a small part of the SPOT-5 and ALOS PALSAR images were processed in this chapter, notably the part that was covered with the airborne LiDAR.

2.3.8 Ancillary Data Preparation

The training data for the k-NN analyses and the regression was stored in a table with 75 rows (one for each forest plot) and columns containing geographic location, the field estimates of forest plot AGB, and individual tree inventories. A forest type map was generated from the airborne CCD image and for the DEM used in k-NN feature types, the 20 m LiDAR product was used.

2.3.9 Optimization of k-NN

A comprehensive test of various configurations was performed by the LOO cross-validation procedure, to investigate the effects of the k-NN configuration on forest AGB estimation accuracy. In these configurations, both the input data (‘feature types’) and mathematical setup (k value and distance measure) of the algorithm were varied. All combinations of different input and distance measures were evaluated, resulting in a total of 300 configurations (Table 2-1). In this way the most valuable data source and the most suitable setup could be identified.

Table 2-1 *k*-NN configurations used in this chapter.

<i>k</i> Value	Distance Measures	Feature Type	Feature Extraction Method
1-10	ED, MD, FD	(1) 4 SPOT-5 HRG bands (2) 4 SPOT-5 HRG bands, IRI, DEM (3) 2 PC bands, IRI, DEM (4) 2 PC bands, IRI, DEM, single ALOS PALSAR HV (5) Multi-temporal ALOS PALSAR HV, DEM	Pixel-wise, 3 × 3

The feature types that were varied included different original spectral or backscattering information, derived indices and ancillary information composition. Five different compositions were used: (1) the full original SPOT-5 HRG spectrum,

(2) feature type (1) plus the most sensitive ancillary information: the Infrared Index (IRI) and DEM, which was determined by SMLR process from all the ancillary information (including IRI, Normalized Difference Infrared Index, DEM and slope), (3) the most significant principle components (PC) and ancillary information, (4) feature type (3) plus the most sensitive ALOS PALSAR polarization, (5) multi-temporal ALOS PALSAR HV polarizations and DEM. The first two PC of the SPOT-5 HRG image were selected because they can describe 97.3% of the original spectral variance. Only HV polarization of ALOS PALSAR was used, because the HV polarization showed much more sensitive to forest AGB estimation than HH polarization.

2.4 Results and Discussion

2.4.1 Evaluation of k -NN Configurations

The comparison of configurations of mathematical setup showed that the pixel-wise extraction method performed consistently worse than the 3×3 window extractions. For this reason, the results presented hereon concern 3×3 window extractions only. All results of the 3×3 window extraction method are shown in Fig. 2-2, together with the results of LOO tests. All factors (feature types, multidimensional distance measures, number of k nearest neighbours, and the extraction methods) affected the performance of k -NN estimates. The optimal k -NN configuration was decided by the Pearson correlation index (R) and root mean square error (RMSE) between k -NN estimates and measured forest AGB values calculated on the basis of LOO procedure. The optimal k -NN configuration for each feature type is shown in Table 2-2.

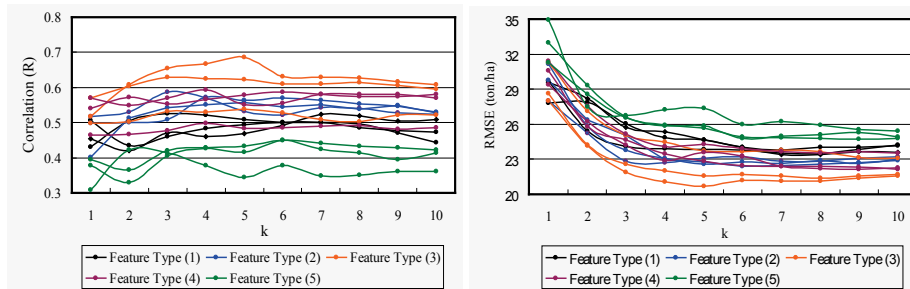


Fig. 2-2 Correlation R (left) and RMSE (right) of LOO tests on the k -NN configurations.

The best configuration was that one with $k = 5$, the MD measure, the feature type (3) using the first two principal components and IRI from original 4 SPOT-5 HRG bands augmented with the DEM information. This configuration generated the most accurate estimates with $R = 0.69$ and $RMSE = 20.70$ tonnes ha^{-1} .

The mathematical setup was analysed further by averaging the results per distance measure and per value of k . Fig. 2-3 plots the performance of the distance measures versus k . It was clear that until $k = 5$, the RMSE consistently decreased with increasing k . The estimations with MD measure were better than the others, except when $k = 1$. The MD and FD configurations converge for higher values of k , while ED performed consistently worse than the other two for all values of $k > 1$. Between $k = 1$ and $k = 5$, the differences in the accuracy of three distance measures was high, up to 0.12 for R and 2.1 (tonnes ha⁻¹) for RMSE.

Additional test (not shown here), indicated that topographically and atmospherically correction of the satellite images was necessary, as uncorrected inputs produced significantly poorer results.

Table 2-2 Results of optimal k -NN estimations assessed by LOO procedure.

Feature Type	k Value	Distance Measures	R	RMSE (tonnes ha ⁻¹)
(1)	3	ED	0.53	24.06
(2)	3	MD	0.59	22.83
(3)	5	MD	0.69	20.70
(4)	4	FD	0.60	22.90
(5)	6	MD	0.45	24.80

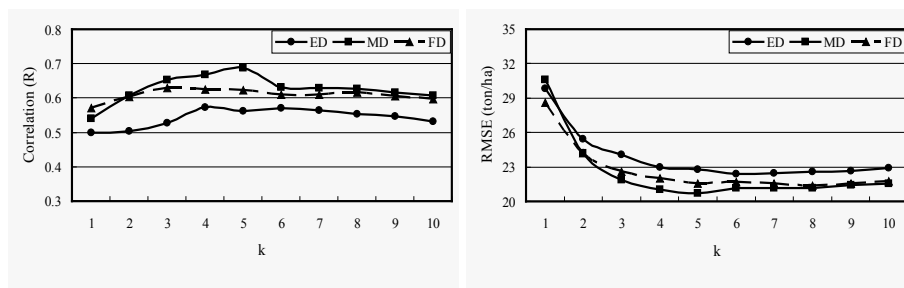


Fig. 2-3 Correlation R (left) and RMSE (right) of the best performance for each distance measure.

2.4.2 Estimations of Regression Models

Six tests were carried out for all feature types, and mean height, height quantiles, and fc from LiDAR points. For the first five regressions, the total reference data from 75 plots was divided into training (38 plots) and test set (37 plots) by nearly half and half by stratified sampling according to the forest AGB grades. For the last regression, based on the estimates from airborne LiDAR data, 2/3 of reference data was used for training and the remainder for validation by stratified sampling as well. For feature type (1), the fitting model was:

$$\hat{Y} = 268.777 - 2430.849 \times r_1 + 491.658 \times r_2 - 655.479 \times r_3 + 61.646 \times r_4 \quad (2-16)$$

with $R = 0.48$ and $RMSE = 39.6$ tonnes ha^{-1} reported by validation process ($r_1 \sim r_4$ are the reflectance of SPOT-5 HRG band1-band 4 respectively).

For feature type (2), the resulting regression model was:

$$\hat{Y} = 117.996 + 201.006 \times r_1 - 598.644 \times r_2 - 2160.15 \times r_3 + 2582.402 \times r_4 + 513.733 \times iri - 0.026 \times dem \quad (2-17)$$

with $R = 0.52$ and $RMSE = 39.1$ tonnes ha^{-1} (iri is IRI information from SPOT-5 HRG and dem is elevation).

For feature type (3), the resulting regression model was:

$$\hat{Y} = 506.247 - 642.741 \times pc_1 - 1859.338 \times pc_2 - 302.520 \times iri - 0.078 \times dem \quad (2-18)$$

with $R = 0.56$ and $RMSE = 37.4$ tonnes ha^{-1} (pc_1 and pc_2 are PC_S 1 and 2 respectively).

Based on feature type (4), the regression model was derived as:

$$\hat{Y} = 418.08 - 619.837 \times pc_1 - 436.592 \times pc_2 - 264.164 \times iri - 0.042 \times dem - 118.892 \times \sigma_{hv} \quad (2-19)$$

with $R = 0.49$ and $RMSE = 28.3$ tonnes ha^{-1} (σ_{hv} is the most sensitive HV polarization of the three temporal ALOS PALSAR intensity data).

For feature type (5), the resulting regression model was:

$$\hat{Y} = 318.641 - 33.216 \times \sigma_{hv1} - 26.175 \times \sigma_{hv2} + 65.021 \times \sigma_{hv3} - 0.043 \times dem \quad (2-20)$$

with $R = 0.43$ and $RMSE = 40.8$ tonnes ha^{-1} ($\sigma_{hv1}, hv2, hv3$ are HV polarization of the three temporal ALOS PALSAR intensity data).

On the basis of LiDAR' estimates of mean height, height quantiles and f_c , the following regression model was found:

$$\hat{Y} = -9.013 + 10.812 \times H_{mean} + 25.105 \times f_c \quad (2-21)$$

with $R = 0.84$ and $RMSE = 15.24$ tonnes ha^{-1} (H_{mean} is the mean tree height).

The regression that included the airborne LiDAR clearly outperformed all others, and showed a high correlation coefficient of 0.84 and low RMSE of 15.20 tonnes ha^{-1} .

2.4.3 Comparison of Results from The Best k-NN Configuration and LiDAR

The promising result of the regression including the LiDAR data was further

compared to the best result of the k -NN analyses (in which no LiDAR data were used). This enabled this chapter to evaluate the applicability of the k -NN approach with SPOT-5 data further than possible with the 75 field sites only. Now, a pixel-by-pixel comparison can be carried out, thus fully exploiting the information of the LiDAR data.

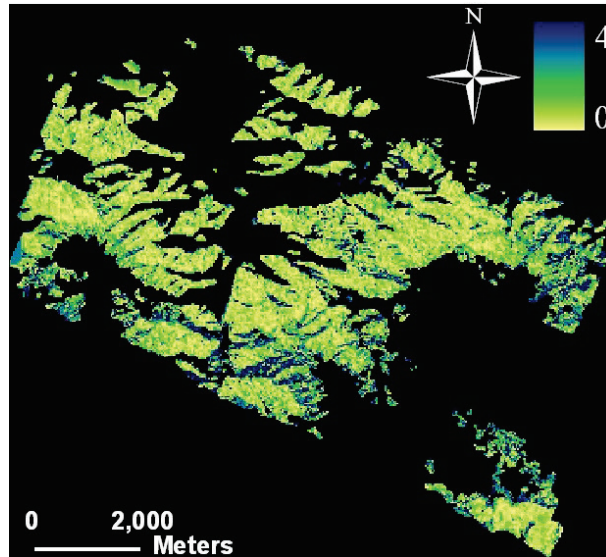


Fig. 2-4 Relative difference map between the best k -NN and LiDAR estimations of forest AGB (in tonnes ha^{-1}).

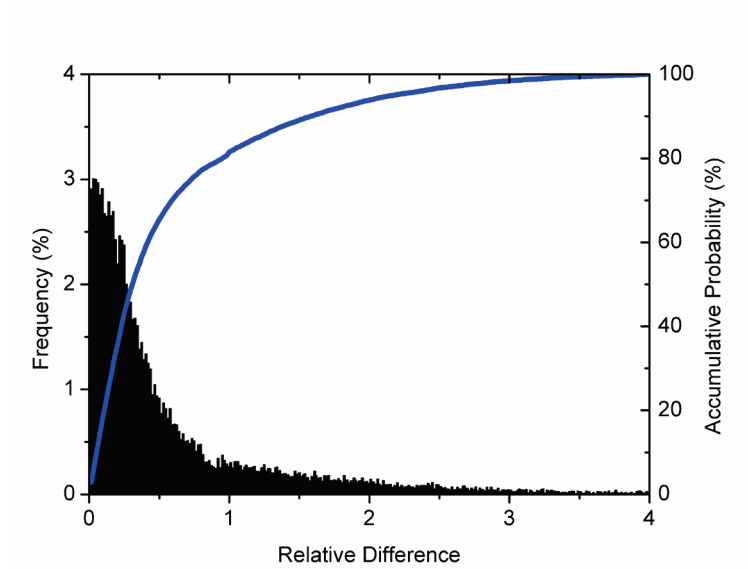


Fig. 2-5 Histogram and accumulative probability distribution of the relative difference map.

The pixel-wise difference between the two methods (regression with LiDAR and k-NN without LiDAR) is shown both spatially (as a map) and statistically (as a histogram) in Fig. 2-4 and Fig. 2-5. The non-parametric k-NN estimation was close to the retrieval from LiDAR data with only a few exceptions. These exceptions were found in valley and ridge areas where the forests are very sparse and it is usually mixed with shrubs and grass. In these highly heterogeneous areas, the k-NN tended to largely overestimate the forest AGB using the SPOT-5 HRG image, causing high relative differences between SPOT-5's and LiDAR's retrievals (with a maximum of about 4). It was, however, also possible that the deviations were caused by the LiDAR data.

2.5 Discussion

Two kinds of advantages of the k-NN method used in this chapter need to be mentioned. The first advantage is that the non-parametric k-NN maps the forest AGB with sufficient accuracy to assist the forest inventory. To obtain the inventory in the cold and arid HRB, it is extremely labour intensive. The second advantage is that the LOO optimization procedure to determine the best k-NN configuration makes the estimation robust and largely reduced the random discrepancies normally produced by training and test dataset separation from reference data. The procedure does not require the separation of the data into a training and a validation data set, the choice of which usually affects the validation evaluation result.

The results showed that the inclusion of more informative variables did not necessarily make the estimation better. On the contrary, the feature type with SPOT-5's compact principle components augmented by IRI and DEM outperformed the synthesis of SPOT-5's PC and ALOS PALSAR HV polarization combined with IRI and DEM. This has several reasons. First, the regression analyses showed that forest AGB was less sensitive to the HV polarization than to other features. Second, the terrain correction for SAR data could only reduce, but not eliminate the influence of the topography in this area. As mentioned in Section 2.2, the forests mainly exist in the shadow slopes which are also the shadows for ALOS PALSAR data.

It is necessary to restate that there are two kinds of forest plot with $20\text{m} \times 20\text{m}$ and $25\text{m} \times 25\text{m}$ size respectively, measured during the campaign, and as general, the plot geographic boundary may overlay several pixel grids. This explains why the 3×3 window extraction method performed better than the pixel-by-pixel comparison with ground data.

For $k > 5$, there seems no clear relationship between the value for k and estimation

performance. Higher values of k imply averaging over a larger number of ground measurements. This results in values for AGB that move away from the extreme values in the ground dataset (in this chapter, the minimum value was 18 tonnes ha⁻¹ and the maximum 175 tonnes ha⁻¹). This averaging effect becomes smaller with increasing k .

The comparison of distance measures showed that MD and FD outperformed the simplest ED measure (for $k > 1$). As previous studies mentioned (Maselli, 2001; Chirici et al., 2008), small modification of the variance-covariance matrix normally could enhance the importance of the most informative input variables without hindering the stability of the response variables. However, when the information content of the feature space variables is relatively uniform, the improvement becomes marginal. In this work, large differences between FD and MD occurred for values of k between 2 and 5, suggesting that the information content of the feature space was inhomogeneous.

Although the regression estimation is easier to perform than k -NN, it requires that a statistical relationship between the measurements and feature space variables exists. This chapter made it clear that the relationship of the forest AGB measurements and remote sensing observation was rather variable, resulting in poor results for the regression.

As airborne LiDAR has the unique advantage in deriving the tree height which is most sensitive to the forest AGB in most cases, it is always expected to derive the best forest AGB results among various remote sensing data sources. In this chapter, the best result was achieved from LiDAR data by SMLR based on the estimates of mean height, height quantiles and f_c , without exception. The regression procedure indicated that the significant independent variables were the mean tree height and f_c .

This chapter suggests that, when more accurate forest AGB is required, the use of high-density airborne LiDAR cloud points or full wave form LiDAR observations are highly valuable due to their precision. In that way, sufficient information on individual trees could be derived, which would be more robust than statistical analyses as performed in this chapter.

2.6 Conclusion

This chapter estimated above ground forest biomass (AGB) from SPOT-5 data, using a non-parametric method trained with field data for a remote forested area with satisfactory accuracy ($R = 0.69$, $RMSE = 20.70$ tonnes ha⁻¹). The results did

not improve when ALOS PALSAR HV information was added, but declined. The terrain influence hindered the predictable ability of the ALOS PALSAR data, independent of the method that was chosen to include the data.

A comparison of the results of the non-parametric method with estimates based on airborne LiDAR, showed that the accumulative distribution probabilities for the relative difference of 0.3 and 1.0 are below of 50% and 85% respectively (Fig. 2-5), which casts a promising light on the application of k-NN method for forest inventory in this cold and arid area.

The non-parametric method used in this chapter might be more applicable to areas where forests are more homogenous. Even though the forests in the study area consist of only one dominant tree species, they are still heterogeneous and fragmented because of the cold and arid environment. The non-parametric forest AGB results obtained in this area encourage further interests to investigate other forest attributes (i.e., basal area and LAI) with this method.

Chapter 3

Improvement of Estimating Forest Above-Ground Biomass over The Qilian Mountains Using Multi-Parameter Remote Sensing Data^{*}

^{*} This chapter is based on:

Tian, X., Li, Z. Y., Su, Z. B., Chen, E. X., van der Tol, C., Li, X., Guo, Y., Li, L. H., & Ling, F. L. (2014). Estimating montane forest above-ground biomass in the upper reaches of the Heihe River Basin using Landsat-TM data. *International Journal of Remote Sensing*, 35, 7339-7362, DOI: 10.1080/01431161.2014.967888.

Abstract

In this chapter, the results of above-ground biomass (AGB) estimates from Landsat Thematic Mapper 5 (TM) images and field data from the fragmented landscape of the upper reaches of the Heihe River Basin (HRB), located in the Qilian Mountains (QMs), are presented. Estimates of AGB are relevant for sustainable forest management, monitoring global change, and carbon accounting. This is particularly true for the QMs, which are a water resource protection zone. This chapter combines forest inventory data from 133 plots with TM images and Advanced Spaceborne Thermal Emission and Reflection Radiometer (ASTER) global digital elevation model (GDEM) V2 products (GDEM) in order to analyse the influence of the sun-canopy-sensor plus C (SCS+C) topographic correction on estimations of forest AGB using the stepwise multiple linear regression (SMLR) and k-Nearest Neighbour (k-NN) methods. For both methods, the results indicated that the SCS+C correction was necessary for getting more reliable forest AGB estimates within this complex terrain. Remotely sensed AGB estimates were validated against forest inventory data using the leave-one-out (LOO) method. An optimized k-NN method was designed by varying both mathematical formulation of the algorithm and remote sensing data input, which resulted in 3000 different model configurations. Following topographic correction, performance of the optimized k-NN method was compared to that of the regression method. The optimized k-NN method ($R^2 = 0.59$, root mean square error (RMSE) = 24.92 tonnes ha⁻¹) was found to perform much better than the regression method ($R^2 = 0.42$, RMSE = 29.74 tonnes ha⁻¹) for forest AGB retrieval over this montane area. The results indicate that the optimized k-NN method is capable of operational application to forest AGB estimates in regions where few inventory data are available.

3.1 Introduction

In **Chapter 2**, forest measurements were integrated with multi-parameter remote-sensing data from the Satellite Probatoire d’Observation de la Terre-5 (SPOT-5) high resolution geometrical (HRG) and also L-band advanced land observation satellite (ALOS) phased array type L-band synthetic aperture radar (PALSAR) data, to investigate the feasibility of parametric and non-parametric methods for estimating forest AGB. This work was conducted within an airborne campaign area, in the small watershed of the Heihe River Basin (HRB) in northwest China.

In fact, for both parametric and non-parametric methods, a well-known drawback is that predictions outside the range of reference data inherently result in large uncertainties (McRoberts, 2009; Magnussen et al., 2010; Baffetta et al., 2012; Breidenbach et al., 2012). Therefore, that the range of variability in forest AGB in the region under study is represented in the reference data (i.e. in the forest inventory data used to train the algorithm) is often considered to be important. As a result, relationships between forest measurements and remotely sensed representations should be established for a large population of forest inventory data. Such a prerequisite is particularly problematic for parametric methods. If simple linear or nonlinear regression formulae are built on a few field measurements located within a large area and if the independent variables are measured with error, the range of AGB will be suppressed and the variation underestimated. Since multispectral signals saturate at low forest AGB levels, the fitted results will be worse when applying multispectral remote-sensing data. All of this is less of a problem for non-parametric models. For the non-parametric k -Nearest Neighbour (k -NN) algorithm, the k ‘nearest’ pixels within the training set and the smallest values of spectral distance measured, d , are used to compute the AGB of the remote-sensing pixel as a weighted average, which, to some extent, may alleviate the impact of the small range of variability.

One of the main reasons for performing the work of this chapter is that the forests in the upper reaches of the HRB are essential for soil and water conservation, water resource protection, and hydrology regulation. The HRB serves as the ‘water tower’ for downstream urban areas and agriculture in an otherwise extremely dry region. Since the 1990s, the HRB has been used as a scientific study region for integrated watershed and land-atmosphere studies. Comprehensive experiments such as the Heihe Basin Field Experiment (HEIFE) (Hu et al., 1994), Watershed Allied Telemetry Experimental Research (WATER) (Li et al., 2009a), and Heihe Watershed Allied Telemetry Experimental Research (HiWATER) (Li et al., 2013b) have been conducted. However, a forest resource monitoring study for the entire

Qilian Mountain region has not yet been conducted. In **Chapter 2**, SPOT-5 HRG data only covered a portion of the area. In an attempt to extend the approach to a larger area, this chapter considered that the Landsat Thematic Mapper (TM) provides more useful spectral information for estimating forest structure than SPOT HRV, albeit with a poorer spatial resolution (Cohen and Spies, 1992; Labrecque et al., 2006). Therefore, for the task of routinely monitoring forest resources, TM imagery may be a useful alternative to expensive SPOT-5 images. Here, this chapter examines forest AGB using free and long-time-continuity TM imagery of the complex montane region of the upper HRB. Since data sets of field measurements are still relatively small, the leave-one-out (LOO) method is used for assessing prediction errors. Since it is almost unbiased, LOO is frequently used as a statistical estimator for the performance of a learning algorithm (Lachenbruch, 1967; Arlot and Celisse, 2010; Meijer and Goeman, 2013).

The goals of this chapter were to: (i) introduce an effective radiometric terrain correction in order to alleviate the impacts of topographical environments on quantifying the montane forest AGB; (ii) apply regression and k -NN methods to TM images for mapping the regional forest AGB; and (iii) test the estimation abilities of regression methods and different configurations of the k -NN algorithm with and without radiometric terrain rectification. The performance of the regression and k -NN methods was systematically compared and evaluated using the LOO. Finally, the optimal k -NN configurations were conducted for estimating the regional forest AGB.

3.2 Ground and Remote Sensing Data

Apart from the forest inventory conducted within the airborne campaign area (introduced in Section 2.2), another measurement for 58 circular forest plots (with diameters ranging from 10 m to 28 m) were used in this chapter. Using the following criteria, a total of 133 forest plots were selected from the measurement database: (1) the prevalence of forest plots dominated by *Picea crassifolia* and (2) forest plots with geographic independency with one another required to avoid spatial autocorrelation. *Picea crassifolia* is the most prevalent tree species within the study area. According to the inventory records, it occupies 99.39% of total measured trees (8667 trees), and therefore, the *Picea crassifolia* growth equations from Wang et al. (1998b), calibrated for the study area, were applied for calculating the forest plot AGB.

For remote-sensing data, four scenes of TM images with ortho-rectification (L1T products on 17 July 2009, 17 July 2009, and two on 11 August 2009) that fully spanned the QMs were acquired from the United States Geological Survey (USGS)

(<http://glovis.usgs.gov>). Corresponding Advanced Spaceborne Thermal Emission and Reflection Radiometer (ASTER) global digital elevation model (GDEM) V2 (GDEM, 30 m) products were obtained from the Japan Aerospace Exploration Agency (JAXA) (<http://gdem.ersdac.jspacesystems.or.jp>). Altitude information was used as an auxiliary for estimating forest AGB. To alleviate terrain impacts on forest AGB retrieval, GDEM products were also used to obtain the sun-canopy-sensor plus C (SCS+C) topographic correction (Soenen et al., 2005). TM images were further processed using radiometric and atmospheric correction (FLAASH model) (Adler-Golden et al., 1999), radiometric terrain correction, and normalization processes in preparation of forest discrimination and forest AGB retrieval.

3.3 Methodology

3.3.1 The SCS+C Radiometric Terrain Correction

Determining topographic effects on classification, image interpretation, and parameter estimation requires quantitative information from satellite imagery and is still problematic. This problem can be very serious in mountainous areas due to large variations in the sun incident angle relative to the ground slope (Ghasemi et al., 2013).

In this chapter, the Sun-Canopy-Sensor Plus C (SCS+C) correction model (Soenen et al., 2005), a modification of the SCS model (Gu and Gillespie, 1998), was employed. For this model, the parameter C_τ (defined in Eq. (3-3) below) was added to the C-correction method. The topographically corrected radiance (TCR), ρ_H , was then calculated using the following equations:

$$\rho_H = \frac{\rho_T (\cos \theta_p \cos \theta_z + C_\tau)}{(\cos \gamma_i + C_\tau)} \quad (3-1)$$

where ρ_T is the radiance of the uncorrected pixel, θ_p is the terrain slope of the pixel, θ_z is the solar zenith angle, γ_i is the incidence angle, and a linear relationship exists between the ρ_T and the $\cos \gamma_i$ of the following form:

$$\rho_T = a_\tau + b_\tau \cos \gamma_i \quad (3-2)$$

The parameter C_τ is a function of the regression slope (b_τ) and the intercept (a_τ), as follows:

$$C_\tau = \frac{a_\tau}{b_\tau} \quad (3-3)$$

$$\cos \gamma_i = \cos \theta_p \cos \theta_z + \sin \theta_p \sin \theta_z \cos(\omega) \quad (3-4)$$

where ω is the difference between the solar azimuth angle (θ_a) and the surface aspect of the slope angle (θ_s).

The values of θ_p , θ_z , γ_i , and θ_a can be obtained from the metadata or header file of the remote sensing image (in this case: the TM image) and θ_s can be derived from digital elevation model (DEM) information (in this case: the GDEM).

C_τ was used to better characterize diffuse sky irradiance (the downwelling spectral irradiance at the surface due to scattered solar flux in the atmosphere). As a result, this treatment can reduce the overcorrection of faintly illuminated pixels (Soenen et al., 2005; Dimitrov and Roumenina, 2013). In this chapter, the constant, C_τ was only added for coniferous forests (*Picea crassifolia*). Approximately 14,000 pixels randomly selected from four scenes (roughly 3 500 pixels for each) were used, and, for each pixel, the radiances in the six bands and the $\cos\gamma_i$ were extracted. Finally, a separate value for C_τ was determined for each spectral band.

3.3.2 Forest Discrimination

To reduce the influence of the other vegetation types (i.e. pastures, shrubs) on estimations of forest AGB, the generation of a forest/non-forest map is necessary for identifying target pixels in TM images. Due to the complex terrain and the fragmented landscape, this chapter opted for a decision-tree classifier for discriminating between forest and non-forest by integrating TM images with GDEM information. Classification of vegetated and non-vegetated areas was performed using the ratio of TM bands 4 and 3. Due to strong absorption by chlorophyll in the red band and strong reflection by mesophyll tissue in the near infrared band, the ratio of the reflectance in the near infrared band to that in the red band is high for vegetation; in other words, the ratio vegetation index (RVI) is high and is clearly different from that in non-vegetated areas. Generally, the RVI is higher than 2.0 in vegetated areas and lower than 2.0 in non-vegetated areas. As a result of comparative analyses, the mean texture information of the fourth band was helpful for further distinguishing forests (≤ 2.5) from the other vegetation types (> 2.5). Moreover, as mentioned previously, niches of *Picea crassifolia* only exist between 2500 m and 3300 m. Using GDEM information, forest/non-forest categories can finally be determined (see Fig. 3-1). A total of 133 forest plots and 43 polygons (with sizes of about 100–600 pixels each) were chosen from high-resolution images in Google Earth for the validation. The criteria for selecting the test polygons were based on visual interpretation of the aerial photographs (the CCD images in Section 2.2) and archive forest compartment map (2003–2007). The overall accuracy of the forest/non-forest map (see Fig. 3-2) was 90.88%, with the value of the kappa coefficient being 0.81 (Table 3-1).

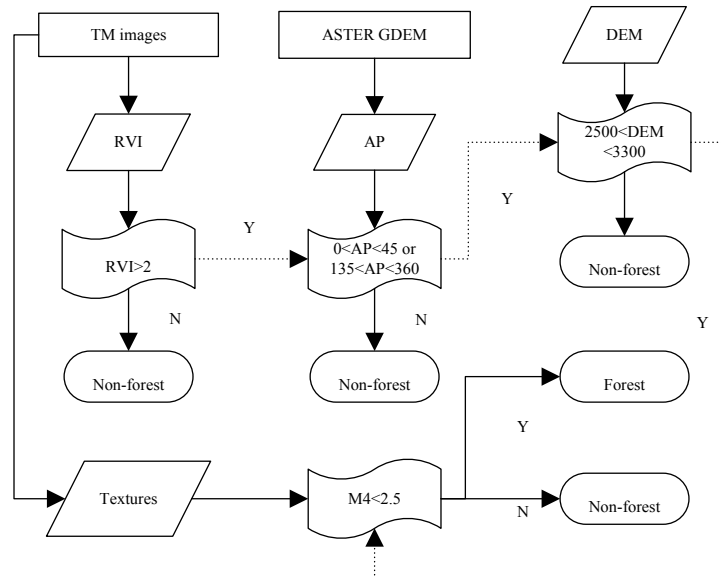


Fig. 3-1 The decision tree for the forest and non-forest classification (RVI is the ratio vegetation index; M4 is the mean texture of band 4 of TM image).

Table 3-1 Confusion matrix for the forest/non-forest map.

Class	Forest	Non-forest	Total	Producer's Accuracy (%)	User's Accuracy (%)
Forest	6017	613	6630	91.68	89.80
Non-forest	546	5538	6084	88.99	91.03
Total	6563	6151	12714		90.88
Kappa Coefficient				0.81	

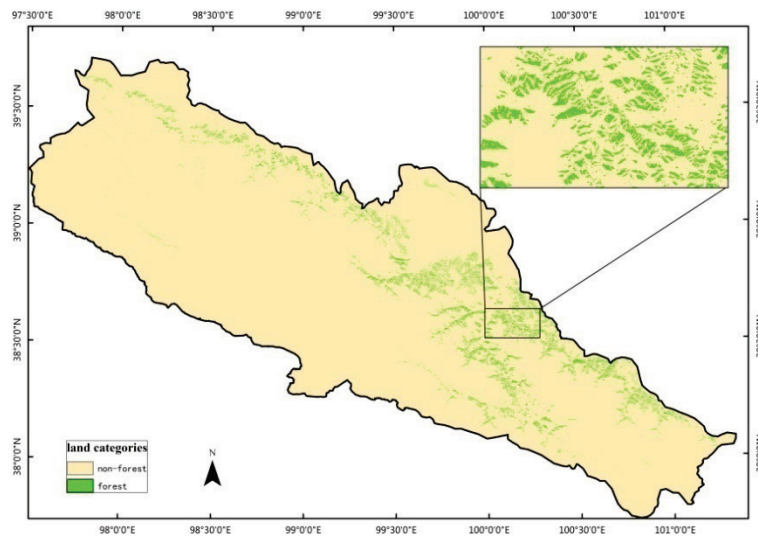


Fig. 3-2 The forest/non-forest map of the study area.

3.3.3 Regression Method

Stepwise multiple linear regression (SMLR) is a classical parametric method. For this chapter, the remote-sensing signals and the indices were the independent variables and the forest AGB was the dependent variable. The goal of retrieving AGB in this way was to be able to compare the results with and without a radiometric terrain correction, and the results of k -NN estimates with those of a conventional parametric method.

Multicollinearity commonly exists between different types of remote-sensing information and tends to degenerate the quality of parameter retrievals. In order to estimate vegetation parameters, a large number of vegetation indices, geographic details, and texture information should be included in the regression. To address this issue, Tasseled Cap transformation and principal component (PC) processes were conducted, and multiple vegetation indices such as the infrared index (IRI), the normalized difference vegetation index (NDVI), the RVI, and others, were calculated. Some important texture information (i.e. mean, variance, homogeneity, contrast, dissimilarity, entropy, second moment, and correlation) for each band within the TM image were extracted using the co-occurrence module in the ENVI software (Exelis Visual Information Solutions, Inc., Boulder, CO, USA). In addition, some terrain details (i.e. aspect, slope, and altitude) were extracted from the GDEM. By selecting the most significant variables (the probability of F-to-enter = 0.05; the probability of F-to-remove = 0.1), a total of 88 feature variables were collected and the SMLR was executed in order to establish the regression relationship between these variables and the forest AGB.

3.3.4 The k -NN Method

The k -NN technique is a non-parametric, multivariate approach for processing observations or combinations of observations from sampling units for obtaining estimations or mapping units (McRoberts et al., 2007; McRoberts, 2012; Gilichinsky et al., 2012). The attractiveness of the method is that it is distribution free in that it does not rely on any underlying probability distribution for estimations, but on forest conditions (Mattioli et al., 2012). When there is good representation of ground sample plots, the method has performed well for biomass estimations. As a result of this performance, the technique is widely used (Labrecque et al., 2006). The detailed expressions of k -NN and the related multidimensional distance measures were given in **Section 2.3.1** and **Section 2.3.2**.

3.3.5 Construction of An Optimal k -NN

Similar optimization of k -NN as that in **Section 2.3.9** was performed except for the inputting feature space variables. Regarding feature space variables, 10 different compositions were composed by comparing the sensitivities of 88 feature variables to the forest AGB. These 10 combinations of feature space variables were used in combination with the three types of distance measure same as those in **Section 2.3.9**; k varied from 1 to 25 and the window sizes from 1×1 to 7×7 (pixels), resulting in a total of 3000 configurations (Table 3-2) that were tested.

Table 3-2 The k -NN configurations used in this chapter.

k Value	Distance Measures	Feature Type	Feature Extraction Method
1-5	ED, MD, FD	(1)Altitude, M_4 , W, B5, B7 (2) Altitude, IRI, NDVI, PC1–PC3 (3) W, ARVI, IRI, B3, B4, B5 (4) IRI, NDVI, PC1–PC3 (5) Altitude, W, S_5 , E_7 (6) Altitude, M_4 , W, PC3s (7) Altitude, IRI, W, M_4 , E_7 , B4/B7 (8) Altitude, IRI, ARVI, B2/B7, B4/B7, M_5 (9) Altitude, IRI, B2, B5, B7 (10) Altitude, PC1–PC3, M_4 , B2/B7	Pixel-wise; 3×3 , 5×5 and 7×7 window

Since they can describe 95.6% of the original spectral variance, the first three PCs of the TM images were selected. The optimal k -NN configuration was determined with pixel-wise accuracy of the estimates with the highest Pearson correlation index (R) and the lowest root mean square error (RMSE). Finally, the best-performing k -

NN configuration (out of the 3000 judged based on LOO performance) was selected for estimating and assessing AGB over QMs.

3.4 Results

3.4.1 The Regression Estimation

The consideration of 88 possible independent variables from the TM and GDEM data, and from the SMLR with strict control parameters (probability of F-to-enter = 0.05; probability of F-to-remove = 0.1), was done in order to determine sensitive variables for fitting the regression of forest AGB. To analyse the influence of the terrain on quantitative retrieval, two regressions were established using feature variables from the uncorrected and corrected (processed by SCS+C) TM data. With respect to this process, the range of variability in the measured forest AGB should correspondingly represent both training and test set. Therefore, the complete reference data set from the 133 plots was divided into a training set (88 plots) and a test set (45 plots) – representing, therefore, nearly two-third and one-third of the plots, respectively – using a stratified sampling method based on forest AGB grades. As the forest AGB range was 18.85 tonnes ha⁻¹ to 220.65 tonnes ha⁻¹, the reference data was separated into five subclasses (50 tonnes ha⁻¹ per stratum): 0–50 tonnes ha⁻¹, 51–100 tonnes ha⁻¹, 101–150 tonnes ha⁻¹, 151–200 tonnes ha⁻¹, and 201–250 tonnes ha⁻¹. Within each subclass, the reference data were randomly assigned to either the training or test data set in the ratio of approximately 2:1.

Without SCS+C, the fitting model was, as follows:

$$\hat{Y} = 652.685 - 0.195 \times DEM + 62.662 \times S7 + 0.772 \times SP \quad (3-5)$$

which had a modeling accuracy corresponding to of a coefficient of determination, R^2 , equal to 0.50 and an RMSE of 26.74 tonnes ha⁻¹. (DEM and S indicate the altitude and the slope derived from the GDEM, respectively; and S_7 is the texture of the second moment in TM band 7).

In contrast, using SCS+C, the following regression model was derived:

$$\hat{Y} = 4235.235 - 0.199 \times DEM - 81.107 \times M5 - 41.238 \times S7 \quad (3-6)$$

For this model, $R^2 = 0.53$ and RMSE = 25.99 tonnes ha⁻¹. (Here, $M5$ is the mean texture of TM band 5.)

The two regressions above were validated at the pixel level using the selected test set. It could be seen that the model that incorporated variables from the SCS+C-corrected TM textures (with $R^2 = 0.33$ and RMSE = 26.44 tonnes ha⁻¹) performed better than the uncorrected model (with $R^2 = 0.15$ and RMSE = 29.73 tonnes ha⁻¹) (see Fig. 3-3). The mean percentage errors (MPEs) for these two models were 24.15% and 26.32%, respectively. Following the SCS+C process, the independent

variable changed from ‘S’ to ‘M5’ by regression model implying that slope impacts on the estimation may be alleviated.

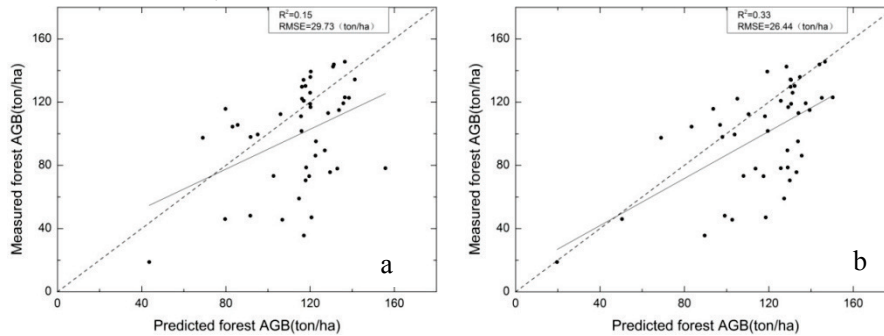


Fig. 3-3 The fitted results of the measured and predicted value based on a stepwise multiple linear regression (the dashed line is a 1:1 fit; (a) Without the SCS+C correction; (b) with the SCS+C correction).

As expected, the estimated accuracy of the parametric method was, in all cases, quite low due to limitations linked to radiometric deviations in the remote-sensing data. Moreover, the complexity of the relationships between forest features and relevant TM reflectance or induced indices affected the performance of the parametric model (Maselli and Chiesi, 2006). As with other regions of northwest China, due to biophysical controlling factors (soil fertility, soil water, topography, and altitude), the forest features in the Qilian Mountains (QMs) tend to vary significantly over a very small area. As seen in Fig. 3-3, the deviations of the model output from the field data were large.

Although a radiometric terrain correction was performed and the results improved as compared to the uncorrected model, routine monitoring of the forest AGB using this parametric method is not an option.

3.4.2 The *k*-NN Estimation

Considerable variation was found in the quality of the *k*-NN model output, depending on the mathematical set-up and the selected feature space variables. Concerning the mathematical framework, the 5×5 window extraction clearly outperformed all of the other sampling methods (not shown). For this reason, presentation of the results here is limited only to the 5×5 window sampling size. The results of the testing using the LOO procedure, for the 5×5 window sampling size, are shown in Fig. 3-4. As mentioned, the accuracy of the various *k*-NN configurations varied a lot. Feature type 8 consistently outperformed all the others, while the prediction accuracy of feature type 4 was always inferior to that of the others.

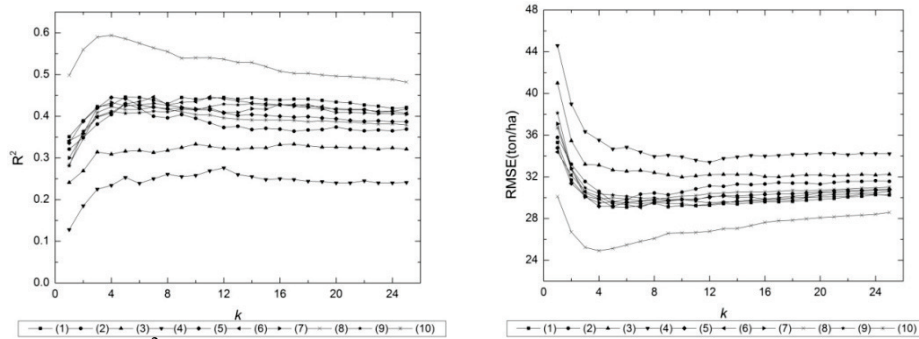


Fig. 3-4 The R^2 and RMSE of the different k -NN configurations.

For each feature type listed in Table 3-2, the optimal k -NN configuration and the results were compared (Table 3-3). The values of k between 10 and 14 for features (3), (4), and (9); and the value of k neighbours between 4 and 7 for the other features were determined using the optimized process. The best configuration was as follows: $k = 4$; distance measure MD; feature (8) using the IRI; the atmospherically resistant vegetation index (ARVI); ratios of band 2 to band 7 and band 4 to band 7; and the mean texture of band 5 augmented with DEM information from the GDEM. This configuration generated the best estimates, with $R^2 = 0.59$, $\text{RMSE} = 24.92 \text{ tonnes ha}^{-1}$, and $\text{MPE} = 20.75\%$. In contrast, the optimized configuration with $k = 12$, the MD measure, and feature (4) composed of the IRI, the NDVI, and the first three PCs produced the poorest estimates for forest AGB, with $R^2 = 0.28$ and $\text{RMSE} = 33.40 \text{ tonnes ha}^{-1}$. The difference in the accuracy of the two configurations above is high – 0.31 for R^2 and 8.48 tonnes ha^{-1} for RMSE. All of the features were mathematically optimized using the MD measure, with the exception of feature (3), which performed a little better than the worst ‘optimal’ configuration. Additional configurations differed marginally with values of R^2 between 0.42 to 0.45 and the RMSE varying from 29.67 to 29.08 tonnes ha^{-1} .

Table 3-3 The results of optimal k -NN estimations assessed using the LOO cross-validation procedure for each feature vector (feature type).

Feature type	k value	Distance measure	R^2	RESM (tonnes ha^{-1})
(1)	5	MD	0.45	29.11
(2)	5	MD	0.43	29.59
(3)	10	MD	0.33	31.99
(4)	12	MD	0.28	33.40
(5)	4	MD	0.45	29.17
(6)	7	MD	0.45	29.08
(7)	4	MD	0.43	29.50
(8)	4	MD	0.59	24.92
(9)	14	MD	0.43	29.57
(10)	7	MD	0.42	29.67

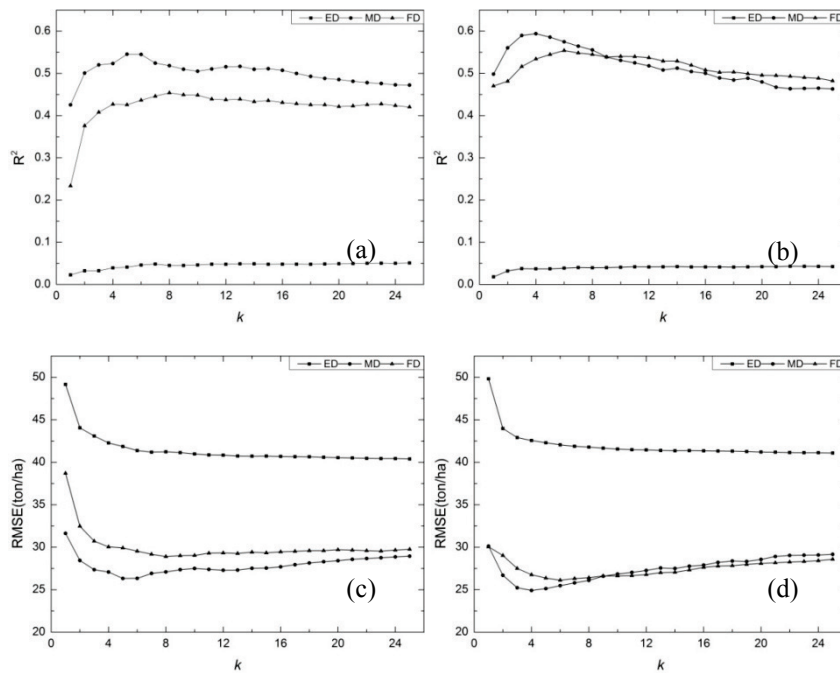


Fig. 3-5 The R^2 ((a) and (b)) and RMSE ((c) and (d)) of the three distance estimations based on uncorrected and corrected Feature (8) in Table 3-1 (where ED is the Euclidean Distance, MD is the Mahalanobis Distance, FD is the Fuzzy Distance, (a) and (c) are provided without the SCS+C correction, and (b) and (d) with the SCS+C terrain correction).

The mathematical set-up was analysed further by comparing the results for the different distance measures used and different values of k . In order to analyse the influence of the SCS+C correction on forest AGB estimations, the model performance was plotted against the value of k for the different distance measures for both terrain- corrected and uncorrected feature (8). The results are shown in Fig. 3-5, illustrated in terms of both R^2 and the RMSE. Clearly for the MD and FD, the terrain-corrected feature vector consistently outperformed the uncorrected feature. Interestingly, it was determined that for one case, the terrain-corrected variant performed worse than the uncorrected variant (lower R^2 and higher RMSE) for the case of the ED measure. The overall accuracies when using the ED for both feature vectors were much lower than when the other two distance measures were used.

For all of the distance measures, R^2 initially increased and the RMSE decreased with increasing k , until a particular value of k was reached. For example, the MD performed best at $k = 5$ for the uncorrected feature input, and at $k = 4$ for the corrected feature input. The performance of the ED changed for corrected and uncorrected feature vectors in the similar manner. FD was inferior to MD for the

corrected feature vector, but slightly better than MD when $k > 9$.

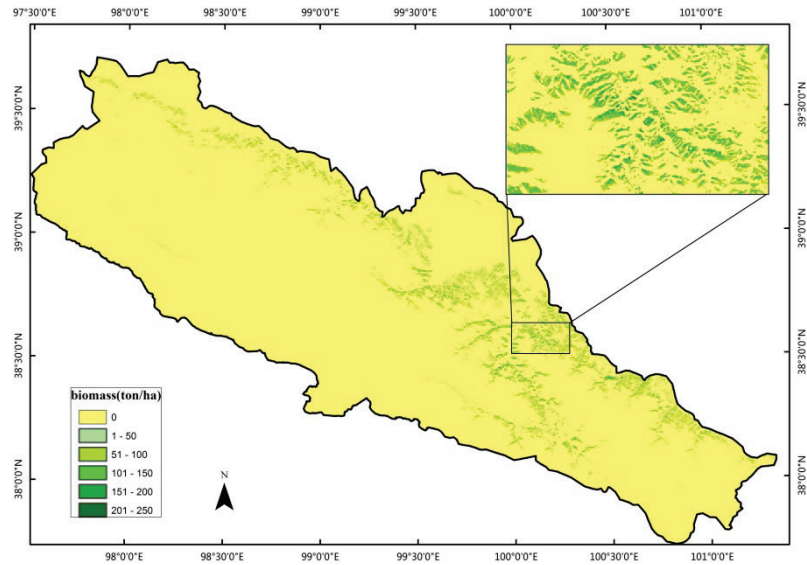


Fig. 3-6 The grade distribution of forest AGB over the QMs.

The best optimized k -NN algorithm out of 3000 configurations was applied in order to derive forest AGB over the QMs. As shown in Fig. 3-6, AGB decreased with increasing altitude and latitude, and increased with increasing longitude. The pattern is similar to that reported by Peng et al. (2011). Validated by the LOO method on the basis of 133 forest plot measurements (see Fig. 3-7), the overall accuracy of forest AGB retrievals was satisfactory. The slope of the graph plotting the field AGB against the remotely sensed AGB was approximately 1, and the offset was 25.04 tonnes ha^{-1} . Differences between the two estimates were much smaller than those estimated by the other configurations.

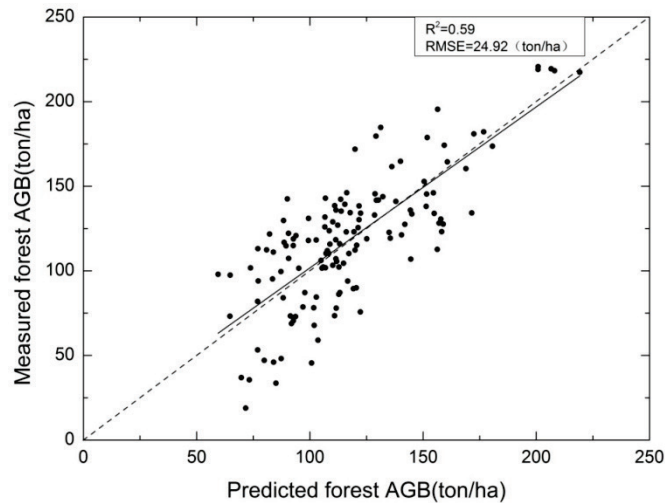


Fig. 3-7 The cross-validation of the optimum k -NN estimation using the SCS+C process (the dashed line represents a 1:1 fit).

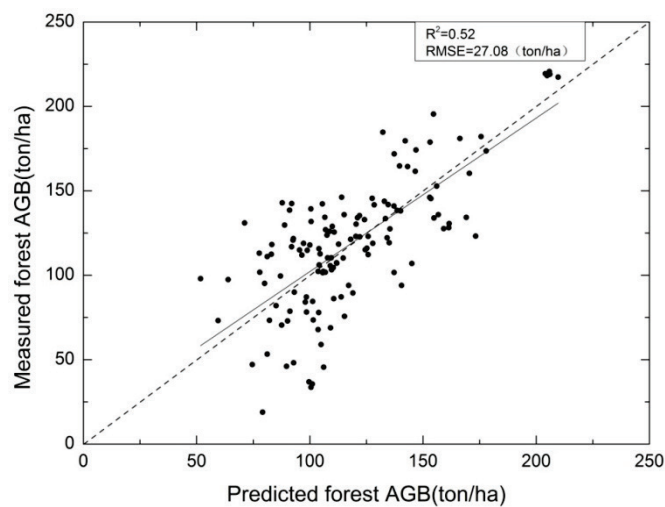


Fig. 3-8 The cross-validation of the optimum k -NN estimation without a SCS+C process (the dashed line represents a 1:1 fit).

To illustrate the influence of SCS+C correction on the montane forest AGB for the k -NN model, validation for the uncorrected feature (8) was also conducted (Fig. 3-8). With a larger deviation ($MPE = 21.67\%$), the overall accuracy of this feature vector ($R^2 = 0.52$ and $RMSE = 27.08$ tonnes ha^{-1}) was a little lower than for the corrected one. This indicates that the SCS+C process had a positive influence on forest AGB estimations using the TM data.

3.4.3 A Comparison of The Performance of The Two Methods

Based on terrain compensatory feature variables, the results of applying the optimized k-NN configuration (with feature (8)) were also compared to those produced using the SMLR method. To compare the results of the two methods, the LOO was also applied to validate the SMLR results. As expected, the performance of the SMLR was worse than that of the k-NN, with $R^2 = 0.42$, $RMSE = 29.74$ tonnes ha^{-1} , and $MPE = 26.20\%$ (Fig. 3-9). In particular, the k-NN method better reproduced the lowest and highest values of the forest AGB than the SMRL method. This was most obviously the case in highly heterogeneous areas such as valleys and ridges where the forests were very sparse and usually mixed with shrubs and grass. In these places, large divergence between the SMRL method and field data occurred. The k-NN method performed better for these areas, although the problem was not completely resolved.

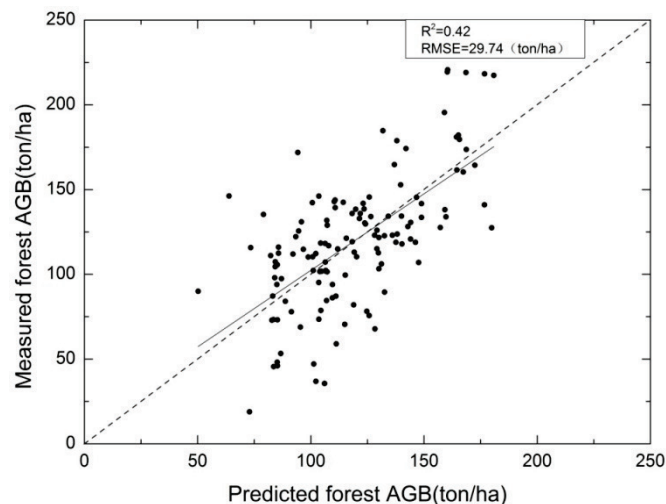


Fig. 3-9 The cross-validation results of the stepwise multiple linear regression (the dashed line is a 1:1 fit).

3.5 Discussion

The most relevant issues to consider when estimating forest AGB over montane areas are still practical problems (Dimitrov and Roumenina, 2013; Sarker et al., 2012). One important practical issue for both parametric and non-parametric methods is the requirement of having sufficient sample plots that represent forest AGB grades and the requirement for precise geo-referencing within the study area (Gilichinsky et al., 2012; Hill et al., 2013). As mentioned previously, making forest inventories for the cold and arid areas of the QMs is extremely labour intensive.

The fragmented landscape pattern and the relatively small patch size of many mountain forests suggest the use of remote-sensing data as an appropriate alternative at finer spatial resolution. However, this chapter concluded that reference data that span the entire variation range of spectral space and forest variable space for a given geographical region are still needed.

In **Chapter 2**, AGB for a small portion of the same study area using the high-resolution geometric (HRG) sensor on board the SPOT-5 satellite (which has 10 m resolution) was assessed. Comparing the results from **Chapter 2** with the present one indicated that SPOT-5 HRG data did not show an obvious advantage, with the exception that it had a slightly lower RMSE ($R^2 = 0.48$ and $RMSE = 20.70$ tonnes ha^{-1}) than the TM images used in this chapter for the entire upper reach of the HRB. Besides that, other differences between the studies can possibly explain the reasons for this difference.

In this chapter, more forest inventory data were used (75 plots were used in **Chapter 2**) that spanned a wider range of AGB (18.85-220.65 tonnes ha^{-1} as compared to the 18.85-175.27 tonnes ha^{-1} utilized in the earlier study), thanks to the larger study area. More feature variables, including textures, terrain types, and vegetation indices, were also derived than in the **Chapter 2**.

Apparently, a higher spatial resolution is not necessarily an advantage, as confirmed by the fact that the 5×5 window (5×5 pixel average) yielded better results than the pixel-by-pixel approach. The 5×5 window generally smoothes the heterogeneity of the forest landscape to some extent. But, from another side, the 5×5 window extraction might enhance the texture information of the target plot. It is necessary to restate that there are two kinds of forest plots, rectangular forest plots with two sizes (20 m \times 20 m and 25 m \times 25 m) and cycloidal forest plots (with diameters ranging from 10 m to 28 m), measured during the campaign. Generally, the plot geographic boundary may overlay several pixel grids or be mismatched with the target plot due to the unavoidable geometric offset. This might explain why the 5×5 window extraction method performed better than the pixel-by-pixel or other methods.

A widely acknowledged problem hindering quantitative thematic information extraction from remote sensing in mountainous areas is the difference in the illumination of slopes with different steepness and azimuth angles (Kane et al., 2008; Reese and Olsson, 2011; Yang et al., 2013). To reduce this difference and to unmask the real reflection characteristics of forest attributes, this chapter introduced the SCS+C model. The correction had a clear positive effect on the quality of the

results for both SMLR and k -NN method (with MD and FD). For SMLR, the model without SCS+C correction obviously underestimated forest AGB and the deviations of its outputs were larger than those from the corrected model. As it accounts for diffuse atmospheric and terrain radiance, this physically based correction can preserve the sun-canopy-sensor geometry and prevent the overcorrection (Ghasemi et al., 2013). It has been shown to provide improved corrections over a wide range of terrain and forest structural conditions, particularly in steep terrains and for slopes facing away from the sun (Soenen et al., 2005; Soenen et al., 2008, 2010). Therefore, after correction, the SMLR compensated for the underestimation of forest AGB to some extent (see Fig. 3-3). For k -NN, one exception was the k -NN configuration that used the Euclidean distance, for which the results were poorer after the topographic correction. Closer inspection of this unexpected deterioration of the results after the topographic correction revealed that topographic correction using linear regression caused an autocorrelation between some variables (slope and reflectance). The simple ED distance measure does not take autocorrelation into account; hence, the information content of the feature space appears inferior following topographic correction. Introducing a variance–covariance matrix into the multispectral distance calculations solves this problem and explains why results using the MD and FD measures improved after the topographic correction. As previous studies have indicated (Maselli, 2001; Chirici et al., 2008), the results are sensitive to the covariance matrix if the information content of the feature vector is heterogeneous. When the information content of the feature vectors is relatively uniform, the improvement becomes marginal. In this chapter, the MD produced better results than the FD until k was greater than 8, suggesting that the information content of the feature vector was inhomogeneous.

The performance of the SMLR considerably improved following the SCS+C topographic correction, indicating that topographic irregularities create non-linear relationships between feature variables and the AGB. The parametric method is unable to capture these relationships well because it is based on the assumption of homogeneity between the relationships linking land surface and remote-sensing signals (Maselli and Chiesi, 2006). Two significant advantages of the optimized k -NN method are its ability to derive a reasonable forest AGB and its versatility, which preserves the spatial patterns of homogeneity and heterogeneity (McRoberts et al., 2007), and explains why, in this chapter, the k -NN method performed better than the SMLR. Here, it is necessary to restate the advantage of the LOO method over other calibration–validation procedures. The LOO approach removes the need to separate forest measurements into a training and a validation set. Since the mechanism for the separation of data into two categories may impact the results, the LOO approach provides an advantage (Weiss, 1991; Fuchs et al., 2009). Moreover,

by not splitting the data into two categories, optimum use of the available data was obtained.

3.6 Conclusion

An optimum k -NN method determined using the LOO procedure was applied in order to derive forest AGB, by integrating forest measurements from TM data as well as GDEM and their relative indices. Satisfactory accuracy was accomplished yielding a coefficient of determination (R^2) of 0.59 and an RMSE of 24.92 tonnes ha⁻¹. Terrain influence hindering the prediction ability of remotely sensed data was mitigated using the SCS+C procedure, independent of the SMLR or the optimum k -NN method.

As evaluated by the LOO procedure, a comparison between the results obtained using the SMLR method and the optimized k -NN configuration indicated that the optimum k -NN configuration outperformed the SMLR ($R^2 = 0.42$, RMSE = 29.74 tonnes ha⁻¹) with a higher R^2 , a lower RMSE, and fewer outliers. With a slightly higher RMSE but a much higher R^2 , the use of k -NN for estimating forest AGB using 30 m-resolution TM data and a GDEM was not less accurate than the results obtained using high-resolution (10 m) SPOT-5 HRG data and airborne LiDAR DEM ($R^2 = 0.48$ and RMSE = 20.70 tonnes ha⁻¹), as applied in **Chapter 2**.

In this chapter, the radiometric terrain compensation method and the k -NN optimization strategy amongst various k -NN configurations have been proven to have positive effects to estimate of the montane forest AGB. Particularly, the two methods exhibited advantages when applied to montane forest areas with limited ground measurements and middle-to-high-resolution remote-sensing data.

Chapter 4

Modeling of Forest Above-Ground Biomass Dynamics Using Multi-Source Remote Sensing Data and Incorporated Models*

* This chapter is based on:

Tian, X., Yan, M., van der Tol, C., Li, Z. Y., Su., Z. B., Chen, E. X., Li, X., Li, L. H., Wang, X. F., Pan, X. D., Gao, L. S., Li, C. M., Fan, W. W., & Ling, F. L. Modeling of forest above-ground biomass dynamics using multi-sourced remote sensing data and incorporated models. *Submitted to Remote Sensing of Environment*

Abstract

This chapter presents a strategy to obtain the dynamics of forest above-ground biomass (AGB) at fine spatial and temporal resolution. Most techniques focus on estimating either AGB or carbon fluxes, but the approach used in this chapter estimated both AGB and carbon fluxes together. Forest AGB dynamics were estimated by combining two types of models driven by field, remote sensing, and ancillary data. The strategy was successfully applied to the Qilian Mountains (QMs).

As a first step, this study improved the efficiency of existing non-parametric methods for estimating forest AGB by applying the random forest (RF) model to pre-select the most relevant RS features in Thematic Mapper 5 (TM) and ASTER GDEM V2 products (GDEM). These features were further used to construct the optimal configurations of the k -Nearest Neighbour (k -NN) and the Support Vector Regression (SVR) models. Validation using forest measurements from 133 plots and the leave-one-out (LOO) method showed that optimal k -NN configuration performed slightly better ($R^2 = 0.62$ and $RMSE = 24.00$ tonnes ha^{-1}) than the SVR's ($R^2 = 0.56$ and $RMSE = 25.78$ tonnes ha^{-1}). Hence the k -NN configuration was used to generate a regional forest AGB reference map for 2009.

As a second step, this study obtained two seasonal cycles (2009 and 2010) of carbon fluxes with the MODIS MOD17 GPP (MOD_17) model that was driven by meteorological inputs of the numerical weather prediction model (WRF), and calibrated to Eddy Covariance (EC) flux tower data. The calibrated model predicted gross primary productivity (GPP) well ($R^2 = 0.91$ and $RMSE = 5.19$ $gC\ m^{-2}\ 8d^{-1}$).

As a third step, this study calibrated the ecological process model (Biome-BioGeochemical Cycles (Biome-BGC)) to these GPP estimates for 30 well-chosen, representative forest plots. The Biome-BGC outputs of GPP and net ecosystem exchange (NEE) were validated against EC data (for GPP: $R^2 = 0.79$, $RMSE = 1.31$ $gC\ m^{-2}\ d^{-1}$; for NEE: $R^2 = 0.68$, $RMSE = 3.09$ $gC\ m^{-2}\ d^{-1}$). This study finally used Biome-BGC to produce longer time series of net primary productivity (NPP), which, after conversion into AGB increments, were compared to dendrochronological measurements ($R^2 = 0.72$ and $RMSE = 47.33$ $g\ m^{-2}\ year^{-1}$). The calibrated Biome-BGC provided estimates of forest carbon fluxes which were converted into the interannual AGB increments according to site-calibrated coefficients. With combination of these interannual forest AGB increments with the AGB map of 2009, the modeling of forest AGB dynamics was accomplished at fine space and time scales.

4.1 Introduction

Forest above-ground biomass (AGB) plays an important role in the carbon and water cycles of the terrestrial biosphere. It affects gross (GPP) and net primary production (NPP), the radiation balance, water interception, and even air quality (Houghton et al., 2000; Sivrikaya et al., 2007; Stephens et al., 2007). Forest AGB, in turn, is affected by these processes (Filella et al., 2004; Huang et al., 2010; Vanderwel et al., 2013). The significance of the interactions between AGB and climate can only be understood if spatial and temporally explicit knowledge of forest AGB, as well as its dynamics, is available. Such knowledge is of great value for understanding processes and for accomplishing scientific and practical tasks in forest management.

Forest AGB dynamics can be described as continuous or gradual (i.e., growth) and discontinuous or abrupt (i.e., disturbance) variations (Wulder et al., 2007; Potapov et al., 2011), together resulting in variations in the productivity and the carbon fluxes of the forest (Main-Knorn et al., 2013). Disturbances include, for example, fires and other natural disasters, and tree felling or planting. These disturbances are outside the scope of the present study.

Several techniques exist to study gradual changes in forest AGB. In the field, the dynamics of forest AGB can be studied by analyzing changes in carbon storage, or by analyzing carbon fluxes. The traditional way of detecting forest AGB dynamics has been inventory-based forest sample surveys. However, for forest inventory to provide reliable dynamic estimates with a satisfactory spatial and temporal resolution, monitoring over large scales requires considerable investments in labour and supplies (Muukkonen and Heiskanen, 2007; Chirici et al., 2008; Riemann et al., 2010; Næsset et al., 2013). The Eddy Covariance (EC) technique provides estimates of CO₂, water, and energy fluxes between the biosphere and atmosphere that are essential for characterizations and dynamic analyses of forest ecosystem processes (Baldocchi and Bowling, 2003; Maselli, et al., 2009; Chiesi, et al., 2011). However, EC techniques provide net CO₂ flux measurements over footprint areas with sizes and shapes that vary with site specific conditions such as EC tower height, canopy physical characteristics, wind speed, terrain and atmospheric stability. As a result, it is impossible to upscale the observations of fluxes to large areas (Osmond et al., 2004; Brillì et al., 2013).

The remote sensing of biophysical variables has been a key component for the quantification of forest structure, stem volume, AGB, physiology, and carbon fluxes in forests (Tonolli et al., 2011; Yang et al., 2012; Neigh et al., 2013; Pregon and

Yamagata, 2013; Solberg et al., 2013; Zarco-Tejada et al., 2013; Fu et al., 2014). This is particularly the case for situations where a finer temporal-interval and a spatial-resolution assessment of forest AGB and its dynamics are required for ecological construction and environmental protection (Moreau et al., 2003; Neeff et al., 2005; Wulder et al., 2007; Zhang and Kondragunta, 2008; Minchella et al., 2009). Remote sensing methods are normally applied for estimating forest AGB dynamics, again by means of either estimating AGB changes in carbon pools using the repeat acquisition of remote sensing data (Wulder et al., 2007; Pflugmacher et al., 2012; Huang et al., 2013; Main-Knorn et al., 2013; Næsset et al., 2013; Zheng et al., 2013), or by an ecological model for the carbon fluxes driven by vegetation indices (e.g. leaf area index (LAI), the fraction of photosynthetically active radiation ($fPAR$), etc.) (Lufafa et al., 2008; Prince and Goward, 1995; Running et al., 2000; Veroustraete et al., 2002, 2004; Maselli et al., 2006; Chiesi et al., 2007; Potter et al., 2009). Although beneficial, the remotely sensed information is insufficient to fully parameterize such models, and a priori information remains necessary. Models solely driven by remote sensing data cannot explain the responses of the forest ecological processes (transpiration, photosynthesis, respiration, allocation, etc.) to climate variations.

The models for carbon fluxes range from relatively simple light use efficiency models (Running et al., 1999; Turner et al., 2003; Running et al., 2004) to detailed ecological process models containing vegetation functional mechanisms for gas exchange, photosynthesis, and biomass allocation (Running and Hunt, 1993; Thornton et al., 2002). An advantage of ecological process models is that they can simulate forest responses to climate change (Braswell et al., 2005; Williams et al., 2005; Euskirchen et al., 2006; Kimball et al., 2007; Keenan et al., 2012; Chen et al., 2013a). However, exploiting the strength of these models is not easy, because the models require a large number of input variables, and site specific calibration (Running and Hunt, 1993; White et al., 2000; Chiesi, et al., 2007; Maselli, et al., 2009; Song et al., 2013b).

In summary, individual methods such as inventory-based methods, remotely sensed methods, EC-based methods, and process-model-based models, with their limitations, may each contribute to analyzing the dynamics of AGB. Inventory-based and remotely sensed methods for forest AGB have strength in their abilities to estimate forest AGB and its dynamics, but have deficiencies in describing the processes that cause the dynamics. EC and process-based models for fluxes can be used for an analysis of forest responses, but they do not provide information about stocks. To understand changes and trends in terrestrial ecosystems and their function as carbon sources and sinks, and to gauge the impact of variations on

terrestrial ecosystems and climate change, ecological process models may be helpful, but these require a large amount of input data. For a better understanding of forest AGB dynamics, this study therefore required a consistent treatment of fluxes and biomass, and a synergy of data sources.

This study proposes a methodology to obtain space-time series of modelling forest AGB. All techniques discussed above have been used. They were connected as schematically depicted in Fig. 4-1.

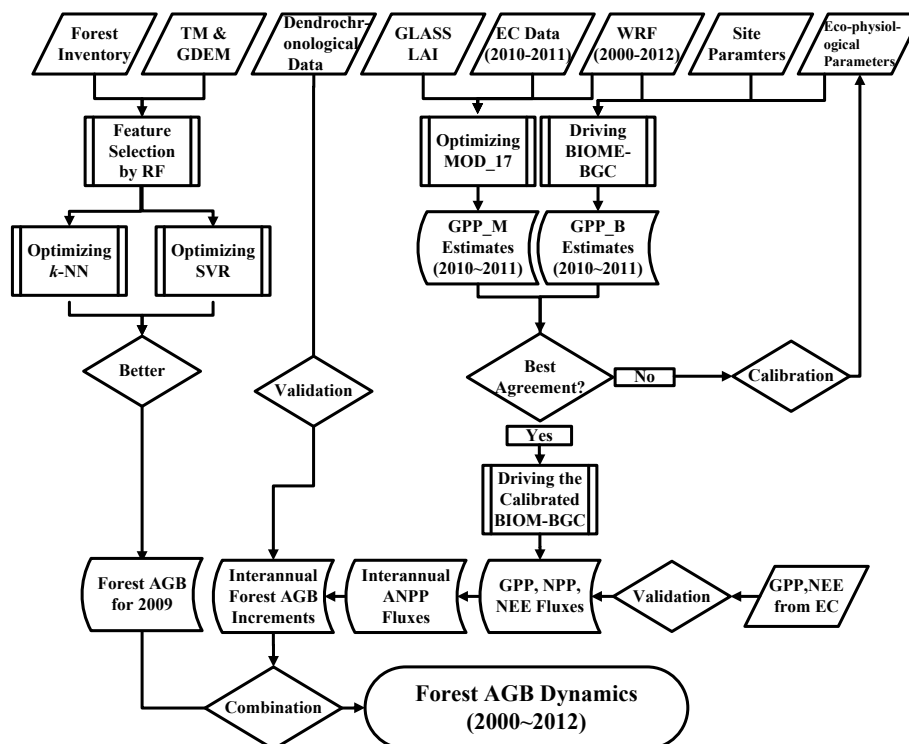


Fig. 4-1 The overall flowchart of this study.

The methodology is composed of three steps. First, forest inventory data were used to optimize models for the remote sensing of AGB. Two different models were applied: Support Vector Regression (SVR) and *k*-Nearest Neighbour (*k*-NN), and the better performing one was applied to obtain a base map of AGB for the year 2009. This study added an additional component to these techniques: before applying the *k*-NN and SVR models, a random forest (RF) model was applied to select features from various types of remotely sensed information. This step improved the efficiency of the *k*-NN and SVR models. The selected feature vectors were then used to design optimal configurations for the other non-parametric

models, the SVR and k -NN. Their performance for estimating forest AGB was evaluated. The better performing retrieval for regional forest AGB between the results from k -NN and SVR was used as the basis for modeling forest AGB dynamics.

Second, a remote sensing model for GPP, the MODIS MOD17 GPP model (MOD_17) (Running et al., 1999), was optimized at the EC site in the study area. The optimized MOD 17 time series of GPP of 30 carefully selected, representative plots were used to calibrate the process-based ecological model (Biome-BioGeochemical Cycle (Biome-BGC)) (Running and Hunt, 1993; Thornton et al., 2002). Lastly, the calibrated Biome-BGC was applied spatially to obtain reliable simulations of regional carbon fluxes. The GPP and the net ecosystem exchange (NEE) produced by Biome-BGC were validated against EC data. Finally, interannual forest AGB increments were calculated from the fluxes of net primary productivity (NPP), as estimated by Biome-BGC. The AGB increments were compared to dendrochronological (tree ring) data, and were combined with the earlier derived AGB values for 2009 in order to model the forest AGB dynamics from 2000 to 2012.

4.2 The Observations and Study Data

The Watershed Allied Telemetry Experimental Research (WATER) that began in 2007 and ended in 2011 (Li et al., 2009a, 2011b), established a network of automatic weather stations (AWS) and EC stations. Only observations from the mountainous forest site (Guantan, 100°15'E, 38°32'N, 2,835 m) were used. The forest EC system consisted of a 3-dimensional sonic anemometer (CSAT-3, Campbell, Inc., USA), a CO₂ and H₂O gas analyzer (LI-7500, LI-COR, Inc., USA), a heat flux plate (HFP01, Campbell, Inc., USA), a four-component radiometer (CM3 and CG3, Kipp and Zonen, USA), a temperature and relative humidity probe (HMP45C, Vaisala, Inc., Finland), a wind speed sensor (014A and 034B, Met One Instruments, Inc., USA), and a data logger (CR5000, Campbell, Inc., USA).

To obtain half-hour flux data, data quality control processes were applied to raw 10 Hz EC data (Zhang et al. 2010b). Processing steps included despiking, coordinate rotation, time lag correction, frequency response correction, WPL correction, and gap filling (Wang et al., 2014). Due to low data quality and too many gaps, measurements from 2008 and 2009 could not be utilized for this study. Measurements obtained from 2010 and 2011, at the mountainous forest site, were used to optimize and validate the MOD_17 and Biome-BGC models.

Same forest inventory measurements, Landsat Thematic Mapper 5 (TM) and Advanced Spaceborne Thermal Emission and Reflection Radiometer (ASTER) global digital elevation model (GDEM) V2 products (GDEM) as those in **Section 3.2** were used to estimate regional forest AGB.

To validate the interannual forest AGB increment, an additional forest inventory consisting of collecting dendrochronological measurements, was conducted for 22 forest plots during May of 2014. Measurements of tree core, diameter breast height (DBH) (cm), and tree height (m) were included. Coring was performed at breast height (1.30 m) in two perpendicular directions for trees with a DBH > 5 cm, and three tree core samples were collected for each DBH grade (six DBH grades for each plot, as follows: 5-10 cm, 10-15 cm, 15-20 cm, 20-25 cm, 26-30 cm, and >30 cm). Well-protected core samples were returned to the laboratory, where they were mounted and finely sanded for cross-dating and annual ring width measurements. Following surface treatment of the samples, the ring width of each core was measured at an accuracy of 0.001 mm using the Lintab5 measuring system. A geometric method developed by Duncan (1989) was used for estimating the pith location when a partial core passed close to the pith. Possible measurement errors and/or dating were checked using the COFECHA program (Holmes 1983). Annual forest AGB increments were then determined using the DBH. Heights were determined using the growth equation as proposed by Wang et al. (1998b).

Forcing data for the MOD_17 model included the vapor pressure deficit (*VPD*), the daily minimum air temperature (T_{min}), and the absorbed photosynthetically active radiation (APAR, MJ day⁻¹). The employed *VPD* and T_{min} were obtained from downscaled (to 1 km), long-term (2000-2012) weather research and forecasting (WRF) model simulations (Pan and Li, 2011; Pan et al., 2012) that included maximum and minimum temperatures (T_{max} and T_{min} , precipitation, relative humidity, and solar radiation). LAI products from time-series (2000-2012) MODIS data obtained using general regression neural networks (GRNNs) (Xiao et al., 2014) (<http://glass-product.bnu.edu.cn>) were applied in order to derive *f*PAR for the initiation of the optimizing MOD_17 model. MODIS GPP products (MOD17, eight-day products, 1 km) (<http://ladsweb.nascom.nasa.gov>) were obtained from the USGS for comparisons with the optimized estimations.

Major input variables for the Biome-BGC model included meteorological data, vegetation eco-physiological parameters, and site condition parameters. Meteorological inputs were also obtained from downscaled WRF simulations. Default eco-physiological parameters for the needle tree (*Picea crassifolia*) as found in the Biome-BGC lookup table were first applied then calibrated using GPP

estimates obtained from the optimized MOD_17. The soil map was reclassified based on the 1:1,000,000 scale soil map of China and 8,595 soil profiles from the Second National Soil Survey (Shangguan et al., 2012).

4.3 Description of Models

4.3.1 Random Forest

The non-parametric regression tree method of RF is a popular and widely used ensemble approach to feature selections for “*small n, large p problems*” (Li et al., 2011a) where n is the samples and p is the inputting features. It was designed to generate robust predications without over-fitting the data while being insensitive to outliers and noise in comparison to single classifiers. RF has roots in classification and regression trees (CART) and consists of a collection of tree-structured classifiers that dictate how input is related to a predictor variable. It uses a tree-based classifier multiple times and aggregates the results, expressed as follows:

$$\{f(\mathbf{x}, \mathbf{R}_k), k = 1, \dots\} \quad (4-1)$$

where \mathbf{R}_k are independent, identically distributed random vectors. Each tree casts a weighted vote for the most similar class at input \mathbf{x} (Breiman, 2001).

To construct an ensemble of decision trees with a defined variance, the “bagging” or “bootstrap aggregating” idea and the random selection of features were embedded within the RF algorithm. Using a different subset, each tree was typically guided using a training set (“bagging” or “bootstrap aggregating”) to improve the generalization ability of the classifier (Mahapatra 2014). Following training, for a decision tree, predictions for the targets could be generated by taking the majority (or average) vote. Votes were determined using a binary test with user-defined thresholds placed at each internal tree node from the root to each leaf. RF is able to address over-fitting problems and the robustness of reliable data, and unbiased predictions can be obtained using “bagging” or “bootstrap aggregating” replicates. The procedure has been proven to be an efficient predictor (or classifier), especially when the number of descriptors is very large (Svetnik et al. 2003; Latifi and Koch, 2012). It has been applied for estimating forest attributes (i.e., forest succession, forest AGB, and timber volume) from remote sensing data (Latifi et al., 2010; Powell et al., 2010; Main-Knorn et al., 2011; Neumann et al., 2012; Avitabile et al., 2012).

However, due to noisy or unbalanced inputs existing amongst trees, RF suffers from instability and it may not remove certain variables contained in multiple trees (Li et

al., 2011a). Moreover, the black box prediction is vague and difficult to interpret in terms of the underlying features (Song et al., 2013).

4.3.2 *k*-Nearest Neighbour

The specific descriptions and expressions of *k*-NN and the related multidimensional distance measures were given in **Section 2.3.1** and **Section 2.3.2**.

4.3.3 Support Vector Regression

The Support Vector Machine (SVM) is a supervised, non-parametric, statistical learning technique (Vapnik, 1995). As a regression version of SVM, SVR performs a linear regression in a high dimensional feature space and returns a non-linear regression (Drucker et al., 1997). To separate groups of input data with similar responses in order to predict a response variable, the process identifies optimum hyperplanes using kernel functions. SVR arrives at an optimum solution by iteratively adjusting hyperplanes based on the errors associated with them.

Here, a concise description of the SVR algorithm is provided. Details can be found in Smola and Schölkopf (2004). Based on the ε -insensitive loss function, SVR explores the results to find a smooth function, $\hat{f}(\mathbf{x})$, with deviations from the targets of y_i ($i = 1, \dots, N$; where N is the number of training samples) no larger than ε for all of the training data. For this purpose, the original m -dimensional input domain is mapped into a higher dimensionality feature space, where the function underlying the data has an increased flatness (ideally, linear). Thus, it is approximated in a linear way, as follows:

$$\hat{f}(\mathbf{x}) = \mathbf{w} * \Phi(\mathbf{x}) + b \quad (4-2)$$

where \mathbf{w} is the weight vector in the feature space, $\Phi(\mathbf{x})$ is the kernel function transforming the inputs into the higher dimensional feature space, and b is the bias.

A linear model is then fitted to the data in the feature space using a convex (easy to handle) optimization problem, as follows:

$$\Psi(\mathbf{w}, \xi) = \frac{1}{2} \|\mathbf{w}\|^2 + C \sum_{i=1}^N (\xi_i + \xi_i^*) \quad (4-3)$$

and it is subject to the following constraints:

$$\begin{cases} y_i - \hat{f}(x_i) \leq \varepsilon + \xi_i \\ \hat{f}(x_i) - y_i \leq \varepsilon + \xi_i^* \\ \xi_i, \xi_i^* \geq 0 \end{cases} \quad i = 1, 2, \dots, N \quad (4-4)$$

where ξ_i and ξ_i^* are slack variables and measure the deviation of the training samples outside the ε -insensitive tube. C is the penalty factor and allows one to tune

the trade-off between the complexity of the function $\hat{f}(\mathbf{x})$ and the tolerance of deviations larger than ε . If C is too large or small, it may cause overfitting or underfitting, respectively. The ε -insensitive loss function $|\xi|_\varepsilon$ is defined as follows:

$$|\xi|_\varepsilon = \begin{cases} 0 & \text{if } |\delta| \leq \varepsilon \\ |\delta| - \varepsilon & \text{otherwise} \end{cases} \quad (4-5)$$

where δ is the deviation of the desired target. Differences between the targets and the estimated values are controlled within the ε tube for a certain tolerance, while a linear penalty is assigned for estimates lying outside the ε -insensitive tube.

The aforementioned constrained optimization issue can be reformulated using a Lagrange function, leading to a solution that is a function of the data expressed in the original m -dimensional feature space, as follows:

$$\hat{f}(\mathbf{x}) = \sum_{i \in N} (a_i - a_i^*) k(x_i, \mathbf{x}) + b \quad (4-6)$$

where $k(x_i, \mathbf{x})$ is a kernel function defined, as follows:

$$k(x_i, \mathbf{x}) = \Phi(x_i) * \Phi(\mathbf{x}) \quad (4-7)$$

thus,

$$\hat{f}(\mathbf{x}) = \sum_{i \in N} (a_i - a_i^*) \Phi(x_i) * \Phi(\mathbf{x}) + b \quad (4-8)$$

where a_i and a_i^* represent the nonzero Lagrange multiplier solution of the quadratic problem. The kernel function must satisfy Mercer's theorem such that it can be associated with some type of inner product within the highly dimensional feature space. Lagrange multipliers weight each training sample according to its importance in determining a solution. Therefore, they lead to the important concept of *sparsity* which means that the solution should be expressed as a function of only the most critical training samples in the support vectors (SVs) (Camps-Valls and Bruzzone, 2005).

Recently, due to remotely sensed data, SVR has become popular for estimating the geo- and bio-physical, and bio-chemical variables of soils (Pasolli et al., 2011, 2012;), forests (Monnet et al., 2011; Gleason and Im, 2012; Shataee, 2013; Li et al., 2014; Zhang et al., 2014b), open water (Camps-Valls et al., 2006; Sun et al., 2014), and etc.. SVR has attractive properties such as applicability, intrinsic generalization capability, the capability to handle high dimensional input spaces (including features arising from different sources), and robustness to the limited availability of training samples.

Despite the desirable performance offered SVR has some deficiencies. For example, the hyper parameters (C and ε), as well as the kernel parameter (γ), must be tuned, in general, using cross-validation methods that result in time consuming

tasks. *Sparsity* is not always achieved and a high number of SVs are, thus, obtained (Camps-Valls et al., 2006). Such deficiencies frequently occur when feature vectors are high dimensional. The reduction of feature vectors generally improves SVR performance (Monnet et al., 2011).

4.3.4 The MOD_17 Model

The MOD_17 model is based on the radiation conversion efficiency concept of light use efficiency (LUE) (Monteith, 1972). A detailed description can be found in Running et al. (1999; 2004). In the MOD_17 model, GPP is calculated, as follows (Running et al., 2000):

$$GPP = \varepsilon_{max} \times f(VPD) \times f(T_m) \times PAR \times fPAR \quad (4-9)$$

where ε_{max} is the maximum LUE, $f(VPD)$ is the scalar of daily VPD , and $f(T_m)$ is the scalar of daily T_{max} and T_{min} . Both scaling factors range from 0 (representing total inhibition) to 1 (indicating no inhibition), and are used to reduce ε_{max} due to environmental constraints (cold temperature, high VPD , both of which reduce photosynthesis) in order to downscale ε_{max} to its actual value, as follows:

$$f(VPD) = \begin{cases} 0 & VPD \geq VPD_{max} \\ \frac{VPD_{max} - VPD}{VPD_{max} - VPD_{min}} & VPD_{min} < VPD \leq VPD_{max} \\ 1 & VPD \leq VPD_{min} \end{cases} \quad (4-10)$$

$$f(T_m) = \begin{cases} 0 & T_m \leq T_{min} \\ \frac{T_m - T_{min}}{T_{max} - T_{min}} & T_{min} < T_m \leq T_{max} \\ 1 & T_m \geq T_{max} \end{cases} \quad (4-11)$$

$fPAR$ is calculated as follows:

$$fPAR = 1 - e^{-k^* \times LAI} \quad (4-12)$$

where k^* is the light extinction coefficient.

The MOD_17 GPP model requires forcing data from the following three sources: 1) biome specific parameters such as ε_{max} , 2) meteorological data (i.e., incoming radiation, air temperature, relative humidity), and 3) $fPAR$. Therefore, MODIS GPP products have been generated using data from MODIS surface reflectance that contain information regarding vegetation phenology, the canopy absorbance of $fPAR$, and climate data from the NASA Data Assimilation Office (DAO) climate model. Specifically, to estimate GPP, biome specific parameters (ε_{max}) are assigned based on an eight class MODIS land cover classification products (with a 1 km resolution) and the associated Biome Parameter Look Up Table (BPLUT) (Hansen et al., 2000; Running et al., 2004; Nightingale et al., 2007; Coops et al., 2007).

Using scalars (0–1) for T_m and VPD, ε_{max} is then modified. Afterward, GPP is the product of $fPAR$ and LUE (Turner et al., 2006).

MODIS GPP products have been evaluated for different ecosystems over various study areas (Reeves et al., 2005; Gebremichael and Barros, 2006; Zhang et al., 2008; Propastin et al., 2012; Jin et al., 2013; Sjoström et al., 2013). Briefly, in addition to some deficiencies of the model, there are three potential sources for uncertainties for the MOD_17 model, as follows: 1) meteorology inputs, 2) radiometry inputs, and 3) biophysical inputs (Heinsch et al., 2006). Specifically, meteorological errors arise from the coarse scale meteorology of the DAO, errors in radiometry can cause miscalculations in the $fPAR$ algorithm, and biophysical misclassifications can lead to land cover classification problems (Coops et al., 2007).

4.3.5 The Biome-BGC Model

As a process-based model, the Biome-BGC model combines scaled-up representations of basic plant biology and geochemistry with ecosystem dynamics and functions in order to simulate processes including the fluxes of carbon, water, and nitrogen on broader temporal and spatial scales (White et al., 2000; Thornton et al., 2002; Su et al., 2007b). Since its original development was based on the FOREST-BGC model (Running and Coughlan, 1988; Running and Gower, 1991; Running and Hunt, 1993), the Biome-BGC model has been applied with success to a variety of forest ecosystem types in different regions (Churkina et al., 1999; White et al., 1999; Churkina et al., 2003; Chiesi et al., 2007, 2013; Maselli et al., 2009; Ueyama et al., 2010; Li et al., 2013a).

Biome-BGC embeds major physical, biogeochemical, and physiological processes and water, carbon, and nitrogen fluxes which can be simulated throughout various pools of vegetation, litter, and soil. Forcing data for the Biome-BGC model include daily meteorological data (temperature, precipitation, humidity, radiation, and daylength), site descriptive parameters (the physical characteristics of a site), and vegetation eco-physiological parameters (the leaf C:N ratio, maximum stomatal conductance, fire and non-fire mortality frequencies, and allocation ratios) characterized by specific site and environmental conditions. Therefore, the model can theoretically be used to assess the effects of climate change or the management of vegetation growth, soil carbon sequestration, and trace gas emissions. The simulation begins from quasi-climax equilibrium, reached using a forward spin-up phase with local eco-climate conditions. The spin-up simulation spans thousands of years (default: 6000 years) until the ecosystem reaches a steady state with respect to

soil carbon fluxes. Once C and N reach a steady state, further simulations for ecosystem changes are performed over time.

Biome-BGC version 4.2 was used in this study. Version 4.2 includes seven parameter settings for seven main biomes (evergreen needle leaf, evergreen broadleaf, deciduous needle leaf, deciduous broadleaf, shrub, C3 grass, and C4 grass). For adaptation to the QMs forest ecosystem that is cold and arid, for this study, the biomes had to be modified. Normally, EC measurements can be used to calibrate these parameters. An added technical issue was how to calibrate the parameters for a large area.

4.4 Methodology

4.4.1 Incorporating Random Forest with The *k*-Nearest Neighbour and The Support Vector Regression

For prediction models using multi-parameter remote sensing data, one key issue to avoid for over-fitting or for complex models is the selection of sensitive feature types from various types of remotely sensed information. In general, feature types are determined using experiences or simple sensitivity analyses with regression analyses (Tian et al., 2012, 2014). RF is a tool that can provide a variable ranking mechanism and can, therefore, be used to select important variables. However, RF typically generates black box predictions that are vague and difficult to interpret (Song et al., 2013a). Therefore, to clarify variable importance, predictor variables were predetermined rather than applied within the CART of the RF method.

In contrast, *k*-NN and SVR are highly interpretable. For example, for *k*-NN, the determined combination of feature types, *k*, the distance measures, and the feature extraction are explicable. For SVR, the regularization coefficient (*C*), the width of the insensitive tube (ϵ), and the kernel types and parameters are describable and can be used to predict a target pixel or the probability of a target pixel. However, since forward feature selection normally brings out information redundancy or deficiency, feature combination prior to the configuration construction comes at an unacceptably high cost.

Therefore, a critical issue is how to develop methods that can optimally combine features to obtain high accuracy. Such is especially the case for high dimensional datasets (in this case: multi-parameter remote sensing information). The novel idea of incorporating RF with *k*-NN and SVR is motivated by the strength of these methods. To our knowledge, few studies have used remote sensing data and integrated RF with *k*-NN or SVR in order to estimate forest AGB. In this study, the

RF was first used to select the composition of optimum feature types. Then, selected feature types were input into the k-NN and SVR in order to construct the optimal configuration. For example, for k-NN, the varying mathematical setup included the k value, the distance measure, and the extracting window size. For SVR, the optimum hyperplane and the corresponding kernel function were determined. The performance of each k-NN and SVR configuration was evaluated using leave-one-out (LOO) cross-validation. Optimal k-NN and SVR values were determined using the highest Pearson correlation index (R) and lowest root mean square error (RMSE) principle for pixel-wise accuracy. Finally, the outperforming configuration for these two methods was applied in order to estimate forest AGB over the study area.

In this study, the wrapper-based RF was applied to select the features (Breiman, 2001) (<http://www.csie.ntu.edu.tw/~cjlin/libsvm>). The same feature types (a total of 88 feature types) and training dataset (forest AGB from 133 plots) as those applied in Chapter 3 were inputted into the RF to perform feature type selection. According to the previous studies (Kohavi and John, 1997; Breiman 2001; Fayad et al., 2014) and the dataset used in this study, the wrapper-based feature selection with parameters of 10 trees, 100 nodes, and tenfold were used for the RF.

SVR was implemented using LIBSVM (<http://www.csie.ntu.edu.tw/~cjlin/libsvm/>) (version 2.9.1). A grid search parameter optimization using a standalone tool, the Weka package (version 3.7.2), was performed and four typical kernel functions (the linear, polynomial, radius basis, and sigmoid functions) were tested.

4.4.2 Incorporating MOD_17 with Biome-BGC

The integration of MOD_17 and Biome-BGC was motivated by the specific advantages and disadvantages of the two models. MOD_17, the remote-sensing-based model, takes advantage of time-series remote sensing data, ensuring that the model is applicable for the space-continuity domain within certain time intervals (i.e., eight days for MODIS). However, MOD_17 relies on the applicability (i.e., data without the contamination of cloudy and rainy conditions) and explicability (i.e., the accuracies of the remote sensing parameters) of remotely sensed data. The model also relies on empirical relationships/constants (i.e., LUE), and loses some of the intrinsic characteristics of ecological processes, resulting in vague depictions for time-continuity ecosystem variations and corresponding environmental causes.

The process-based model, Biome-BGC, on the other hand, has strength based on its state-of-the-art knowledge of major ecological, biophysical, biochemical, and hydrological processes. As a result, Biome-BGC can precisely represent the time-

continuity characteristics of the aforementioned processes but suffers from high complexity, difficult calibrations, and great computational intensity. The model is also prone to good performance at site scale after elaborate calibrations but dubious results for space-continuity applications over large areas.

Previous studies yielding reliable results have indicated the possibility of incorporating remote-sensing-based model (the C-Fix) with process-based models (the Biome-BGC) to simulate the carbon flux over Mediterranean forest ecosystems (Chiesi et al., 2007, 2011; Maselli et al., 2008). However, the feasibility of this integration strategy is not understood for water-limited forest ecosystems located within arid and cold regions.

In this study, EC measurements, refined time-series downscaled WRF meteorological data, and MODIS fPAR products from GLASS LAI were used to optimize the MOD_17 model. Integration of the MOD_17 and Biome-BGC models was performed by calibrating the Biome-BGC using GPP simulations from the MOD_17 model. Prior to the calibration, to effectively determine the optimal configurations for the Biome-BGC model over the forest ecosystem, a sensitivity analysis (not shown here) was performed. Under conditions of cold and arid climates, the growing season for local forests is dry and it has a critical impact on the photosynthesis and evapotranspiration (ET). As a result, some parameters were found to be sensitive factors (Table 4-1). In general, these factors control the responses by regulating the water loss of forests against summer drought (Chiesi et al., 2007). Different configurations of the Biome-BGC model were performed against GPP simulations from the optimized MOD_17 GPP model. To this aim, 30 plots for the local monotonous tree (*Picea crassifolia*) were selected with considerations of various stand conditions such as slope and aspects of the terrain; the age, height, and AGB levels of trees; locations near other wet (reservoir, river) or dry (bare soil, shrubs, or pasture) land cover types; and climatic conditions (rainfall, temperature, VPD, etc.). Eight-day GPP estimates over two years (2010-2011) were computed for all of the conditions by applying the optimized MOD_17 model, which was used as a reference for calibrating the Biome-BGC configurations. A total of 2,760 (30 plots \times 46 layers/plot/year \times 2 years) GPP values from the Biome-BGC were plotted against those reference values from MOD_17 model. After obtaining a best fit, the optimal configuration of the Biome-BGC was established.

4.4.3 Simulations of Carbon Fluxes and Conversion of NPP Estimates to Forest AGB Increments

Following the calibration process, climate, vegetation eco-physiological parameters, and site condition parameters were applied in order to run the improved Biome-BGC model for the *Picea crassifolia* forest ecosystem over the QMs. Resolution of the model grid was set to 1 km, the same as for the forest AGB reference map and GPP outputs from the MOD_17 model. Following a spin-up simulation for 6000 years, the Biome-BGC began to simulate daily forest fluxes over 13 years (from 2000 to 2012). Daily NPP simulations were then aggregated into the annual NPP sums. The annual sums were further divided into annual below-ground NPP (BNPP) and above-ground NPP (ANPP) according to the carbon allocation ratio of *Picea crassifolia* (6.05% and 93.95% of total NPP, respectively) as concluded from field measurements (Wang et al., 2000).

According to study of Wang et al. (2000), the ratio of litter fall to the total carbon sequestration approximates to 39.39%, and as it indicated by Zhong and Yin (2008), the mortality was set to 3%, annually. Therefore, multiplying the annual ANPP to the ratios of (1-39.39%) and (1-3%) gave the amount of carbon fixation for the annual AGB increment. Finally, the annual forest AGB increment can be easily obtained by dividing the carbon content factor (ratio between biomass and carbon storage) of *Picea crassifolia* (= 0.5243) into the carbon amount of the annual AGB increment (Wang et al., 2000).

4.5 Results

4.5.1 Determination of The Optimal Configurations for The *k*-Nearest Neighbour and Support Vector Regression

Eight most relevant feature types were determined by RF, as follows: DEM, PC3s, S4, M5, IRI, and ARVI. DEM is the altitude from the GDEM product, and PC3s, S4, M5, IRI, and ARVI are the first three principal components, the second moment texture, the mean texture, the infrared index, and the atmospherically resistant vegetation index of the TM image, respectively. Remotely sensed feature types were then inputted into the *k*-NN and SVR algorithms. By varying the configurable parameters (*k* neighbors, distance measures, and feature extractions for *k*-NN; and the regularization coefficient (*C*), the width of the insensitive tube (ϵ), and the kernel types and parameters for SVR) for *k*-NN and SVR, various configurations of the two models were constructed then the performance of each configuration was evaluated using the LOO method. Optimal configurations for these two methods were determined according to the error minimization criterion (the highest *R*² and the lowest RMSE). For *k*-NN, the optimal configuration was *k* = 3, MD measure,

and a 5×5 window sampling size. For SVR, the best configuration was a radius basis function (RBF) with the free parameters of $C = 1024$, $\varepsilon = 64$, and $\gamma = 1.0$.

4.5.2 The Forest Above-Ground Biomass Estimation

Validated by forest measurements from 133 plots using the LOO method, optimal configurations (with the feature types selected by RF) of k-NN and SVR generated reliable forest AGB estimates. Estimates for these two algorithms against ground measurements are shown in Fig. 4-2. The AGB at all of the eight plots with an AGB lower than 50 tonnes ha⁻¹ were overestimated using both algorithms. For the eight plots, larger deviations were produced with SVR than those obtained by k-NN. On the contrary, underestimations for high-level AGB plots were found during the performance of both models. For example, several plots with an AGB higher than 200 tonnes ha⁻¹ were underestimated. Again, larger deviations were produced with SVR as compared to those obtained with k-NN. Overall, the optimal k-NN configuration performed slightly better than that of the optimal SVR (with a $R^2 = 0.62$ and a RMSE = 24.00 tonnes ha⁻¹ of k-NN versus a $R^2 = 0.56$ and a RMSE = 25.78 tonnes ha⁻¹ of SVR). Therefore, the optimal k-NN configuration was applied in order to estimate regional forest AGB over the QMs of 2009. The AGB map was used as the background for forest AGB dynamic analyses from 2000 to 2012.

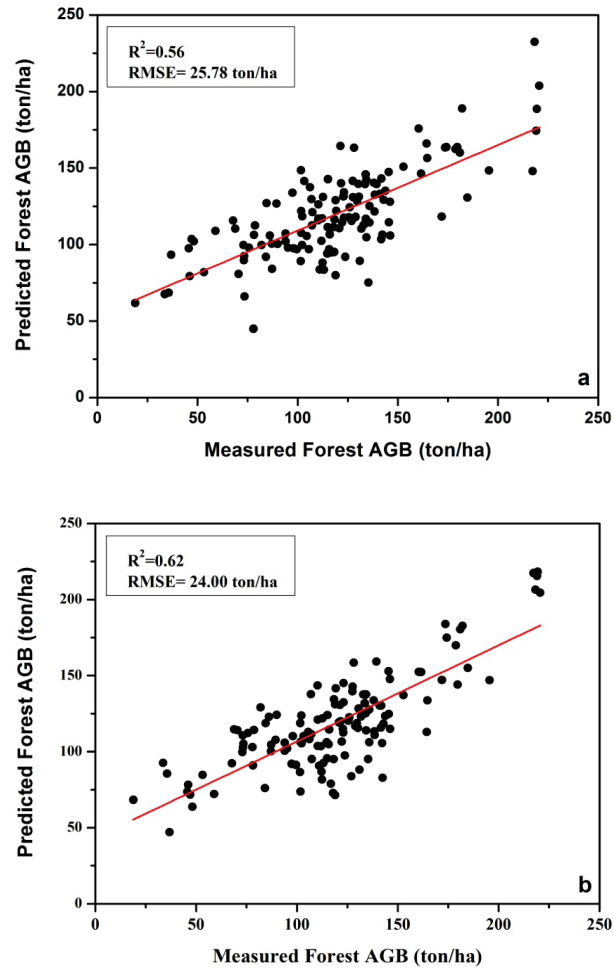


Fig. 4-2 Cross-validation for optimum SVR and k-NN estimations ((a) is from SVR; (b) is from k-NN).

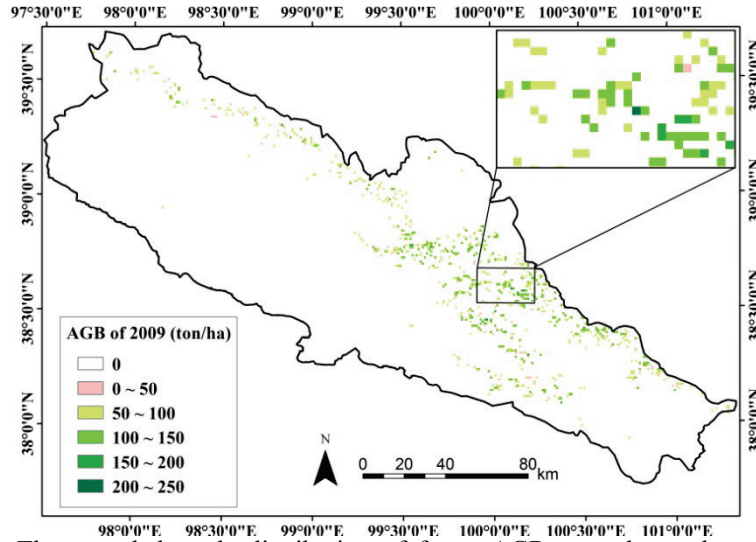


Fig. 4-3 The upscaled grade distribution of forest AGB over the study area (1 km resolution).

The basic forest AGB map was upscaled to 1 km to keep the same resolution as the grids for both the MOD_17 GPP and Biome-BGC models (Fig. 4-3).

4.5.3 Incorporation of The MOD_17 GPP Model with The Biome-BGC Model

In advance of using GPPs from the MOD_17 model to calibrate the Biome-BGC model, this study evaluated the performance of the optimized MOD_17 model. To analyze the effect of inputting parameters collected from three sources (biome-specific, meteorological, and $fPAR$ parameters) on model behavior, this study compared the original MODIS GPP products and the GPPs obtained from the optimized MOD_17 model using the calibrated maximum LUE (ε_{max}), the downscaled WRF outputs, and the $fPAR$ from GLASS LAI.

To determine the achieved improvement, the GPPs available from two years of EC measurements were used (Fig. 4-4). Obviously, the results of the optimized MOD_17 model (a $R^2 = 0.91$ and a $RMSE = 5.19 \text{ gC m}^{-2} \text{ 8d}^{-1}$) were much better than the original MODIS GPP products (a $R^2 = 0.47$ and a $RMSE = 20.27 \text{ gC m}^{-2} \text{ 8d}^{-1}$). MODIS GPP products were significantly lower than EC measurements. Such highly underestimated performance was also reported by Zhang et al. (2008) and Wang et al. (2013c).

Using site-calibrated ε_{max} for *Picea crassifolia*, refined WRF outputs and $fPAR$, the MOD_17 model agreed with the EC measurements with the exception of a slight underestimation during the spring and winter of 2010 and an overestimation during

the spring of 2011.

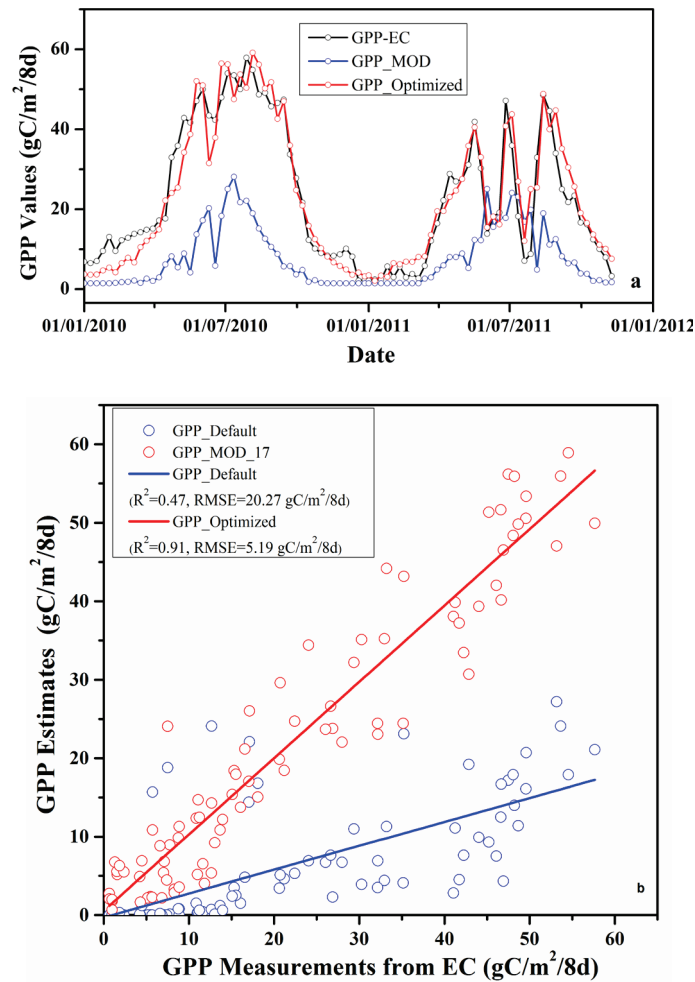


Fig. 4-4 Comparisons and validations of the GPPs from the original MODIS products and from the optimized MOD_17 GPP model.

The optimized behavior of the MOD_17 model gave the confidence for calibrating the Biome-BGC using MOD_17 GPP outputs over the QMs. By fitting the GPPs from various parameterization schemes for Biome-BGC against the GPPs from the optimized MOD_17 model, the Biome-BGC was calibrated according to the best fit between them (a $R^2=0.77$ and a $RMSE = 8.46 \text{ gC m}^{-2} \text{ 8d}^{-1}$) (Fig. 4-5). For example, the calibrated sensitive parameters for model performance during 2010 and 2011 are provided in

Table 4-1.

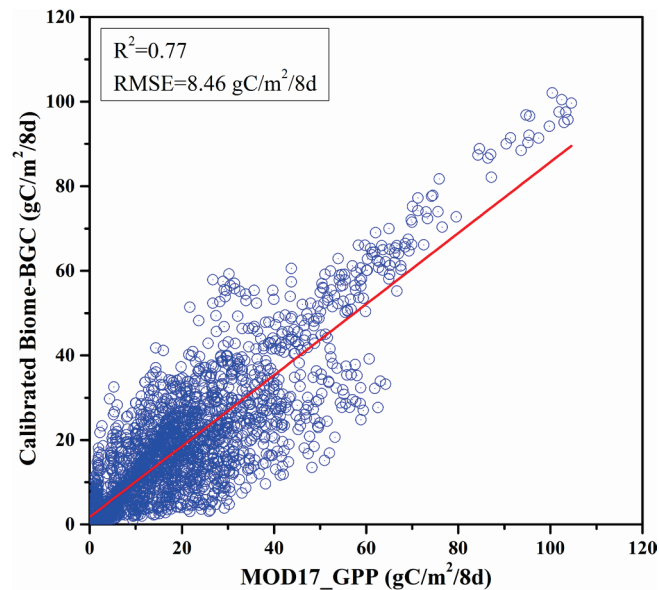


Fig. 4-5 The best fit relationship between the GPPs from the Biome-BGC and MOD_17 models eight day outputs ($P < 0.001$).

Table 4-1 The calibrated parameter settings for the optimal configuration of the Biome-BGC model.

Parameters	Value	Unit
Fine root C:leaf C	2.0	ratio
C:N of leaves	40	kgC/kgN
C:N of fine roots	90	kgC/kgN
Fraction of leaf in rubisco	0.08	DIM
Maximum stomatal conductance	0.0022	m/s
Cuticular conductance	0.000022	m/s
Boundary layer conductance	0.09	m/s
Leaf water potential: Start of conductance reduction	-0.5	MPa
Leaf water potential: Complete conductance reduction	-8	MPa
Vapor pressure deficit: Start of conductance reduction	600	Pa
Vapor pressure deficit: Complete conductance reduction	3900	Pa

In a similar manner as for the overall tendency in Fig. 4-4, this study also found great improvements in GPP and NEE estimations using the calibrated Biome-BGC as compared with the Biome-BGC using the default driven parameters as (Fig. 4-6 ~ Fig. 4-7).

The default model highly underestimated GPP and NEE throughout the EC measurements. Before calibration $R^2 = 0.67$ and $RMSE = 5.82 \text{ gC m}^{-2} \text{ d}^{-1}$ for GPP

and $R^2 = 0.47$ and $RMSE = 5.30 \text{ gC m}^{-2} \text{ d}^{-1}$ for NEE, and after calibration $R^2 = 0.79$ and $RMSE = 1.31 \text{ gC m}^{-2} \text{ d}^{-1}$ for GPP and $R^2 = 0.68$ and $RMSE = 3.09 \text{ gC m}^{-2} \text{ d}^{-1}$ for NEE. It is noteworthy that only GPP (not NEE) of Biome-BGC was calibrated. In general, the GPPs and NEEs from the calibrated Biome-BGC agreed very well with EC measurements with two exceptions. There is a slight underestimation of both GPP and NEE during the spring of 2010 and 2011, and an underestimate of NEE during autumn, especially for 2011. The performance of the calibrated Biome-BGC led this study to apply it to regional forest carbon flux simulations for the years 2000 to 2012 on finer time scales (one day resolution).

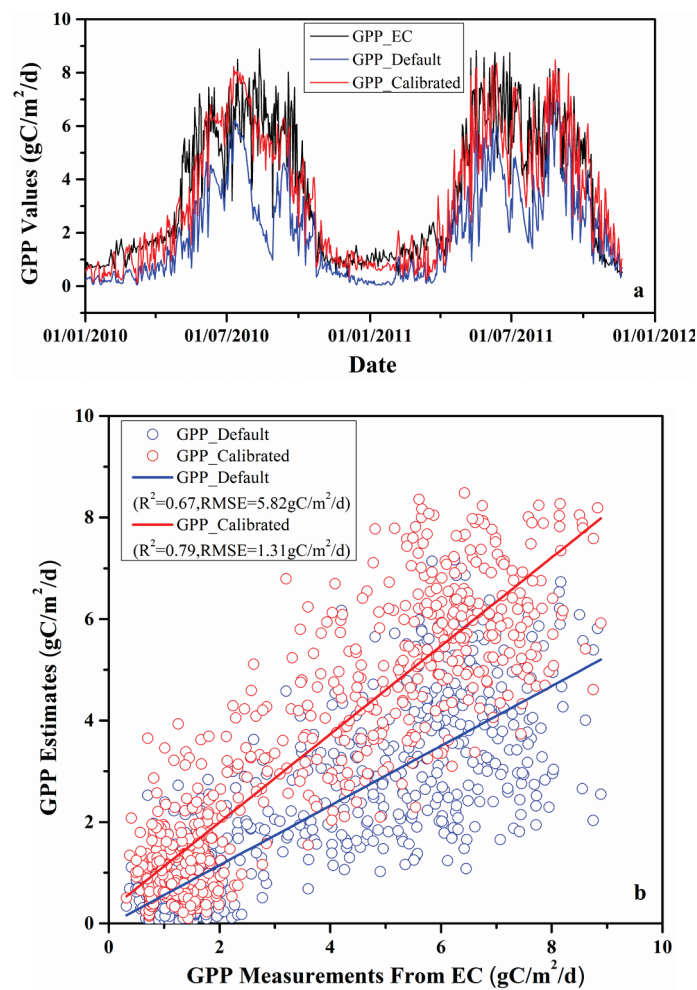


Fig. 4-6 Comparisons and validations of the GPPs from the default and calibrated Biome-BGC.

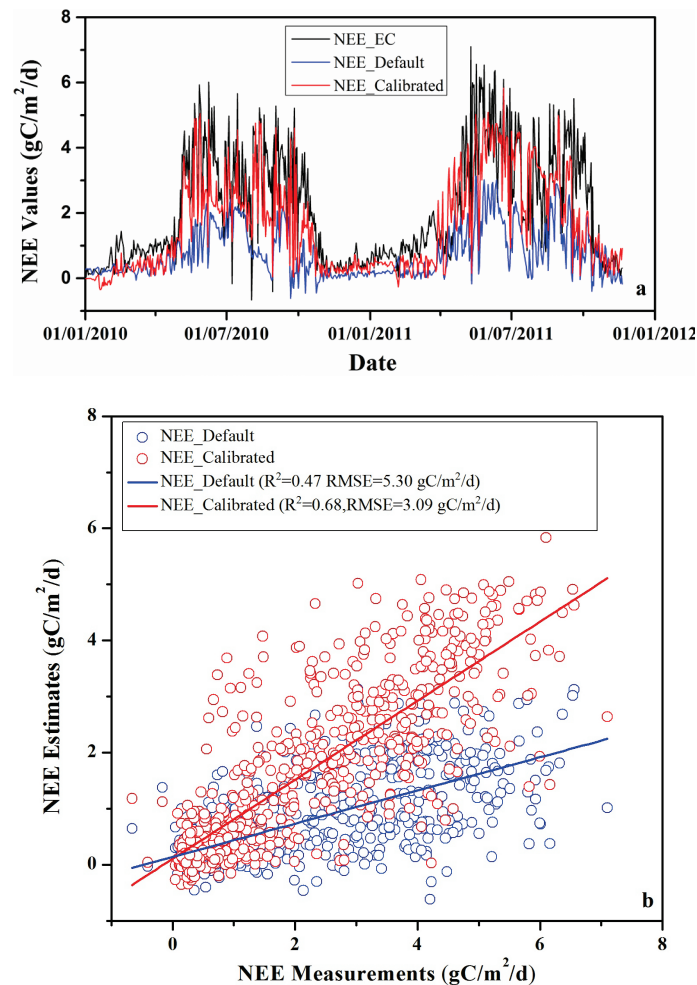


Fig. 4-7 Comparisons and validations of the NEEs from the default and calibrated Biome-BGC.

4.5.4 Simulations of Annual Forest Carbon Flux and Dynamic Analyses of Forest AGB

The time-series (13 years) annual AGB increments were validated using calculations from tree ring data. As shown in Fig. 4-8, simulated annual AGB increments were largely consistent with the measurements and a very high accuracy of $R^2 = 0.72$, and $RMSE = 47.33 \text{ gC m}^{-2} \text{ year}^{-1}$ was achieved.

In addition to the upscaled forest AGB map for 2009, regional annual forest AGB increments are provided in Fig. 4-9. Using the high-accuracy forest AGB map as the reference, forest AGB dynamic information was obtained by progressively adding (after 2009) or subtracting (before 2009) the interannual forest AGB value.

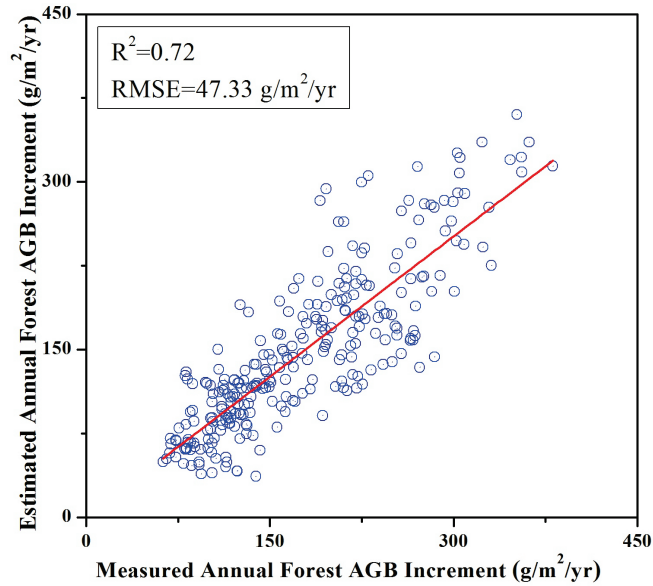
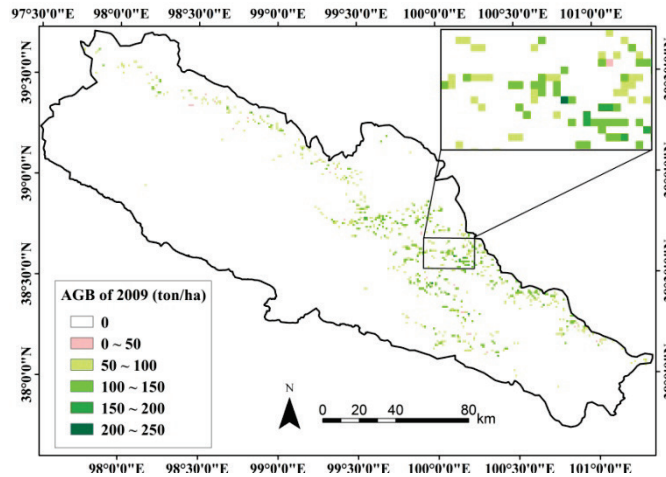
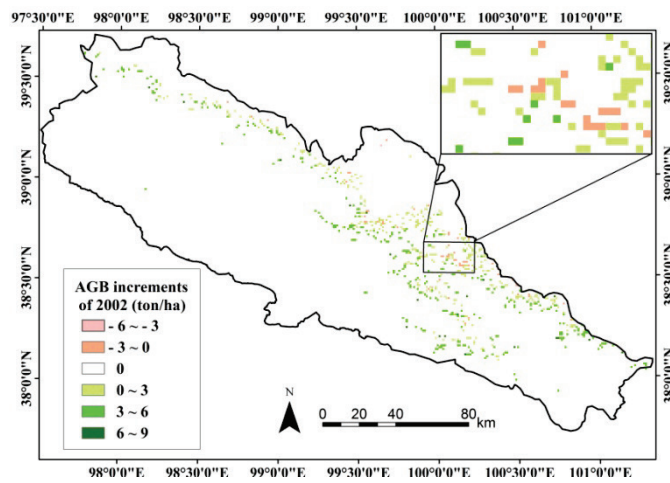
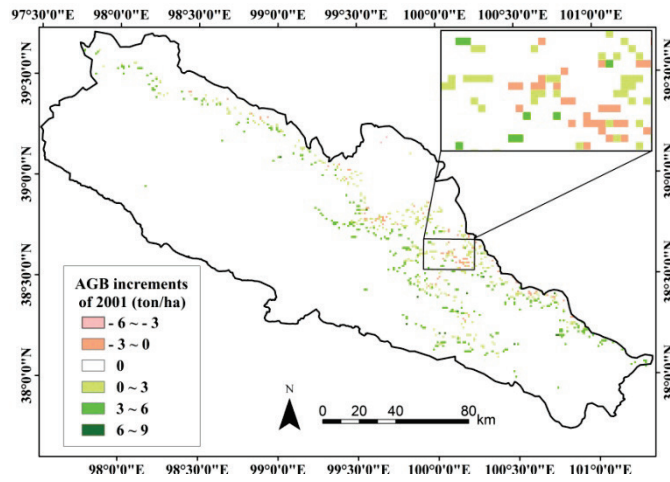
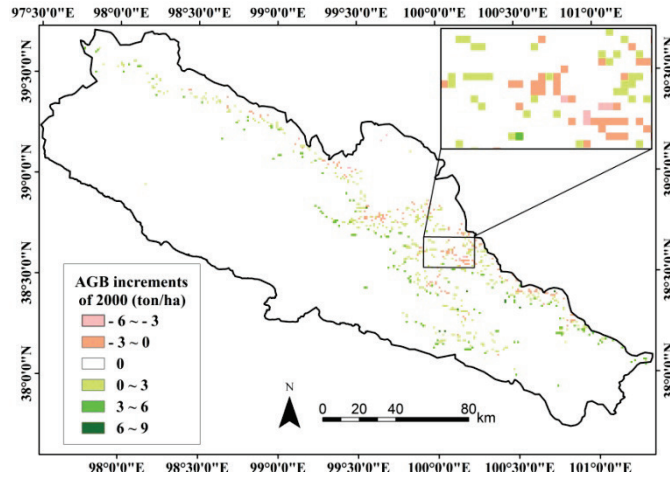
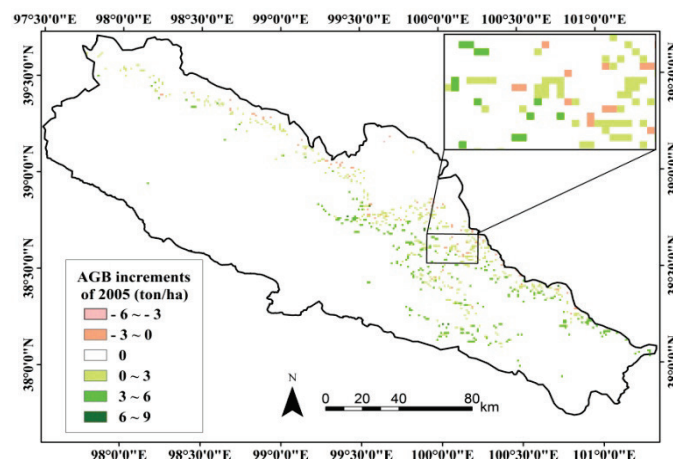
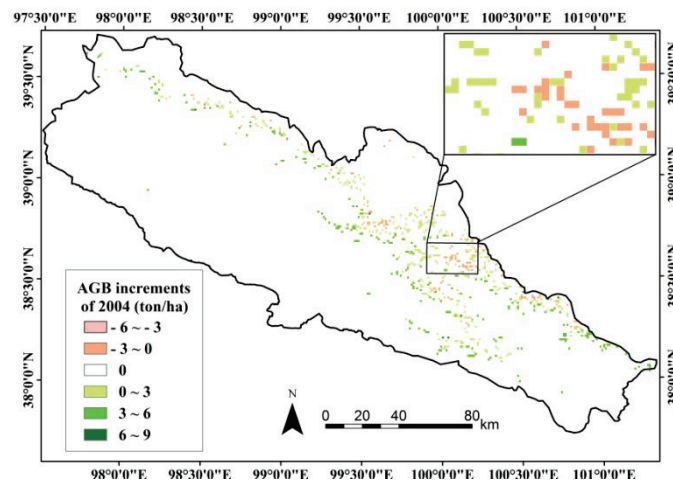
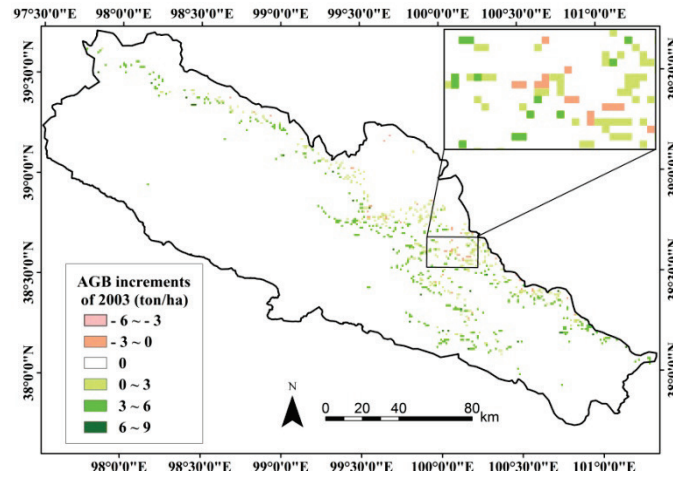


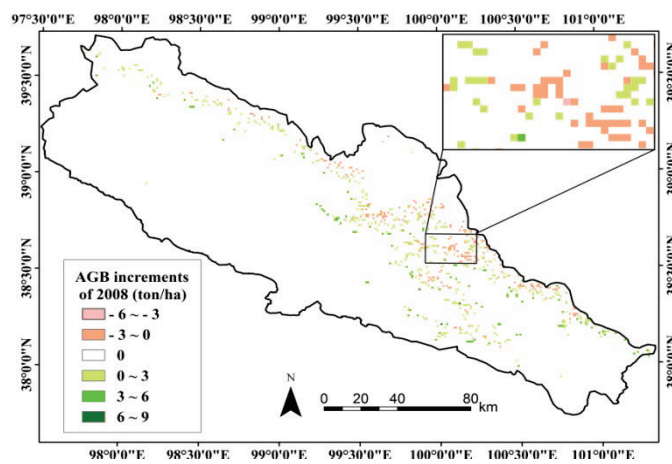
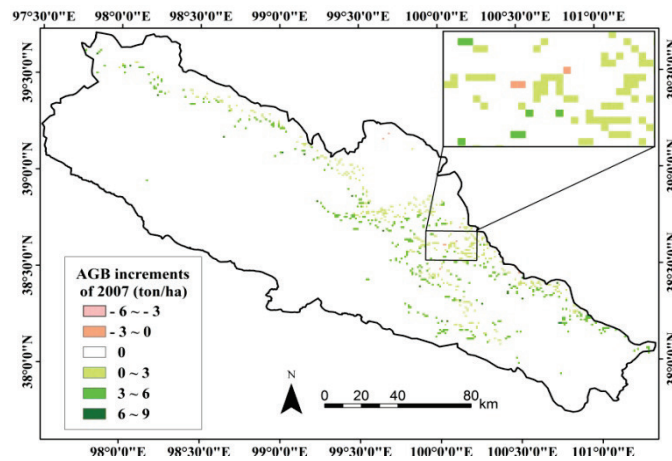
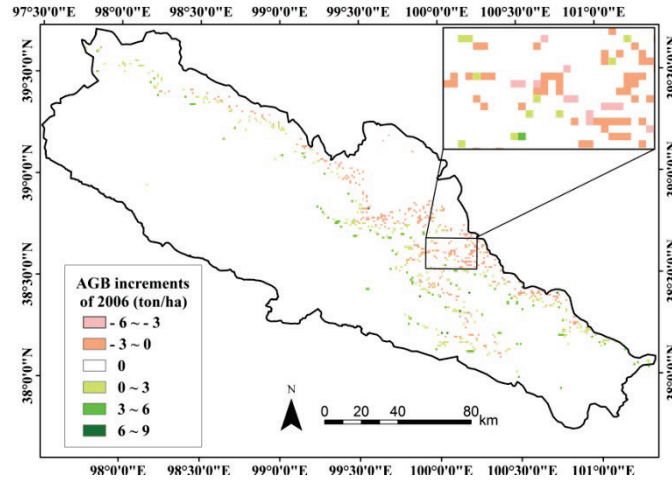
Fig. 4-8 Validation of thirteen-years of annual forest AGB increments converted from the ANPPs of the calibrated Biome-BGC using calculations from tree ring data.

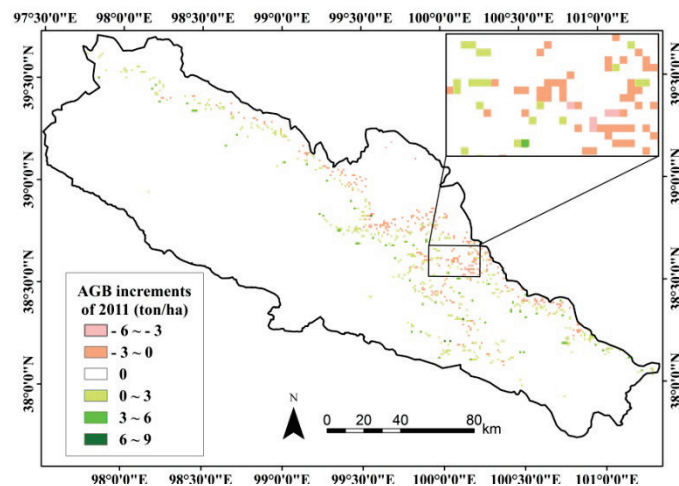
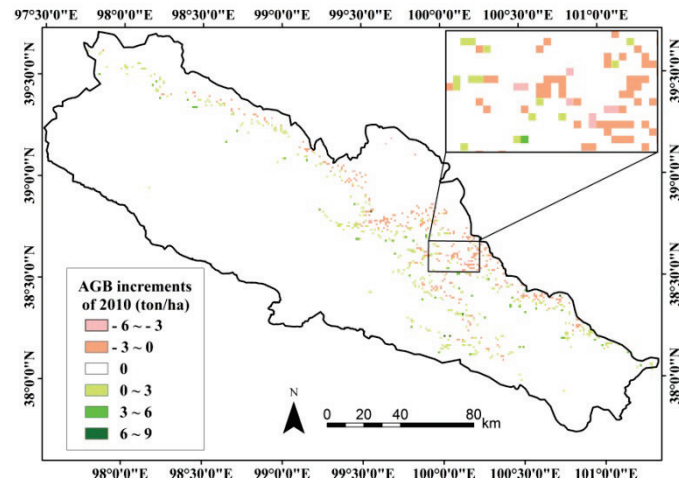
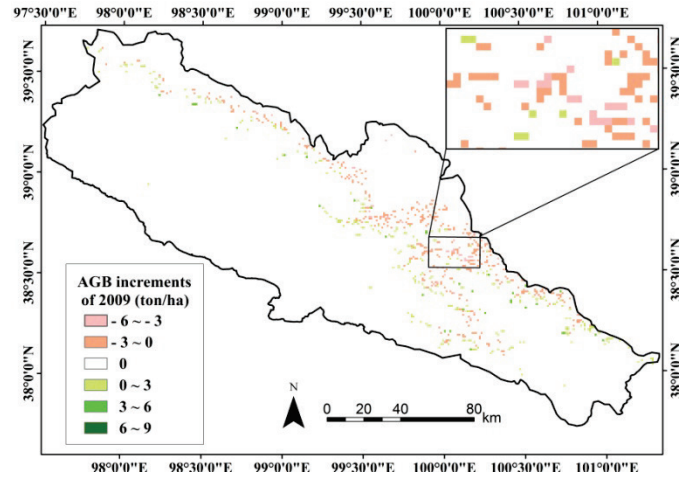
The variations of interannual NPP, ANPP fluxes, AGB increments and total amounts of forests over QMs are shown in Table 4-2. It can be found in Table 4-2, that the lowest NPP and ANPP (thus AGB increment) estimates were in 2009 and the highest values in 2003. As the annual ANPP did not compensate the AGB loss due to tree mortality, the forest AGB increment of 2009 was negative.











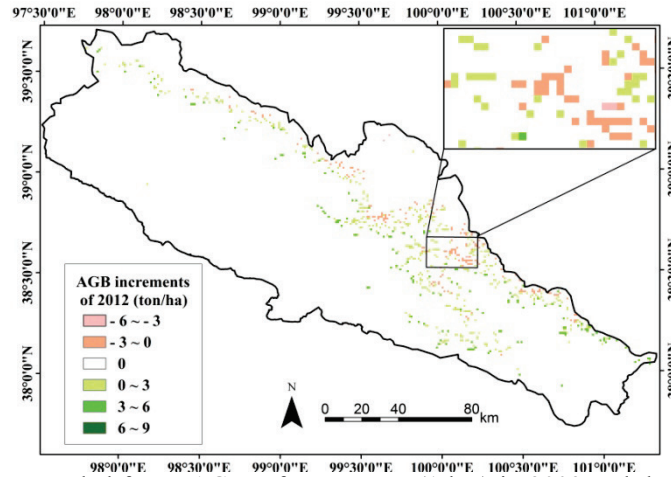


Fig. 4-9 The upscaled forest AGB reference map (1 km) in 2009 and the annual forest AGB increments from 2000 to 2012.

Table 4-2 Statistics of interannual average NPP, ANPP fluxes, and total amounts AGB of forests over the QMs from 2000 to 2012.

Year	Forest Fluxes ($\text{gC m}^{-2} \text{ year}^{-1}$)		Forest AGB ($10^3 \text{ tonnes year}^{-1}$)	
	<i>NPP</i>	<i>ANPP</i>	<i>Increments</i>	<i>Total Amounts</i>
2000	207	206	107	6466
2001	261	260	85	6551
2002	289	287	206	6757
2003	302	301	223	6980
2004	256	255	155	7135
2005	264	263	165	7300
2006	170	169	25	7325
2007	228	227	108	7432
2008	207	206	74	7506
2009	131	131	-37	7469
2010	177	176	30	7499
2011	190	190	48	7547
2012	241	240	119	7666

4.6 Discussion

Using multi-sourced and remotely sensed data, non-parametric methods have indicated superiority for estimating forest attributes as compared to habitual statistical methods such as stepwise multiple linear regression (SMLR). When using various types of remotely sensed information, the critical issue is how to construct optimal configurations for non-parametric methods. The inputting of remotely

sensed feature types, model parameters and operators, and training data have serious impacts on model performance. The determination of an optimal configuration for such models depends on previous experience and excessive processing time. For example, selecting eight feature types out from 88 features (for the case presented) will result in numerous combinations of feature vectors then result in exhaustive comparisons for these combinations.

Most studies rely on stepwise variable selection (Næsset, 2002; Heurich and Thoma, 2008) or sensitivity analyses (Tian et al., 2012). However, they were based on statistical assumptions of regressions (linear or nonlinear) that may not be suitable for non-parametric methods which normally contain flexible assumptions, especially for the spectral signatures with spatial variability. Plentiful feature types and small training samples pose (for this case 133 plots) the problem of *curse of dimensionality* (ill-posed problems). As a result, the risk of over-fitting the training sample would increase for the parametric methods.

Non-parametric methods (for this case RF, SVR, and k -NN) may be less prone to overfit training samples when bootstrap or LOO sampling methods are utilized (Powell et al., 2010; Mountrakis et al., 2011; Gleason and Im, 2012). To alleviate this problem and to enhance numeric and algorithmic stability, feature selection must be performed prior to the quantitative application of highly dimensional remotely sensed data. However, determination of the best feature composition is time-consuming, scenario-dependent, and sometimes requires a priori knowledge (Camps-Valls and Bruzzone, 2005).

In this study, due to its black box process, an RF was utilized for selecting feature types rather than for estimating forest AGB. Using the selected feature types, both SVR and k -NN overestimated plots with the lowest biomass (<50 tonnes ha^{-1}) and underestimated plots with the highest biomass (>200 tonnes ha^{-1}). Both of the estimation deviations for k -NN were less than those for SVR. The possible explanation is that, in spite of good performance for SVR as shown in previous studies, a main problem still exists. The SVR embeds a fixed-cost function that implicitly assumes a specific density model for errors (or residuals), independent of their statistical nature. Such a scenario will lead to instability when remotely sensed data containing uncertainty and noise is present (Camps-Valls, 2006). For the QMs that contain extremely heterogeneous topographic and landscape conditions, data noise could be a problem. Moreover, if C is too large (small) and if the hyperplane is not optimized, overfitting (underfitting) problems may occur (Xie et al., 2008). Since the result depends on simply weighted relationships between k nearest spectral distances, k -NN does not suffer from this assumption. Although the forest

inventory data used in this study spanned a wide range of AGB levels (18.85-220.65 tonnes ha⁻¹), most were concentrated at the AGB level of 75-150 tonnes ha⁻¹. Another widely acknowledged issue for non-parametric methods is a requirement for sufficient sample plots that represent forest AGB grades (Gilichinsky et al., 2012; Hill et al., 2013). Without sufficient sample plots, obvious biased estimations are apt to arise for AGB levels. Here, it is necessary to emphasize that terrain hinders AGB estimations obtained from remote sensing within the QMs, as validated in the **Chapter 2 and 3**. In this study, the performances of selected features with and without a SCS+C correction were very different. Without terrain relief for remotely sensed features, SVR and *k*-NN generated estimates with a $R^2 = 0.35$ and a RMSE = 33.21 tonnes ha⁻¹ and a $R^2 = 0.45$ and a RMSE = 29.36 tonnes ha⁻¹, respectively (not provided here). Obviously, both performed in an inferior manner as compared to models embedding terrain corrected features.

The incorporation of remotely-sensed-based models with process-based models exploits the powers of both models for simulating forest carbon fluxes. Such integration has been determined to be valid for Mediterranean forests; however, no existing experiments regarding feasibility for cold and arid forests have been performed. Different from previous studies (Chiesi et al., 2007; Maselli et al., 2008), this study integrated the MOD_17 and Biome-BGC models. As compared to original MODIS GPP products, GPPs generated by the optimized MOD_17 model agreed much better with EC measurements. Improvement was obtained with three sources of refinement for the input parameters. The first was the calibrated ε_{max} for *Picea crassifolia* obtained using site measurements. The second was climate driven forces (VPD_{max} , VPD_{min} , T_{max} , T_{min}) downscaled from WRF simulations, and the last was $fPAR$ generated from the GLASS LAI product using the Beer Law approach (Jarvis and Leverenz, 1983). The latter types of estimates (WRF and GLASS) have been determined to be reliable (Pan and Li, 2011; Pan et al., 2012; Xiao et al., 2014). In particular, GLASS LAI products displayed much better descriptions for the seasonal viabilities of *Picea crassifolia* than the original MODIS LAIs applied to generate original MODIS GPP products (not provided here). Although the optimized MOD_17 GPP model performed very well, it could not depict critical ecological processes within the forest. Ecological processes (i.e., transpiration, respiration, allocation, etc.), with their time-continuity characteristics, are extremely important for exploring climate, environmental, and forest stand condition impacts on forest dynamics (changes in forest ecology, forest hydrology, and forest attributes). Understanding these processes definitely requires more complex simulations for forest eco-physiology and forest eco-hydrology using process-based models.

Due to the extreme fluctuation of meteorological and various environmental conditions for forests over the QMs, calibrations of process-based models should fully consider the spatial variability of the ecosystem. In general, site measurements can fix variability within the calibration process, but they are difficult to extrapolate to other areas. Based on space-continuity representations of ecosystem characteristics, the optimized MOD_17 GPP model, fulfilling the premise of good performance for simulating forest carbon fluxes (in this case GPPs), was coupled with the Biome-BGC model in order to adopt an innovative calibration strategy for producing reliable carbon fluxes within the space-time continuum. The adoption of this calibration strategy circumvented the current data scarcity for ground truth data in describing forest carbon fluxes. Such integration could also provide reliability for simulating other terrestrial ecosystems whose processes are normally simpler than forest ecosystems.

On the whole, the carbon fluxes (including GPPs, NEEs) simulated using the calibrated Biome-BGC were consistent with EC measurements. Nevertheless, as compared to EC measurements, NEEs during the autumn of 2011 were largely underestimated. The most likely reason may be that soil respiration was highly overestimated. Further exploration should focus on improvements of soil respiration simulations, a pervasive issue for process-based models. Within this study area, dense moss is distributed under the forest canopy and may have irregularly impacted soil respiration over a large area.

The dendrochronological measurements used in this study were first tested for their ability to validate annual forest AGB increments that were originally converted from the NPP generated by the calibrated Biome-BGC. The measurement provided an authentic alternative to the EC for validating forest carbon fluxes on an annual scale. However, it is worth noting that the conversion coefficients for biomass allocation (above/below ground), the carbon content factor and the mortality were not strictly consistent with the 'true' values for natural forests. As we know, the former two coefficients should vary according to the status of the forests (i.e., forest age, forest AGB, forest stand density (SD) (trees ha⁻¹)), although this set of parameters relies on 'harvest' measurements that are rigidly prohibited. For the mortality ratio, due to the self thinning adaption, the matured or over-matured forests would definitely change the SD in order to keep the ecosystem balance, resulting in decreasing forest AGB until the equilibrium of the ecosystem is obtained. It is well known that the forest AGB variations should obey a parabolic relationship with age, due to mortality which can be normally established on the basis of measured forest AGB values against measured forest ages. In this study, an empirical constant of 3% from the previous study (Zhong and Yin, 2008) was used

which would bias the interannual forest AGB increments. The calibrated mortality model based on the local forest AGB and ages' maps can be expected to control this biased behavior by providing stand-calibrated mortality ratios of forests.

The dendrochronological measurements collected from the field work took the spatial variability (various climate, environmental, and stand conditions) of the forests into account, and did a fairly good job of representing the overall characteristics of the ecosystem. Good agreement for carbon fluxes validated using EC measurements with a fine time resolution and dendrochronological measurements with sophisticated considerations for the spatial variability of forest processes made the incorporated strategy credible and replicable.

The methodology used in the present study for the dynamic modeling of forest AGB information represents a sophisticated and innovative use of data and models that, to our knowledge, has not been proposed in previous studies. The high-accuracy forest AGB map in 2009 was used as the reference then combined with interannual forest AGB increments based on process-based simulations in order to obtain interannual forest AGB dynamics. Forest changes such as afforestation and deforestation, however, were not considered in this study. Afforestation and deforestation for the locations studied have not been recorded or quantitatively reported. However, within the conserved forest ecosystem, these activities have not been carried out intensively because forest managers understand the need to balance water demands for tree growth. Therefore, this type of anthropogenic activity poses some, but not a large effect, on local forest processes. With the exception of a few occasions of small natural disturbance (tree mortality caused by wind, land collapse, and water scarcity), deforestation has less influence. Interannual forest AGB dynamic information can also be utilized as a support for the routine analysis of climate and environmental variations on forest ecosystem processes.

4.7 Conclusion

Feature type selection using RF opens the possibility of effectively constructing optimal configurations for both SVR and k -NN for estimating forest AGB. When working with a small training sample and high-dimensional remotely sensed information, optimal configurations for the latter two non-parametric methods were capable of embedding the selected feature types by generating reliable estimates and reducing the risk of the overfitting problem. The substantial comparability of forest AGB estimates obtained using these two methods indicated that sufficient reference plots representing AGB grades were also important in addition to parameters related to configurations. In the context of modeling for forest AGB dynamics, the slightly outperforming k -NN configuration was applied in order to

produce a regional forest AGB map. The map was then used as the basis for the starting point for the 2000 to 2012 time-series analyses for forest AGB dynamics.

Three refined input sources were determined to largely improve GPP simulations for the MOD_17 model as compared with original MODIS GPP products driven by default parameters. The capacity of the optimized MOD_17 GPP model to precisely represent the space-continuity GPP characteristics of the forests were incorporated using the Biome-BGC model in order to depict time-continuity and critical processes within the forest, after using the GPPs from former models to calibrate the latter model over forests with various conditions (various climate, environmental, and stand conditions). Due to extreme heterogeneity within the QMs, the selection of forest plots that represents local conditions may be suboptimal for the calibration phase.

In fact, such incorporation can make the Biome-BGC model more resistant to the impacts of environmental variability, and forest stand diversity, which would bias the simulations. Such an incorporation strategy can also alleviate the ‘ill-simulation’ problem associated with process-based models, where errors from calibration phases are likely to be propagated to the end of the simulation. Validated by EC and dendrochronological measurements in terms of GPP, NEE, and the annual forest AGB increment primarily converted from NPP, the calibrated Biome-BGC generated reliable forest carbon fluxes for the space-time-continuum. By combining interannual forest AGB increments indirectly from the Biome-BGC with the basic status of forest AGB of 2009, interannual forest AGB dynamic information can be easily obtained. The dynamic modeling of forest AGB can capture detailed characteristics of additional forest processes (transpiration, photosynthesis, respirations, allocations, etc.) on finer space and time scales, and provide a sophisticated understanding of these processes. Beyond this chapter, the impacts of climatic variations on these processes can be analyzed using the meteorological driving data. This comprehensive knowledge is vital for sustainable forest management.

Chapter 5

Estimating Zero-Plane Displacement Height and Aerodynamic Roughness Length Using Synthesis of LiDAR and SPOT-5 Data*

* This chapter is based on:
Tian, X., Li, Z. Y., van der Tol, C., Su, Z., Li, X., He, Q. S., Bao, Y. F., Chen, E. X., & Li, L. H. (2011). Estimating zero-plane displacement height and aerodynamic roughness length using synthesis of LiDAR and SPOT-5 data. *Remote Sensing of Environment*, 115, 2330-2341. DOI:10.1016/j.rse.2011.04.033.

Abstract

In this chapter, a combination of low and high-density airborne light detection and ranging (LiDAR) and Satellite Probatoire d'Observation de la Terre-5 (SPOT-5) high resolution geometrical (HRG) data were used in conjunction with ground measurements of forest structure to parameterize four models for zero-plane displacement height d (m) and aerodynamic roughness length z_{0m} (m), over the forests in the airborne campaign area. The forest structural parameters including tree height (Ht) (m), first branch height (FBH) (m), crown width (CW) (m) and stand density (SD) (trees ha^{-1}) were derived by stepwise multiple linear regressions (SMLR) of ground-based forest measurements and height quantiles and fractional canopy cover (f_c) derived from the low-density LiDAR data. The high-density LiDAR data, which covered a much smaller area than the low-density LiDAR data, were used to relate SPOT-5's reflectance to the effective plant area index (PAI_e) of the forest. This was done by linear spectrum decomposition and Li-Strahler geometric-optical models. The result of the SPOT-5 spectrum decomposition was applied to the whole area to calculate PAI_e (and leaf area index LAI). Then, four roughness models were applied to the study area with these vegetation data derived from the LiDAR and SPOT-5 as input. For validation, measurements at an Eddy Covariance (EC) site in the study area were used. Finally, the four models were compared by plotting histograms of the accumulative distribution of modeled d and z_{0m} in the study area. The results showed that the model using by frontal area index (FAI) produced best d estimate, and the model using both LAI and FAI generated the best z_{0m} . Furthermore, all models performed much better when the representative tree height was Lorey's mean height instead of using an arithmetic mean.

5.1 Introduction

The Monin–Obukhov Similarity (MOS) theory (Monin and Obukhov, 1954; Foken, 2006) has been frequently used in atmospheric models for numerical weather prediction and climate research (Su et al., 2001). Two parameters play a central role in MOS theory, notably the zero-plane displacement d and the roughness height z_{0m} (Garratt, 1994; Yang and Friedl, 2003). These two parameters significantly influence the momentum exchange between the atmosphere and land surface, and yet they are difficult to estimate in practice. Therefore, studies on d and z_{0m} can improve the understanding of the mechanism of momentum transport (Brutsaert, 1999; Krishnan and Kunhikrishnan, 2002; Koloskov et al., 2007).

Many methods exist to estimate d and z_{0m} . These methods can be classified as either experimental or remote sensing based. Experimental methods are based on measurements of the vertical wind profile in and above the canopy. A disadvantage of experimental methods is that the results are only locally valid, and scaling to the grid cell of a climate or land surface model is difficult (Schaudt and Dickinson, 2000). As a consequence, most these models employ general expressions for d and z_{0m} as a function of the vegetation height h , for example $d/h = 2/3$ and $z_{0m}/h = 1/8$ (Garratt, 1994), or use a look-up table based on the land cover types (Dorman and Sellers, 1989; Wieringa 1986). Neither of these techniques can capture variations of the density of roughness elements. Alternatives that make the inclusion of these variations in density possible are remote sensing based methods. Robust scaling of d and z_{0m} to regional applications using remote sensing data may result in representative values for grid cells in models (Nakai et al., 2008; Su, 2002; Verhoef et al., 1997; Wang et al., 1998a; Wieringa, 1993).

In past decades, several models have been developed for d and z_{0m} as functions of (remotely sensed) vegetation physical structural parameters, such as leaf area index (LAI) (Choudhury and Monteith, 1988), frontal area index (FAI) (Raupach, 1994; Schaudt and Dickinson 2000), stand density (SD) and stem-branch-leaf distributions (Nakai et al., 2008). Once these parameters and vegetation height can be retrieved from remote sensing data with sufficient accuracy, they can be easily integrated into these models to estimate regional d and z_{0m} values.

Nevertheless, theoretical and practical problems have limited the retrieval of the vegetation parameters from remote sensing data (Braswell et al., 2003; Hu et al., 2004; Olthof and Fraser, 2007). The optical spectrum is insensitive to some of the parameters of interest (for example, vegetation height). To some other parameters it is only sensitive up to a limit above which the signal saturates (for example, LAI).

In addition, retrieval techniques usually suffer from ill-posedness, especially in sparsely vegetated areas with the fragmental landscape. Therefore, application of estimating biophysical characteristics from remote sensing should be more reasonable when it is based on physical algorithms, such as Geometric–Optical and Radiative Transfer (GORT) model, rather than direct inference from spectral indices (Hall et al., 1995; Song and Woodcock, 2002).

Airborne laser scanning (ALS) has recently led to a revolution in remote sensing technology for characterizing the canopy structure, due to its ability to measure three-dimensional information (Koukoulas and Blackburn, 2005; Maltamo et al., 2004). The airborne light detection and ranging (LiDAR) sensor provides multiple echoes per laser pulse. It has been applied successfully for measuring and monitoring vegetation structural data across the landscape (Popescu and Wynne, 2004; Reutebuch et al., 2005; Salas et al., 2010).

This chapter used a combination of forest inventories, airborne LiDAR and a satellite SPOT-5 HRG image as input for four existing models for d and z_{0m} . The four models were validated against d and z_{0m} derived from Eddy Covariance (EC) and wind profile measurements in a needle forest located in the study area. The four tested models are those of Choudhury and Monteith (1988), Raupach (1994), Schaudt and Dickinson (2000) and Nakai et al. (2008) (hereafter, CM88, RA94, SD00, NA08 respectively).

First, by means of stepwise multiple linear regression models (SMLR), low-density airborne LiDAR data was used to derive the forest structural parameters needed to drive the four roughness models. Moreover, for models' requests, the LAI input was calculated based on the experimental adjustment coefficient and the effective plant area index (PAI_e) which was derived from the synthesis of high-density LiDAR and SPOT-5 HRG data. Second, these parameters were validated against field measurements obtained in the study area. Then, the validities of the four models were compared by using forest structural measurements and forest structural retrievals from remote sensing data respectively. Finally, the four resulting maps (generated with the four models) of d and z_{0m} were used for further statistical analyses.

5.2 Site Observation

In this study, the EC measurements in June and August 2008 were used when the airborne LiDAR data and SPOT-5 image were acquired, respectively. The descriptions of the EC site, instruments and data processing have been given in **Section 4.2**. Only the EC data under the neutral conditions during these months

(June-August) were applied to Eqs. (5-1) and (5-2). Moreover, to avoid the effect of the EC tower's shadow, only a few wind speed measurements within a limited range of the wind directions were used (Nakai et al., 2008). As azimuth angle of the sonic anemometer (CSAT-3) is about 75° (clockwise from north), the range was chosen as from 45° (equal to $75^\circ - 30^\circ$) to 105° (and to $75^\circ + 30^\circ$). The representative d and z_{0m} were obtained by averaging the d and z_{0m} calculations from u_1 , u_2 and the friction velocity u^* , under the neutral conditions within this range.

To calculate d and z_{0m} at forest site, under neutral conditions ($|z/L| < 0.05$, where L is the Obukhov length), based on EC measurements: friction velocity (m s^{-1}) at heights z_1 (20 m) and two wind speeds μ_1 , μ_2 (m s^{-1}) at heights z_1 and z_2 (24 m), the following equations were used (Rooney, 2001; Nakai et al., 2008),

$$d = \frac{z_2 \exp(ku_1 / u^*) / \exp(ku_2 / u^*) - z_1}{\exp(ku_1 / u^*) / \exp(ku_2 / u^*) - 1} \quad (5-1)$$

$$z_{0m} = \frac{z_1 - d}{\exp(ku_1 / u^*)} \quad (5-2)$$

Within the airborne campaign areas, the PAIe of some forest plots were also measured with LAI-2000 (LI-COR, Inc., USA).

5.3 Methodology

5.3.1 Remote Sensing Models for Estimating d and z_{0m}

Four models were used to calculate d and z_{0m} from forest structural parameters in this chapter, and Table 5-1 lists the required input for each of the four models. The estimation of the forest structural parameters from LiDAR and SPOT was described in Section 5.3.3.

Table 5-1 Required inputs for the four tested roughness models.

Model	LAI	Ht	CW	FBH	SD
CM88	*	*			
RA94		*	*	*	*
SD00	*	*	*	*	*
NA08	*	*			*

The first model is that of Choudhury and Monteith (1988). They used the second-order closure model results of Shaw and Pereira (1982) to estimate d and z_{0m} as follows:

$$d = h \left[\ln(1 + X^{1/6}) + 0.03 \ln(1 + X^6) \right] \quad (5-3)$$

$$z_{0m} = \begin{cases} z_{0s} + 0.28hX^{1/2} & \text{for } 0 \leq X \leq 0.2 \\ 0.3h(1 - d/h) & \text{for } 0.2 < X \leq 2 \end{cases} \quad (5-4)$$

where $X = 0.2LAI$, h is the height of the vegetation, and z_{0s} is the soil surface roughness, generally taken as 0.01m or 0.1 of the height of the vegetation understory, for raw and vegetated substrates respectively (Shuttleworth and Wallace, 1985; Yang and Friedl, 2003).

The second model, Raupach (1994), used observation data to fit the estimation of normalized displacement height d/h and roughness length z_{0m}/h , related to FAI (λ):

$$\frac{d}{h} = 1.0 - \frac{1.0 - \exp(-\sqrt{a_1\lambda})}{\sqrt{a_1\lambda}} \quad (5-5)$$

$$\frac{z_{0m}}{h} = a_2 \exp(-b_2\lambda^{c_2})\lambda^{d_2} + \frac{z_{00}}{h} \quad (\lambda \leq 0.152) \quad (5-6)$$

$$\frac{z_{0m}}{h} = \frac{a_3}{\lambda^{d_3}} [1.0 - \exp(-b_3\lambda^{c_3})] + f_2 \quad (\lambda > 0.152) \quad (5-7)$$

where $a_1 = 15.0$, $a_2 = 5.86$, $b_2 = 10.9$, $c_2 = 1.12$, $d_2 = 1.33$, $a_3 = 0.0537$, $b_3 = 10.9$, $c_3 = 0.874$, $d_3 = 0.510$ and $f_2 = 0.00368$ and $z_{00}/h = 0.00086$.

Frontal area index is calculated from the frontal area, A_f , of each individual needle tree as:

$$A_f = h_s * w_s + \frac{1}{2} h_c * w_c \quad (5-8)$$

where h_s is the FBH, w_s is DBH, h_c is the height of the crown (i.e. Ht-FBH), w_c is the CW. Then the FAI (λ) is calculated by total A_f divided by the total area of the plot.

In this chapter, Eq. (5-8) was further simplified by assuming that the frontal area of the stem is much smaller than the frontal area of the crown (Schaudt and Dickinson, 2000):

$$A_f = \frac{1}{2} h_c * w_c \quad (5-9)$$

The third model is that of Schaudt and Dickinson (2000), who estimated z_{0m}/h and d/h over coniferous forest by following expressions:

$$f_z = 0.3299L_p^{1.5} + 2.1713 \quad \text{for } L_p < 0.8775 \quad (5-10)$$

$$f_z = 1.6771 \exp(-0.1717L_p) + 1.0 \quad \text{for } L_p \geq 0.8775 \quad (5-11)$$

$$L_p = \frac{f_v}{f_c} LAI - \frac{f_b}{f_c} L_b \quad (5-12)$$

$$f_d = 1.0 - 0.3991 \exp(-0.1779 L_p) \quad (5-13)$$

where L_p is the mean plant LAI, L_b is background LAI, f_b is the fraction of the understory vegetation ($f_v = f_c + f_b$). Multiplying f_z to right hand side (RHS) of Eq. (5-6) or Eq. (5-7) gives roughness length as a function of both LAI and FAI. The d/h is quantified by multiplying Eq. (5-13) by Eq. (5-5).

The fourth model is that of Nakai et al. (2008). They considered the effects of SD, stems/branches and leaves on d/h , based on the following assumptions:

- The fundamental d/h is mainly determined by the SD.
- The seasonal variation depends on the LAI, and the degree of this variation is decided by the SD.
- Total d/h is the collection of above components.

Therefore, the total effect of stems/branches and leaves on d/h was written as follows:

$$\frac{d}{h} = 1.0 - \frac{1.0 - \exp(-\alpha \rho_s)}{\alpha \rho_s} \frac{1.0 - \exp(-\beta A)}{\beta A} \quad (5-14)$$

where ρ_s is SD and A is LAI. Nakai et al. (2008) obtained values of the coefficients α and β of $\alpha = 0.000724$ and $\beta = 0.273$ by fitting Eq. (5-14) to monthly averaged d/h from the EC measurements in their five forest sites. Finally, z_{0m}/h was parameterized by linear regression between d/h and z_{0m}/h as follows:

$$\frac{z_{0m}}{h} = 0.264 \left(1.0 - \frac{d}{h}\right) \quad (5-15)$$

5.3.2 Model Sensitivity

In order to compare model sensitivities and their dependencies on the roughness elements conditions, a sensitivity analysis for four models was performed. The sensitivity (S_j) of the model to an input parameter (j) can be expressed as:

$$S_j = \frac{Y_j - Y_r}{Y_r} * 100 \quad (5-16)$$

where Y_j is the modeling result driven by testing variable j , Y_r is the result predicted by the reference variable r .

The sensitivity tests were conducted for Ht , LAI, FAI and SD variables which directly and significantly affect the d and z_{0m} computations in the four models, as

presented in Eqs. (5-3) ~ (5-7) and Eqs. (5-10) ~ (5-16). The tree measurement at the EC site was used as the reference data r and $0.25 \times r$, $0.75 \times r$, $1.25 \times r$ and $1.75 \times r$ were used as the testing variables respectively, because this range of values can represent the majority of local roughness element conditions in the study area. The testing variables were then applied to the four models with reference values used for all other inputs to derive the d and z_{0m} values respectively.

As the variations in all model estimates of d and z_{0m} were the same as the prescribed tree height deviations (i.e. d and z_{0m} respond linearly to h in all models), the result of tree height sensitivity was not presented here. The sensitivity results of LAI, FAI and SD are shown in Table 5-2. In general, the models are more sensitive to variations in tree height than in other parameters, except for FAI in RA94 and SD00: in these models S_j reaches values to +100% when FAI reduces by -75%. This value exceeds the sensitivity to tree height in both models (-75%). As both RA94 and SD00 used the same expression to derive d and z_{0m} by FAI, they are equally sensitive to FAI. The sensitivity to FAI of the SD00 model also exceeds the sensitivity to LAI. In NA08, SD deviation generated higher discrepancy in both d and z_{0m} estimates than that LAI produced. It is also found that the sensitivity to LAI, FAI and SD, is asymmetric: decreases engender higher S_j than increases. This suggests that at higher values, the response of the models to these variables saturates. The only exception is LAI is for CM88: when LAI is decreased by 75%, then the error ($S_j = +15.7\%$) is smaller than when it is increased by 75% ($S_j = -25.5\%$). This is a particular case, caused by the alternative expression for LAI used for values of LAI smaller than 1 in this model (see Eq. (5-4)).

Table 5-2 Sensitivities of the four models with different input parameter variations, as fractions of their reference values.

Parameters Models*	LAI				FAI				SD			
	0.25	0.75	1.25	1.75	0.25	0.75	1.25	1.75	0.25	0.75	1.25	1.75
Deviation	$S_f(\%)$				$S_f(\%)$				$S_f(\%)$			
CM88- d	-16.3	-3.8	3.8	12.8	-	-	-	-	-	-	-	-
CM88- z_{0m}	15.7	7.6	-7.6	-25.5	-	-	-	-	-	-	-	-
RA94- d	-	-	-	-	-22.6	-4.0	2.8	6.6	-	-	-	-
RA94- z_{0m}	-	-	-	-	100	15.8	-10.1	-24.8	-	-	-	-
SD00- d	-16.1	-4.6	3.9	10.2	-22.6	-4.0	2.8	6.6	-	-	-	-
SD00- z_{0m}	26.8	7.7	-6.6	17.2	100	15.8	-10.1	-24.8	-	-	-	-
NA08- d	-25.2	-7.2	6.2	16.4	-	-	-	-	-28.2	-7.9	6.7	17.5
NA08- z_{0m}	37.4	10.7	-9.3	-24.3	-	-	-	-	41.8	11.7	-10.0	-26.0

*- d and - z_{0m} are d and z_{0m} models in CM88, RA94, SD00 and NA08, respectively.

The sensitivities of these four models presented here are local sensitivities that somewhat depend on the selection of the reference values. In this chapter, only one

EC station in forested area is available. A more detailed sensitivity analysis with other reference values is not very useful for this study, because the choice of reference values would be rather subjective.

5.3.3 Forest Structural Parameters Estimated by Remote Sensing Data

The airborne LiDAR data was used to retrieve the f_c , Ht, CW, FBH, SD and PAIe of the forest. Specifically, the PAIe was derived by integration of linear spectrum decomposition model with Li-Strahler's geometric-optical model. In this way, SPOT-5 and LiDAR data were combined, and uncertainties brought about by mixed pixels could be reduced (Section 5.3.3.2).

5.3.3.1 LiDAR data process

Both low and high-density LiDAR data were processed. The low-density LiDAR points were used to extract the digital surface model (DSM) and the digital elevation model (DEM). First, the ground and vegetation points were identified from the overall airborne LiDAR points using Terrasolid software. Then, the DEM with 0.5 m resolution was generated based on the ground points and DSM from the vegetation points. The normalized point (vegetation height) was defined as the height difference between the DSM and the DEM. In order to reduce the influence of the low shrubs, a threshold of 1.3 m was defined to remove normalized points below it in order to refine the vegetation points (He, 2010). The fractional vegetation cover f_c was defined as the complementary of the fraction of laser beam pulses that reached the ground:

$$f_c = 1 - \frac{P}{P_0} \quad (5-17)$$

where P_0 is the emitted laser beam and P is the penetrated beam.

The other relevant structural parameters were obtained by regression analyses against field measurements in plots with a size of 20 by 20 m. This spatial resolution was chosen in order to be consistent with the measured plot scale. SMLR between two LiDAR parameters, notably the height quantiles (Magnussen, 1998; Næsset, 2004; Lim and Treitz, 2004) and f_c , and forest measurements of Ht, CW, FBH, and SD were carried out.

The quantile describes the distribution and location of the sample, expressed as:

$$P(X \leq \theta_p) = p \quad (5-18)$$

where $P(X \leq \theta_p)$ is the cumulative distribution function, X is the population, θ_p is the quantile of population X at p ($0 < p < 1$).

According to their heights, at each plot, the vegetation points were sorted by

ascending order, from $p = 5\%$ to $p = 95\%$ (5% interval), resulting in 19 quantiles ($H_{05} \dots H_{95}$, respectively).

Table 5-3 Stepwise multiple linear regressions for the forest structural parameters used in this chapter.

Forest Parameters	Significant Statistics	Regression Models	Correlation (R^2)
H_{avg}	H_{05}	$Y_{H_{avg}} = 3.525 + 1.025 * X_{H_{05}}$	0.70
H_L	H_{90}, H_{35}	$Y_{H_L} = 1.944 + 0.533 * X_{H_{90}} + 0.386 * X_{H_{35}}$	0.83
FBH	H_{05}	$Y_{FBH} = -0.145 + 0.581 * X_{H_{05}}$	0.67
CW	H_{65}, f_c	$Y_{CW} = 1.643 + 0.136 * H_{65} + 0.805 * f_c$	0.36
SD	H_{95}	$Y_{SD} = 3467.4 - 137.41 * X_{H_{95}}$	0.40

* H_{avg} is the arithmetical average tree height, f_c is the fractional canopy cover and H_{05} , H_{35} , H_{65} , and H_{95} are the height quantiles of 5%, 35%, 65% and 95% respectively

As the stepwise multiple regressions were performed on basis of above 20 statistics (19 quantiles, and f_c , about 75% of measured forest plots (65 out of 85, by stratified sampling)) were used to establish the relationships between above statistics and the forest parameters needed in the four remote sensing roughness models. The optimal regressions were found with SPSS statistical software (see Table 5-3).

For high-density LiDAR data covered area, f_c was also calculated as the ratio of the number of refined vegetation points over the total number of points.

5.3.3.2 Synthesis of LiDAR and SPOT-5 data

The high resolution DEM from the airborne LiDAR point cloud data was used to geocode the aerial CCD image, thereafter both of them were applied to do the ortho-rectification and topographic correction for the SPOT-5 image. The atmospheric correction for SPOT-5 image was processed with the FLAASH model. In Li-Strahler model, the average directional reflectance of a pixel can be expressed as a linear combination of the following four components (Li and Strahler, 1985):

$$S = K_{sc}G_{sc} + K_{sb}G_{sb} + K_{dc}G_{dc} + K_{db}G_{db} \quad (5-19)$$

where S is the mean reflectance from the target surface, G_{sc} , G_{sb} , G_{dc} and G_{db} are the reflected signals of sunlit crown, sunlit background, shadowed canopy and shadowed background, respectively. K 's are the areal proportions of the four components. Taking G_0 as the overall reflectance of sc , dc and db and, Eq. (5-19) can be simplified as:

$$S = K_{sb}G_{sb} + (1 - K_{sb})G_0 \quad (5-20)$$

and

$$K_{sb} = \exp\{-\pi m[\sec\theta_i' + \sec\theta_v' - O(\theta_i, \theta_v, \varphi)]\} \quad (5-21)$$

where θ_i and θ_v are solar and satellite zenith angle respectively, φ is the azimuth angle between sun and satellite, $O(\theta_i, \theta_v, \varphi)$ is an 'overlap' function, expressed as:

$$O(\theta_i, \theta_v, \varphi) = (t - \sin t \cos t)(\sec\theta_i' + \sec\theta_v') / \pi \quad (5-22)$$

$$\cos t = \frac{h \sqrt{D^2 + (\tan\theta_i' \tan\theta_v' \sin\phi)^2}}{b \sec\theta_i' + \sec\theta_v'} \quad (5-23)$$

$$D = \sqrt{\tan^2\theta_i' + \tan^2\theta_v' - 2 \tan\theta_i' \tan\theta_v' \cos\phi} \quad (5-24)$$

$$\tan\theta' = \frac{b}{r} \tan\theta \quad (5-25)$$

where, h is tree height, b and r are major and minor radius of crown.

As the crucial parameter in Eq. (5-21), the treeness m connects the remote sensing signal and forest structure. It is defined as:

$$m = \rho * r_0^2 \quad (5-26)$$

where ρ is the stand density, r_0 is the average crown width.

Assuming the trees are distributed randomly in the plot, f_c can be also expressed by m (Li and Strahler, 1985),

$$f_c = 1 - e^{-\pi m} \quad (5-27)$$

According to Monsi and Saeki (2005), the light attenuated by the vegetation canopy is related to vegetation structure and LAI, expressed as,

$$I = I_0 e^{-K * LAI} \quad (5-28)$$

where I and I_0 are light radiation intensities below and above the canopy respectively, k is extinction coefficient. Similarly, for penetrated laser beam of LiDAR, it follows the relation with the emitted laser beam as:

$$P = P_0 e^{-K * LAI} \quad (5-29)$$

Therefore Eq. (5-17) can be converted into:

$$1 - f_c = e^{-K * LAI} \quad (5-30)$$

As the laser echoes from the leaves were not separated from the overall return points in this chapter, the derivation was PAIe rather than LAI. Assuming that the leaf inclination angle complies with spherical-shape distribution, k equals to 0.5. Considering that the airborne LiDAR data are taken from the nadir-looking observation, PAIe can be estimated as (Bao, 2009):

$$PAIe \approx -2 \ln(1 - f_c) = 2\pi m \quad (5-31)$$

After accurate inversion of f_c from dense LiDAR, parameter m was calculated with

Eq. (5-26). This m was then used together with the geometric data of the SPOT-5 image to calculate K_{sb} with Eqs. (5-21) ~ (5-25). In this way a K_{sb} map for the area of the high-density LiDAR campaign was generated. Based on the S samples of the SPOT-5 image selected from this area, and substituting their K_{sb} into the linear spectrum decomposition Eq. (5-20), the dimidiated end members G_{sb} and G_0 were obtained by factor analysis (Bao, 2009).

The values of G_{sb} and G_0 found in this way were applied to the whole low-density LiDAR campaign area, including to the part where dense LiDAR data were not collected. Now the values for G_{sb} and G_0 were used in the other direction, first to generate the K_{sb} map for the processed SPOT-5 image (Eq. (5-20)), second to calculate m by inverted Eq. (5-21) and Eqs. (5-22) ~ (5-25), and finally, to calculate PAIe from m with Eq. (5-31).

As CM88, SD00 and RA08 use LAI as input rather than PAIe, the effects of tree trunk, branch and foliage clumping on transforming PAIe to LAI should be taken account into. The following formula developed by Chen and Cihlar (1996) was used in this chapter,

$$LAI = (1 - \alpha) * PAIe * \gamma_e / \Omega_e \quad (5-32)$$

where α is the woody-to-total area ratio, γ_e is the needle-to-shoot area ratio and Ω_e is the element clumping index. In the study area, for *Picea crassifolia*, α , γ_e and Ω_e were found as 0.18, 1.23 and 0.88 respectively (Zou et al., 2009). These values in Eq. (5-32) result in a ratio of LAI over PAIe of 1.15. One more point to be noted is that, as only a small amount of understory mosses live on the forest floor, and the points below 1.3 m have been separated from vegetation points, the LAI derived from LiDAR and SPOT-5 was also used as a surrogate for L_p in Eqs. (5-10) ~ (5-13).

5.4 Results

5.4.1 Forest Structural Parameters Estimated from Airborne LiDAR and SPOT-5 Data

The variables FBH, CW, SD and Ht (actually the Lorey's mean height (Lorey, 1878), discussed in **Section 5.4.3**, were derived at the plot scale by the relevant height quantiles and f_c from LiDAR vegetation points using regression expressions listed in Table 5-3. Based on linear decomposition and Li-Strahler models, PAIe and LAI were obtained by use of high-density LiDAR cloud point and SPOT-5 reflectance (**Section 5.3.3.2**).

For the Lorey's mean height (H_L), FBH, CW and SD (see Fig. 5-1 (a) ~ (d)), the stratified selection of 65 forest plots were used for training the regression models

and the remaining 20 plots were used for validation. Actually, the original LAI-2000 measurement was PAIe, therefore, instead of LAI, PAIe estimates were validated directly using the measurements at 32 forest plots (see Fig. 5-1 (e)). On the whole, the highest R^2 among the retrievals was about 0.77 for H_L (RMSE = 1.35 m), followed by PAIe with $R^2 = 0.75$ (RMSE = 0.59), and the lowest R^2 was about 0.47 for SD (RMSE = 534.52 trees), a little lower than FBH's ($R^2 = 0.50$, RMSE = 1.03 m) and CW's ($R^2 = 0.59$, RMSE = 0.68 m).

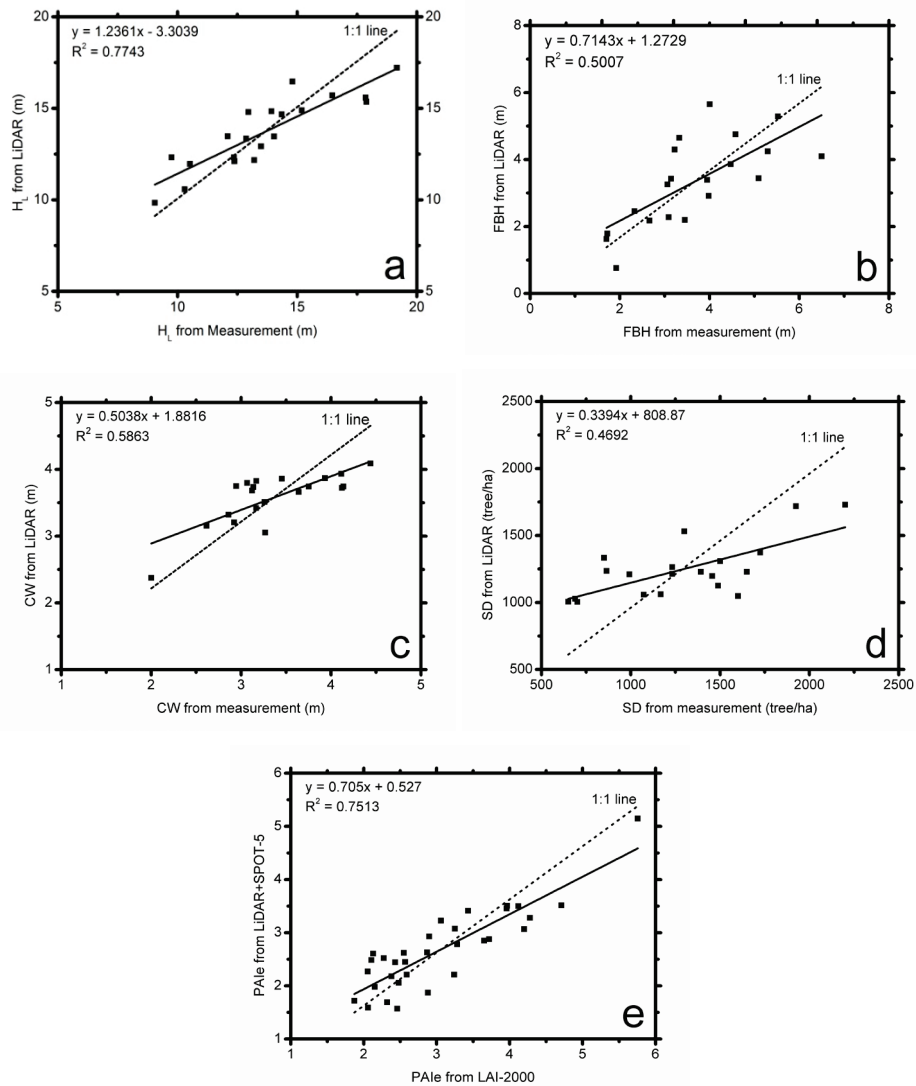
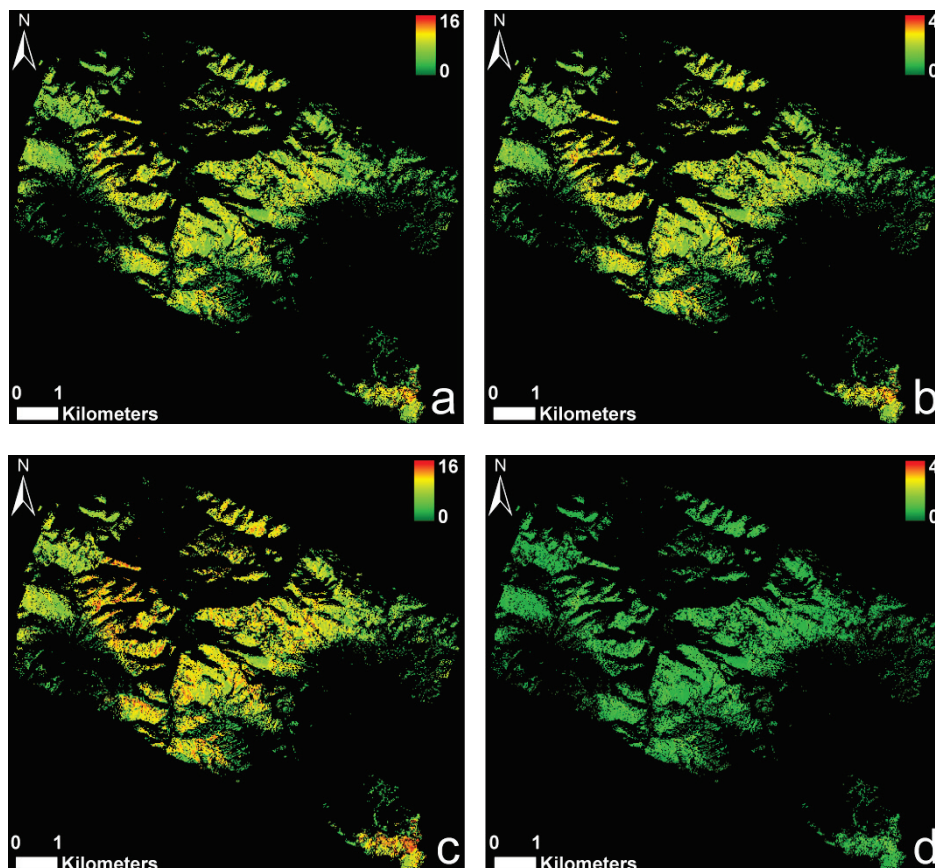


Fig. 5-1 Validation of HL (a), FBH (b), CW (c), SD (d) and PAIe (e) estimates from LiDAR and SPOT-5 data. HL for Lorey's mean height, FBH for first branch height, CW for crown width, SD for stand density and PAIe for effective plant area index.

5.4.2 The d and z_{0m} Maps from Remote Sensing Models

Because the tree heights were available, the four maps of d and z_{0m} , corresponding to the four models, were generated (Fig. 5-2) rather than the fractional maps (d/h 's and z_{0m}/h 's in some previous studies). As input, H_L and the LiDAR and SPOT-5 retrieved data were used.

Overall, the RA94 generated the highest d values with average of 10.61 but lowest z_{0m} values with average of 0.50. On the contrary, NA08 produced the lowest d values with average of 6.82 but highest z_{0m} values with average of 1.57. Both CM88 and SD00 derived the intermediate d and z_{0m} maps with d average of 8.93 and 7.97, and with average z_{0m} of 1.16 and 1.03, respectively. When using the arithmetic mean tree heights instead of H_L , the mean d and z_{0m} values were 6.59 and 0.42, 4.52 and 1.04, 5.91 and 0.77, 4.95 and 0.88, for RA94, NA08, CM88 and SD00, respectively. The overall tendencies and patterns in the maps remained similar, but averaged d and z_{0m} values were lower for all four models than using the H_L .



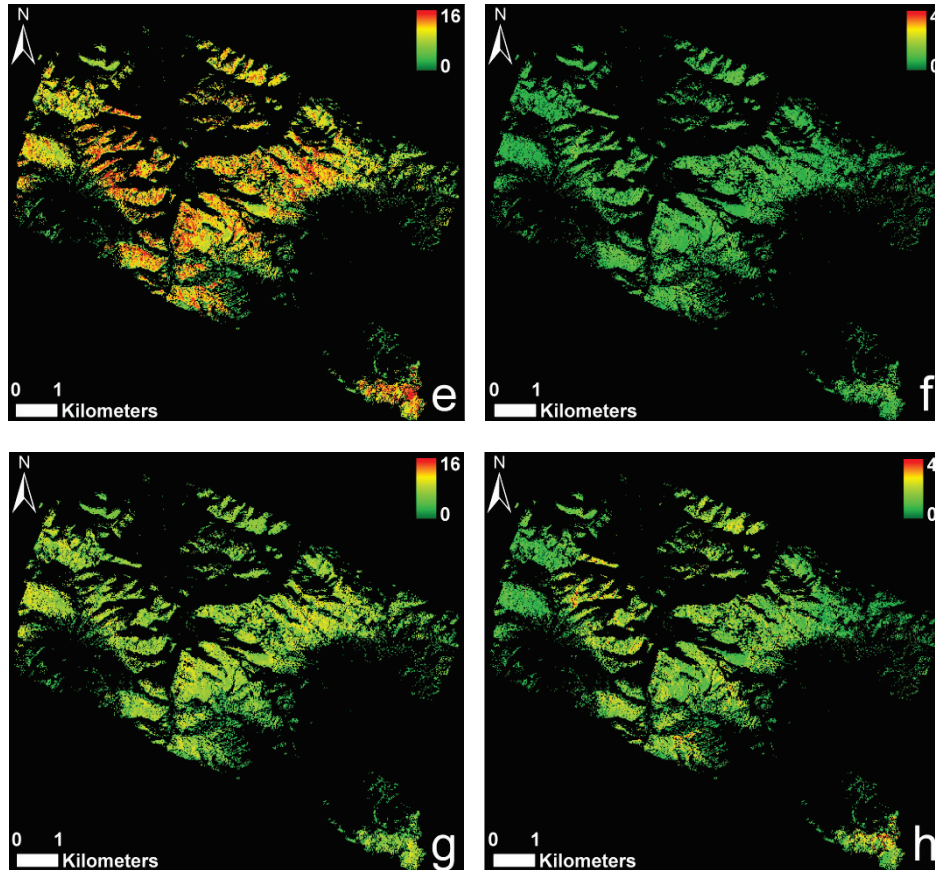


Fig. 5-2 Area-wide d (left) and z_{0m} (right) maps based on CM88 (a, b), RA94 (c, d), SD00 (e, f) and NA08 (g, h) model (unit: meter). CM88, RA94, SD00 and NA08 are the models of Choudhury and Monteith (1988), Raupach (1994), Schaudt and Dickinson (2000) and Nakai et al. (2008), respectively.

5.4.3 Validation and Comparison of d and z_{0m} Results

The results of the four methods for d and z_{0m} estimates at the EC site are shown in

Table 5-5. As input, the forest inventory data, listed in Table 5-4 were used. It turned out that for all methods, and both for d and z_{0m} , it was better to use H_L as representative tree height than H_{avg} . Indeed, the representative tree height of the plot would be better expressed by weighting the tree heights of individual trees with the basal areas than taking an arithmetic mean (Nakai et al., 2008). Furthermore, Nakai et al. (2010) proposed that the cumulative basal area inflection (CuBI) height was better index of aerodynamically-determined canopy height than H_L , because H_L would be prone to a small value if there are a large number of low trees.

But, the CuBI height seemed to be not applicable to some forest plots. For example, in the EC site, only Logistic function and Beta growth function, Eq. (5-4) and Eq. (5-10) in Nakai et al. (2010), can fit the plot of the measured cumulative basal area against ascending tree height, and the other four functions were failed to produce the fitting curve. However, the inflection points of these two fitting curves were unrealistically high with 20.38 and 20.71 m respectively, which were higher than the highest tree with 18.50 m.

Table 5-4 Input parameters based on tree measurements.

Forest parameter	Measurement	LiDAR-SPOT-5 Estimation
Leaf area index	3.44	3.77
Frontal Area Index	1.38	1.48
Stand density	1440(trees ha ⁻¹)	1265(trees ha ⁻¹)
Arithmetical average tree height	9.50(m)	10.50(m)
Weighted average tree height	14.52(m)	14.33(m)

Table 5-5 Comparison of d and z_{0m} from remote sensing models using the site measurements as inputs with the EC measurements (unit: meter).

Method	d with H_{avg}	d with H_L	z_{0m} with H_{avg}	z_{0m} with H_L
CM88	6.32	9.66	0.95	1.46
RA94	7.43	11.36	0.44	0.67
SD00	5.82	8.90	0.84	1.28
NA08	5.67	8.67	1.01	1.54
EC	12.60		1.05	

Table 5-5 shows that the RA94 produced the highest d but lowest z_{0m} at this site, and NA08 generated the lowest d but highest z_{0m} . The other two models rendered intermediate outcomes for both d and z_{0m} . The RA94 was the closest to the EC measurement of d , but underestimated z_{0m} , whereas the SD00 was the closest to the EC measurement of z_{0m} , but underestimated d .

For these reasons, this chapter used H_L for further analyses in this chapter:

$$H_l = \frac{\sum_{i=1}^N H_i * A_i}{\sum_{i=1}^N A_i} \quad (5-33)$$

where H_i is single tree height, A_i is the tree basal area, N is the total of the trees.

In analogy to

Table 5-5, Table 5-6 shows d and z_{0m} for the EC site, now using retrievals from LiDAR and SPOT-5 data as input. It should be noted that the site geographic boundary contains some sub-pixels of remote sensing estimates. Therefore, inside the site boundary, a zonal statistic analysis was performed to extract the average values of input parameters needed in the d and z_{0m} models. Comparing

Table 5-5 and Table 5-6 shows that the values for d and z_{0m} derived with the two input data sets are similar. It did not make a difference whether the LiDAR and SPOT-5 or the field measurements were used as input for the four models. After all, the remote sensing retrievals matched the measurements well (see Table 5-4). The differences among the four models were higher than the differences caused by the input data.

Table 5-6 Comparison of d and z_{0m} from remote sensing models using LiDAR and SPOT-5 estimates as inputs with the EC measurements (unit: meter).

Method	d with H_{avg}	d with H_L	z_{0m} with H_{avg}	z_{0m} with H_L
CM88	7.09	9.67	1.02	1.40
RA94	8.29	11.32	0.46	0.63
SD00	6.60	9.00	0.87	1.19
NA08	6.21	8.58	1.13	1.57
EC	12.60		1.05	

For further analyses, under the condition of only one validation point (the EC station), the histogram and accumulative probability of the relative difference might be the integrative illustration for the mutual area-wide maps' comparison. Although SD00 largely underestimated the d , it reproduced the EC measurement of z_{0m} well. Considering that most land surface models are more sensitive to z_{0m} than to d , this chapter used d and z_{0m} values from SD00 as the references to calculate the relative difference and to cross-compare the models,

$$S_{rd} = \frac{|S_v - S_{SD00}|}{S_{SD00}} \quad (5-34)$$

where S_{rd} is the relative difference of d or z_{0m} , S_{SD00} is the SD00 modeled d or z_{0m} and S_v is the derived d or z_{0m} from the other three models.

Then, the d and z_{0m} values of each pixel in the maps of SD00 and other three models were used to generate the d and z_{0m} relative difference maps by Eq. (5-34). The statistical information of these relative difference maps was shown by their histograms and accumulative probability density curves (see Fig. 5-3).

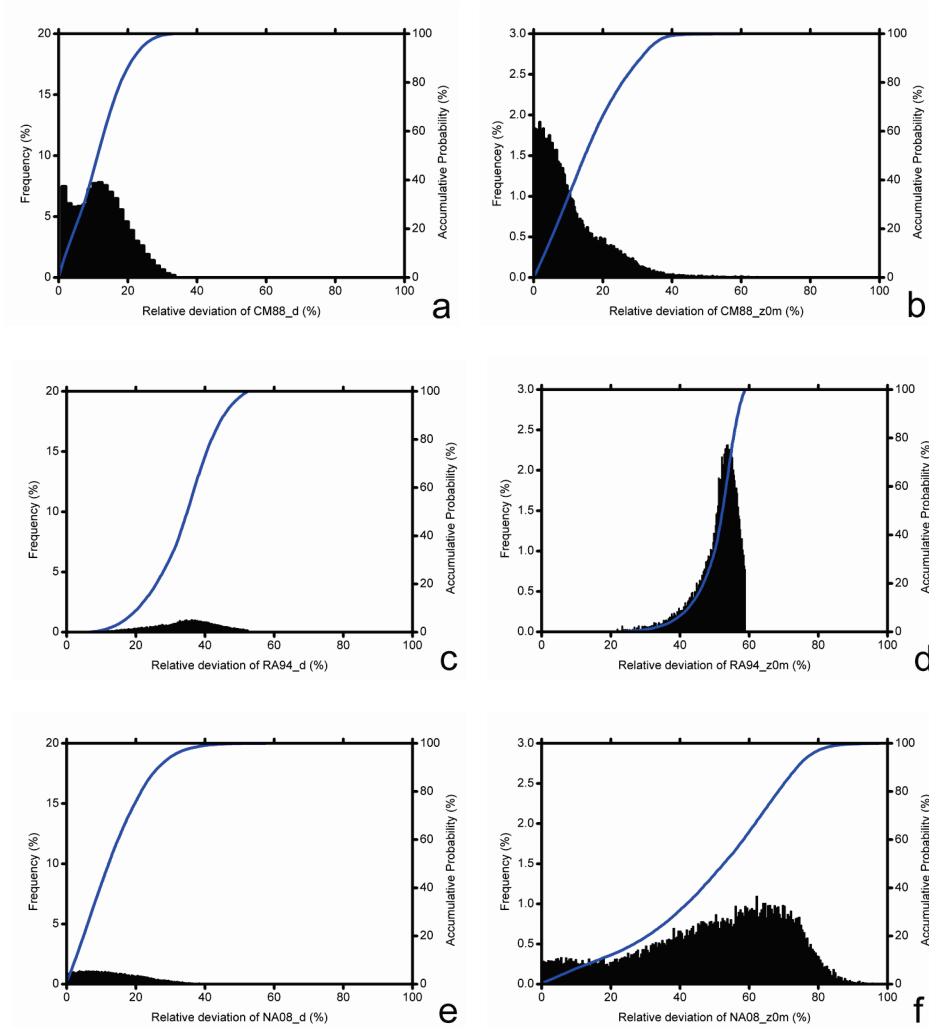


Fig. 5-3 Histograms (black column) and accumulative probability (blue line) of relative difference of d (left) and z_{0m} (right) from CM88 (a, b), RA94 (c, d) and NA08 (e, f) on basis of SD00 estimates.

By analyses of these information, as a whole, for CM88, the relative difference of d (dr_d) was moderate with mean (\bar{u}) = 0.13, standard deviation (σ) = 0.08, but the relative difference of z_{0m} (dr_{z0m}) (\bar{u} = 0.17 and σ = 1.08) was lowest among them. Contrarily, NA08's dr_d (\bar{u} = 0.14, σ = 0.09) was lowest but the dr_{z0m} (\bar{u} = 0.50, σ = 0.21) was similar to dr_{z0m} (\bar{u} = 0.51, σ = 0.06) of RA94 which generated the highest dr_{z0m} (\bar{u} = 0.34, σ = 0.09). The accumulative probability density functions of the differences dr_d and dr_{z0m} , showed that 95% of the area had values of dr_d and dr_{z0m} below 26% and 36% for CM88, below 48% and 57% for RA94, and below 31% and 77% for NA08.

5.5 Discussion

In this chapter, the statistics of the cloud point of LiDAR measurements were used to retrieve the vertical structure of the canopy. A more accurate alternative is to use high-density airborne LiDAR cloud points or full waveform LiDAR observations. In this way sufficient information on individual trees could be derived. The disadvantage of this approach is that a single flight was insufficient: more overpasses were needed.

As the remote sensing d and z_{0m} models concerned, the LAI based model, CM88, was originally designed for agriculture, thus it might be more applicable in low vegetation area than in high canopy cover. For herbaceous plant or crop, CM88 could represent the roughness element density by LAI, but, for forest, there is no clear relationship between roughness element density (here refers to SD) and LAI. However, according to CM88, z_{0m}/h will monotonically decrease with increasing LAI. It has been well recognized that z_{0m} widely varies (Shaw and Pereira, 1982; Garratt, 1994). It would decline when the canopy aggregates and the high foliage density opposes a resistance to the airflow, as the airflow exerts drag only near the top of the canopy. Conversely, when the canopy becomes sparser, the drag would reduce again. Therefore, z_{0m} should peak at some intermediate value of the roughness element density (Schautd and Dickinson, 2000). Schautd and Dickinson (2000) illustrated this kind of z_{0m} variation with LAI and f_c in forest area and Zhou et al. (2006) also figured out it in both experimental agriculture and forest sites.

For RA94, there is also the analogous problem to express the roughness element density by FAI. The experiments of Raupach (1994) were mainly carried out on dense vegetation or solid blocks, and might not be well suited for sparse roughness element (Schautd and Dickinson, 2000). For uniformly distributed forest with homogeneous canopy shape, FAI might be proportional to the tree density. Due to the complexity of the canopy shapes and overlaps of the crowns, it is hard to determine the relationship between FAI and the density. Moreover, the site dependent coefficients (i.e. a_1 - a_3 , b_2 , b_3 , c_2 , c_3 , d_2 , d_3 in RA94) might be suitable at the specific patches, but probably be invalid at elsewhere.

A generally applicable model would probably consider more factors affecting the d and z_{0m} , such as limiting infinite LAI by FAI (as in SD00), and inter-site difference presented by SD and seasonal variations depicted by LAI (as in NA08). As NA08's z_{0m} expression was established by linear fitting the observed d/h against z_{0m}/h , the site calibrated coefficient might be not appropriate to this site. SD00 also involves site dependent coefficients, as it was developed on basis of RA94. Although, the SD00 produced the most close z_{0m} to the EC observation, but it underestimate the d

to a large extent as well. It might be explained by that, as the EC tower is surrounded by mountains which are close to (about several hundred meters) and higher than the tower, the winds could be elevated by them.

It is necessary to stress that, although DSM and DEM from LiDAR were used to retrieve the height quantiles, the effect of topography on d and z_{0m} was not taken into account in this chapter. For the models using FAI (RA94 and SD00), the computation of FAI should consider the variation of the elevation. Moreover, the shape of frontal surface perpendicular to the airflow depends on the wind direction and then FAI will fairly vary. To analyze the topographic and wind directional effects, the footprint of the EC tower should be determined firstly. For this purpose, high-density LiDAR data covering the EC tower could be used, as this can provide precise individual tree structural information. The local landscape and topography is very complex, and therefore, a careful analysis of high-density LiDAR data would be required. This is beyond the scope of this chapter. It could also be of interests if the performances of geometrical models (i.e. RA94, SD00) and those of computational fluid dynamics models are cross-compared.

Generally, a better model performance at the site scale does not mean a wider applicability. For regional retrieval the crucial point is whether the model inputs can be retrieved with sufficient accuracy from remote sensing. Once the robust relevant vegetation structural parameters can be derived by remote sensing method, such as applying interferometric Synthetic Aperture Radar (InSAR) and polarimetric interferometric SAR (POLInSAR) techniques for satellite SAR data, analyzing point cloud or waveform data from satellite vegetation canopy LiDAR, these kinds of remote sensing d and z_{0m} models can be practically applied at regional scale. In advance to that, this chapter explored to take the advantages of LiDAR point cloud in providing precise three-dimensional information and SPOT-5 imagery in high spatial resolution and multi-spectral information to derive the area-wide d and z_{0m} maps.

Besides the bio-spatial maps including H_L , FBH, CW, SD and LAI retrievals needed by the land surface model, maps of d and z_{0m} can improve eco-hydrological process simulation for the local watersheds. In the study area, eco-hydrological processes in Dayekou and Pailugou watersheds are much critical for the following reaches supported by upper snow-melting water resource. Moreover, these high resolution thematic maps are directly applicable for the d and z_{0m} up-scaling study. These in turn are very important for estimating the regional heat transfer when the medium resolution satellite data (i.e. Landsat TM, ASTER, MODIS) are applied by remote sensing energy balance models such as SEBS (Su, 2002).

5.6 Conclusion

This chapter presented the first study to apply airborne LiDAR point cloud data and satellite SPOT-5 image to estimate the d and z_{0m} . Based on four models (CM88, RA94, SD00, and NA08), the generated area-wide d and z_{0m} maps are more applicable than the normalized d/h and z_{0m}/h maps which were normally retrieved from satellite remote sensing data with absence of roughness element height information.

At the forest site, using the inventoried forest structural data, it was tested by EC measurements that, using H_L , all models performed much better than using the average tree height. Using representative roughness height, among all the model's performances, SD00 outperformed the others in estimating z_{0m} , but it estimated d much lower, and RA94 performed most closely to the measurement in retrieving d , but it rendered the lowest outcome of z_{0m} . The lowest d but largest z_{0m} estimates came from the NA08. CM88 it produced intermediate values of d and z_{0m} .

Reasonable H_L ($R^2 = 0.77$), FBH ($R^2 = 0.50$), CW ($R^2 = 0.59$) and SD ($R^2 = 0.47$) estimates were derived by the regression models related to the height quantiles and f_c from low-density LiDAR point cloud data. Taking the effects of tree trunk, branch and leaf cluster into account, LAI was calculated by multiplying experimental adjustment coefficient (1.15) and inversed PAIe ($R^2 = 0.75$) from synthesis of high-density LiDAR (small area) and SPOT-5 data (large area) based on linear spectrum decomposition and Li-Strahler models. Subsequently, using these retrievals, the four remote sensing d and z_{0m} models were applied to retrieve the area-wide d and z_{0m} maps. During this process, the tendency of each model behaviour coincided to its former performance driven by forest measurements at the site.

For the comparisons of their entire maps, histograms of relative deviation, using the SD00 as a reference, were analyzed by their statistics information and accumulative probability distributions. On the whole, the variances of other three models compared with the SD00 maps complied with the tendencies as those from site comparisons carried out by both measurement and remote sensing derived results.

Chapter 6

Simulation of Evapotranspiration Using Time-Series
Parameterization of The Surface Energy Balance System
(SEBS) Over Forests Within The Qilian Mountains^{*}

^{*} This chapter is based on:

Tian, X., van der Tol, C., Su, Z. B., Li, Z. Y., Chen, X. L., Yan, M., Li, X., Chen, E. X., Li, L. H., Wang, X. F., Pan, X. D., Ling, F. L., Li, C. M., & Fan, W. W. Simulation of evapotranspiration using time-series parameterization of the Surface Energy Balance System (SEBS) over forests within the Qilian Mountains. *In Submission*

Abstract

Many remote sensing based land surface models resolve evapotranspiration (ET) from land surface energy balance, using land surface temperature (LST) as the primary input. These models are typically very sensitive to the surface roughness, a parameter that is difficult to estimate, especially for forests. This chapter proposes a long-term parameterization scheme for two critical roughness parameters, zero-plane displacement height (d) and aerodynamic roughness length (z_{0m}), which this study further uses in the Surface Energy Balance System (SEBS). First, regression relationships between forest vertical parameters (Lorey height and the frontal area index (FAI)) and measured forest above-ground biomass (AGB) were calibrated. Next, interannual Lorey height and FAI values were derived from regression models and corresponding forest AGB dynamics simulated from synergistic simulations based on two ecological models (the MODIS MOD17 (MOD_17) GPP and the Biome-BioGeochemical Cycles (Biome-BGC) models) and a forest basis map for 2009 obtained from the Landsat Thematic Mapper 5 (TM). Using refined eight-day Global LAnd Surface Satellite (GLASS) LAI products, these dynamic forest vertical parameters were applied for estimating eight-day d and z_{0m} values. d and z_{0m} values were further inputted into the kB^{-1} model in order to derive the heat roughness length (z_{0h}) values. With the incorporation of original MODIS products (the Normalized Difference Vegetation Index (NDVI) and land surface temperature (LST)), refined GLASS Albedo products, and downscaled meteorological estimates obtained from the Weather Research and Forecasting (WRF) model, the SEBS model was used to simulate long-term forest ET from 2000 to 2012 within the Qilian Mountains (QMs). As compared with MODIS MOD16 ET (MOD16_ET) products, ET estimates from the SEBS agreed much better with Eddy Covariance (EC) measurements (a $R^2 = 0.80$ and a RMSE = 0.21 mm day^{-1}). The results of SEBS in estimating ET performs well if the variability of forest roughness parameters is taken into account.

6.1 Introduction

The hydrological cycle is critical for the function and sustainability of terrestrial ecosystems (Bouwer et al., 2008). As the principle component of terrestrial hydrology, evapotranspiration (ET) is affected by both biophysical and environmental processes at the interface of soils, vegetation, and the atmosphere, thereby linking hydrological, energy and carbon processes (Fisher et al., 2008; Jung et al., 2010; Liu et al., 2013). Globally, ET returns approximately 60% of land-based precipitation to the atmosphere (Oki and Kanae, 2006; Trenberth et al., 2007) and consumes more than 50% of the solar radiation absorbed by the land surface (Trenberth et al., 2009). Through ET and photosynthesis, ET is dynamically connected with water, energy and carbon processes. Therefore, within the atmospheric surface layer, ET affects environmental conditions through the turbulent exchange of momentum, heat, and moisture (Molders and Raabe, 1996; Koster et al., 2004; Spracklen et al., 2012). In return, environmental variation controls diverse physical and eco-physiological processes within terrestrial ecosystems and, finally, alters the mass and energy exchange of land-atmosphere interactions leading to direct climate impacts (Jung et al., 2010; Githui et al., 2012; Campos et al., 2013; Keenan et al., 2013). Considering the importance of ET, the characterization of its spatiotemporal variability is critical for better understanding interactions between the land and atmosphere, the sustainable management of water resources, and the response of terrestrial ecosystems under climate change (Wang et al., 2009, 2013b; Yuan et al., 2010; Fisher et al., 2011; Zeng et al., 2012).

As one of the most important parts of the terrestrial ecosystem, global forests account for approximately 45% of total terrestrial ET (Oki and Kanae, 2006). Under conditions of global warming, forest ET has been considered to be an important indicator of water availability in natural ecosystems as well as for human needs (Jackson et al., 2001). In particular, the routine monitoring of the forest ET in the headwaters of basins is critical, because these headwaters often provide water to ecosystems downstream. Knowledge of the dynamics of the headwaters is therefore relevant for the sustainable development of entire basins. The water supply in the cold and arid Heihe River Basin (HRB) located in northwestern China is entirely dependent on its headwaters, and water conflicts are severe and information regarding forest processes is urgently needed.

In situ measurements using weighing lysimeters, Bowen ratios, sap flow meters, Eddy Covariance (EC) and scintillometers are considered reliable for quantifying ET individual sites or small footprints (Li et al., 2009b; Wang and Dickinson, 2012; Liu et al., 2013). However, these types of measurements are unsuitable for large

scales. An alternative approach is to use remote sensing information in order to characterize spatiotemporal land surface information over large areas. With the incorporation of meteorological and other auxiliary data, remote-sensing-based methods can map various large-scale patterns of ET in a globally consistent and economically feasible manner by linking surface parameters and energy balance with ET (Kustas and Norman, 1996; Su, 2002; Ju et al., 2010; Yang et al., 2012). In general, land surface parameters retrieved from remote sensing data such as the Normalized Difference Vegetation Index (NDVI), the leaf area index (LAI), Albedo, temperature and Emissivity have been used to drive ET models (Yuan et al., 2010; Ryu et al., 2011).

The following four types of remote-sensing-based ET models having been developed in the past few decades: 1) surface energy balance models (Bastiaanssen et al., 1998; Su, 2002; Miralles et al., 2011; Anderson et al., 2012), 2) empirical statistical models (Wang and Liang, 2008), 3) physical models (Mu et al., 2007; Zhang et al., 2010a) and 4) water balance models (Rodell et al., 2011; Sahoo et al., 2011). Although they have been applied over a number of study areas, uncertainties related to the disadvantage of these models and their inputs, and parameterization and scaling schemes still exist (Su et al., 2006; Fernández-Prieto et al., 2012; Jia et al., 2012; Liu et al., 2013; Chen et al., 2013; Chen et al., 2014). As far as remote sensing techniques are concerned, the availability of measurements or simulations of land surface and atmospheric parameters has been increasing, and the improvement of model performance through the integration of various techniques and data sources has received renewed global interest.

As one of the most widely used and validated ET models, the Surface Energy Balance System (SEBS) developed by Su (2002) estimates turbulent heat fluxes by means of Monin-Obukhov Similarity (MOS) theory (Monin and Obukhov, 1954; Foken, 2006). Several important parameters are a part of MOS and SEBS including zero-plane displacement (d), roughness height (z_{0m}), and heat roughness height (z_{0h}). The scalar z_{0h} can be calculated from z_{0m} using the kB^{-1} model that provides excess resistance for heat transfer. For d and z_{0m} , experimental methods based on measurements of turbulent fluxes can provide estimates, but are only locally valid and cannot be scaled to larger areas. Alternatively, remotely sensed methods have been developed for these parameters using functions of vegetation structural parameters (i.e., LAI, (Choudhury and Monteith, 1988), frontal area index (FAI) (Raupach, 1994), both LAI and FAI (Schmidt and Dickinson 2000), stand density (SD) (trees ha⁻¹) and stem-branch-leaf distributions (Nakai et al., 2008)). For the kB^{-1} model, some studies have improved its parameterization (Su et al. 2001; Yang et al., 2002; Chen et al., 2013b). However, few have focused on forests.

The previous study in **Chapter 5** demonstrated the advantages and disadvantages for four notable models for retrieving d and z_{0m} values in forests located within the Qilian Mountains (QMs), the headwater area of the HRB. A key parameter needed for d and z_{0m} estimates is forest height. Other vegetation structure parameters further affect the ratios of d or z_{0m} over forest height (d/h or z_{0m}/h) to vegetation structural parameters. In combination with forest measurements, remote sensing is capable of providing reliable instantaneous retrievals of forest heights that can be used to parameterize d and z_{0m} models on certain time scales when forest structural parameters (height, LAI, FAI, etc.) and thus d/h or z_{0m}/h are assumed to be unchanged. For long-term parameterization, LAI can easily be obtained from moderate resolution remote sensing data (i.e., MODIS) within a fine time resolution. However, the time-series retrieval for other parameters is a problem, especially for young and immature forests. Normally, the structure (including height and FAI) of young and immature forests greatly changes within a few years. If constant structural information is used to parameterize the d , z_{0m} and z_{0h} , then uncertainties will be propagated into ET due to the sensitivity of ET to these parameters in models such as SEBS.

This chapter proposes a time-series parameterization scheme for d , z_{0m} , and z_{0h} using a combination of forest AGB dynamics and remote sensing data. Specifically, the use of regression relationships for forest vertical parameters (forest height, actually the Lorey's mean height (Lorey, 1878), and FAI) versus forest AGB were established based on measurements. Thus, interannual vertical parameters from 2000 to 2012 were connected with the corresponding forest AGB dynamics obtained from the synergistic simulations in **Chapter 4**. The refined MODIS LAI products from the Global Land Surface Satellite (GLASS), together with these vertical parameters were applied in order to parameterize d , z_{0m} , and, then, z_{0h} using the outperforming roughness model determined in **Chapter 5** and the kB^{-1} model. Afterward, the original MODIS products (NDVI and LST), the refined GLASS Albedo products, and downscaled weather research and forecasting (WRF) simulations were applied in order to drive the SEBS so that estimates for forest ET over the QMs, from 2000 to 2012, were obtained. Finally, two-year (2010-2011) comparisons amongst MODIS MOD16 ET (MOD16_ET) products, SEBS ET outputs and EC measurements were conducted.

6.2 The Observations and Study Data

The EC and forest inventory measurements used in this chapter were the same as those in **Section 4.2**. The major input variables for SEBS include meteorological data (air temperature, wind speed, air and vapor pressures, and downwelling shortwave and long-wave radiation), and land surface parameters (LAI, LST,

Albedo and NDVI). Meteorological forcing data for the HRB downscaled from estimates of the WRF model by using the meteorological model (MicroMet) (Liston et al., 2006), were used in this study. Past experiments have determined that the data is reliable (Pan and Li, 2011; Pan et al., 2012). Land surface parameters were derived from MODIS data. Innovative MODIS products including LAI and Albedo were obtained from GLASS (<http://glass-product.bnu.edu.cn>) (Liang et al., 2013), and others including NDVI and LST were downloaded from the National Aeronautics and Space Administration (NASA) (<http://ladsweb.nascom.nasa.gov>). To perform multiple comparisons, 1 km, eight-day MOD16_ET products obtained from 2000 to 2012 were downloaded from the Numerical Terradynamic Simulation Group (NTSG) (<http://www.ntsg.umt.edu/project/mod16>) of the University of Montana.

6.3 Methodology

6.3.1 The Surface Energy Balance System

SEBS is an advanced single source model developed by Su (2002) for estimating turbulent heat fluxes based on energy balance (EB) and employs the evaporative fraction (ETF) for estimating actual ET (AET) by accounting for water limiting (wet-limit and dry-limit) cases (wetness and dryness). Briefly, SEBS consists of the functions of land surface parameters derived from remote sensing data, a model of dynamic roughness lengths with a reference to heat transfer, and the determination of ETF.

Abiding by the theories of EB, bulk atmospheric similarity (BAS) (Brutsaert, 1999) and MOS (Monin and Obukhov, 1954), based on a combination of physical land surface parameters obtained from remote sensing data and meteorological forcing data, SEBS has proven to be a reliable remote-sensing-based ET model in numerous studies conducted over multiple ecosystems and under various climate and landscape conditions (Su, et al., 2005; Pan et al., 2008; Sobrino et al., 2013; Chirouze et al., 2014; Ma et al., 2014; Pardo et al., 2014). However, few studies have focused on forests (Zhou et al., 2006; Ershadi et al., 2014; Zhuo et al., 2014), especially those located in cold and arid regions.

A concise description of the SEBS algorithm is provided below. Details can be found in Su (2002). Basically, the surface energy balance is expressed as follows:

$$R_n = G_0 + H + \lambda E \quad (6-1)$$

where G_0 is the soil heat flux; R_n is the net radiation; H is the sensible heat flux; and λE is the latent heat flux (λ is the latent heat of vaporization ($J g^{-1}$) and E is the AET). Surface available energy ($H+\lambda E$) is generally used to partition the energy

exchange for heat and water vapor. The unit for Eq. (6-1) is watts per square meter (Wm^{-2}).

To derive sensible and latent heat fluxes, the theory of BAS (for the mixed layer of the atmosphere) or MOS (for the atmospheric surface layer (ASL)) was employed. In most cases, MOS relationships for profiles of mean wind speed, u (ms^{-1}), and mean temperature, $\theta_0 - \theta_a$, were applied in SEBS, and the integral form was written as follows (Monin and Obukhov, 1956):

$$u = \frac{u_*}{k} \left[\ln\left(\frac{z-d}{z_{0m}}\right) - \Psi_m\left(\frac{z-d}{L}\right) + \Psi_m\left(\frac{z_{0m}}{L}\right) \right] \quad (6-2)$$

$$\theta_s - \theta_a = \frac{H}{ku_* \rho c_p} \left[\ln\left(\frac{z-d}{z_{0h}}\right) - \Psi_h\left(\frac{z-d}{L}\right) + \Psi_h\left(\frac{z_{0h}}{L}\right) \right] \quad (6-3)$$

where u_* is the friction velocity (m s^{-1}) calculated as $(\tau_0/\rho)^{1/2}$; τ_0 is the surface shear stress (kg m s^{-2}); ρ is the air density (kg m^{-3}); $k = 0.41$ is von Karman's constant; z is the height of the measurement; d is the zero displacement height (m); z_{0m} is the aerodynamic roughness length for momentum transfer; θ_0 is the potential temperature (K) at the surface; θ_a is the potential air temperature (K) at z ; c_p is the specific heat capacity of air at constant pressure ($\text{J kg}^{-1} \text{K}^{-1}$); z_{0h} is the roughness height for heat transfer (scalar); and Ψ_m and Ψ_h are the stability correction functions for momentum and heat transfer. L is the Obukhov length (m) defined, as follows:

$$L = -\frac{\rho c_p u_*^3 \theta_v}{kgH} \quad (6-4)$$

where g is the acceleration of gravity (m s^{-2}) and θ_v is the atmospheric virtual potential temperature (K).

Obviously, both the zero-plane displacement height (d) and the roughness lengths (z_{0m} and z_{0h}) are critical parameters for determinations of momentum and heat transfer between the land surface and the atmosphere. The kB^{-1} model linking z_{0m} to z_{0h} is expressed as follows:

$$z_{0h} = \frac{z_{0m}}{\exp(kB^{-1})} \quad (6-5)$$

where kB^{-1} is a scalar heat transfer coefficient called the inverse Stanton number.

In SEBS, Su (2002) proposed kB^{-1} as follows:

$$kB^{-1} = f_c^2 kB_{fc}^{-1} + 2f_c f_s kB_{fcfs}^{-1} + f_s^2 kB_{fs}^{-1} \quad (6-6)$$

where f_c is the fractional canopy coverage and f_s is that of soil; kB_{fc}^{-1} represents the canopy; kB_{fs}^{-1} represents bare soil; and kB_{fcfs}^{-1} represents mixed bare soil and canopy.

The energy balance of a limiting case at dryness and wetness are then used to estimate the relative evaporative fraction (Λ_r), as follows:

$$\Lambda_r = 1 - \frac{H - H_{wet}}{H_{dry} - H_{wet}} \quad (6-7)$$

where H_{wet} is H at wetness and H_{dry} is dryness. Both were estimated as described in Su (2002).

The evaporative fraction (Λ) is calculated as follows:

$$\Lambda = \frac{\lambda E}{R_n - G_0} = \frac{\Lambda_r \times \lambda E_{wet}}{R_n - G_0} \quad (6-8)$$

where λE_{wet} is λE at wetness.

Finally, λE is determined by the following equation:

$$\lambda E = \Lambda \times (R_n - G_0) \quad (6-9)$$

In practice, the remote sensing data used in SEBS represents instantaneous information of the land surface. The evaporative coefficient is assumed to be constant throughout the day, and, finally, daily evapotranspiration is expressed, as follows:

$$E_{daily} = \sum_{h=0}^{24} \left[\Lambda \times \frac{(R_n - G_0)}{\lambda \rho} \right] = 8.64 \times 10^7 \times \Lambda \times \frac{\overline{R_n} - \overline{G_0}}{\lambda \rho} \quad (6-10)$$

where E_{daily} is the daily ET (mm d^{-1}) and $\overline{R_n}$ and $\overline{G_0}$ are the mean daily net radiation (Wm^{-2}) and mean daily soil heat fluxes that can be assumed to be negligible for the entire day.

In brief, SEBS generally requires two sets of driving data, remotely sensed land surface parameters (for example, Albedo, LST, LAI and NDVI) and meteorological data (for example, air temperature, wind speed, air and vapor pressures, and downwelling shortwave and long-wave radiation).

6.3.2 Roughness Length Models

Based on the aforementioned importance of d , z_{0m} and z_{0h} , the parameterization scheme should first optimize d and z_{0m} through use of the roughness model and z_{0h} through use of the kB^{-1} model. The process of estimating d and z_{0m} was validated using EC measurements in our previous study. The model of Schaudt and Dickinson (2000) (SD00) indicated superiority for estimating z_{0m} but was compromised for d . Since ET estimates are more sensitive to z_{0m} and z_{0m} directly affects the z_{0h} value, the SD00 model was employed to parameterize d and z_{0m} . Three parameters, including forest height, LAI and FAI, are required for the SD00 model (see **Section 5.3.1**)

6.3.3 Long-Term Parameterization for SEBS

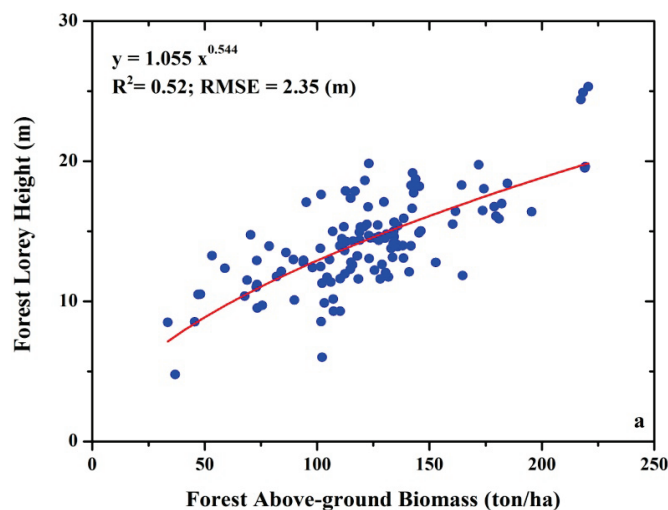
For dynamic parameterization of d , z_{0m} , and, thus, z_{0h} , the long-term (from 2000 to 2012) eight-day GLASS LAI products were directly inputted into the SD00 model. No remote sensing products for forest height and FAI are currently available although these products could be retrieved from a combination of multi-temporal remote sensing data and corresponding forest measurements with short time intervals (at least several years intervals, i.e., 3-5 years). Due to the limited accessibility of forest areas, comprehensive forest measurements over the QMs at such short time intervals are impractical.

To derive long-term forest vertical parameters, forest Lorey height and FAI, regression relationships were first established between these parameters and forest AGB based on field survey measurements. As a result of these two regression models (Lorey height versus AGB and FAI versus AGB), the interannual forest Lorey height and the FAI were then regressed using interannual forest AGB dynamics from the study in **Chapter 4**.

6.4 Results

6.4.1 The Parameterization of SEBS

Forest Lorey height was fitted against forest AGB based on both the DBH and tree height measurements from 119 plots (out of the total 133 plots). FAI versus forest AGB was based on tree height, FBH and crown width measurements from 70 plots (Fig. 6-1).



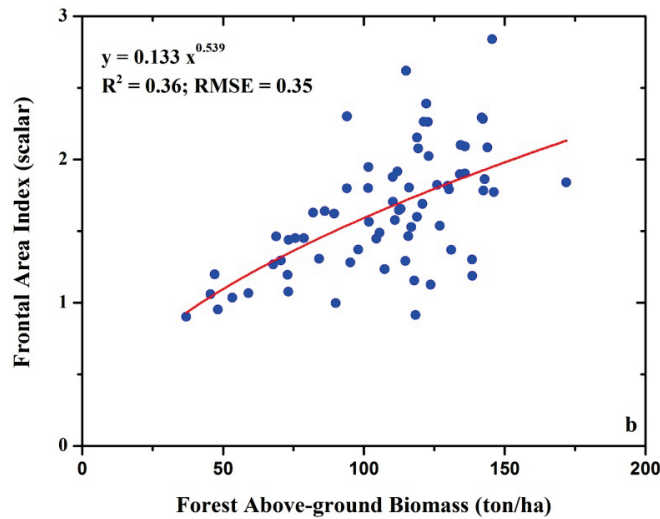


Fig. 6-1 The fitting regression of forest Lorey height (a) and FAI (b) against forest AGB based on measurements.

For Lorey height, the fitting regression was:

$$Y_L = 1.055 \times X^{0.544} \quad (6-11)$$

with $R^2 = 0.52$ and $RMSE = 2.35$ meters.

For FAI, the fitting regression was, as follows:

$$Y_{FAI} = 0.133 \times X^{0.539} \quad (6-12)$$

with $R^2 = 0.36$ and $RMSE = 0.35$ (scalar).

Interannual forest Lorey height and FAI parameters were derived from Eqs. (6-11) ~ (6-12), and corresponding forest AGB dynamics. Afterwards, eight-day GLASS LAI products were applied into SD00 model to estimate corresponding eight-day d and z_{0m} , d and they were further applied in order to estimate eight-day z_{0h} values using the kB^{-1} model.

6.4.2 A Comparison of ET Estimates between EC Measurements, SEBS Simulations and MODIS MOD16 Products

By incorporating original eight-day MODIS products (NDVI, LST), eight-day GLASS Albedo products, and the downscaled WRF estimates (air temperature, wind speed, air and vapor pressure, and downwelling shortwave and long-wave radiation), the parameterized SEBS was employed to simulate eight-day ET from 2000 to 2012. Comparisons amongst the eight-day average ET estimates during 2010 and 2011 from EC, SEBS and MODIS products are shown in Fig. 6-2. Validated using EC measurements, the parameterized SEBS generated reliable eight-day average ET with a $R^2 = 0.80$ and a $RMSE = 0.21 \text{ mm day}^{-1}$. The

MOD16_ET model biased the simulations with a $R^2 = 0.35$ and a RMSE = 0.76 mm day⁻¹.

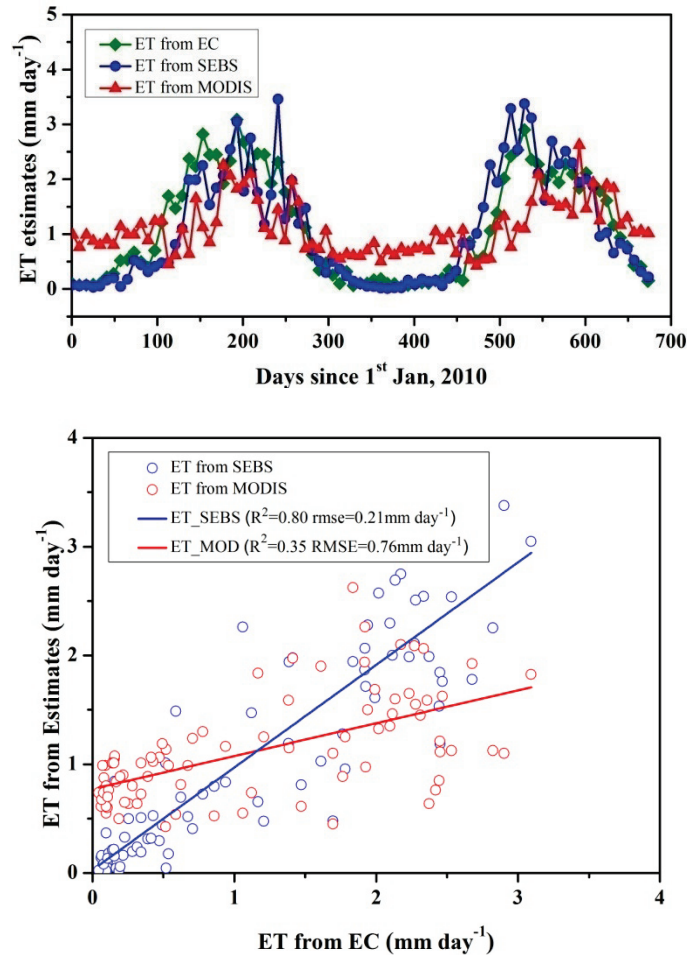


Fig. 6-2 Validation of the eight-day average SEBS simulated ET by EC measurements.

SEBS slightly underestimated ET during the forest growing seasons (summer and autumn) during 2010 but overestimated ET for the growing seasons during 2011. Clearly, the MOD16_ET model largely underestimated ET for the growing seasons but significantly overestimated ET during the spring seasons when SEBS matched well with EC measurements.

6.4.3 Interannual ET Simulations Using SEBS

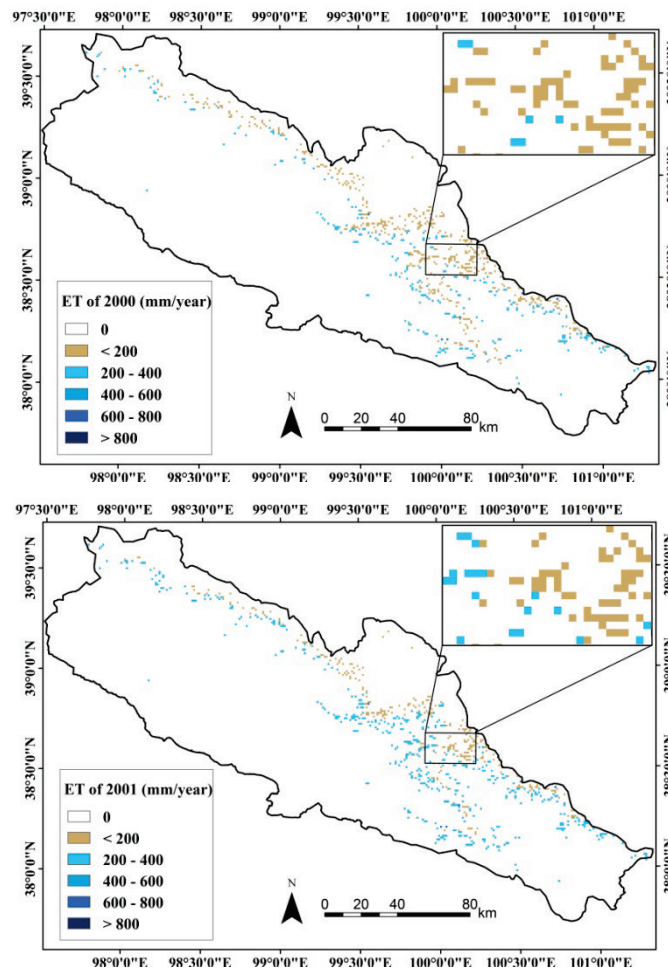
Interannual annual ET averages QM forests are listed in Table 6-1. This table shows that the highest annual average of forest ET (316.73 mm) occurred during 2003 and

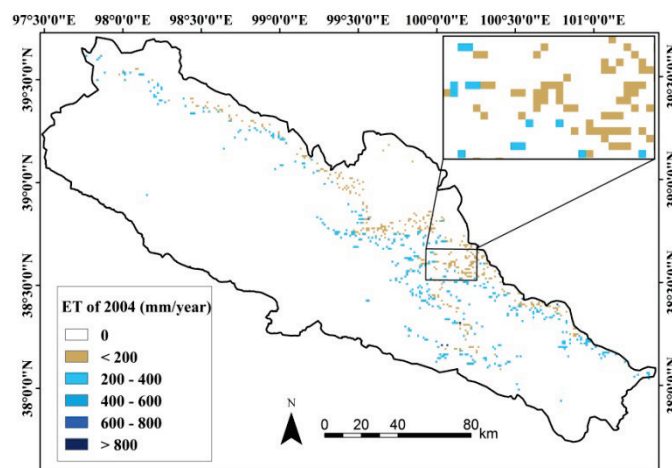
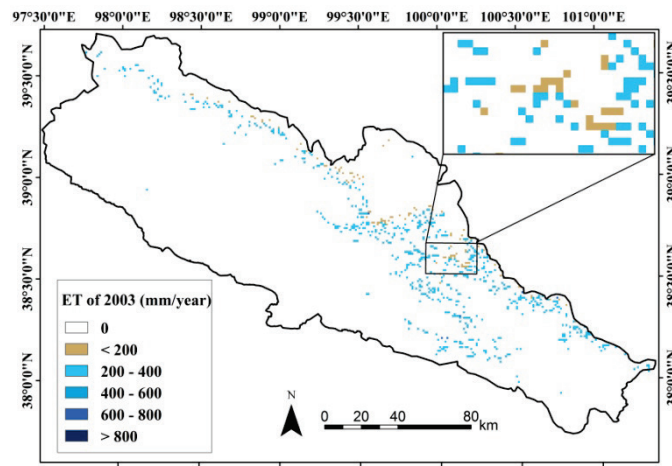
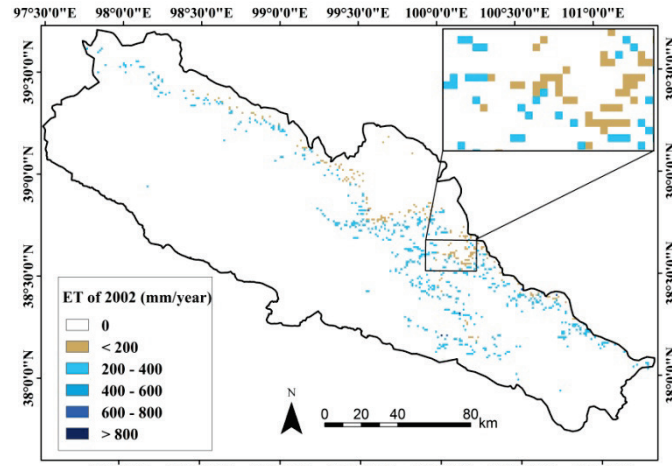
Simulation of Evapotranspiration Using SEBS

the lowest (201.60 mm) occurred during 2009. Corresponding forest ET dynamics of from 2000 to 2012 are provided in Fig. 6-3.

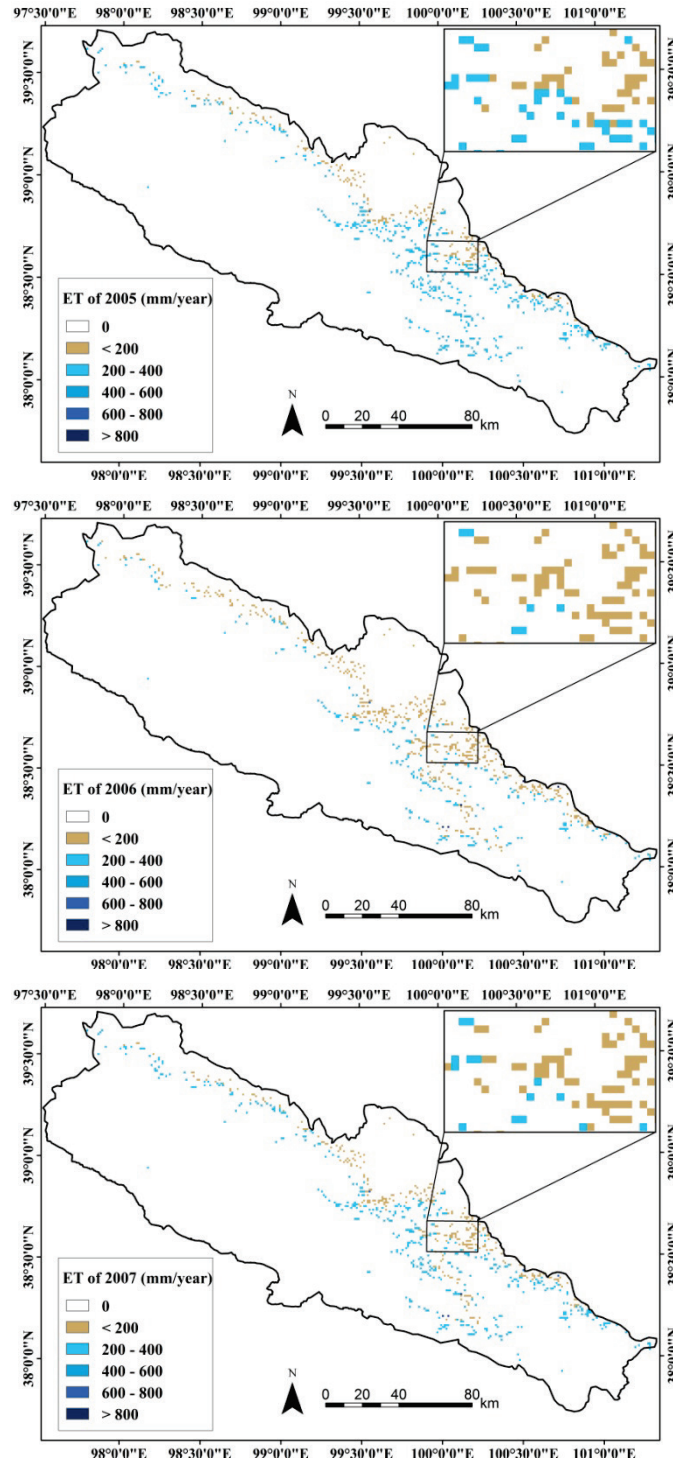
Table 6-1 The statistics for interannual forest ET averages (ET) (unit: mm) simulated by SEBS over the QMs from 2000 to 2012.

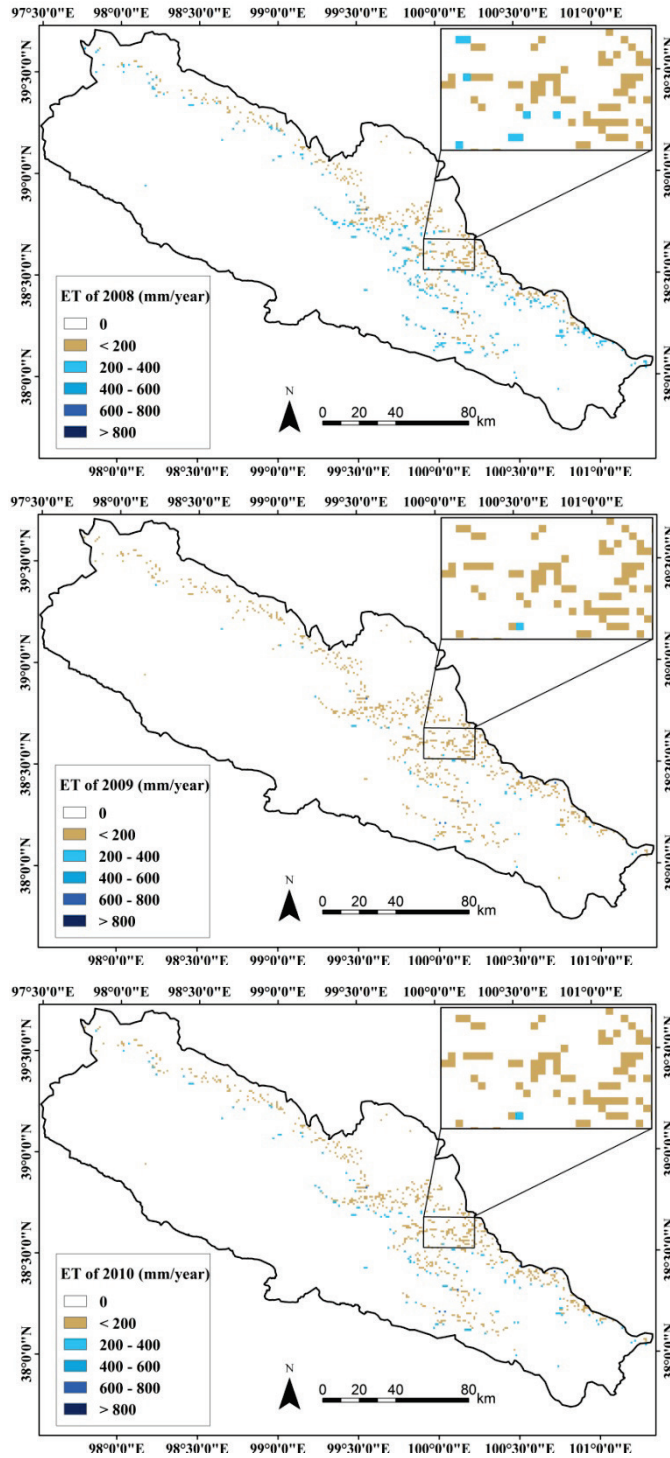
Year	2000	2001	2002	2003	2004	2005	2006
ET	244.14	281.23	299.21	316.73	271.24	289.60	247.60
Year	2007	2008	2009	2010	2011	2012	
ET	277.37	254.53	201.60	221.86	236.39	289.67	





Simulation of Evapotranspiration Using SEBS





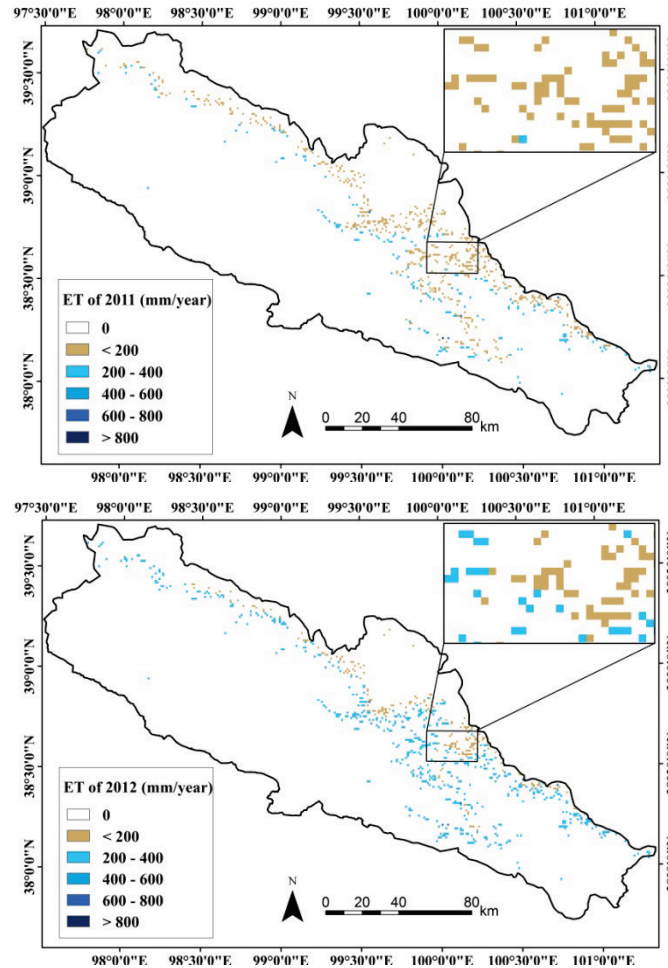


Fig. 6-3 Interannual dynamics of forest ET simulated by SEBS over the QMs from 2000 to 2012.

6.5 Discussion

The zero-plane displacement height (d) and aerodynamic roughness length (z_{0m}) have been widely used in ET models that include MOS theory, such as the SEBS model. As indicated by previous studies (Schmidt and Dickinson, 2000; Nakai et al., 2008; Tian et al., 2011), vegetation vertical parameters (i.e., height and FAI) are critical for estimates of d and z_{0m} obtained via remote-sensing-based roughness models (Raupach, 1994; Schmidt and Dickinson, 2000; Nakai et al., 2008). However, few studies have focused on the long term parameterization scheme of z_{0m} and d while considering the variation of vertical vegetation information in time. Vegetation height is commonly derived from vegetation indexes (i.e., NDVI, LAI) using time-series remote sensing data, which may be suitable for low vegetation

(for example, pastures, crops, shrubs, etc.). However, this is not possible for growing forests. Vegetation indexes in the QM represent a mixture of the top canopy and the understory in forest gaps. Therefore, NDVI and LAI cannot provide vertical dynamic information for forests.

In this study, dynamic forest vertical information of height and FAI were obtained from field calibrated regression models and interannual forest AGB variations. In particular, instead of the arithmetical mean height, Lorey height was derived by considering its better expression to forest stand status as well as to d and z_{0m} (Nakai et al., 2008; Tian et al., 2011). Considering the high heterogeneity of local forests, regression relationships (forest Lorey height versus forest AGB and FAI versus forest AGB) established on the basis of forest measurements were reasonable. However, due to natural and anthropogenic disturbances as well as the self-adaption of forests, Lorey height and FAI are apt to defy the regressions. For example, as a result of self-thinning adaption, matured or over-matured forests would definitely change SD (trees ha^{-1}) in order to keep ecosystem balance, resulting in an increase in forest height but a decrease in forest AGB. As it is well known, forest AGB levels should obey a parabolic relationship between forest AGB and forest age. In this study, regression models based on measurements without forest age information would be biased. Because, in practice, different forest heights exist in stands that have a similar forest AGB level but various stand densities. Further exploration should take forest stand age and forest SD into account. Alternatively, continuous national forest inventories with a five-year interval and upcoming active spaceborne remote sensing (Synthetic Aperture Radar (SAR) and Light Detection and Ranging (LiDAR)) with the ability to derive multi-temporal forest vertical parameters could be helpful for calibrating the deviations for local forest vertical information.

Further improvement of ET can be obtained from more accurate meteorological inputs, although in this study meteorological inputs have been verified to be reliable. Some improvement of wind speed and downwelling long-wave radiation estimates are still possible (Pan et al., 2012). As indicated by the HiWATER team, other improvements for long-term MODIS LST inputs can also be expected (Zhou et al., 2014). Using unreliable meteorological inputs and MODIS LST products for SEBS would result in deterioration for the agreement of both H and λE and, thus, ET with EC measurements (Su et al., 2007a; Tang et al., 2011; Zhou et al., 2014). The SEBS model has been proven to be reliable for multi-scale ET estimations. However, only a few studies have hitherto focused on short term simulations within forests (Zhou et al., 2012; Ershadi et al., 2014). Due to complicated heat transfer mechanisms within forests and their surroundings, SEBS cannot consistently

capture the ET process. For the cold and arid forests with high heterogeneity in this study, climate and environmental factors were found to enhance the complexity of the ET process. For example, melting snow in the canopy and underground possibly has a large impact on the ET process. Some sharply increasing daily ET values were found for EC measurements during the later spring and early summer indicate that this is the case. Further improvements should be expected if soil moisture simulations and snow melt monitoring modules are embedded into the SEBS algorithm (Gökmen et al., 2012). Such additions could make SEBS more applicable for multiple biomes and various climate and environmental conditions.

6.6 Conclusion

This study proposed a time-series parameterization scheme (for the years 2000 to 2012) for two critical parameters (d and z_{0m}) using MOS theory which is the basic mechanism for the SEBS. Two parameters (forest height and FAI) of the SD00 model were calibrated against forest measurements using regression models. In **Chapter 5**, it was shown that the SD00 model outperformed other aerodynamic roughness models (the SD00 model) in estimating z_{0m} . The two regression equations were linked to interannual forest AGB dynamics from **Chapter 4**. By combining GLASS LAI products, forest height and FAI dynamics were applied in order to derive d and z_{0m} using the SD00 model. d and z_{0m} were further employed in order to derive z_{0h} using the kB^{-1} model. These three parameters were applied to parameterize the SEBS model from 2000 to 2012. With the incorporation of original MODIS products (NDVI, LST), GLASS Albedo products and downscaled WRF estimates, the parameterized SEBS was employed to simulate eight-day forest ET over the QMs. As compared to MOD16_ET products, the SEBS estimates were much better and agreed well with EC measurements with the exception of the growing seasons for which SEBS underestimated forest ET during 2010 and overestimated ET during 2011.

The dynamic parameterization scheme employed in this study is more realistic than assuming ‘static’ conditions with constant d , z_{0m} and z_{0h} . The spatial distribution of forest ET estimates provide valuable information for sustainable management of forest and water resources, which are extremely important to the QMs and the entire HRB river basin.

Chapter 7

Synthesis

7.1 Introduction

Forests form one of most important components of the terrestrial ecosystems, and they play a multi-functional role in the biosphere. This role has been the subject of many scientific studies. Forests dynamically regulate the water, energy, and momentum fluxes occurring at the land surface through the processes of photosynthesis and evapotranspiration (ET). The biggest terrestrial carbon pool is forest (McKinley et al., 2011), and its carbon dynamics contribute significantly to global carbon balance. Forests also extraordinarily affect the water balance through hydrological processes such as rainfall interception, water uptake during transpiration, water return to the atmosphere via ET affecting energy balance. Furthermore, forests affect the radiation balance through radiation attenuation and the atmospheric turbulence through surface roughness (Mendez-Barroso et al., 2014).

Forest carbon stocks and fluxes are as dynamic as forest properties (i.e., the area of forest land use), processes (i.e., ecological and hydrological) and changes with natural and anthropogenic disturbances, climate constraints, and forest growth and mortality. Due to the presence of continuous forest inventories, forest above-ground biomass (AGB) dynamics can be quantified (Goodale et al., 2002). Although reasonable results for such inventories can be obtained, they are time consuming and require considerable investments in labour costs. The inventories are designed to provide total forest AGB from averaged wood volume/biomass by multiplying forest areas using administrative units. A complete forest inventory once at the national scale of China takes 5 years. Thus, the method cannot provide forest AGB distributions at fine spatiotemporal resolutions that are compatible with changes in forest properties (Houghton 2005). The method also cannot provide information on critical processes such as ecological and hydrological functions.

The Eddy Covariance (EC) technique has been proven to be a reliable ‘record’ of fine time-resolution variations within forest ecosystems but only has validity within a fairly small footprint area. Similar strengths and weaknesses as those of EC measurements exist for process-based ecological models. These models can simulate critical processes but, due to the complex set of parameters required through measurements or calibrations, the scaling issue is also a problem. In contrast, remote sensing techniques can provide spatial dynamic information for forests, but are unable to capture the characteristics of processes.

Given the implications of global warming, understanding the dynamics and the resulting carbon stocks and fluxes of forests has been the focus of substantial

research (Gray et al., 2014). Accompanying forest AGB dynamics, forest ET, which is an essential part of the hydrological cycle, varies as well, due to the interaction between the land and atmosphere.

Water availability is generally perceived to be a major control of the forest ecosystem functions, presented as patterns of net primary productivity (NPP) or above-ground NPP (ANPP) across regions and biomes (Lauenroth, 1979; Zhang et al., 2014). Both NPP and ANPP are important components of the carbon fluxes with direct links with forest AGB. The scientific community and policy-makers share a common interest in quantifying regional forest AGB and ET and, thus, in identifying and evaluating the potential changes of ecosystem. Three types of approaches are available for quantitatively presenting these two parameters and can be ascribed as statistical, process-based, or remote sensing-based. Each approach has its own characteristics, as well as strengths and the weaknesses. In practice, large uncertainties exist for estimations of forest AGB and ET (Hayes et al., 2012; Gray and Whittier, 2014), and these uncertainties hamper our understanding of the dynamics of the Earth system (Wang et al., 2013; Sun and Mu, 2014).

This study was motivated by a desire to obtain reliable and reasonable estimations for the dynamics of forest AGB and ET in a water-limited catchment of the Heihe River Basin (HRB), where the forest ecosystem is located in the Qilian Mountains (QMs), the headwater of the basin. This headwater is eco-hydrologically extremely important to the entire region, as it provides the water that forms a large oasis in a desert. The proposed dynamic modeling in this thesis resulted in realistic and reliable data of AGB and ET. This was obtained by the use of multi-parameter remote sensing data in combination with various field measurements and model strategies that had individual advantages embedded in their methodologies. As compared with those from the each individual model, the results with finer spatiotemporal resolution obtained are duplicable and applicable over biomes in other areas.

As per the response to the problems, scientific questions, and objectives as stated in **Chapter 1**, the main results and a discussion and conclusion are provided in the following sections. Finally, the limitations of this study and an outlook of future work are presented.

7.2 Results

7.2.1 Estimations of Forest Above-Ground Biomass

To estimate forest AGB within the airborne campaign area of intensive measurements, in combination with forest field measurements, multi-parameter remote sensing data and two typical methods, parametric stepwise multiple linear regression (SMLR) and non-parametric k -Nearest Neighbour (k -NN), were employed. The multi-parameter remote sensing data included a Satellite Probatoire d'Observation de la Terre-5 (SPOT-5) high resolution geometrical (HRG) image, multi-temporal dual-polarization Advanced Land Observing Satellite (ALOS) Phased Array type L-band Synthetic Aperture Radar (PALSAR), and airborne light detection and ranging (LiDAR) data. Model performance was evaluated using the leave-one-out (LOO) method described in **Chapter 2**. The best performing non-parametric method was reliable and it had the ability to tackle the overfitting problem that tends to occur when remotely sensed information is high-dimensional and the reference sample from field measurements is small. Considering the high cost of airborne LiDAR data as well as high resolution satellite data (in this case SPOT-5 HRG), it is difficult to apply them over large forested areas. Moreover, the complexities of local landscape heterogeneity and local terrain conditions hindered the applicability of Synthetic Aperture Radar (SAR) data using backscattering or coherence information.

For these reasons, this thesis used free and long-time-continuity Landsat Thematic Mapper 5 (TM) imagery and free Advanced Spaceborne Thermal Emission and Reflection Radiometer (ASTER) Global Digital Elevation Model (GDEM) products to estimate regional forest AGB as an alternative in **Chapter 3**. To alleviate terrain relief, a sun-canopy-sensor plus C (SCS+C) correction was performed while pre-processing the inputting spectral types from TM. Despite the lower resolutions of TM and ASTER (30m) compared to SPOT-5 HRG (10m), the optimized non-parametric k -NN performed equally well. This good performance was thanks to the larger reference sample representing a wider range of AGB values and higher dimensional spectral types than that used in **Chapter 2**. However, the high dimension caused a problem in the optimization of the k -NN model: the selection of the optimal inputting vector for k -NN was difficult to determine, time-consuming, scenario-dependent, and it required a priori knowledge. In short, it required a high level of experience with estimating forest AGB.

In order to arrive at an effective way for selecting an optimal spectral vector for the sake of estimating forest AGB at large scale, the incorporation of random forest (RF) with k -NN and with Support Vector Regression (SVR) were provided in

Chapter 4. The good comparability of forest AGB estimates obtained using these two incorporative strategies indicated their ability for tackling the time-consuming feature selection and avoiding an overfitting risk. After validated against field measurements, reliable estimates for forest AGB were obtained from both combinations. The optimal k -NN configuration performed slightly better than that of SVR, where in both cases the selected spectral vectors were obtained from RF. Hence, k -NN was employed to estimate the regional forest AGB of 2009. This strategy showed that reliable AGB data can be obtained from high-dimensional remotely sensed information with a small sample.

7.2.2 Modeling of Forest Above-Ground Biomass Dynamics

The regional forest AGB map from the aforementioned optimal k -NN configuration was the starting point for the time-series modeling of forest AGB dynamics from 2000 to 2012. A remote-sensing-based model was combined with a process-based model to obtain forest carbon fluxes. By using these two models we could exploit the advantages of both in simulating the interannual forest carbon fluxes. The remote-sensing-based model (MODIS MOD17 (MOD_17)) was first optimized by the measurements and the refined driving parameters (i.e., maximum light use efficiency (ε_{max}), the fraction of photosynthetically active radiation ($fPAR$), and the meteorological parameters). As compared with original MODIS gross primary productivity (GPP) products, GPP estimates obtained from the optimized MOD_17 model were of much higher quality. The incorporating strategy was to use these GPP estimates to calibrate the process-based model 'Biome-BioGeochemical Cycles' (Biome-BGC). To take account of the overall representativeness of the characteristics of the forests over the QMs, GPP estimates over 30 well-chosen pixels (1km resolution), obtained from the optimized MOD_17 model, were employed to calibrate the Biome-BGC model. After finding the best fitting relationship between GPP estimates of MOD_17 and Biome-BGC, the optimal configuration of the Biome-BGC was determined. Afterward, the calibrated Biome-BGC was driven using forcing data for forest carbon fluxes simulations from 2000 to 2012. As compared with those achieved using a single model, as outlined in **Chapter 4**, finer spatiotemporal resolution simulations of forest carbon fluxes, including GPP, NPP and net ecosystem exchange (NEE), were obtained.

Based on the conversion ratios of NPP to ANPP, and ANPP to AGB, as determined from empirical constants (the carbon content index and the tree mortality portion) by long-term observations in previous studies, interannual forest NPP estimates were converted to interannual forest AGB increments. The modeling of interannual forest AGB dynamics was accomplished using a combination of interannual AGB increments with a forest AGB basis map of 2009 obtained using the incorporation

of RF with k -NN. Both EC and dendrochronological measurements were used to validate the obtained result: EC was used to validate carbon fluxes, and the dendrochronology to validate interannual forest AGB increments. The results proved the comparability and applicability of this incorporation strategy: the calibrated Biome-BGC represented the heterogeneity of the forest ecosystem on one hand, and it could describe the critical processes and reveal the related mechanisms in the interaction of forest and atmosphere on the other hand. This strategy can be duplicated over biomes under various climate and environmental conditions but it is subject to the feasibility and validity of remote-sensing-based models.

7.2.3 *The Long-Term Parameterization and Evapotranspiration Simulation of The Surface Energy Balance System*

This thesis further addressed a problem in the remote sensing of ET in **Chapter 5**. Two roughness parameters, the zero-plane displacement height, d (m) and the aerodynamic roughness length z_{0m} (m), are difficult to estimate a priori but have a strong effect on simulated ET of the surface energy balance system (SEBS). In this thesis they were estimated by a synthesis of airborne LiDAR cloud points and a satellite SPOT-5 HRG image taken within the airborne campaign area. With sufficiently accurate estimates for forest structural parameters, including forest height (both the arithmetic mean height (H_{avg}) (m) and the Lorey mean height (H_L) (m)), the first branch height (FBH) (m), the crown width (CW) (m) and stand density (SD) (trees ha^{-1}), the fractional canopy coverage (f_c), the effective plant area index (PAI_e), and the leaf area index (LAI), four remote-sensing-based d and z_{0m} models were verified and evaluated using EC measurements. Through sensitivity analyses and the comparison of results, forest height was the most sensitive parameter within these models and it was also determined that using H_L was better for both d and z_{0m} estimates than H_{avg} . The model from Schaudt and Dickinson (2000) (SD00 Model) outperformed the others in estimating z_{0m} but was compromised when calculating d .

SEBS uses Monin–Obukhov Similarity (MOS) theory to estimate aerodynamic resistance, and this resistance is sensitive to the d , z_{0m} and thus to the heat transfer height z_{0h} , as shown by previous studies (Zhou et al., 2006; Chen et al., 2013). Using the SD00 model, the long-term parameterization of d and z_{0m} , taking forest growth into account, was conducted by employing forest structural dynamic parameters including LAI, the frontal area index (FAI) and H_L . In particular, dynamic information for FAI and H_L was derived from regression models calibrated by fitting FAI and H_L against forest AGB based on measurements and the interannual forest AGB dynamics obtained in **Chapter 4**. Estimates of d and z_{0m} were further employed in order to derive z_{0h} using the kB^{-1} model and the auxiliary

information (i.e., fractional vegetation coverage (f_v) and fractional soil coverage (f_s) and their mixed coverage (f_{cs}) estimated from MODIS Normalized Difference Vegetation Index (NDVI) products). Driven by refined Global Land Surface Satellite (GLASS) Albedo products, original MODIS NDVI and land surface temperature (LST) products, and reliable meteorological estimates downscaled from Weather Research and Forecasting Model (WRF), in **Chapter 6**, SEBS was performed for long-term forest ET simulations over the QMs. As compared with the original MODIS ET products (eight-day), the corresponding eight-day averages of ET simulations from SEBS agreed better with the two-year EC measurements. The result implied that the parameterization scheme for SEBS could generate reasonable ET estimates over the forest for cold and arid conditions.

7.2.4 Impacts of Climatic Variations on Forest ANPP, ET and, thus, Water Use Efficiency

The estimates of interannual ANPP obtained from **Chapter 4** combined with estimates of the corresponding ET from **Chapter 6** made it possible to calculate a water use efficiency (WUE) as ANPP:ET.

The statistics of the dynamics of interannual ANPP, ET, thus WUE are listed in Table 7-1. Together with these dynamics, the meteorological driving data from the downscaled WRF are shown in Fig. 7-1. These statistics were only calculated for the growing seasons (from 1 April to 30 September) for the forests over the QMs. The overall trends of ANPP, ET and WUE over the study period show a decline, but interannual variations are large. From 2000 to 2003, annual ANPP and ET increased. ANPP and ET were low in 2004, 2006 and 2009, but after 2009, they climbed steadily. Similar trend of WUE was found in Fig. 7-1, except that it did not peak in 2003, and it did not fall sharply in 2004 but only slightly. Interestingly, the similar troughs in the WUE trend were found in 2006 and 2009 as those of ANPP and ET, which indicates that (1) ANPP and ET respond in a similar direction to interannual weather variations, but (2) variations in ANPP are relatively larger than those in ET.

Table 7-1 The statistics for interannual averages of forest ANPP (unit: gC m⁻²), ET (unit: mm), and WUE (unit: kgC m⁻³) over the QMs from 2000 to 2012.

Year	2000	2001	2002	2003	2004	2005	2006
ANPP	206.26	259.86	287.10	300.72	255.21	262.81	169.08
ET	244.14	281.23	299.21	316.73	271.24	289.60	247.60
WUE	0.84	0.92	0.96	0.95	0.94	0.91	0.68
Year	2007	2008	2009	2010	2011	2012	
ANPP	227.29	205.81	130.71	175.98	189.52	239.88	
ET	277.37	254.53	201.60	221.86	236.39	289.67	
WUE	0.82	0.81	0.65	0.79	0.80	0.83	

The climatic drivers, the downwelling short wave (DSW) radiation, the mean temperature, precipitation and the vapor pressure deficit (VPD) during the growing season were further inspected. Ascending trends for interannual variations of mean temperature, precipitation were found, while VPD showed large fluctuations but no overall trend. DSW showed a gradual decline.

It is clear that precipitation did not limit the forest ANPP and ET in the QMs, but (low) DSW, and (high) VPD did. For example, the driest season of 2003 with the second lowest VPD, a low temperature, but sufficient DSW, pushed the ANPP and ET to the summit. In 2012, VPD was the lowest, precipitation was high and DSW intermediate, causing ANPP and ET to climb to the second highest peak. The minimum values of ANPP and ET were found in years with low DSW and high VPD: 2006 and 2009. In other years, the anomalies in meteorological forcing did not drive ANPP and ET to extremes. For example, in 2004 both VPD and DSW were low, and ANPP and ET took intermediate values (low VPD indicates high ANPP, but low DSW indicates low ANPP). In 2008 the exact opposite happened: high VPD and high DWS, again leading to intermediate ANPP and ET.

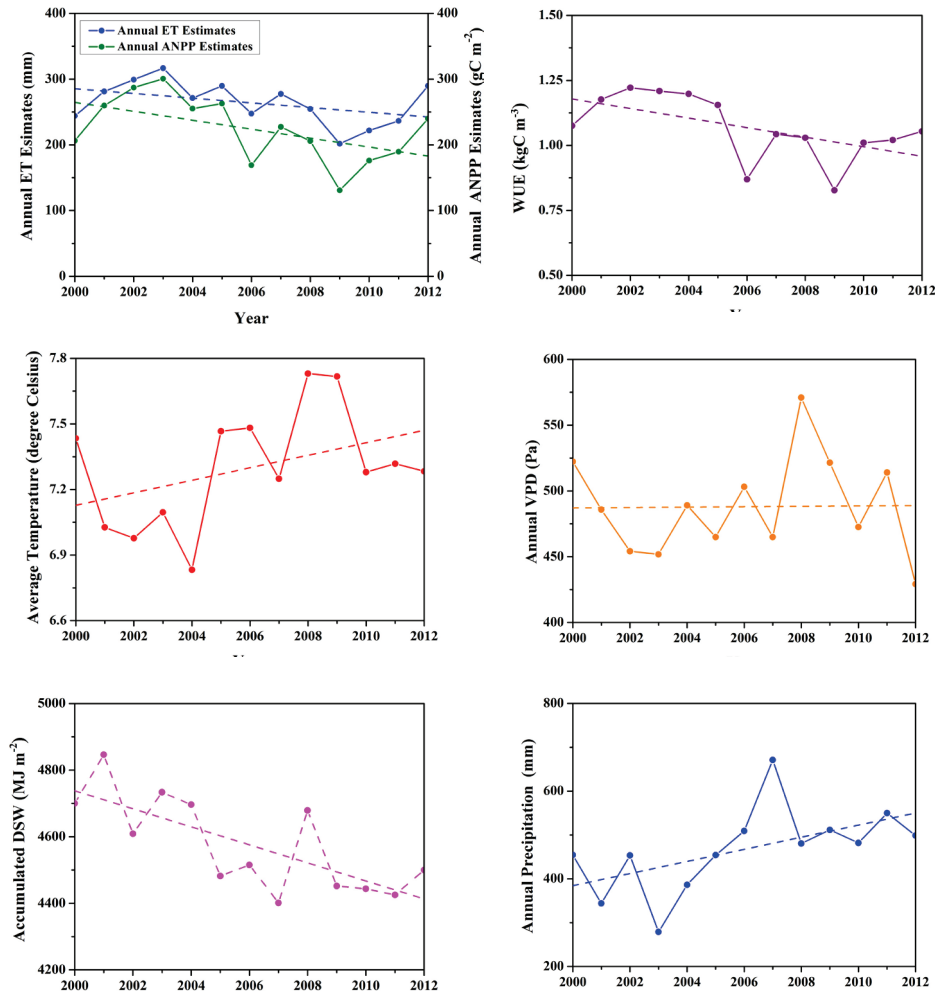


Fig. 7-1 Interannual ANPP, ET, WUE and the meteorological statistics for the growing seasons in forested areas over the QMs (the dash lines are the trendlines).

7.3 Discussion and Conclusions

The non-parametric methods often perform better than parametric methods for estimating forest AGB by remote sensing data, due to its more flexible assumption. Besides the model choice, the representativeness of the reference samples to forest AGB grades within the study area was also important for the target estimates of both methods. Parametric methods (i.e., SMLR) are abided to the law of large numbers, which means the larger the reference sample the better the expression of the predictor. Non-parametric methods (i.e., k -NN) rely on the weighted averages of the reference values for the k neighbours. If a low or high AGB level is absent in

overall forests, and then both of them bias the estimates. This is problematic in the QMs, where the forest area is hard to reach for measurements.

When various remotely sensed information with high dimension is involved, a critical issue is how to select features for establishing the optimal configuration for the non-parametric models. Based on the 'bootstrap' sampling method, the RF method can evaluate the importance of the inputting features for estimates with more reliability and more efficiency as compared to selecting features using a regression method or a sensitivity analysis. Regression involves a high risk of the overfitting, and linear or non-linear assumptions are needed. Hence, these selections based on the regression or the sensitivity analysis may not be suitable for non-parametric methods, especially for a spectral signature with a spatial variability. Alternatively, the incorporation of RF with other non-parametric methods is more reasonable and could sidestep experience-based and time-consuming optimization processes for the configurations.

In the QMs, terrain relief is also an important factor for quantitative estimations based on remote sensing data. Due to extremely serious overlays and shadows and speckles contaminating SAR images, it is eventually difficult to apply SAR data for estimating forest AGB over the QMs. For optical data (both SPOT-5 HRG and TM), the impacts of terrain on forest AGB estimates were alleviated using the SCS+C correction method. By accounting for diffuse atmospheric and terrain radiance, this physically based correction can preserve sun-canopy-sensor geometry and prevent overcorrection which can improve the predictive ability of optical data.

The incorporation of the remote-sensing-based model with the process-based model exploited the powers of both models for estimating carbon fluxes. Following the parameterization from three input sources including maximal light use efficiency (ε_{max}) and the meteorological parameters and LAI, the MOD_17 was largely improved and generated more reliable GPP estimates as compared to the original MODIS GPP products. The site-calibrated ε_{max} was suitable for the entire forest because *Picea crassifolia* is the overwhelming species (according the measurements it occupies 99.39% of total measured trees) in the QMs. The latter two inputs have been shown to be reliable and can, thus, represent the seasonal viabilities of forests and climate. The reliable GPP estimates obtained from the optimized MOD_17 were used to calibrate the Biome-BGC which in turn simulated a net flux (NPP, NEE). In particular, during the calibration, GPP estimates from the optimized MOD_17 model over 30 well-chosen plots allowed representation of the spatial variability of the local forest ecosystem. This strategy optimally exploited the limited available ground truth data on carbon fluxes.

Validated by fine (daily) temporal EC measurements, the carbon fluxes (including GPPs, NPPs, and NEEs) simulated by the calibrated Biome-BGC were trustworthy. To verify the corresponding interannual forest AGB increments originally converted from NPP estimates from the calibrated Biome-BGC, fine spatial dendrochronological measurements (multiple sites) were first applied for validating forest AGB increments over the QMs. These dendrochronological measurements would also be valuable for studying the ecological evolution and paleoclimate of the QMs because tree rings can be traced back to the 19th century, but such analysis is beyond the scope of the present research.

The proposed modeling of forest AGB dynamics based on the combination of reliable forest AGB with the interannual increment inherited some merits of multi-parameter remote sensing techniques and the mechanism-based incorporation of various models (including RF with k -NN and MOD_17 with Biome-BGC). When quantitative and spatiotemporal changes of forests are known to occur (e.g., afforestation and deforestation), the corresponding forest AGB dynamics can be easily updated by modifying the specific pixels' properties in the maps. As a result, fine spatiotemporal variations of forest AGB with supports for capturing the characteristics of critical processes and changes within forests can be portrayed.

For forest ET simulations, the parameterization of d and z_{0m} is critical to the SEBS model. As this thesis demonstrated, the SD00 model had superiority in estimating z_{0m} , albeit not in estimating d . Considering that z_{0m} directly determines z_{0h} , an accurate estimate of z_{0m} was preferred to an accurate estimate of d . Hence, the SD00 model was employed for the long-term parameterization of SEBS. As the most influential forest structural parameter affecting both d and z_{0m} in all of the studied roughness length models, forest height was also essential for the parameterization. It is common practice to derive d and z_{0m} from the remotely sensed vegetation indexes (i.e., NDVI, LAI, etc.). This is appropriate for low vegetation (i.e., pastures, crops, shrubs), because variations in vertical structures in low vegetations may not be relevant. However, structure parameters are critical in forests (i.e., forest height, FAI). The instantaneous information for forest vertical parameters can be derived from active remote sensing (i.e., LiDAR, interferometric SAR (InSAR)), but long-term dynamic information for these parameters is currently not available. Although ICESat-GLAS LiDAR has been proven to be reliable for providing multi-temporal information for vegetation, due to serious data gaps, it is not suitable for the QMs. Only few tracks of data were found in this region and most of the footprints were located within non-forest areas. Alternatively, the proposed long-term parameterization scheme which incorporated the refined GLASS LAI products with forest height (the Lorey height) and FAI information from the aforementioned

forest AGB dynamics can capture the variations of d and z_{0m} over time. Based on this parameterization strategy, SEBS was proven to generate reliable forest ET estimates and also implied that dynamic vertical information was more reasonable than taking them as ‘static’ constants. Furthermore, the use of refined MODIS products and reliable meteorological inputs can also provide credits for reliable ET estimates.

In conclusion, using multi-source remote sensing data, reasonable forest AGB estimates over the QMs were obtained by incorporating two non-parametric methods, RF and k -NN. The feature types’ selection obtained using RF opened the possibility for effectively constructing optimal configurations for k -NN. With the ‘bootstrap’ and LOO sampling methods, this incorporation was capable of tackling the overfitting problem. The SCS+C method was proven to have the ability to alleviate terrain impacts on quantitative estimations of forest AGB using remotely sensed data. Following the optimization of site measurements, refined $fPAR$ and reliable meteorological inputs, the remote-sensing-based MOD_17 model generated GPP estimates with satisfactory accuracy. After calibration by the MOD_17 GPP estimates over well-chosen forest plots representing diverse conditions (for the climate, the environment and the stand), the Biome-BGC was more resistant to impacts of climate variation, environmental variability and forest stand diversity. The ‘ill-simulation’ problem of the process-based model, where errors from the calibration phase are apt to be propagated to the end of the simulation, was also avoided using this incorporation strategy.

Validated by EC and dendrochronological measurements in terms of GPP and NEE, interannual forest AGB increments were primarily converted from NPP estimates and the calibrated Biome-BGC generated most reliable forest carbon fluxes within the space-time-continuum that has been produced thus far. By combining interannual forest AGB increments with the basic map of forest AGB for 2009, interannual forest AGB dynamics were obtained. This methodology for modelling the forest AGB dynamics described other forest processes: transpiration, photosynthesis, respiration, allocation, etc., at finer space and time scales and provided a sophisticated understanding of these processes. This comprehensive knowledge is vital for sustainable development and deep-insight into the protection of the water resources provided by the ecosystem, thus contributing essential information in resolving serious conflicts between the ecology and economy.

With the incorporation of various remote sensing products (NDVI, LST, Albedo, LAI, etc.) and meteorological forcing data, the parameterized SEBS outperformed the MODIS ET model driven by default inputs. Validated by two years of EC

measurements, SEBS estimates agreed well with EC measurements, with an exception that during the growing seasons, SEBS underestimated forest ET in 2010 but overestimated it in 2011. The spatial distribution of forest ET estimates would be valuable for the sustainable management of forest and water resources which are extremely important to the QMs and, thus, the entire HRB.

During the thirteen years simulations, large fluctuations were found for ANPP, ET and thus WUE. Dividing interannual forest ET summations into corresponding forest ANPP aggregations provided implications for interannual WUE dynamics. Interannual forest ANPP, ET, and, thus, WUE dynamics were further used as support for analyzing the impact of climatic and environmental variations on forest ecosystem processes. This type of information is critical for local, regional and national governments for the sake of the sustainable development of local ecosystems and water sources.

7.4 Limitations and Future Work

After accomplishing reliable estimates of forest AGB, forest carbon fluxes and dynamic processes over the QMs at fine spatiotemporal scale, several limitations remain. Here, suggestions for follow-up research are presented.

First, the incorporation of RF with k -NN was loosely combined, in the manner in which RF was employed for selecting features based on a decision tree and a 'bootstrap'. Based on LOO, k -NN 'took over' these features for constructing the optimal configuration. However, the result did not indicate that the 'optimal' RF was consistently the same as that within the k -NN configuration. Thus, when using k -NN, possible 'suboptimal' features could bias the estimates. The innovative method of random k -NN feature selection that couples the RF and k -NN algorithms, as proposed by Li et al., (2011a), has been proven to be a fast and stable alternative to RF. But, the procedure was designed to be suitable for a gene classification study. Therefore, an adaptation to this method has been conducted for estimating forest AGB in our study. As far as the remote sensing data is concerned, more attention should be given to new (i.e., Landsat Thematic Mapper-8) and upcoming data (i.e., the high-resolution constellation of China, including high resolution SAR and optical remote sensing satellites) instead of only TM. With the new sensors, data that are free or partly free are of interest for forestry applications. Here, it is necessary to mention that these high resolution data will be very useful for the scaling issues that were not considered in this study. When upscaling the estimates from 30 m to 1 km for the forest/non-forest map or for the forest AGB map, the problem of "mixed pixels" occurred, an actually common problem within this study area due to the heterogeneity of the local forest landscapes. Cooperation with an

additional research team addressing the scaling issue started in 2013. The upcoming general scaling method is expected to improve the representative of ‘mixed pixel’. Second, in an unchained way, the incorporation of two ecological models was also performed. Although the forest plots were well-chosen for the calibration, some uncertainties still persisted (i.e., the forest properties’ changed after the calibration). Data assimilation has proven to be a valuable technique for coordinating the simulations of the process and, thus, can capture the changing characteristics of forests. As a result, model behavior could be improved. Normally, for process-based model simulations, the status parameters (i.e., LAI) retrieved from remote sensing are coupled to the model using filters (i.e., ensemble Kalman and sequential importance resampling (SIR) particle filters). However, in the Biome-BGC model, the LAI calculated from leaf biomass is the output rather than a state parameter. Alternatively, leaf biomass or other parameters (e.g., chlorophyll content) can be employed for the data assimilation process. To simulate the forest stably and adaptably, this topic should be considered in future work.

In this thesis, for the conversion of interannual forest ANPP to AGB dynamics, a few empirical constants were utilized. The mortality ratio was, in particular, the critical factor for conversion and largely impacted AGB dynamics. More ecological mechanism-based models with forest stand density (SD) and forest stand age are expected to describe these forest changes (SD and, thus, AGB) throughout the simulation period, which can indeed suppress overestimates or underestimates of AGB dynamics. Alternatively, the five year interval for continuous forest inventories could also help us calibrate the ratios by calculating AGB increments over five years.

Third, four remote sensing models for estimating d and z_{0m} were evaluated, but none of them took the vertical information other than LAI and FAI (i.e., the leaf area density (LAD)) of the forests into account. In fact, LAD affects momentum and heat transfers in both vertical and horizontal directions. Moreover, the FAI plane against the wind direction could be metamorphic due to the overlays of the crowns at the vertical profile, which was not considered in these models, neither in this thesis. Using airborne or ground-based LiDAR data, three-dimensional (3D) information for the forest could easily be obtained. In combination with ground measurements (i.e., EC, forest survey), this 3D information could be used to reconstruct vertical profiles of LAD and FAI for the four major cross directions (north, south, east and west). Until present, measurements, including EC, forest surveys, airborne and ground-based LiDAR, etc., at several sites have been obtained through “Complicate Observations and Multi-Parameter Land Information Constructions on Allied Telemetry Experiment (COMPLICATE)” (Tian et al., in

submission). Future work should apply 3D information for these parameters in order to model d and z_{0m} . Using forest dynamic vertical parameters (height and FAI) improves the output of SEBS, but further comparative analyses between the ET estimates obtained using this scheme and the other possible alternatives have not been conducted yet. Such comparison should be carried out in the future. Another point is that the kB^{-1} model should also take vertical structural parameters of the forest into account. Based on LiDAR campaigns over the aforementioned sites, comprehensive measurements could be expected to provide a more precise expression for the kB^{-1} model.

Finally, only the AGB, the carbon fluxes and the ET dynamics of forests over the QMs were studied. However, it is well known that carbon fluxes and the ET of grasses and shrubs inhabiting the northern slope are also critical for eco-hydrological studies of the entire HRB basin. In particular, ET within the northern slope is very high, so that, normally, no runoff occurs from these slopes. Future work should jointly simulate these dynamics for the entire vegetation ecosystem. For the analyses of the impacts of climatic variations on the forest photosynthesis and ET processes, only the trends were appraised. Future work should comprehensively and quantitatively explore their impacts in order to provide the support relevant for sustainable management and development for local ecosystem and water recourses.

Bibliography

- Adler-Golden, S.M., Matthewa, M.W., Bernsteina, L.S., Levinea, R.Y., Berka, A., Richtsmeier, S.C., et al. (1999). Atmospheric correction for short-wave spectral imagery based on MODTRAN4. *SPIE Proceeding, Imaging Spectrometry*, 3753, 61–69.
- Amini, J., & Sumantyo, J.T.S. (2009). Employing a method on SAR and optical images for forest biomass estimation. *IEEE Transactions on Geoscience and Remote Sensing*, 47, 4020–4026.
- Anderson, R.G., Jin, Y., & Goulden, M.L. (2012). Assessing regional evapotranspiration and water balance across a Mediterranean montane climate gradient. *Agricultural and Forest Meteorology*, 166–167, 10–22.
- Arlot, S., & Celisse, A. (2010). A survey of cross-validation procedures for model selection. *Statistics Surveys*, 4, 40–79.
- Avitabile, V., Baccini, A., Friedl, M.A., & Schullius, C. (2012). Capabilities and limitations of Landsat and land cover data for aboveground woody biomass estimation of Uganda. *Remote Sensing of Environment*, 117, 366–380.
- Baffetta, F., Corona, P., & Fattorini, L. (2012). A matching procedure to improve *k*-NN estimation of forest attribute maps. *Forest Ecology and Management*, 272, 35–50.
- Baldocchi, D.D., & Bowling, D.R. (2003). Modelling the discrimination of (CO₂)-C-13 above and within a temperate broad-leaved forest canopy on hourly to seasonal time scales. *Plant Cell and Environment*, 26, 231–244.
- Bao, Y.F. (2009). Study on methods of forest parameters extraction from multi-source remote sensing data. PhD-thesis (in Chinese). Beijing, The China: Institute of Remote Sensing Applications, Chinese Academy of Sciences.
- Bastiaanssen, W.G.M., Menenti, M., Feddes, R.A., & Holtslag, A.A.M. (1998). A remote sensing surface energy balance algorithm for land (SEBAL). 1. Formulation. *Journal of Hydrology*, 212-213, 198-212.
- Berry, J., & Bjorkman, O. (1980). Photosynthetic response and adaptation to temperature in higher plants. *Annual Review of Plant Physiology and Plant Molecular Biology*, 31, 491–543.
- Berry, J.A., Beerling, D.J., & Franks, P.J. (2010). Stomata: key players in the earth system, past and present. *Current Opinion in Plant Biology*, 13, 232–239.
- Berthelot, M., Friedlingstein, P., Ciais, P., Dufresne, J.L., & Monfray, P. (2005). How uncertainties in future climate change predictions translate into future terrestrial carbon fluxes. *Global Change Biology*, 11, 959–970.
- Betts, R.A. (2000). Offset of the potential carbon sink from boreal afforestation by decreases in surface albedo. *Nature*, 408, 187–190.

- Boisvenue, C., & Running, S.W. (2006). Impacts of climate change on natural forest productivity evidence since the middle of the 20th century. *Global Change Biology*, *12*, 862–882.
- Bonan, G.B. (1993). Physiological derivation of the observed relationship between net primary production and mean annual air temperature. *Tellus Series B-Chemical and Physical Meteorology*, *45*, 397–408.
- Bouwer, L., Biggs, T., & Aerts, C. (2008). Estimates of spatial variation in evaporation using satellite-derived surface temperature and a water balance model. *Hydrological Processes*, *22*, 670–682.
- Braswell, B.H., Hagen, S.C., Frolking, S.E., & Salas, W.A. (2003). A multivariable approach for mapping sub-pixel land cover distributions using MISR and MODIS: Application in the Brazilian Amazon region. *Remote Sensing of Environment*, *87*, 243–256.
- Braswell, B.H., Sacks, W.J., Linder E., & Schimel, D.S. (2005). Estimating diurnal to annual ecosystem parameters by synthesis of a carbon flux model with eddy covariance net ecosystem exchange observations. *Global Change Biology*, *11*, 335–355.
- Breidenbach, J., Naesset, E., & Gobakken, T. (2012). Improving *k*-nearest neighbor predictions in forest inventories by combining high and low density airborne laser scanning data. *Remote Sensing of Environment*, *117*, 358–365.
- Breiman, L. (2001). Random forests. *Machine Learning*, *45*, 5–32.
- Brilli, L., Chiesi, M., Maselli, F., Moriondo, M., Gioli, B., Toscano, P., et al. (2013). Simulation of olive grove gross primary production by the combination of ground and multi-sensor satellite data. *International Journal of Applied Earth Observation and Geoinformation*, *23*, 29–36.
- Brown, S. (2002). Measuring carbon in forests: current status and future challenges. *Environmental Pollution*, *116*, 363–372.
- Brown, S.M., Petrone, R.M., Chasmer, L., Mendoza, C., Lazerjan, M.S., Landhausser, S. M., et al. (2014). Atmospheric and soil moisture controls on evapotranspiration from above and within a Western Boreal Plain aspen forest. *Hydrological Processes*, *28*, 4449–4462.
- Brutsaert, W. (1999). Aspects of bulk atmospheric boundary layer similarity under free convective conditions. *Reviews of Geophysics*, *37*, 439–451.
- Campos, G.E.P., Moran, M.S., Huete, A., Zhang, Y.G., Bresloff, C., Huxman, T. E., et al. (2013). Ecosystem resilience despite large-scale altered hydroclimatic conditions. *Nature*, *494*, 349–352.
- Camps-Valls, G., & Bruzzone, L. (2005). Kernel-based methods for hyperspectral image classification. *IEEE Transactions on Geoscience and Remote Sensing*, *43*, 1351–1362.

- Camps-Valls, G., Gomez-Chova, L., Munoz-Mari, J., Vila-Frances, J., Amoros-Lopez, J., & Calpe-Maravilla, J. (2006). Retrieval of oceanic chlorophyll concentration with relevance vector machines. *Remote Sensing of Environment*, *105*, 23–33.
- Chapin, F.S. (2003). Effects of plant traits on ecosystem and regional processes: A conceptual framework for predicting the consequences of global change. *Annals of Botany*, *91*, 455–463.
- Chen, B., Arain, M.A., Khomik, M., Trofymow, J.A., Grant, R.F., Kurz, W.A., et al. (2013a). Evaluating the impacts of climate variability and disturbance regimes on the historic carbon budget of a forest landscape. *Agricultural and Forest Meteorology*, *180*, 265–280.
- Chen, J.M., & Cihlar, J. (1996). Retrieving leaf area index of boreal conifer forests using Landsat TM Images. *Remote Sensing of Environment*, *55*, 153–162.
- Chen, W.J., Blain, D., Li, J. H., Keohler, K., Fraser, R., Zhang, Y., et al. (2009). Biomass measurements and relationships with Landsat-7/ETM+ and JERS-1/SAR data over Canada's western sub-arctic and low arctic. *International Journal of Remote Sensing*, *30*, 2355–2376.
- Chen, X.L., Su, Z.B., Ma, Y.M., Yang, K., Wen, J., & Zhang, Y. (2013b). An Improvement of Roughness Height Parameterization of the Surface Energy Balance System (SEBS) over the Tibetan Plateau. *Journal of Applied Meteorology and Climatology*, *52*, 607–622.
- Chen, Y., Xia J. Z., Liang, S.L., Feng, J.M., Fisher, J.B., Li, X., et al. (2014). Comparison of satellite-based evapotranspiration models over terrestrial ecosystems in China. *Remote Sensing of Environment*, *140*, 279–293.
- Cheng, G.D., Li, X, Zhao, W.Z., Xu, Z.M., Feng, Q., Xiao, S.C., et al. (2014). Integrated study of the water-ecosystem-economy in the Heihe River Basin. *National Science Review*, *1*, 413–428.
- Chiesi, M., Maselli, F., Moriondo, M., Fibbi, L., Bindi, M., & Running, S.W. (2007). Application of BIOME-BGC to simulate Mediterranean forest processes. *Ecological Modelling*, *206*, 179–190.
- Chiesi, M., Fibbi, L., Genesio, L., Gioli, B., Magno, R., Maselli, F., et al. (2011). Integration of ground and satellite data to model mediterranean forest processes. *International Journal of Applied Earth Observation and Geoinformation*, *13*, 504–515.
- Chiesi, M., Maselli, F., Chirici, G., Corona, P., Lombardi, F., Tognetti, R., et al. (2013). Assessing most relevant factors to simulate current annual increments of beech forests in Italy. *iForest–Biogeosciences and Forestry*, *7*, 115–122.
- Chirici, G., Barbati, A., Corona, P., Marchetti, M., Travaglini, D., Maselli, F., et al. (2008). Non-parametric and parametric methods using satellite imagery for

- estimating growing stock volume in alpine and Mediterranean forest ecosystems. *Remote Sensing of Environment*, 112, 2686–2700.
- Chirouze, J., Boulet, G., Jarlan, L., Fieuzal, R., Rodriguez, J.C., Ezzahar, J., et al. (2014). Intercomparison of four remote-sensing-based energy balance methods to retrieve surface evapotranspiration and water stress of irrigated fields in semi-arid climate. *Hydrology and Earth System Sciences*, 18, 1165–1188.
- Choudhury, B.J., & Monteith, J.L. (1988). A four-layer model for the heat budget of homogeneous land surfaces. *The Quarterly Journal of the Royal Meteorological Society*, 114, 373–398.
- Churkina, G., Running, S.W., & Schloss, A.L. (1999). Comparing global models of terrestrial net primary productivity (NPP): the importance of water availability. *Global Change Biology*, 5, 46–55.
- Churkina, G., Tenhunen, J., Thornton, P., Falge, E.M., Elbers, J.A., Erhard, M., et al. (2003). Analyzing the ecosystem carbon dynamics of four European coniferous forests using a biogeochemistry model. *Ecosystems*, 6, 168–184.
- Ciais, P., Reichstein, M., Viovy, N., Granier, A., Ogee, J., Allard, V. et al. (2005). Europe-wide reduction in primary productivity caused by the heat and drought in 2003. *Nature*, 437, 529–533.
- Cohen, W.B., & Spies, T.A. (1992). Estimating structural attributes of Douglas-Fir/Western Hemlock forest stands from Landsat and SPOT imagery. *Remote Sensing of Environment*, 41, 1–17.
- Coops, N.C., White, J.D., & Scott, N.A. (2004). Effect of forest fragmentation on broad scale estimates of forest biomass accumulation. *International Journal of Remote Sensing*, 20, 819–838.
- Coops, N.C., Black, T.A., Jassal, R.P.S., Trofymow, J.A.T., & Morgenstern, K. (2007). Comparison of MODIS, eddy covariance determined and physiologically modelled gross primary production (GPP) in a Douglas-fir forest stand. *Remote Sensing of Environment*, 107, 385–401.
- Dai, Z.H., Birdsey, R.A., Johnson, K.D., Dupuy, J.M., Hernandez-Stefanoni, J.L., & Richardson, K. (2014). Modeling carbon stocks in a secondary tropical dry forest in the Yucatan Peninsula, Mexico. *Water Air and Soil Pollution*. doi: 10.1007/s11270-014-1925-x.
- Danson, F.M., & Curran, P.J. (1993). Factors affecting the remotely sensed response of coniferous forest plantations. *Remote Sensing of Environment*, 43, 55–65.
- De Jong, S.M., Pebesma, E.J., & Lacaze, B. (2003). Above ground biomass assessment of Mediterranean forests using airborne imaging spectrometry: The DAIS Peyne experiment. *International Journal of Remote Sensing*, 24, 1505–1520.

- Dimitrov, P.K., & Roumenina, E.K. (2013). Combining SPOT 5 imagery with plotwise and standwise forest data to estimate volume and biomass in mountainous coniferous site. *Central European Journal of Geosciences*, 5, 208–222.
- Dobson, M.C., Ulaby, F.T., Le Toan, T., Beaudoin, A., Kasischke, E.S., & Christensen, N. (1992). Dependence of radar backscatter on coniferous forest biomass. *IEEE Transactions on Geoscience and Remote Sensing*, 30, 412–415.
- Dorman, J.L., & Sellers, P.J. (1989). A global climatology of albedo, roughness length and stomatal resistance for atmospheric general circulation models as represented by the Simple Biosphere model (SiB). *Journal of Applied Meteorology*, 28, 833–855.
- Drucker, H., Burges, C.J.C., Kaufman, L., Smola, A., & Vapnik, V. (1997). Support vector regression machines. In *Advances in Neural Information Processing Systems* (pp. 155–161). MIT Press.
- Duncan, R. (1989). An evaluation of errors in tree age estimates based on increment cores in kahikatea (*Dacrycarpus dacrydioides*). *New Zealand Natural Sciences*, 16, 31–37.
- Dury, M., Hambuckers, A., Warnant, P., Henrot, A., Favre, E., Ouberdous, M., et al. (2011). Responses of European forest ecosystems to 21(st) century climate: assessing changes in interannual variability and fire intensity. *iForest-Biogeosciences and Forestry*, 4, 82–99.
- Enquist, B.J., Kerkhoff, A.J., Huxman, T.E., & Economo, E.P. (2007). Adaptive differences in plant physiology and ecosystem paradoxes: insights from metabolic scaling theory. *Global Change Biology*, 13, 591–609.
- Ershadi, A., McCabe, M.F., Evans, J.P., Chaney, N.W., & Wood, E.F. (2014). Multi-site evaluation of terrestrial evaporation models using FLUXNET data. *Agricultural and Forest Meteorology*, 187, 46–61.
- Euskirchen, E.S., McGuire, A.D., Kicklighter, D.W., Zhuang, Q., Clein, J.S., Dargaville, R.J., et al. (2006). Importance of recent shifts in soil thermal dynamics on growing season length, productivity, and carbon sequestration in terrestrial high-latitude ecosystems. *Global Change Biology*, 12, 731–750.
- Fayad, I., Baghdadi, N., Gond, V., Bailly, J.S., Barbier, N., El Hajj, M., et al. (2014). Coupling potential of ICESat/GLAS and SRTM for the discrimination of forest landscape types in French Guiana. *International Journal of Applied Earth Observation and Geoinformation*, 33, 21–31.
- Fazakas, Z., Nilsson, M., & Olsson, H. (1999). Regional forest biomass and wood volume estimation using satellite data and ancillary data. *Agricultural and Forest Meteorology*, 98–99, 417–425.

- Fernández-Prieto, D., van Oevelen, P., Su, Z., & Wagner, W. (2012). Editorial “Advances in Earth observation for water cycle science”. *Hydrology and Earth System Sciences*, *16*, 543–549.
- Filella, I., Penuelas, J., Llorens, L., & Estiarte, M. (2004). Reflectance assessment of seasonal and annual changes in biomass and CO₂ uptake of a Mediterranean shrubland submitted to experimental warming and drought. *Remote Sensing of Environment*, *90*, 308–318.
- Finley, A.O., McRoberts, R.E., & Ek, A.R. (2006). Applying an efficient *k*-nearest neighbor search to forest attribute imputation. *Forest Science*, *52*, 130–135.
- Fisher, J.B., Tu, K.P., & Baldocchi, D.D. (2008). Global estimates of the land-atmosphere water flux based on monthly AVHRR and ISLSCP-II data, validated at 16 FLUXNET sites. *Remote Sensing of Environment*, *112*, 901–919.
- Fisher, J.B., Whittaker, R.J., & Malhi, Y. (2011). ET come home: potential evapotranspiration in geographical ecology. *Global Ecology and Biogeography*, *20*, 1–18.
- Foken, T. (2006). 50 years of the Monin–Obukhov similarity theory. *Boundary-Layer Meteorology*, *119*, 431–447.
- Foody, G.M., Cutler, M.E., Mcmorrow, J., Pelz, D., Tangki, H., Boyd, D.S., et al. (2001). Mapping the biomass of Bornean tropical rain forest from remotely sensed data. *Global Ecology and Biogeography*, *10*, 379–387.
- Foody, G.M. (2003). Remote sensing of tropical forest environments: towards the monitoring of environmental resources for sustainable development. *International Journal of Remote Sensing*, *24*, 4035–4046.
- Fournier, R.A., Luther, J.E., Guindon, L., Lambert, M.C., Piercey, D., Hall, R.J., et al. (2003). Mapping aboveground tree biomass at the stand level from inventory information: test cases in Newfoundland and Quebec. *Canadian Journal of Forest Research*, *33*, 1846–1863.
- Franco-Lopez, H., Ek, A.R., & Bauer, M.E. (2001). Estimation and mapping of forest stand density, volume and cover type using the *k*-nearest neighbors method. *Remote Sensing of Environment*, *77*, 251–274.
- Friedlingstein, P., Houghton, R.A., Marland, G., Hackler, J., Boden, T.A., Conway, T. J., et al. (2010). Update on CO₂ emissions. *Nature Geoscience*, *3*, 811–812.
- Fu, D.J., Chen, B.Z., Zhang, B.Z., Zhang, H.F., Wang, J., Black, T.A., et al. (2014). Estimating landscape net ecosystem exchange at high spatial–temporal resolution based on Landsat data, an improved upscaling model framework, and eddy covariance flux measurements. *Remote Sensing of Environment*, *141*, 90–104.

- Fuchs, H., Magdon, P., Kleinn, C., & Flessa, H. (2009). Estimating aboveground carbon in a catchment of the siberian forest tundra: combining satellite imagery and field inventory. *Remote Sensing of Environment*, *113*, 518–531.
- Gao, Q., Yu, M., & Yang, X.S. (2000). An analysis of sensitivity of terrestrial ecosystems in China to climatic change using spatial simulation. *Climatic Change*, *47*, 373–400.
- García, M., Riaño, D., Chuvieco, E., & Danson, F.M. (2010). Estimating biomass carbon stocks for a Mediterranean forest in central Spain using LiDAR height and intensity data. *Remote Sensing of Environment*, *114*, 816–830.
- Garratt, J.R. (1994). The atmospheric boundary layer. Cambridge. New York: Cambridge University Press.
- Gebremichael, M., & Barros, A.P. (2006). Evaluation of MODIS Gross Primary Productivity (GPP) in tropical monsoon regions. *Remote Sensing of Environment*, *100*, 150–166.
- Ghasemi, N., Mohammadzadeh, A., & Sahebi, M.R. (2013). Assessment of different topographic correction methods in ALOS AVNIR-2 data over a forest area. *International Journal of Digital Earth*, *6*, 504–520.
- Gilichinsky, M., Heiskanen, J., Barth, A., Wallerman, J., Egberth, M., & Nilsson, M. (2012). Histogram matching for the calibration of k -NN stem volume estimates. *International Journal of Remote Sensing*, *33*, 7117–7131.
- Githui, F., Selle, B., & Thayalakumaran, T. (2012). Recharge estimation using remotely sensed evapotranspiration in an irrigated catchment in southeast Australia. *Hydrological Processes*, *26*, 1379–1389.
- Gleason, C.J., & Im, J. (2012). Forest biomass estimation from airborne LiDAR data using machine learning approaches. *Remote Sensing of Environment*, *125*, 80–91.
- Gokmen, M., Vekerdy, Z., Verhoef, A., Verhoef, W., Batelaan, O., & van der Tol, C. (2012). Integration of soil moisture in SEBS for improving evapotranspiration estimation under water stress conditions. *Remote Sensing of Environment*, *121*, 261–274.
- Gonzalez, P., Asner, G.P., Battles, J.J., Lefsky, M.A., Waring, K.M., & Palace, M. (2010). Forest carbon densities and uncertainties from LiDAR, QuickBird, and field measurements in California. *Remote Sensing of Environment*, *114*, 1561–1575.
- Goodale, C.L., Apps, M.J., Birdsey, R.A., Field, C.B., Heath, L.S., Houghton, R.A., et al. (2002). Forest carbon sinks in the Northern Hemisphere. *Ecological Applications*, *12*, 891–899.
- Gou, X., Chen, F., Yang, M., Li, J., Peng, J., & Jin, L. (2005). Climatic response of thick leaf spruce (*Picea crassifolia*) tree-ring width at different elevations over

- Qilian Mountains, northwestern China. *Journal of arid environments*, 61, 513–524.
- Govind, A., Chen J.M., McDonnell, J., Kumari, J., & Sonnentag, O. (2011). Effects of lateral hydrological processes on photosynthesis and evapotranspiration in a boreal ecosystem. *Ecohydrology*, 4, 394–410.
- Gray, A.N., & Whittier, T.R. (2014). Carbon stocks and changes on Pacific Northwest national forests and the role of disturbance, management, and growth. *Forest Ecology and Management*, 328, 167–178.
- Gu, D., & Gillespie, A. (1998). Topographic normalization of Landsat TM images of forest based on subpixel sun-canopy-sensor geometry. *Remote Sensing of Environment*, 64, 166–175.
- Hall, F.G., Shimabukuro, Y., & Huemmrich, K.F. (1995). Remote sensing of forest biophysical structure using mixture decomposition and geometric reflectance models. *Ecological Applications*, 5, 993–1013.
- Hall, R.J., Skakun, R.S., Arsenault, E.J., & Case, B.S. (2006). Modeling forest stand structure attributes using Landsat ETM+ data: application to mapping of above ground biomass and stand volume. *Forest Ecology and Management*, 225, 378–390.
- Hansen, M.C., DeFries, R.S., Townshend, J.R.G., & Sohlberg, R. (2000). Global land cover classification at 1 km spatial resolution using a classification tree approach. *International Journal of Remote Sensing*, 21, 1331–1364.
- Hawkins, B.A., Field, R., Cornell, H.V., Currie, D.J., Guegan, J., Kaufman, D.M., et al. (2003). Energy, water, and broad-scale geographic patterns of species richness. *Ecology*, 84, 3105–3117.
- Hayes, D.J., Turner, D.P., Stinson, G., McGuire, A.D., Wei, Y., West, T.O., et al. (2012). Reconciling estimates of the contemporary North American carbon balance among terrestrial biosphere models, atmospheric inversions, and a new approach for estimating net ecosystem exchange from inventory-based data. *Global Change Biology*, 18, 1282–1299.
- He, Q.S. (2010). *Study on forest biomass synergy inversion from multi-source remote sensing data*. PhD-thesis (in Chinese). Beijing, the China: Institute of Remote Sensing Applications, Chinese Academy of Sciences.
- Heinsch, F.A., Zhao, M.S., Running, S.W., Kimball, J.S., Nemani, R.R., Davis, K.J., et al. (2006). Evaluation of remote sensing based terrestrial productivity from MODIS using regional tower eddy flux network observations. *IEEE Transactions on Geoscience and Remote Sensing*, 44, 1908–1925.
- Heurich, M., & Thoma, F. (2008). Estimation of forestry stand parameters using laser scanning data in temperate, structurally rich natural European beech (*Fagus sylvatica*) and Norway spruce (*Picea abies*) forests. *Forestry*, 81, 645–661.

- Hill, T.C., Williams, M., Bloom, A.A., Mitchard, E.T.A., Ryan, C.M., & Bond-Lamberty, B. (2013). Are inventory based and remotely sensed above-ground biomass estimates consistent? *PLOS One*, *8*, e74170.
- Holmes, R.L. (1983). Computer-assisted quality control in tree-ring dating and measurement. *Tree-Ring Bulletin*, *43*, 69–78.
- Holmström, H., Nilsson, M., & Ståhl, G. (2001). Simultaneous estimations of forest parameters using aerial photograph interpreted data and the k nearest neighbor method. *Scandinavian Journal of Forest Research*, *16*, 67–78.
- Holmström, H., & Fransson, J. (2003). Combining remotely sensed optical and radar data in k -NN estimation of forest variables. *Forest Science*, *49*, 409–418.
- Houghton, R.A., Skole, D.L., Nobre, C.A., Hackler, J.L., Lawrence, K.T., & Chomentowski, W.H. (2000). Annual fluxes of carbon from deforestation and regrowth in the Brazilian Amazon. *Nature*, *403*, 301–304.
- Houghton, R.A., Lawrence, K.T., Hackler, J.L., & Brown, S. (2001). The spatial distribution of forest biomass in the Brazilian Amazon: a comparison of estimates. *Global Change Biology*, *7*, 731–746.
- Houghton, R.A. (2005). Aboveground forest biomass and the global carbon balance. *Global Change Biology*, *11*, 945–958.
- Hu, B., Miller, J.R., Chen, J.M., & Hollinger, A. (2004). Retrieval of the canopy leaf area index in the BOREAS flux tower sites using linear spectral mixture analysis. *Remote Sensing of Environment*, *89*, 176–188.
- Hu, Y.Q., Gao, Y.X., Wang, J.M., Ji, G.L., Shen, Z.B., Cheng, L.S., et al. (1994). Some achievements in scientific research during HEIFE. *Plateau Meteorology*, *13*, 225–236. (In Chinese)
- Huang, C., Li, Y.F., Liu, G.H., Zhang, H.L., & Liu, Q.S. (2014). Recent climate variability and its impact on precipitation, temperature, and vegetation dynamics in the Lancang River headwater area of China. *International Journal of Remote Sensing*, *35*, 2822–2834.
- Huang, C.Y., Asner, G.P., Barger, N.N., Neff, J.C., & Floyd, M.L. (2010). Regional aboveground live carbon losses due to drought-induced tree dieback in piñon–juniper ecosystems. *Remote Sensing of Environment*, *114*, 1471–1479.
- Huang, W.L., Sun, G.Q., Dubayah, R., Cook, B., Montesano, P., Ni, W. J., et al. (2013). Mapping biomass change after forest disturbance: Applying LiDAR footprint-derived models at key map scales. *Remote Sensing of Environment*, *134*, 319–332.
- Huxman, T.E., Smith, M.D., Fay, P.A., Knapp, A.K., Shaw, M.R., Loik, M.E., et al. (2004). Convergence across biomes to common rain-use efficiency. *Nature*, *429*, 651–654.

- Jackson, R.B., Carpenter, S.R., Dahm, C.N., McKnight, D.M., Naiman, R.J., Postel, S.L., et al. (2001). Water in a changing world. *Ecological Application*, *11*, 1027–1045.
- Jarvis, P.G., & Leverenz, J.W. (1983). Productivity of temperate, deciduous and evergreen forests. In O. L. Lange, P.S. Nobel, C.B. Osmond, and Dr.H. Ziegler (Eds), *Physiological Plant Ecology IV* (pp. 233–280). New York: Springer-Verlag.
- Jasechko, S., Sharp, Z.D., Gibson, J.J., Birks, S.J., Yi, Y., & Fawcett, P.J. (2013). Terrestrial water fluxes dominated by transpiration. *Nature*, *496*, 347–350.
- Jia, Z.Z., Liu, S.M., Xu, Z.W., Chen, Y.Y., & Zhu, M.J. (2012). Validation of remotely sensed evapotranspiration over the Hai River Basin, China. *Journal of Geophysical Research–Atmospheres*. doi: 10.1029/2011jd017037.
- Jin, C., Xiao, X.M., Merbold, L., Arneith, A., Veenendaal, E., & Kutsch, W.L. (2013). Phenology and gross primary production of two dominant savanna woodland ecosystems in Southern Africa. *Remote Sensing of Environment*, *135*, 189–201.
- Ju, W.M., Gao, P., Wang, J., Zhou, Y.L., & Zhang, X.H. (2010). Combining an ecological model with remote sensing and GIS techniques to monitor soil water content of croplands with a monsoon climate. *Agricultural Water Management*, *97*, 1221–1231.
- Kane, V.R., Gillespie, A.R., McGaughey, R., Lutz, J.A., Ceder, K., & Franklin, J.F. (2008). Interpretation and topographic compensation of conifer canopy self-shadowing. *Remote Sensing of Environment*, *112*, 3820–3832.
- Kasischke, E.S., Melack, J.M., & Dobson, M.C. (1997). The use of imaging radars for ecological applications—a review. *Remote Sensing of Environment*, *59*, 141–156.
- Katila, M., & Tomppo, E. (2001). Selecting estimation parameters for the Finnish multisource national forest inventory. *Remote Sensing of Environment*, *76*, 16–32.
- Keenan, T.F., Davidson, E., Moffat, A.M., Munger, W., & Richardson, A.D. (2012). Using model-data fusion to interpret past trends, and quantify uncertainties in future projections, of terrestrial ecosystem carbon cycling. *Global Change Biology*, *18*, 2555–2569.
- Keenan, T.F., Hollinger, D.Y., Bohrer, G., Dragoni, D., Munger, J.W., Schmid, H.P., et al. (2013). Increase in forest water-use efficiency as atmospheric carbon dioxide concentrations rise. *Nature*, *499*, 324–327.
- Kerkhoff, A.J., Enquist, B.J., Elser, J.J. & Fagan, W.F. (2005). Plant allometry, stoichiometry and the temperature-dependence of primary productivity. *Global Ecology and Biogeography*, *14*, 585–598.

- Kimball, J.S., Zhao, M., McGuire, A.D., Heinsch, F.A., Clein, J., Calef, M., et al. (2007). Recent climate-driven increases in vegetation productivity for the western arctic: evidence of an acceleration of the northern 5 terrestrial carbon cycle. *Earth Interactions*, *11*, 1–30.
- Kohavi, R., & John, G.H. (1997). Wrappers for feature subset selection. *Artificial Intelligence*, *97*, 273–324.
- Komatsu, H., Kume, T., & Otsuki, K. (2008). The effect of converting a native broadleaved forest to a coniferous plantation forest on annual water yield: a paired catchment study in northern Japan. *Forest Ecology and Management*, *255*, 880–886.
- Koloskov, G., Mukhamejanov, K., & Tanton, T.W. (2007). Monin–Obukhov length as a cornerstone of the SEBAL calculations of evapotranspiration. *Journal of Hydrology*, *335*, 170–179.
- Koster, R.D., Dirmeyer, P.A., Guo, Z.C., Bonan, G., Chan, E., Cox, P., et al. (2004). Regions of strong coupling between soil moisture and precipitation. *Science*, *305*, 1138–1140.
- Koukoulas, S., & Blackburn, G.A. (2005). Mapping individual tree location, height and species in broadleaved deciduous forest using airborne LiDAR and multispectral remotely sensed data. *International Journal of Remote Sensing*, *26*, 431–455.
- Kreft, H., & Jetz, W. (2007). Global patterns and determinants of vascular plant diversity. *Proceedings of the National Academy of Sciences of the United States of America*, *104*, 5925–5930.
- Krishnan, P., & Kunhikrishnan, P.K. (2002). Some characteristics of atmospheric surface layer over tropical inland region during southwest monsoon period. *Atmospheric Research*, *62*, 111–124.
- Kuplich, T., Salvatori, V., & Curran, P. (2000). JERS-1/SAR backscatter and its relationship with biomass of regenerating forests. *International Journal of Remote Sensing*, *21*, 2513–2518.
- Kurvonen, L., Pulliainen, J., & Hallikainen, M. (1999). Retrieval of biomass in boreal forest from multitemporal ERS-1 and JERS-1 SAR images. *International Journal of Remote Sensing*, *37*, 198–205.
- Kustas, W., & Norman, J. (1996). Use of remote sensing for evapotranspiration monitoring over land surfaces. *Hydrological Sciences Journal (United Kingdom)*, *41*, 495–516.
- Labrecque, S., Fournier, R.A., Luther, J.E., & Piercey, D E. (2006). A comparison of four methods to map forest biomass from Landsat-TM and inventory data in Western Newfoundland. *Forest Ecology and Management*, *226*, 129–144.

- Lachenbruch, P.A. (1967). An almost unbiased method of obtaining confidence intervals for the probability of misclassification in discriminant analysis. *Biometrics*, 23, 639–645.
- Latifi, H., Nothdurft, A., & Koch, B. (2010). Non-parametric prediction and mapping of standing timber volume and biomass in a temperate forest: application of multiple optical/LiDAR-derived predictors. *Forestry*, 83, 395–407.
- Latifi, H. & Koch, B. (2012). Evaluation of most similar neighbour and random forest methods for imputing forest inventory variables using data from target and auxiliary stands. *International Journal of Remote Sensing*, 33, 6668–6694.
- Lauenroth, W.K. (1979). Grassland primary production: North American grasslands in perspective. In N. French (Ed.), *Perspectives in Grassland Ecology* (pp. 3–24). New York: Springer.
- Law, B.E., Falge, E., Gu, L., Baldocchi, D.D., Bakwin, P., Berbigier, P., et al. (2002). Environmental controls over carbon dioxide and water vapour exchange of terrestrial vegetation. *Agricultural and Forest Meteorology*, 113, 97–120.
- Lawrence, R.L., & Ripple, W.J. (1998). Comparisons among vegetation indices and band-wise regression in a highly disturbed, heterogeneous landscape: Mount St. Helens, Washington. *Remote Sensing of Environment*, 64, 91–102.
- Leboeuf, A., Beaudoin, A., Fournier, R.A., Guindon, L., Luther, J.E., & Lambert, M.C. (2007). A shadow fraction method to map biomass of Northern boreal black spruce forest using QuickBird imagery. *Remote Sensing of Environment*, 110, 488–500.
- Lee, J.E., Lintner, B.R., Boyce, C.K., & Lawrence, P.J. (2011). Land use change exacerbates tropical South American drought by sea surface temperature variability. *Geophysical Research Letters*. doi: 10.1029/2011GL049066.
- Lefsky, M.A., Cohen, W.B., Harding, D.J., Parker, G.G., Acker, S.A., & Gower, S.T. (2002a). LiDAR remote sensing of above ground biomass in three biomes. *Global Ecology and Biogeography*, 11, 393–399.
- Lefsky, M.A., Cohen, W.B., Parker, G.G., & Harding, D.J. (2002b). LiDAR remote sensing for ecosystem studies. *BioScience*, 52, 19–30.
- Le Toan, T., Beaudoin, A., & Guyon, D. (1992). Relating forest biomass to SAR data. *IEEE Transactions on Geoscience and Remote Sensing*, 30, 403–411.
- Li, L.J., Tilley, D.R., Lu, H.F., Ren, H., & Qiu, G.Y. (2013a). Comparison of an energy systems mini-model to a process-based eco-physiological model for simulating forest growth. *Ecological Modelling*, 263, 32–41.
- Li, M., Im, J., Quackenbush, L.J., & Liu, T. (2014). Forest biomass and carbon stock quantification using airborne LiDAR Data: A case study over

- Huntington Wildlife Forest in the Adirondack Park. *IEEE Journal of Selected Topics in Applied Earth Observations and Remote Sensing*, 7, 3143–3156.
- Li, S., Harner, E.J., & Adjeroh, D.A. (2011a). Random k -NN feature selection—a fast and stable alternative to random forests. *BMC bioinformatics*, 12, 450.
- Li, X., Li, X.W., Li, Z. Y., Ma, M. G., Wang, J., Xiao, Q., et al. (2009a). Watershed allied telemetry experimental research. *Journal of Geophysical Research-Atmospheres*, 114, D22103, doi:10.1029/2008JD011590.
- Li, X., Li, X.W., Roth, K., Menenti, M., & Wagner, W. (2011b). Preface “Observing and modeling the catchment scale water cycle”. *Hydrology and Earth System Sciences*, 15, 597–601.
- Li, X., Cheng, G.D., Liu, S.M., Xiao, Q., Ma, M.G., Jin, R., et al. (2013b). Heihe watershed allied telemetry experimental research (HiWATER): scientific objectives and experimental design. *Bulletin of the American Meteorological Society*, 94, 1145–1160.
- Li, X.W., & Strahler, A.H. (1985). Geometric–optical modeling of a conifer forest canopy. *IEEE Transactions on Geoscience and Remote Sensing*, GE-23, 705–721.
- Li, Z. L., Tang, R.L., Wan, Z.M., Bi, Y.Y., Zhou, C.H., Tang, B.H., et al. (2009b). A review of current methodologies for regional evapotranspiration estimation from remotely sensed data. *Sensors*, 9, 3801–3853.
- Liang, E.Y., Shao, X.M., Eckstein, D., Huang, L., & Liu, X.H. (2006). Topography- and species-dependent growth responses of *Sabina przewalskii* and *Picea crassifolia* to climate on the northeast Tibetan Plateau. *Forest Ecology and Management*, 236, 268–277.
- Liang, S.L., Zhao, X., Liu, S.H., Yuan, W.P., Cheng, X., Xiao, Z.Q., et al. (2013). A long-term Global LAnd Surface Satellite (GLASS) data-set for environmental studies. *International Journal of Digital Earth*, 6, 5–33.
- Lim, K.S., & Treitz, P.M. (2004). Estimation of above ground forest biomass from airborne discrete return laser scanner data using canopy based quantile estimators. *Scandinavian Journal of Forest Research*, 19, 558–570.
- Lindner, M., Maroschek, M., Netherer, S., Kremer, A., Barbati, A., Garcia-Gonzalo, J., et al. (2010). Climate change impacts, adaptive capacity, and vulnerability of European forest ecosystems. *Forest Ecology and Management*, 259, 698–709.
- Liu, S.Y., Sun, W.X., Shen, Y.P., & Li, G. (2003). Glacier changes since the Little Ice Age maximum in the western Qilian Shan, northwest China, and consequences of glacier runoff for water supply. *Journal of Glaciology*, 49, 117–124.

- Liu, Y., Zhou, Y., Ju, W., Chen, J., Wang, S., He, H., et al. (2013). Evapotranspiration and water yield over China's landmass from 2000 to 2010. *Hydrology and Earth System Sciences*, 17, 4957–4980.
- Lorey, T. (1878). Die mittlere Bestandeshöhe. *Allg. Forst- u. J. - Ztg.*, 54, 149–155.
- Lu, D., Batistella, M., & Moran, E. (2005). Satellite estimation of aboveground biomass and impacts of forest stand structure. *Photogrammetric Engineering and Remote Sensing*, 71, 967–974.
- Lu, D. (2006). The potential and challenge of remote sensing based biomass estimation. *International Journal of Remote Sensing*, 27, 1297–1328.
- Lucas, R.M., Lee, A.C., & Bunting, P. J. (2008). Retrieving forest biomass through integration of CASI and LiDAR data. *International Journal of Remote Sensing*, 29, 1553–1577.
- Luckman, A., Baker, J., Kuplich, T.M., Yanasse, C.C.F., & Frery, A.C. (1997). A study of the relationship between radar backscatter and regenerating tropical forest biomass for spaceborne SAR instruments. *Remote Sensing of Environment*, 60, 1–13.
- Lufafa, A., Bolte, J., Wright, D., Khouma, M., Diedhiou, I., Dick, R. P., et al. (2008). Regional carbon stocks and dynamics in native woody shrub communities of Senegal's Peanut Basin. *Agriculture, Ecosystems and Environment*, 128, 1–11.
- Luther, J.E., Fournier, R.A., Piercey, D.E., Guindon, L., & Hall, R. J. (2005). Biomass mapping using forest type and structure derived from Landsat TM imagery. *International Journal of Applied Earth Observation and Geoinformation*, 8, 173–187.
- Ma, W.Q., Ma, Y.M., & Ishikawa, H. (2014). Evaluation of the SEBS for upscaling the evapotranspiration based on in-situ observations over the Tibetan Plateau. *Atmospheric Research*, 138, 91–97.
- Magnussen, S., & Boudewyn, P. (1998). Derivations of stand heights from airborne laser scanner data with canopy based quantile estimators. *Canadian Journal of Forest Research*, 28, 1016–1031.
- Magnussen, S., Tomppo, E., & McRoberts, R. (2010). A model-assisted *k*-nearest neighbour approach to remove extrapolation bias. *Scandinavian Journal of Forest Research*, 25, 174–184.
- Mahapatra, D. (2014). Analyzing training information from random forests for improved image segmentation. *IEEE Transactions on Image Processing*, 23, 1504–1512.
- Main-Knorn, M., Moisen, G.G., Healey, S.P., Keeton, W.S., Freeman, E.A., & Hostert, P. (2011). Evaluating the remote sensing and inventory-based estimation of biomass in the Western carpathians. *Remote Sensing*, 3, 1427–1446.

- Main-Knorn, M., Cohen, W.B., Kennedy, R.E., Grodzki, W., Pflugmacher, D., Griffiths, P., et al. (2013). Monitoring coniferous forest biomass change using a Landsat trajectory-based approach. *Remote Sensing of Environment*, 139, 277–290.
- Maltamo, M., Eerikäinen, K., Pitkänen, J., Hyypä, J., & Vehmas, M. (2004). Estimation of timber volume and stem density based on scanning laser altimetry and expected tree size distribution functions. *Remote Sensing of Environment*, 90, 319–330.
- Maselli, F. (2001). Extension of environmental parameters over the land surface by improved fuzzy classification of remotely sensed data. *International Journal of Remote Sensing*, 22, 3597–3610.
- Maselli, F., Chirici, G., Bottai, L., Corona, P., & Marchetti, M. (2005). Estimation of Mediterranean forest attributes by the application of k -NN procedures to multi-temporal Landsat ETM + images. *International Journal of Remote Sensing*, 26, 3781–3796.
- Maselli, F., Barbati, A., Chiesi, M., Chirici, G., & Corona, P. (2006). Use of remotely sensed and ancillary data for estimating forest gross primary productivity in Italy. *Remote Sensing of Environment*, 100, 563–575.
- Maselli, F., & Chiesi, M. (2006). Evaluation of statistical methods to estimate forest volume in a Mediterranean region. *IEEE Transactions on Geoscience and Remote Sensing*, 44, 2239–2250.
- Maselli, F., Chiesi, M., Fibbi, L., & Moriondo, M. (2008). Integration of remote sensing and ecosystem modelling techniques to estimate forest net carbon uptake. *International Journal of Remote Sensing*, 29, 2437–2443.
- Maselli, F., Papale, D., Puletti, N., Chirici, G., & Corona, P. (2009). Combining remote sensing and ancillary data to monitor the gross productivity of water-limited forest ecosystems. *Remote Sensing of Environment*, 113, 657–667.
- Mattioli, W., Quatrini, V., Di Paolo, S., Di Santo, D., Giuliarelli, D., Angelini, A., Portoghesi, L., & Corona, P. (2012). Experimenting the Design-Based k -NN Approach for Mapping and Estimation under Forest Management Planning. *IForest—Biogeosciences and Forestry*, 5, 26–30.
- McKinley, D.C., Ryan, M.G., Birdsey, R.A., Giardina, C.P., Harmon, M.E., Heath, L.S., et al. (2011). A synthesis of current knowledge on forests and carbon storage in the United States. *Ecological Applications*, 21, 1902–1924.
- McRoberts, R.E., Tomppo, E.O., Finley, A.O., & Heikkinen, J.H. (2007). Estimating areal means and variances of forest attributes using the k -nearest neighbours technique and satellite imagery. *Remote Sensing of Environment*, 111, 466–480.
- McRoberts, R.E. (2009). Diagnostic tools for nearest neighbors techniques when used with satellite imagery. *Remote Sensing of Environment*, 113, 489–499.

- McRoberts, R.E. (2012). Estimating forest attribute parameters for small areas using nearest neighbors techniques. *Forest Ecology and Management*, 272(SI), 3–12.
- Meijer, R.J., & Goeman. J.J. (2013). Efficient approximate k -fold and leave-one-out cross-validation for ridge regression. *Biometrical Journal*, 55, 141–155.
- Méndez-Barroso, L. A., Vivoni, E. R., Robles-Morua, A., Mascaro, G., Yépez, E. A., Rodríguez, J.C., et al. (2014). A modeling approach reveals differences in evapotranspiration and its partitioning in two semiarid ecosystems in Northwest Mexico. *Water Resources Research*, 50, 3229–3252.
- Michaletz, S.T., Cheng, D.J., Kerkhoff, A.J., & Enquist, B.J. (2014). Convergence of terrestrial plant production across global climate gradients. *Nature*. doi:10.1038/nature13470.
- Minchella, A., Del Frate, F., Capogna, F., Anselmi, S., & F. Manes. (2009). Use of multitemporal SAR data for monitoring vegetation recovery of mediterranean burned areas. *Remote Sensing of Environment*, 113, 588–597.
- Miralles, D.G., Holmes, T. R. H., De Jeu, R.A.M., Gash, J.H., Meesters, A.G.C.A., & Dolman, A.J. (2011). Global land-surface evaporation estimated from satellite-based observations. *Hydrology and Earth System Sciences*, 15, 453–469.
- Moghaddam, M., Dungan, J.L., & Acker, S. (2002). Forest variable estimation from fusion of SAR and multispectral optical data. *IEEE Transactions on Geoscience and Remote Sensing*, 40, 2176–2187.
- Mohamed, M.A.A., Babiker, I.S., Chen, Z.M., Ikeda, K., Ohta, K., & Kato, K. (2004). The role of climate variability in the inter-annual variation of terrestrial net primary production (NPP). *Science of the Total Environment*, 332, 123–137.
- Molders, N., & Raabe, A. (1996). Numerical investigations on the influence of subgrid-scale surface heterogeneity on evapotranspiration and cloud processes. *Journal of Applied Meteorology*, 35, 782–795.
- Monin, A.S., & Obukhov, A.M. (1954). Basic laws of turbulent mixing in the ground layer of the atmosphere. *Trudy Geofizicheskogo Instituta, Akademiya Nauk SSSR*, 24, 163–187.
- Monnet, J.M., Chanussot, J., & Berger, F. (2011). Support vector regression for the estimation of forest stand parameters using airborne Laser scanning. *IEEE Geoscience and Remote Sensing Letters*, 8, 580–584.
- Monsi, M., & Saeki, T. (2005). On the factor light in plant communities and its importance for matter production. *Annals of Botany*, 95, 549–567.
- Monteith, J.L. (1972). Solar radiation and productivity in tropical ecosystems. *Journal of Applied Ecology*, 9, 747–766.

- Moreau, S., Bosseno, R., Gu, X.F., & Baretc, F. (2003). Assessing the biomass dynamics of Andean bofedal and totora high-protein wetland grasses from NOAA/AVHRR. *Remote Sensing of Environment*, 85, 516–529.
- Mountrakis, G., Im, J., & Ogole, C. (2011). Support vector machines in remote sensing: A review. *ISPRS Journal of Photogrammetry and Remote Sensing*, 66, 247–259.
- Mu, Q., Heinsch, F.A., Zhao, M., & Running, S.W. (2007). Development of a global evapotranspiration algorithm based on MODIS and global meteorology data. *Remote Sensing of Environment*, 111, 519–536.
- Muinsonen, E., Maltamo, M., Hyppänen, H., & Vainikainen, V. (2001). Forest stand characteristics estimation using a most similar neighbor approach and image spatial structure information. *Remote Sensing of Environment*, 78, 223–228.
- Mutanga, O., & Skidmore, A.K. (2004). Narrow band vegetation indices overcome the saturation problem in biomass estimation. *International Journal of Remote Sensing*, 25, 3999–4014.
- Muukkonen, P., & Heiskanen, J. (2007). Biomass estimation over a large area based on standwise forest inventory data and ASTER and MODIS satellite data: A possibility to verify carbon inventories. *Remote Sensing of Environment*, 107, 617–624.
- Næsset, E. (2002). Predicting forest stand characteristics with airborne scanning laser using a practical two-stage procedure and field data. *Remote Sensing of Environment*, 80, 88–99.
- Næsset, E. (2004). Practical large scale forest stand inventory using a small footprint airborne scanning laser. *Scandinavian Journal of Forest Research*, 19, 164–179.
- Næsset, E. (2007). Airborne laser scanning as a method in operational forest inventory: status of accuracy assessments accomplished in Scandinavia. *Scandinavian Journal of Forest Research*, 22, 433–442.
- Næsset, E., & Gobakken, T. (2008). Estimation of above and below-ground biomass across regions of the boreal forest zone using airborne laser. *Remote Sensing of Environment*, 112, 3079–3090.
- Næsset, E., Bollandsås, O.M., Gobakken, T., Gregoire, T.G., & Ståhl, G. (2013). Model-assisted estimation of change in forest biomass over an 11 year period in a sample survey supported by airborne LiDAR: A case study with post-stratification to provide “activity data”. *Remote Sensing of Environment*, 128, 299–314.
- Nakai, T., Sumida, A., Daikoku, K., Matsumoto, K., van derMolen, M.K., Kodama, Y., et al. (2008). Parameterisation of aerodynamic roughness over boreal, cool- and warm-temperate forests. *Agricultural and Forest Meteorology*, 148, 1916–1925.

- Nakai, T., Sumida, A., Kodama, Y., Hara, T., & Ohta, T. (2010). A comparison between various definitions of forest stand height and aerodynamic canopy height. *Agricultural and Forest Meteorology*, *150*, 1225–1233.
- Neeff, T., Graca, P.M.D., Dutra, L.V., & Freitas, C.D.C. (2005). Carbon budget estimation in Central Amazonia: Successional forest modeling from remote sensing data. *Remote Sensing of Environment*, *94*, 508–522.
- Neigh, C.S.R., Nelson, R.F., Ranson, K.J., Margolis, H.A., Montesano, P.M., Sun, G.Q., et al. (2013). Taking stock of circumboreal forest carbon with ground measurements, airborne and spaceborne LiDAR. *Remote Sensing of Environment*, *137*, 274–287.
- Nelson, B.W., Mesquita, R., Pereira, J.L.G., De Souza, S.G.A., Batista, G.T., & Couto, L.B. (1999). Allometric regression for improved estimate of secondary forest biomass in the central Amazon. *Forest Ecology and Management*, *117*, 149–167.
- Nelson, R., Krabill, W., & Tonelli, J. (1988). Estimating forest biomass and volume using airborne laser data. *Remote Sensing of Environment*, *24*, 247–267.
- Nelson, R., Jimenez, J., Schnell, C.E., Hartshorn, G.S., Gregoire, T.G., & Oderwald, R. (2000a). Canopy height models and airborne lasers to estimate forest biomass: two problems. *International Journal of Remote Sensing*, *21*, 2153–2162.
- Nelson, R.F., Kimes, D.S., Salas, W.A., & Routhier, M. (2000b). Secondary forest age and tropical forest biomass estimation using Thematic Mapper imagery. *Bioscience*, *50*, 419–431.
- Nemani, R.R., Keeling, C.D., Hashimoto, H., Jolly, W.M., Piper, S.C., Tucker, C.J., et al. (2003). Climate-driven increases in global terrestrial net primary production from 1982 to 1999. *Science*, *300*, 1560–1563.
- Neumann, M., Saatchi, S.S., Ulander, L.M.H., & Fransson, J.E.S. (2012). Assessing performance of L- and P-band polarimetric interferometric SAR data in estimating boreal forest above-ground biomass. *IEEE Transactions on Geoscience and Remote Sensing*, *50*, 714–726.
- Nightingale, J.M., Coops, N.C., Waring, R.H., & Hargrove, W.W. (2007). Comparison of MODIS gross primary production estimates for forests across the USA with those generated by a simple process model, 3-PGS. *Remote Sensing and Environment*, *109*, 500–509.
- Oki, T., & Kanae, S. (2006). Global hydrological cycles and world water resources. *Science*, *313*, 1068–1072.
- Olthof, I., & Fraser, R.H. (2007). Mapping northern land cover fractions using Landsat ETM+. *Remote Sensing of Environment*, *107*, 496–509.

- Osmond, B., Ananyev, G., Berry, J.A., Langdon, C., Kolber, Z., Lin, G., et al. (2004). Changing the way we think about global change research: scaling up in experimental ecosystem science. *Global Change Biology*, 10, 393–407.
- Ouyang, S., Wan, X.P., Wu, Y.L., Sun, J.X., & Osbert. (2014). Contrasting responses of net primary productivity to inter-annual variability and changes of climate among three forest types in northern China. *Journal of Plant Ecology*, 7, 309–320.
- Palacios-Orueta, A., Chuvieco, E., Parra, A., & Carmona-Moreno, C. (2005). Biomass burning emissions: a review of models using remote sensing data. *Environmental Monitoring and Assessment*, 104, 189–209.
- Pan, M., Wood, E.F., Wojcik, R., & McCabe, M.F. (2008). Estimation of regional terrestrial water cycle using multi-sensor remote sensing observations and data assimilation. *Remote Sensing of Environment*, 112, 1282–1294.
- Pan, X.D., & Li, X. (2011). Validation of WRF model on simulating forcing data for Heihe River Basin. *Sciences in Cold and Arid Regions*, 3, 0344–0357.
- Pan, X.D., Li, X., Shi, X.K., Han, X.J., Luo, L.H., & Wang, L.X. (2012). Dynamic downscaling of near-surface air temperature at the basin scale using WRF—a case study in the Heihe River Basin, China. *Frontier of Earth Science*, 6, 314–323.
- Pan, Y.D., Birdsey, R.A., Fang, J.Y., Houghton, R., Kauppi, P.E., Kurz, W.A. et al. (2011). A large and persistent carbon sink in the world's forests. *Science*, 333, 988–993.
- Pardo, N., Sanchez, M.L., Timmermans, J., Su, Z.B., Perez, I.A., & Garcia, M.A. (2014). SEBS validation in a Spanish rotating crop. *Agricultural and Forest Meteorology*, 195, 132–142.
- Parresol, B.R. (1999). Assessing tree and stand biomass: a review with examples and critical comparisons. *Forest Science*, 45, 573–593.
- Pasolli, L., Notarnicola, C., & Bruzzone, L. (2011). Estimating soil moisture with the support vector regression technique. *IEEE Geoscience and Remote Sensing Letters*, 8, 1080–1084.
- Pasolli, L., Notarnicola, C., & Bruzzone, L. (2012). Multi-objective parameter optimization in support vector regression: general formulation and application to the retrieval of soil moisture from remote sensing data. *IEEE Journal of Selected Topics in Applied Earth Observations and Remote Sensing*, 5, 1495–1508.
- Patenaude, G., Hill, R.A., Milne, R., Gaveau, D.L.A., Briggs, B.B.J., & Dawson, T.P. (2004). Quantifying forest above ground carbon content using LiDAR remote sensing. *Remote Sensing of Environment*, 93, 368–380.

- Patenaude, G., Milne, R., & Dawson, T.P. (2005). Synthesis of remote sensing approaches for forest carbon estimation: reporting to the Kyoto Protocol. *Environmental Science and Policy*, 8, 161–178.
- Peng, S.Z., Zhao, C.Y., Zhen, X.L., Xu, Z.L., & He, L. (2011). Spatial distribution characteristics of the biomass and carbon storage of Qinghai Spruce (*Picea crassifolia*) forests in Qilian Mountains. *Chinese Journal of Applied Ecology*, 22, 1689–1694. (In Chinese)
- Peregon, A., & Yamagata, Y. (2013). The use of ALOS/PALSAR backscatter to estimate above-ground forest biomass: A case study in western Siberia. *Remote Sensing of Environment*, 137, 139–146.
- Peters, E.B., Wythers, K.R., Bradford, J.B., & Reich, P.B. (2013). Influence of disturbance on temperate forest productivity. *Ecosystems*, 16, 95–110.
- Pflugmacher, D., Cohen, W.B., & Kennedy, R.E. (2012). Using Landsat-derived disturbance history (1972–2010) to predict current forest structure. *Remote Sensing of Environment*, 122, 146–165.
- Phillips, O.L., Aragao, L.E.O.C., Lewis, S.L., Fisher, J.B., Lloyd, J., Lopez-Gonzalez, G., et al. (2009). Drought Sensitivity of the Amazon Rainforest. *Science*, 323, 1344–1347.
- Piao, S.L., Fang, J.Y., Zhou, L.M., Zhu, B., Tan, K., & Tao, S. (2005). Changes in vegetation net primary productivity from 1982 to 1999 in China. *Global Biogeochemical Cycles*, 19, GB2027.
- Piao, S.L., Friedlingstein, P., Ciais, P., Viovy, N., & Demarty, J. (2007). Growing season extension and its impact on terrestrial carbon cycle in the Northern Hemisphere over the past 2 decades. *Global Biogeochemical Cycles*. doi: 10.1029/2006GB002888.
- Piao, S.L., Ciais, P., Lomas, M., Beer, C., Liu, H.Y., Fang, J.Y., et al. (2011). Contribution of climate change and rising CO₂ to terrestrial carbon balance in East Asia: a multi-model analysis. *Global Planet Change*, 75, 133–42.
- Popescu, S.C., & Wynne, R.H. (2004). Seeing the trees in the forest: using LiDAR and multispectral data fusion with local filtering and variable window size for estimating tree height. *Photogrammetric Engineering and Remote Sensing*, 70, 589–604.
- Potapov, P., Turubanova, S., & Hansen, M.C. (2011). Regional-scale boreal forest cover and change mapping using Landsat data composites for European Russia. *Remote Sensing of Environment*, 115, 548–561.
- Potter, C., Klooster, S., & Genovese, V. (2009). Carbon emissions from deforestation in the Brazilian Amazon Region. *Biogeosciences*, 6, 2369–2381.
- Powell, S.L., Cohen, W.B., Yang, Z., Pierce, J.D., & Alberti, M. (2008). Quantification of impervious surface in the Snohomish water resources

- inventory area of western Washington from 1972–2006. *Remote Sensing of Environment*, *112*, 1895–1908.
- Powell, S.L., Cohen, W.B., Healey, S.P., Kennedy, R.E., Moisen, G.G., Pierce, K.B., et al. (2010). Quantification of live aboveground forest biomass dynamics with Landsat time-series and field inventory data: A comparison of empirical modeling approaches. *Remote Sensing of Environment*, *114*, 1053–1068.
- Pregitzer, K.S., & Euskirchen, E.S. (2004). Carbon cycling and storage in world forests: biome patterns related to forest age. *Global Change Biology*, *10*, 2052–2077.
- Prince, S.D., & Goward, S.N. (1995). Global primary production: a remote sensing approach. *Journal of Biogeography*, *22*, 815–835.
- Propastin, P., Ibrom, A., Knohl, A., & Erasmi, S. (2012). Effects of canopy photosynthesis saturation on the estimation of gross primary productivity from MODIS data in a tropical forest. *Remote Sensing of Environment*, *121*, 252–260.
- Qin, D.J., Zhao, Z.F., Han, L.F., Qian, Y.P., Ou, L., Wu, Z.Q., et al. (2012). Determination of groundwater recharge regime and flowpath in the Lower Heihe River basin in an arid area of Northwest China by using environmental tracers: Implications for vegetation degradation in the Ejina Oasis. *Applied Geochemistry*, *27*, 1133–1145.
- Rahman, M.M., Csaplovics, E., & Koch, B. (2008). Satellite estimation of forest carbon using regression models. *International Journal of Remote Sensing*, *29*, 6917–6936.
- Ranson, K.J., & Sun, G. (1994). Mapping biomass of a northern forest using multi-frequency SAR data. *IEEE Transactions on Geoscience and Remote Sensing*, *32*, 388–396.
- Ranson, K.J., Sun, G., Weishampel, J.F., & Knox, R.G. (1997). Forest biomass from combined ecosystem and radar backscatter modeling. *Remote Sensing of Environment*, *59*, 118–133.
- Raupach, M.R. (1994). Simplified expressions for vegetation roughness length and zero-plane displacement as a function of canopy height and area index. *Boundary-Layer Meteorology*, *71*, 211–216.
- Reese, H., & Olsson, H. (2011). C-correction of optical satellite data over alpine vegetation areas: A comparison of sampling strategies for determining the empirical C-parameter. *Remote Sensing of Environment*, *115*, 1387–1400.
- Reeves, M.C., Zhao, M., & Running, S. W. (2005). Usefulness and limits of MODIS GPP for estimating wheat yield. *International Journal of Remote Sensing*, *26*, 1403–1421.

- Ren, G.Y., Zhou, Y.Q., Chu, Z.Y., Zhou, J.X., Zhang, A.Y., Guo, J., et al. (2008). Urbanization effects on observed surface air temperature trends in North China. *Journal of Climate*, *21*, 1333–1348.
- Ren, G.Y., Ding, Y.H., Zhao, Z.C., Zheng, J.Y., Wu, T.W., Tang, G.L., et al. (2012). Recent progress in studies of climate change in China. *Advances in Atmospheric Sciences*, *29*, 958–977.
- Reutebuch, S.E., Andersen, H.E., & McGaughey, R.J. (2005). Light detection and ranging (LiDAR): an emerging tool for multiple resource inventory. *Journal of Forestry*, *103*, 286–292.
- Richardson, A.D., Hollinger, D.Y., Aber, J.D., Ollinge, S.V., & Braswell, B.H. (2007). Environmental variation is directly responsible for short-but not long-term variation in forest-atmosphere carbon exchange. *Global Change Biology*, *13*, 788–803.
- Riemann, R., Wilson, B.T., Lister, A., & Parks, S. (2010). An effective assessment protocol for continuous geospatial datasets of forest characteristics using USFS Forest Inventory and Analysis (FIA) data. *Remote Sensing of Environment*, *114*, 2337–2352.
- Rientjes, T.H.M., Muthuwatta, L.P., Bos, M.G., Booij, M.J., & Bhatti, H.A. (2013). Multi-variable calibration of a semi-distributed hydrological model using streamflow data and satellite-based evapotranspiration. *Journal of Hydrology*, *505*, 276–290.
- Rodell, M., McWilliams, E.B., Famiglietti, J.S., Beaudoin, H.K., & Nigro, J. (2011). Estimating evapotranspiration using an observation based terrestrial water budget. *Hydrological Processes*, *25*, 4082–4092.
- Rooney, G.G. (2001). Comparison of upwind land use and roughness length measured in the urban boundary layer. *Boundary-Layer Meteorology*, *100*, 469–486.
- Roy, P.S., & Ravan, S.A. (1996). Biomass estimation using satellite remote sensing data—an investigation on possible approaches for natural forest. *Journal of Biosciences*, *21*, 535–561.
- Running, S.W., & Coughlan, J.C. (1988). A general model of forest ecosystem processes for regional applications. I. Hydrological balance, canopy gas exchange and primary production processes. *Ecological Modelling*, *42*, 125–154.
- Running, S.W., & Gower, S.T. (1991). FOREST-BGC, a general model of forest ecosystem processes for regional applications. II. Dynamic carbon allocation and nitrogen budgets. *Tree Physiology*, *9*, 147–160.
- Running, S.W., & Hunt, E.R. (1993). Generalization of a forest ecosystem process model for other biomes, Biome-BGC, and an application for global-scale

- models. In J.R. Ehleringer, & C.B. Field (Eds.), *Scaling Physiological Processes: Leaf to Globe* (pp. 141–158). San Diego: Academic Press.
- Running, S.W., Nemani, J.M., Glassy, J.M., & Thornton, P.E. (1999). MODIS daily photosynthesis and annual net primary production (NPP) product (MOD17). *Algorithm theoretical basis*, document V.3.0.
- Running, S.W., Thornton, P.E., Nemani, R., & Glassy J.M. (2000). Global terrestrial gross and net primary productivity from the earth observation system. In O.E. Sala, R.B. Jackson, & H.A. Mooney (Eds.), *Methods in Ecosystem Science* (pp. 44–57). New York: Springer-Verla.
- Running, S.W., Nemani, R.R., Heinsch, F.A., Zhao, M., Reeves, M., & Jolly, M. (2004). A continuous satellite-derived measure of global terrestrial primary productivity: Future science and applications. *Bioscience*, *56*, 547–560.
- Russell, A.E., Raich, J.W., Arrieta, R.B., Valverde-Barrantes, O., & Gonzalez, E. (2010). Impacts of individual tree species on carbon dynamics in a moist tropical forest environment. *Ecological Applications*, *20*, 1087–1100.
- Ryu, Y., Baldocchi, D.D., Kobayashi, H., van Ingen, C., Li, J., Black, T.A., et al. (2011). Integration of MODIS land and atmosphere products with a coupled-process model to estimate gross primary productivity and evapotranspiration from 1 km to global scales. *Global Biogeochemical Cycles*. doi: 10.1029/2011gb004053.
- Saatchi, S.S., Houghton, R.A., dos Santos Alvalá, R.C., Soares, J.V., & Yu, Y. (2007). Distribution of aboveground live biomass in the Amazon basin. *Global Change Biology*, *13*, 816–837.
- Sader, S.A., Waide, R.B., Lawrence, W.T., & Joyce, A.T. (1989). Tropical forest biomass and successional age class relationships to a vegetation index derived from Landsat TM data. *Remote Sensing of Environment*, *28*, 143–156.
- Sahoo, A.K., Pan, M., Troy, T.J., Vinukollu, R.K., Sheffield, J., & Wood, E.F. (2011). Reconciling the global terrestrial water budget using satellite remote sensing. *Remote Sensing of Environment*, *115*, 1850–1865.
- Salas, C., Ene, L., Gregoire, T.G., Næsset, E., & Gobakken, T. (2010). Modelling tree diameter from airborne laser scanning derived variables: a comparison of spatial statistical models. *Remote Sensing of Environment*, *114*, 1277–1285.
- Santini, M., Collalti, A., & Valentini, R. (2014). Climate change impacts on vegetation and water cycle in the Euro-Mediterranean region, studied by a likelihood approach. *Regional Environmental Change*, *14*, 1405–1418.
- Santos, J.R., Pardi Lacruz, M.S., Araujo, L.S., & Keil, M. (2002). Savanna and tropical rainforest biomass estimation and spatialization using JERS-1 data. *International Journal of Remote Sensing*, *23*, 1217–1229.

- Santos, J.R., Freitas, C.C., Araujo, L.S., Dutra, L.V., Mura, J.C., Gama, F.F., et al. (2003). Airborne P-band SAR applied to the aboveground biomass studies in the Brazilian tropical rainforest. *Remote Sensing of Environment*, 87, 482–493.
- Sarker, M.L.R., Nichol, J., Ahmad, B., Busu, I., & Rahman, A.A. (2012). Potential of texture measurements of two-date dual polarization PALSAR data for the improvement of forest biomass estimation. *ISPRS Journal of Photogrammetry and Remote Sensing*, 69, 146–166.
- Schaudt, K.J., & Dickinson, R.E. (2000). An approach to deriving roughness length and zero-plane displacement height from satellite data, prototyped with BOREAS data. *Agricultural and Forest Meteorology*, 104, 143–155.
- Schimel, D.S., House, J.I., Hibbard, K.A., Bousquet, P., Ciais, P., Peylin, P., et al. (2001). Recent patterns and mechanisms of carbon exchange by terrestrial ecosystems. *Nature*, 414, 169–172.
- Schroeder, P., Brown, S., Birdsey, M.O.J., & Cieszewski, R.C. (1997). Biomass estimation for temperate broadleaf forests of the US using inventory data. *Forest Science*, 43, 424–434.
- Shangguan, W., Dai, Y.J., Liu, B.Y., Ye, A.Z., & Yuan, H. (2012). A soil particle-size distribution dataset for regional land and climate modelling in China. *Geoderma*, 171, 85–91.
- Shataee, S. (2013). Forest attributes estimation using aerial laser scanner and TM data. *Forest Systems*, 22, 484–496.
- Shaw, R., & Pereira, A. (1982). Aerodynamic roughness of a plant canopy: A numerical experiment. *Agricultural Meteorology*, 26, 51–65.
- Shuttleworth, W., & Wallace, J. (1985). Evaporation from sparse crops—An energy combination theory. *The Quarterly Journal of the Royal Meteorological Society*, 111, 839–855.
- Singh, N., Patel, N.R., Bhattacharya, B.K., Soni, P., Parida, B.R., Parihar, J.S. (2014). Analyzing the dynamics and inter-linkages of carbon and water fluxes in subtropical pine (*Pinus roxburghii*) ecosystem. *Agricultural and Forest Meteorology*, 197, 206–218.
- Sivrikaya, F., Keleş, S., & Çakir, G. (2007). Spatial distribution and temporal change of carbon storage in timber biomass of two different forest management units. *Environmental Monitoring and Assessment*, 132, 429–438.
- Sjostrom, M., Zhao, M., Archibald, S., Arneth, A., Cappelare, B., Falk, U., et al. (2013). Evaluation of MODIS gross primary productivity for Africa using eddy covariance data. *Remote Sensing of Environment*, 131, 275–286.
- Smola, A.J., & Schölkopf, B. (2004). A tutorial on support vector regression. *Statistics and Computing*, 14, 199–222.
- Sobrinho, J.A., Gomez, M., Jimenez-Munoz, C., & Olioso, A. (2007). Application of a simple algorithm to estimate daily evapotranspiration from NOAA-AVHRR

- images for the Iberian Peninsula. *Remote Sensing of Environment*, 110, 139–148.
- Soenen, S.A., Peddle, D.R., & Coburn, C.A. (2005). SCS+C: a modified Sun-Canopy-Sensor topographic correction in forested terrain. *IEEE Transactions on Geoscience and Remote Sensing*, 43, 2148–2159.
- Soenen, S.A., Peddle, D.R., Coburn, C.A., Hall, R.J., & Hall, F.G. (2008). Improved topographic correction of forest image data using a 3-D canopy reflectance model in multiple forward mode. *International Journal of Remote Sensing*, 29, 1007–1027.
- Soenen, S.A., Peddle, D.R., Hall, R.J., Coburn, C.A., & Hall, F.G. (2010). Estimating above ground forest biomass from canopy reflectance model inversion in mountainous terrain. *Remote Sensing of Environment*, 114, 1325–1337.
- Solberg, S., Astrup, R., Breidenbach, J., Nilsen, B., & Weydahl, D. (2013). Monitoring spruce volume and biomass with InSAR data from TanDEM-X. *Remote Sensing of Environment*, 139, 60–67.
- Song, C., & Woodcock, C.E. (2002). The spatial manifestation of forest succession in optical imagery: The potential of multiresolution imagery. *Remote Sensing of Environment*, 82, 271–284.
- Song, L., Langfelder, P., & Horvath, S. (2013a). Random generalized linear model: a highly accurate and interpretable ensemble predictor. *BMC Bioinformatics*. doi: 10.1186/1471-2105-14-5.
- Song, X.D., Bryan, B.A., Almeida, A.C., Paul, K.I., Zhao, G., & Ren, Y. (2013b). Time-dependent sensitivity of a process-based ecological model. *Ecological Modelling*, 265, 114–123.
- Spracklen, D.V., Arnold, S.R., & Taylor, C.M. (2012). Observations of increased tropical rainfall preceded by air passage over forests. *Nature*, 489, 282–285.
- Steininger, M.K. (2000). Satellite estimation of tropical secondary forest above-ground biomass data from Brazil and Bolivia. *International Journal of Remote Sensing*, 21, 1139–1157.
- Stephens, B.B., Gurney, K.R., Tans, P.P., Sweeney, C., Peters, W., Bruhwiler, L., et al. (2007). Weak northern and strong tropical land carbon uptake from vertical profiles of atmospheric CO₂. *Science*, 316, 1732–1735.
- Su, H., Wood, E.F., McCabe, M.F., & Su, Z. (2007a). Evaluation of remotely sensed evapotranspiration over the CEOP EOP-1 reference sites. *Journal of the Meteorological Society of Japan*, 85A, 439–459.
- Su, H.B., McCabe, M.F., Wood, E.F., Su, Z., & Prueger, J.H. (2005). Modeling evapotranspiration during SMACEX: Comparing two approaches for local- and regional-scale prediction. *Journal of Hydrometeorology*, 6, 910–922.

- Su, H.X., Sang W.G., Wang, Y.X., & Ma, K.P. (2007b). Simulating *Picea schrenkiana* forest productivity under climatic changes and atmospheric CO₂ increase in Tianshan Mountains, Xinjiang Autonomous Region, China. *Forest Ecology and Management*, 246, 273–284.
- Su, Z., Schmugge, T., Kustas, W.P., & Massman, W.J. (2001). An evaluation of two models for estimation of the roughness height for heat transfer between the land surface and the atmosphere. *Journal of Applied Meteorology*, 40, 1933–1951.
- Su, Z. (2002). The Surface Energy Balance System (SEBS) for estimation of turbulent heat fluxes. *Hydrology and Earth System Sciences*, 6, 85–99.
- Su, Z.B., Zhang, T., Ma, Y.M., Jia, L., & Wen, J. (2006). Energy and water cycle over the Tibetan Plateau: Surface energy balance and turbulent heat fluxes. *Advances in Earth Science*, 21, 1224–1236.
- Sun, D.Y., Qiu, Z.F., Li, Y.M., Shi, K., & Gong, S. Q. (2014). Detection of total phosphorus concentrations of turbid inland waters using a remote sensing method. *Water Air and Soil Pollution*, 225, 1953.
- Sun, G.D., & Mu, M. (2014). The analyses of the net primary production due to regional and seasonal temperature differences in eastern China using the LPJ model. *Ecological Modelling*, 289, 66–76.
- Sun, G.Q., Ranson, K.J., & Kharuk, V.I. (2002). Radiometric slope correction for forest biomass estimation from SAR data in the western Sayani Mountains, Siberia. *Remote Sensing of Environment*, 79, 279–287.
- Svetnik, V., Liaw, A., Tong, C., Cullberson, C., Sheridan, R.P., & Feuston, B.P. (2003). Random forest: a classification and regression tool for compound classification and QSAR modelling. *Journal of Chemical Information and Computer Sciences*, 43, 1947–1958.
- Tan, K., Piao, S., Peng, C., & Fang, J. (2007). Satellite-based estimation of biomass carbon stocks for northeast China's forests between 1982 and 1999. *Forest Ecology and Management*, 240, 114–121.
- Tang, R.L., Li, Z.L., Jia, Y.Y., Li, C.R., Sun, X.M., Kustas, W.P., et al. (2011). An intercomparison of three remote sensing-based energy balance models using Large Aperture Scintillometer measurements over a wheat-corn production region. *Remote Sensing of Environment*, 115, 3187–3202.
- Thenkabail, P.S., Stucky, N., Griscom, B.W., Ashton, M.S., Diels, J., Van Der Meer, B., et al. (2004). Biomass estimations and carbon stock calculations in the oil palm plantations of African derived savannas using IKONOS imagery. *International Journal of Remote Sensing*, 25, 5447–5472.
- Thornton, P.E., Law, B.E., Gholz, H.L., Clark, K.L., Falge, E., Ellsworth, D.E., et al. (2002). Modeling and measuring the effects of disturbance history and

- climate on carbon and water budgets in evergreen needleleaf forests. *Agricultural and Forest Meteorology*, 113, 185–222.
- Tian, X., Li, Z.Y., van der Tol, C., Su, Z., Li, X., He, Q.S., et al. (2011). Estimating zero-plane displacement height and aerodynamic roughness length using synthesis of LiDAR and SPOT-5 data. *Remote Sensing of Environment*, 115, 2330–2341.
- Tian, X., Su, Z.B., Chen, E.X., Li, Z.Y., van der Tol, C., Guo, J.P., et al. (2012). Estimation of forest above-ground biomass using multi-parameter remote sensing data over a cold and arid area. *International Journal of Applied Earth Observation and Geoinformation*, 14, 160–168.
- Tian, X., Li, Z. Y., Su, Z. B., Chen, E.X., van der Tol, C., Li, X., et al. (2014). Estimating montane forest above-ground biomass in the upper reaches of the Heihe River Basin using Landsat-TM data. *International Journal of Remote Sensing*, 35, 7339-7362.
- Tian X., Li Z.Y., Li X. W., Chen E.X., Liu Q. H., Yan G.J., et al.. The complicate observations and multi-parameter land information constructions on allied telemetry experiment. *In submission*
- Tomppo, E., & Halme, M. (2004). Using coarse scale forest variables as ancillary information and weighting of variables in k -NN estimation: a genetic algorithm approach. *Remote Sensing of Environment*, 92, 1–20.
- Tomppo, E.O., Gagliano, C., De Natale, F., Katila, M., & McRoberts, R.E. (2009). Predicting categorical forest variables using an improved k -nearest neighbor estimator and Landsat imagery. *Remote Sensing of Environment*, 113, 500–517.
- Tonolli, S., Dalponte, M., Neteler, M., Rodeghiero, M., Vescovo, L., & Gianelle, D. (2011). Fusion of airborne LiDAR and satellite multispectral data for the estimation of timber volume in the Southern Alps. *Remote Sensing of Environment*, 115, 2486–2498.
- Trenberth, K.E., Smith, L., Qian, T., Dai, A., & Fasullo, J. (2007). Estimates of the global water budget and its annual cycle using observational and model data. *Journal of Hydrometeorology*, 8, 758–769.
- Trenberth, K.E., Fasullo, J.T., & Kiehl, J. (2009). Earth's global energy budget. *American Meteorological Society*, 90, 311–323.
- Tuominen, S., & Pekkarinen, A. (2005). Performance of different spectral and textural aerial photograph features in multi-source forest inventory. *Remote Sensing of Environment*, 94, 256–268.
- Turner, D.P., Ritts, W.D., Cohen, W.B., Gower, S.T., Zhao, M.S., Running, S. W., et al. (2003). Scaling gross primary production (GPP) over boreal and deciduous forest landscapes in support of MODIS GPP product validation. *Remote Sensing of Environment*, 88, 256–270.

- Turner, D.P., Ritts, W.D., Zhao, M.S., Kurc, S.A., Dunn, A.L., Wofsy, S.C., et al. (2006). Assessing interannual variation in MODIS-based estimates of gross primary production. *IEEE Transactions on Geoscience and Remote Sensing*, 44, 1899–1907.
- Ueyama, M., Ichii, K., Hirata, R., Takagi, K., Asanuma, J., Machimura, T., et al. (2010). Simulating carbon and water cycles of larch forests in East Asia by the BIOME-BGC model with AsiaFlux data. *Biogeosciences*, 7, 959–977.
- Valle, D., Staudhammer, C.L., Cropper, W.P., & Gardingen, P.R. (2009). The importance of multimodel projections to assess uncertainty in projections from simulation models. *Ecological Applications*, 19, 1680–1692.
- Vanderwel, M.C., Coomes, D.A., & Purves, D.W. (2013). Quantifying variation in forest disturbance, and its effects on aboveground biomass dynamics, across the eastern United States. *Global Change Biology*, 19, 1504–1517.
- Vapnik, V. (1995). *The nature of statistical learning theory*. New York: Springer-Verlag.
- Vedrova, E.F. (2011). Biogeneous carbon fluxes in the boreal forests of Central Siberia. *Biology Bulletin*, 38, 65–76.
- Verhoef, A., McNaughton, K.G., & Jacobs, A.F.G. (1997). A parameterization of momentum roughness length and displacement height for a wide range of canopy densities. *Hydrology and Earth System Sciences*, 1, 81–91.
- Veroustraete, F., Sabbe, H., & Eerens, H. (2002). Estimation of carbon mass fluxes over Europe using the C-Fix model and Euroflux data. *Remote Sensing Environment*, 83, 376–399.
- Veroustraete, F., Sabbe, H., Rasse, D.P., & Bertels, L. (2004). Carbon mass fluxes of forests in Belgium determined with low resolution optical sensors. *International Journal of Remote Sensing*, 25, 769–792.
- Wang, G.X., & Cheng, G.D. (1999). Water resource development and its influence on the environment in arid areas of China—the case of the Hei River basin. *Journal of Arid Environments*, 43, 121–131.
- Wang, J.D., Guo, W.D., & Li, H.Q. (2013a). Application of extended Fourier amplitude sensitivity test (EFAST) method in land surface parameter sensitivity analysis. *Acta Physica Sinica*, 62, 050202.
- Wang, J.M., Bastiaanssen, W.G.M., Ma, Y., & Pelgrum, H. (1998a). Aggregation of land surface parameters in the oasis–desert systems of Northwest China. *Hydrological Processes*, 12, 2133–2147.
- Wang, J.Y., Ju, K.J., Fu, H.E., Chang, X.X., & He, H.Y. (1998b). Study on biomass of water conservation forest on north slope of Qilian mountains. *Journal of Fujian College of Forestry*, 18, 319–323. (in Chinese).

- Wang, J.Y., Che, K.J., & Jiang, Z.R. (2000). A study on carbon balance of *Picea crassifolia* in Qilian Mountains. *Journal of Northwest Forestry University*, 15, 9–14 (in Chinese).
- Wang, K., & Liang, S. (2008). An improved method for estimating global evapotranspiration based on satellite determination of surface net radiation, vegetation index, temperature, and soil moisture. *Journal of Hydrometeorology*, 9, 712–727.
- Wang, K., & Dickinson, R.E. (2012). A review of global terrestrial evapotranspiration: observation, modeling, climatology, and climatic variability. *Reviews of Geophysics*. doi: 10.1029/2011rg000373.
- Wang, P.Y., Li, Z.Q., & Gao, W.Y. (2011). Rapid Shrinking of Glaciers in the Middle Qilian Mountain Region of Northwest China during the Last similar to 50 Years. *Journal of Earth Science*, 22, 539–548.
- Wang, S., Yang, Y., Trishchenko, A.P., Barr, A.G., Black, T.A., & McCaughey, H. (2009). Modelling the response of canopy stomatal conductance to humidity. *Journal of Hydrometeorology*, 10, 521–532.
- Wang, S., Yang, Y., Luo, Y., & Rivera. A. (2013b). Spatial and seasonal variations in evapotranspiration over Canada's landmass. *Hydrology and Earth System Sciences*, 17, 3561–3575
- Wang, S.Q., Zhou, L., Chen, J.M., Ju, W.M., Feng, X.F., & Wu, W.X. (2011). Relationships between net primary productivity and stand age for several forest types and their influence on China's carbon balance. *Journal of Environmental Management*, 92, 1651–1662.
- Wang, X.F., Ma, M.G., Li, X., Song, Y., Tan, J.L., Huang, G.H., et al. (2013c). Validation of MODISGPP product at 10 flux sites in northern China. *International Journal of Remote Sensing*, 34, 587–599.
- Wang, X.F., Ma, M.G., Song, Y., Tan, J.L., & Wang, H.B. (2014). Coupling of a biogeochemical model with a simultaneous heat and water model and its evaluation at an alpine meadow site. *Environmental Earth Sciences*. doi: 10.1007/s12665-014-3300-z.
- Weiss, S.M. (1991). Small sample error rate estimation for *k*-NN classifiers. *IEEE Transactions on Pattern Analysis and Machine Intelligence*, 13, 285–289.
- White, M.A., Running, S.W., & Thornton, P.E. (1999). The impact of growing-season length variability on carbon assimilation and evapotranspiration over 88 years in the eastern US deciduous forest. *International Journal of Biometeorology*, 42, 139–145.
- White, M.A., Thornton, P.E., Running, S.W., & Nemani, R.R. (2000). Parameterisation and sensitivity analysis of the BIOME-BGC terrestrial ecosystem model: net primary production controls. *Earth Interactions*, 4, 1–85.

- Wieringa, J. (1986). Roughness-dependent geographical interpolation of surface wind speed averages. *Quarterly Journal of the Royal Meteorological Society*, *112*, 867–889.
- Wieringa, J. (1993). Representative roughness parameters for homogeneous terrain. *Boundary-Layer Meteorology*, *63*, 323–363.
- Williams, M., Schwarz, P.A., Law B.E., Irvine, J., & Kurpius M.R. (2005). An improved analysis of forest carbon dynamics using data assimilation. *Global Change Biology*, *11*, 89–105.
- Woodbury, P.B., Smith, J.E., & Heath, L.S. (2007). Carbon sequestration in the U.S. forest sector from 1990 to 2010. *Forest Ecology and Management*, *241*, 14–27.
- Wulder, M.A., Han, T., White, J.C., Sweda, T., & Tsuzuki, H. (2007). Integrating profiling LIDAR with Landsat data for regional boreal forest canopy attribute estimation and change characterization. *Remote Sensing of Environment*, *110*, 123–137.
- Xiao, Z.Q., Liang, S.L., Wang, J.D., Chen, P., Yin, X.J., Zhang, L.Q., et al. (2014). Use of general regression neural networks for generating the GLASS Leaf Area Index Product from time-series MODIS surface reflectance. *IEEE Transactions on Geoscience and Remote Sensing*, *52*, 209 – 223.
- Xie, X.S., Liu, W.T., & Tang, B.Y. (2008). Space based estimation of moisture transport in marine atmosphere using support vector regression. *Remote Sensing of Environment*, *112*, 1846–1855.
- Xu, C., Li, Y.T., Hu, J., Yang, X.J., Sheng, S., Liu, M.S., et al. (2012). Evaluating the difference between the normalized difference vegetation index and net primary productivity as the indicators of vegetation vigor assessment at landscape scale. *Environmental Monitoring and Assessment*, *184*, 1275–1286.
- Yang, G.J., Pu, R.L., Zhang, J.X., Zhao, C. J., Feng, H.K., & Wang, J.H. (2013). Remote sensing of seasonal variability of fractional vegetation cover and its object-based spatial pattern analysis over mountain areas. *ISPRS Journal of Photogrammetry and Remote Sensing*, *77*, 79–93.
- Yang, J., Weisberga, P.J., & Bristowa, N.A. (2012). Landsat remote sensing approaches for monitoring long-term tree cover dynamics in semi-arid woodlands: Comparison of vegetation indices and spectral mixture analysis. *Remote Sensing of Environment*, *119*, 62–71.
- Yang, K., Koike, T., Fujii, H., Tamagawa, K., & Hirose, N. (2002). Improvement of surface flux parametrizations with a turbulence related length. *The Quarterly Journal of the Royal Meteorological Society*, *128*, 2073–2087.
- Yang, R., & Friedl, M.A. (2003). Determination of roughness lengths for heat and momentum over boreal forests. *Boundary-Layer Meteorology*, *107*, 581–603.

- Yang, Y., Shang, S., & Jiang, L. (2012). Remote sensing temporal and spatial patterns of evapotranspiration and the responses to water management in a large irrigation district of North China. *Agricultural and Forest Meteorology*, *164*, 112–122.
- Yrjö, R. (2005). Multi-temporal JERS SAR data in boreal forest biomass mapping. *Remote Sensing of Environment*, *97*, 263–275.
- Yu, D., Shi, P.J., Han, G., Zhu, W.Q., Du, S. Q., & Xun, B. (2011). Forest ecosystem restoration due to a national conservation plan in China. *Ecological Engineering*, *37*, 1387–1397.
- Yuan, W.P., Liu, S.G., Yu, G.R., Bonnefond, J.M., Chen, J.Q., Davis, K., et al. (2010). Global estimates of evapotranspiration and gross primary production based on MODIS and global meteorology data. *Remote Sensing of Environment*, *114*, 1416–1431.
- Zarco-Tejada, P.J., Morales, A., Testi, L., & Villalobos, F.J. (2013). Spatio-temporal patterns of chlorophyll fluorescence and physiological and structural indices acquired from hyperspectral imagery as compared with carbon fluxes measured with eddy covariance. *Remote Sensing of Environment*, *133*, 102–115.
- Zeng, Z.Z., Piao, S.L., Lin, X., Yin, G.D., Peng, S.S., Ciais, P., et al. (2012). Global evapotranspiration over the past three decades: estimation based on the water balance equation combined with empirical models. *Environmental Research Letters*. doi: 10.1088/1748-9326/7/1/014026.
- Zhang, G.G., Kang, Y.M., Han, G.D., & Sakurai, K. (2011). Effect of climate change over the past century on the distribution, extent and NPP of ecosystems of Inner Mongolia. *Global Change Biology*, *17*, 377–389.
- Zhang, K., Kimball, J.S., Nemani, R.R., & Running, S.W. (2010a). A continuous satellite-derived global record of land surface evapotranspiration from 1983 to 2006. *Water Resources Research*, *46*, W09522.
- Zhang, X., Susan Moran, M., Zhao, X., Liu, S., Zhou, T., Ponce-Campos, G.E. et al. (2014a). Impact of prolonged drought on rainfall use efficiency using MODIS data across China in the early 21st century. *Remote Sensing of Environment*, *150*, 188–197.
- Zhang, X.Y., & Kondragunta, S. (2008). Temporal and spatial variability in biomass burned areas across the USA derived from the GOES fire product. *Remote Sensing of Environment*, *112*, 2886–2897.
- Zhang, Y.Q., Yu, Q., Jiang, J., & Tang, Y.H. (2008). Calibration of Terra/MODIS gross primary production over an irrigated cropland on the North China Plain and an alpine meadow on the Tibetan Plateau. *Global Change Biology*, *14*, 757–767.

- Zhang, Y.Z., Liang, S.L., & Sun, G.Q. (2014b). Forest biomass mapping of northeastern China using GLAS and MODIS data. *IEEE Journal of Selected Topics in Applied Earth Observations and Remote Sensing*, 7, 140–152.
- Zhang, Z.H., Wang, W.Z., Ma, M.G., Wu, Y.R., & Xu, Z.W. (2010b). The processing methods of eddy covariance flux data and products in “WATER” Test. *Remote Sensing Technology and Application*, 25, 788–796. (in Chinese).
- Zhao, M.S., & Running, S.W. (2010). Drought-induced reduction in global terrestrial net primary production from 2000 through 2009. *Science*, 329, 940–943.
- Zhao, W.J., Liu, X.D., Jin, M., Che, Z.X., Jing, W.M., & Ma, Y. (2012). Analysis on Community Structure of *Picea crassifolia* Forests in the Qilian Mountains. *Arid Zone Research*, 29, 615–620. (in Chinese).
- Zheng, D., Rademacher, J., Chen, J., Crow, T., Bresee, M., Le Moine, J., et al. (2004). Estimating aboveground biomass using Landsat 7 ETM+ data across a managed landscape in Northern Wisconsin, USA. *Remote Sensing of Environment*, 93, 402–411.
- Zheng, D.L., Heath, L.S., Ducey, M.J., & Smith, J.E. (2013). Forest carbon dynamics associated with growth and disturbances in Oklahoma and Texas, 1992–2006. *Southern Journal of Applied Forestry*, 37, 216–225.
- Zhong, Q.X. & Yin, C.L. (2008). The major natural disaster and the corresponding protection of the water conservation forests in Qilian Mountains. *Agricultural science and technology and information* 2, 21-22. (in Chinese).
- Zhou, J., Zhang, X., Zhan, W.F., & Zhang, H.L. (2014). Land Surface Temperature Retrieval from MODIS Data by Integrating Regression Models and the Genetic Algorithm in an Arid Region. *Remote Sensing*, 6, 5344–5367.
- Zhou, Y., Zhu, Q., Chen, J.M., Wang, Y.Q., Liu, J., Sun, R., et al. (2007). Observation and simulation of net primary productivity in Qilian mountain, Western China. *Journal of Environmental Management*. 85, 574–584.
- Zhou, Y.L., Sun, X.M., Zhu, Z.L., Zhang, R.H., Tian, J., Liu, Y.F., et al. (2006). Surface roughness length dynamic over several different surfaces and its effects on modeling fluxes. *Science In China Series D: Earth Sciences*, 49, 262–272.
- Zhou, Y.L., Ju, W.M., Sun, X.M., Wen, X.F., & Guan, D.X. (2012). Significant Decrease of Uncertainties in Sensible Heat flux Simulation Using Temporally Variable Aerodynamic Roughness in Two Typical Forest Ecosystems of China. *Journal of Applied Meteorology and Climatology*, 51, 1099–1110.
- Zhuo, G., La, B., Pubu, C., & Luo, B. (2014). Study on daily surface evapotranspiration with SEBS in Tibet Autonomous Region. *Journal of Geographical Sciences*, 24, 113–128.

- Zobitz, J.M., Desai, A.R., Moore, D.J.P., & Chadwick, M.A. (2011). A primer for data assimilation with ecological models using Markov Chain Monte Carlo (MCMC). *Oecologia*, *167*, 599–611.
- Zobitz, J.M., Moore, D.J.P., Quaife, T., Braswell, B.H., Bergeson, A., Anthony, J. A., et al. (2014). Joint data assimilation of satellite reflectance and net ecosystem exchange data constrains ecosystem carbon fluxes at a high-elevation subalpine forest. *Agricultural and Forest Meteorology*, *195*, 73–88.
- Zou, J., Yan, G.J., Zhu, L., & Zhang, W.M. (2009). Woody-to-total area ratio determination with a multispectral canopy imager. *Tree Physiology*, *29*, 1069–1080.

Bibliography

Summary

As the critical component in the terrestrial ecosystem, forests are significant dynamic factors modifying the carbon, water, energy and momentum fluxes through the photosynthesis and evapotranspiration (ET) processes. The scientific community and policy makers share an interest in estimating variations and uncertainties in these fluxes. It has been generally agreed that water availability is the primary factor limiting forest ecosystem functions, which is normally presented as dynamics of the forest carbon (net primary productivity (NPP), above-ground NPP (ANPP)), ET and thus water use efficiency (WUE). This issue has been much sensitive over the Qilian Mountains (QMs), the headwater of the Heihe River Basin (HRB) which is home to various water-limited ecosystems (glacier, frozen soil, alpine meadow, montane forest located within the upper reach; the irrigated crops within the middle reach; and the riparian ecosystem and desert within the lower reach). Although numerous studies have been conducted for HRB, forest carbon and ET dynamics have not been assessed before.

This study is the first to analyse the dynamics of above ground biomass (AGB) and ET of the headwater forests in the QMs, and their relations to climate. This is relevant for local ecosystem and water management. The techniques are novel and duplicable, and they can be applied elsewhere as well. By multi-disciplinary techniques (based on multi-parameter remote sensing, eco-hydrological and meteorological knowledge) and comprehensive measurements (forest survey, eddy covariance (EC) and dendrochronological measurements), the long-term dynamic modeling of the forest AGB which is inherently linked with NPP and long-term simulations of forest ET were conducted over the QMs.

This study first evaluated the performance of the parametric (multivariate regression) and non-parametric (the k -Nearest Neighbour) methods to estimate forest AGB based on multi-parameter high-resolution remote sensing data, including airborne LiDAR, and spaceborne ALOS PALSAR and SPOT-5 HRG data, within a small watershed where an intensive airborne campaign was conducted. The result showed that the non-parametric method outperformed the parametric method. Afterwards, higher dimensional indexes from lower resolution remote sensing data, including the Landsat Thematic Mapper 5 (TM) and Advanced Spaceborne Thermal Emission and Reflection Radiometer (ASTER) global digital elevation model (GDEM) V2 products, as well as more forest AGB measurements with broader AGB levels, were employed in the k -NN method for estimating montane forest AGB at regional scale. The result did not show an obvious

disadvantage to that from the aforementioned study, with the exception that it had a slightly higher RMSE.

In general, when working with the high-dimensional remote sensing data and small reference samples from the measurements, estimations of forest AGB by parametric methods have a high risk of overfitting and as a result, they are biased. The non-parametric methods with the 'bootstrap' or leave-one-out (LOO) sampling method can avoid this risk but they largely rely on the optimization process for their configurations. The selection of the remotely sensed features is the predominant issue for the optimization which has been generally based on the background experience, scenario independence. The proposed incorporation of two notable non-parametric methods (random forest (RF) and k -Nearest Neighbour (k -NN)) tremendously improved the efficiency of the forest AGB estimations and then reliable forest AGB map of 2009 was obtained (with $R^2 = 0.62$ and $RMSE = 24.00$ tonnes ha^{-1}).

As the simulation of forest carbon fluxes is concerned, two kinds of methods have been frequently used in recent decades, the remote-sensing-based and process-based methods. Driven by the eco-physiological parameters from remote sensing data, the former model can capture the spatial variation of forest ecosystem but is limited to the instantaneous observation. The process-based model can simulate the critical forest processes by the interaction between ecosystem and the atmosphere, but it is weak in presenting the spatial variation and practically difficult to be extended to the other sites. The first try of incorporating the MODIS MOD_17 (MOD_17) gross primary productivity (GPP) model with the Biome-BioGeochemical Cycles (Biome-BGC) inherited the strengths of these two models. The MOD_17 was optimized through three sources of inputs and then the GPP estimates at the site were validated by EC measurements. As compared to the original MODIS GPP products (with $R^2 = 0.47$ and $RMSE = 20.27$ $gC\ m^{-2}\ 8d^{-1}$), the GPP from the optimized MOD_17 were largely improved (with $R^2 = 0.91$ and $RMSE = 5.19$ $gC\ m^{-2}\ 8d^{-1}$). After fulfilling the premise of being reliable, GPP estimates (over 30 well-considered forest plots) from optimized MOD_17 model were used for calibrating the Biome-BGC. As a result, the calibrated Biome-BGC has been more resistant to the impacts of environmental variability (climatic conditions, locations) and forest stand diversity (stand density, terrain conditions). Validated by the EC and dendrochronological measurements in terms of GPP (with $R^2 = 0.79$ and $RMSE = 1.31$ $gC\ m^{-2}\ d^{-1}$), NEE (with $R^2 = 0.68$ and $RMSE = 3.09$ $gC\ m^{-2}\ d^{-1}$) and interannual forest AGB increments (with $R^2 = 0.72$, and $RMSE = 47.33$ $gC\ m^{-2}\ year^{-1}$) original converted from NPP estimates of Biome-BGC, the behaviour of the calibrated Biome-BGC showed the strength in the reliable estimations of forest

carbon fluxes at finer spatiotemporal scale. Combining the forest AGB map of 2009 with the interannual forest AGB increments, the dynamic modeling of forest AGB was accomplished, which generated the good estimates of forest AGB dynamics over 13 year (from 2000 to 2012).

Two important parameters exist in the Monin–Obukhov Similarity (MOS) theory that is basic theory of the surface energy balance system (SEBS), the zero-plane displacement height, d (m), and the aerodynamic roughness length z_{0m} (m). For regional application in forests of these two parameters has to recur to the remote-sensing-based model linking them with the forest structural parameters (i.e., leaf area index (LAI), frontal area index (FAI), stand density and height). Using the reasonable retrievals by synthesis of airborne light detection and ranging (LiDAR) data and Satellite Probatoire d’Observation de la Terre-5 (SPOT-5) high resolution geometrical (HRG) image, four d and z_{0m} models were driven and substantially compared. The outperforming model in estimating z_{0m} was so called SD00 model embedded the LAI, FAI, as well as forest height. The SD00 was then applied for the time-series parameterization for the SEBS model. Instead of using the ‘static’ forest height and FAI for the long-term parameterization, the dynamic forest height and FAI regressed from the calibrated model based on the forest measurements were used in SD00 model. Driven by the refined inputs, the parameterized SEBS simulates the forest ET over QMs from 2000 to 2012. The 8-day ET estimates from SEBS were validated by the EC measurement and it was shown that SEBS can capture the spatial and temporal variation of forest ET. The ET estimates of SEBS (with $R^2 = 0.80$ and $RMSE = 0.21 \text{ mm day}^{-1}$) were much better than those of MOD16 ET (with $R^2 = 0.35$ and $RMSE = 0.76 \text{ mm day}^{-1}$).

The interannual WUE variations of forests over QMs were explored by dividing aforementioned interannual ANNP from the calibrated Biome-BGC by the interannual ET from SEBS. Based on the long-term meteorological estimates, the impacts of climatic variations of the growing seasons (April to September) on the ANPP, ET and thus WUE were analyzed. The overall trends of forest ANPP, ET and WUE over the study period show a decline with large variations.

The methodology of dynamic modeling of forest AGB and ET is duplicable and can be applied to biomes with various environmental and climatic conditions. The estimates of interannual forest AGB and ET over QMs are realistic and support the local sustainable development and management of forest ecosystem and water resources.

Summary

Samenvatting

Bossen zijn een belangrijk onderdeel van de biosfeer op aarde. Ze dragen significant bij aan de totale fotosynthese en verdamping. Wetenschappers en beleidsmakers hebben een gedeelde interesse in goede schattingen van de fotosynthese en de verdamping van bossen, en van de bijbehorende betrouwbaarheidsintervallen. De beschikbaarheid van water is vaak de beperkende factor voor ecosysteemfuncties van bos, waaronder de netto primaire productie (NPP) en de bovengrondse NPP (ANPP), de verdamping (ET) en de efficiëntie van watergebruik (WUE). In deze studie zijn de bossen in het Qiliangebergte (QM) onderzocht, het bovenstroomse deel van het stroomgebied van de rivier de Heihe (HRB). Dit stroomgebied bevat van bovenstrooms naar benedenstrooms gletsjers, permafrost, alpenweide, hooggelegen naaldbos, geïrrigeerde akkerbouw, oevervegetatie en woestijn. Hoewel er al veel onderzoek is gedaan naar de HRB, zijn de koolstof opslag en dynamiek van de verdamping nooit eerder bepaald.

Dit is de eerste studie naar de dynamiek van de bovengrondse biomassa (AGB) en verdamping (ET) van het brongebied van het Qiliangebergte. De gebruikte technieken zijn vernieuwend en ze kunnen ook toegepast worden in andere gebieden. De volgende meetmethodes zijn toegepast: veldinventarisatie, eddy-covariantie (EC), dendrochronologie, en multi-parameter aardobservatie. De metingen zijn gebruikt in ecohydrologische modellen om de dynamiek van de bovengrondse biomassa (AGB) en de NPP en ET te bepalen voor een periode van 13 jaar.

Als eerste zijn twee methodes voor AGB schattingen met aardobservatiedata met elkaar vergeleken: een parametrische methode (multivariate regressie), en een non-parametrische methode (*k*-Nearest Neighbour). Beide technieken zijn toegepast op drie soorten aardobservatiedata met hoge resolutie: een LiDAR op een vliegtuig, radarmetingen met een satelliet (ALOS PALSAR), en metingen met de SPOT-5 HRG satelliet. De data zijn verzameld voor een klein stroomgebied binnen de QM. De non-parametrische methode bleek de beste van de twee. Nadien is de non-parametrische methode opnieuw gebruikt met data van sensoren met iets minder goede spectrale en ruimtelijke resolutie: de Landsat Thematic Mapper 5 (TM), aangevuld met data van Advanced Spaceborne Thermal Emission and Reflection Radiometer (ASTER) voor een hoogtemodel van het terrein (GDEM). Het aantal veldinventarisaties is uitgebreid en een groter gebied is bestudeerd. De resultaten waren vrijwel even goed als in de eerste studie met data van hogere resolutie.

De parametrische methode heeft het nadeel dat er snel overparameterisatie optreedt, zeker als er veel satellietproducten tegelijk worden gebruikt en het aantal veldmetingen klein is. Non-parameterische methodes met de 'bootstrap' of 'leave-on-out' (LOO) selectiemethode zijn minder gevoelig voor overparameterisatie, maar het resultaat hangt af van het optimalisatieproces. De keuze van de kenmerkende satellietproducten het grootste probleem, en is vereist enige ervaring. De keuze werd veel eenvoudiger door twee non-parametrische methodes op een rij te gebruiken: eerst random forest (RF) voor de selectie van kenmerkende satellietproducten, en daarna pas k -Nearest Neighbour (k -NN). Dit verbeterde de efficiëntie van de AGB schattingen enorm, en een betrouwbare kaart van AGB werd verkregen voor het jaar 2009 ($R^2 = 0.62$ en $RMSE = 24.00$ ton ha^{-1}).

Voor het schatten van fluxen (NPP en ET) zijn in de afgelopen decennia twee soorten modellen gebruikt: procesmodellen en modellen gebaseerd op satellietdata. De laatste categorie van modellen is in staat om de ruimtelijke variabiliteit van het ecosysteem te voorspellen, maar de toepasbaarheid wordt beperkt door de beschikbaarheid van data. Procesmodellen beschrijven de interacties tussen ecosysteem en atmosfeer, maar de ruimtelijke representativiteit is gering. Resultaten van één locatie zijn daarom niet geldig voor andere locaties. In deze studie zijn de beide soorten modellen gecombineerd: het MODIS MOD 17 (MOD 17) model gebaseerd op satellietdata, en het procesmodel Biome-BioGeochemical Cycles (Biome-BGC) procesmodel. Door de twee te combineren is de kracht van beide benut. Het MOD 17 model voor Bruto Primaire Productie (GPP) is geoptimaliseerd door middel van drie databronnen, en de GPP schattingen zijn gevalideerd met EC metingen. Vergeleken met het originele MOD 17 GPP product (met $R^2 = 0.47$ en $RMSE = 20.27$ $gC\ m^{-2}\ 8d^{-1}$), is het geoptimaliseerde GPP model veel beter (met $R^2 = 0.91$ en $RMSE = 5.19$ $gC\ m^{-2}\ 8d^{-1}$). Het geoptimaliseerde product is verder gebruikt om Biome-BGC te kalibreren voor 30 representatieve locaties in het studiegebied. Het gekalibreerde Biome-BGC levert schattingen van NPP en GPP op fijne ruimtelijke én temporele resolutie. De nauwkeurigheid van het product was goed, bleek na validatie van GPP ($R^2 = 0.79$ en $RMSE = 1.31$ $gC\ m^{-2}\ d^{-1}$) en NEE ($R^2 = 0.68$ en $RMSE = 3.09$ $gC\ m^{-2}\ d^{-1}$) tegen EC data, en van AGB toenames ($R^2 = 0.72$ en $RMSE = 47.33$ $gC\ m^{-2}\ jaar^{-1}$) tegen dendrochronologie data. Door de AGB kaart van 2009 te combineren met AGB toenames, kon een goede schatting van de dynamiek van AGB worden gemaakt voor een periode van 13 jaar (2000 tot en met 2012).

Het model SEBS voor ruimtelijke ET uit satellietdata gebruikt de 'Monin-Obukhov Similarity' (MOS) theorie. In deze theorie zijn de verplaatsingshoogte d (m) en de ruwheidslengte z_{0m} (m) belangrijke parameters. Om deze twee parameters te

schatten, moeten ze geassocieerd worden structuurparameters: de horizontale (LAI) en de verticale projectie (FAI) van het bladoppervlak, de stamdichtheid en de hoogte van de bomen. Deze structuur parameters moeten op hun beurt geassocieerd worden met satelliet- en vliegtuigdata door middel van een model. In deze studie zijn vier modellen met elkaar vergeleken. Alle vier werden ze gedreven door data van een LiDAR op een vliegtuig en data van een satelliet: de 'Satellite Probatoire d'Observation de la Terre-5' (SPOT-5). Het beste model bleek het SD00 model te zijn, waarin LAI, FAI en de hoogte van de bomen worden gebruikt. Het SD00 model is vervolgens gebruikt om een tijdreeks van z_{0m} (m) en d the maken voor SEBS. Met deze verfijnde invoer van SEBS is de verdamping (ET) van de QMs gesimuleerd voor de periode 2000 tot 2012. De 8-daagse ET schattingen van SEBS zijn gevalideerd met EC metingen, waaruit bleek dat SEBS de variabiliteit van ET in ruimte en tijd goed wist te schatten. De ET schattingen van SEBS waren veel beter ($R^2 = 0.80$ en $RMSE = 0.21 \text{ mm d}^{-1}$) dan die van het MODIS product MOD 16 ($R^2 = 0.35$ en $RMSE = 0.76 \text{ mm day}^{-1}$).

De jaarlijkse verschillen in waterefficiëntie (WUE) van de bossen in het QMs zijn berekend als de verhouding tussen ANNP van Biome-BGC en ET van SEBS. De tijdserie van WUE is gebruikt om de effecten van het weer tijdens het groeiseizoen (april tot september) te analyseren. Er is een neergaande trend in ANPP, ET en WUE over de periode van 2000 tot 2012, maar er zijn ook grote verschillen tussen de jaren.

De gebruikte methode om AGB en ET te modelleren is reproduceerbaar en kan ook toegepast worden in andere biomen en andere klimaatzones. De realistische schattingen van AGB en ET over het Qiliangebergte, zoals verkregen in deze studie, ondersteunen de duurzame ontwikkeling van het ecosysteem en het beheer van de waterhuishouding.

Author's Biography

Xin Tian was born in February 1979 in Guizhou Province, China. He got the Bachelor Degree on the Environmental Science from Beijing Forestry University (BFU) in 2001 and then he got the Master Degree on Forest Management in 2004 from BFU. Since 2004, he has been working in the Research Institute of Forest Resource Information Techniques (IFRIT), Chinese Academy of Forestry (CAF) and he got the associate professor position at IFRIT in 2011. His research interests cover quantitative retrieval of forest structural parameters, forest eco-hydrological simulation, by use of multi-sensor remote sensing techniques.

This study was funded and supported by the 'Sandwich' PHD fellowship and Foundation Fellowship Program from the Faculty of Geo-Information Science and Earth Observation (ITC), University of Twente, the Netherlands. The research in this thesis was jointly funded and supported by National Basic Research Program of China (973 Program) (Grant 2013CB733404); National Natural Science Foundation (Grant 41101379); Fundamental Research Funds for the Central Non-profit Research Institution of IFRIT, CAF (Grant IFRIT201302); National High Technology Research and Development Program (863 Program) (Grant 2011AA120405); Dragon Forest (Grant ID_2583; ID_5314, ID_10666), Dragon Drought (Grant ID_2608; ID_5341; ID_10603) under the framework of the international cooperation "Dragon Programme" between the Ministry of Science and Technology (MOST) of the P. R. China and European Space Agency (ESA).

ITC Dissertation List

http://www.itc.nl/research/phd/phd_graduates.aspx